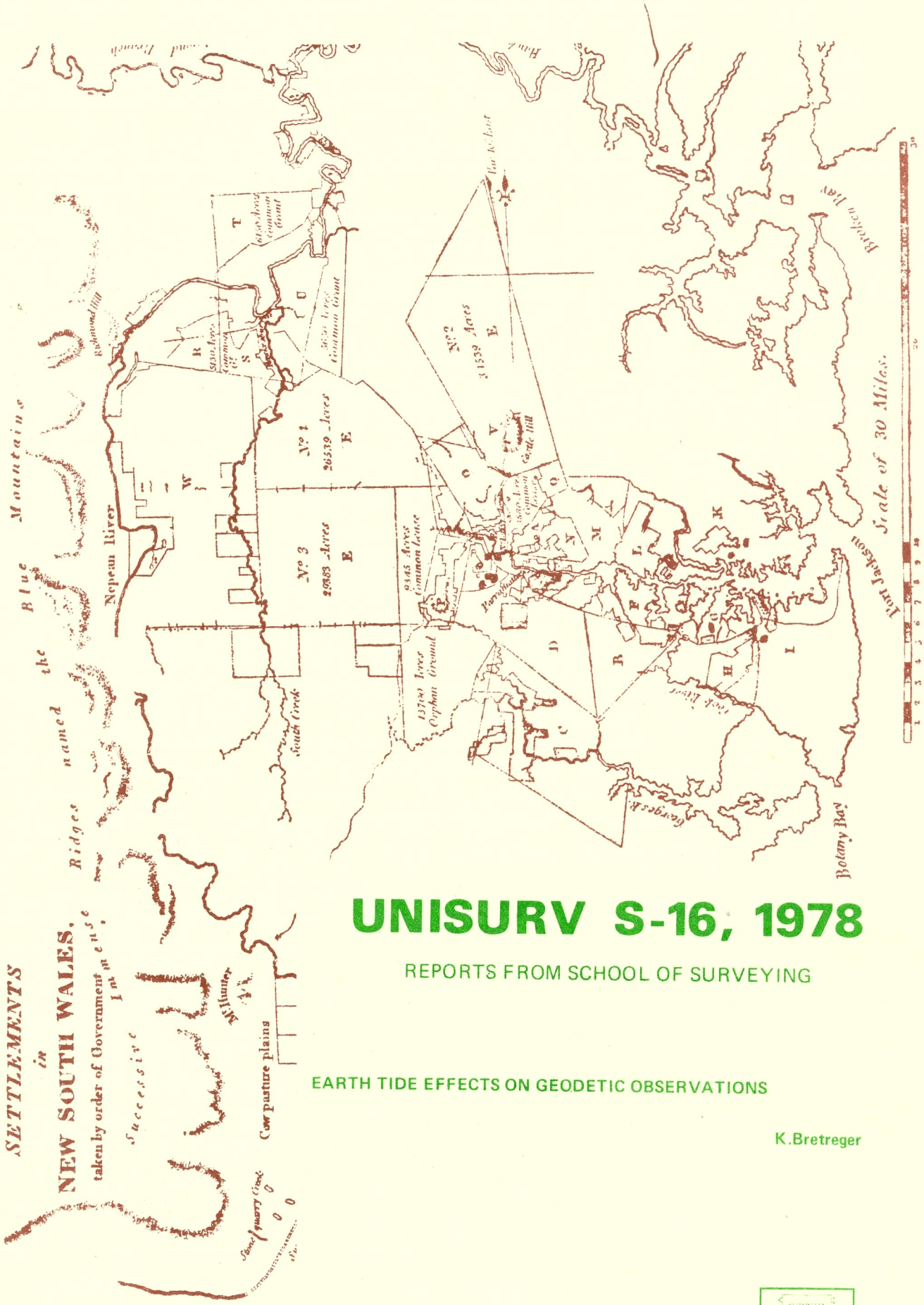

UNISURV S-16, 1978

REPORTS FROM SCHOOL OF SURVEYING

EARTH TIDE EFFECTS ON GEODETIC OBSERVATIONS

K.Bretreger

Published by
THE SCHOOL OF SURVEYING
THE UNIVERSITY OF NEW SOUTH WALES
SYDNEY, AUSTRALIA

UNISURV REPORT NO. S16, 1978

EARTH TIDE EFFECTS ON GEODETIC OBSERVATIONS

by

K. BRETREGER

Received January, 1978

SCHOOL OF SURVEYING,
THE UNIVERSITY OF NEW SOUTH WALES,
P.O. BOX 1,
KENSINGTON, N.S.W. 2033, AUSTRALIA.

National Library of Australia
Card No. and ISBN
0 85839 023 6

ABSTRACT

The Earth tide formulation is developed in the view of investigating ocean loading effects. The nature of the ocean tide load leads to a proposal of a combination of quadratures methods and harmonic representation being used in the representation of the loading potential. This concept is developed and extended by the use of truncation functions as a means of representing the stress and deformation potentials, and the radial displacement in the case of both gravity and tilt observations.

Tidal gravity measurements were recorded in Australia and Papua New Guinea between 1974 and 1977, and analysed at the International Centre for Earth Tides, Bruxelles. The observations were analysed for the effect of ocean loading on tidal gravity with a view to modelling these effects as a function of space and time. It was found that present global ocean tide models cannot completely account for the observed Earth tide residuals in Australia. Results for a number of models are shown, using truncation function methods and the Longman-Farrell approach.

Ocean tide loading effects were computed using a simplified model of the crustal response as an alternative to representation by the set of load deformation coefficients h'_n, k'_n. It is shown that a ten parameter representation of the crustal response is adequate for representing the deformation of the Earth tide by ocean loading at any site in Australia with a resolution of ±2 μgal provided extrapolation is not performed over distances greater than 10^3 km. This is assessed as being of sufficient accuracy for all purposes in high precision geodesy.

The formulation of solid Earth and ocean tide perturbations of satellites is reviewed, and these equations used to obtain graphs of the variations in the orbital elements of four satellites Beacon Explorer - C (BEC), GEOS 1, GEOS 2 and GEOS 3, with particular reference to the latter. The effect of Earth tides on satellite altimetry measurements is examined with the view of suitable corrections, if required.

A numerical estimate is given on the possibility of determining ocean tide models from satellite altimetry, based on the signal-to-noise ratio. The degradation of the analysis is obtained by progressively adding specified levels of randomly distributed white noise which simulates observational and orbital errors. The conditions for the successful recovery of tidal signals are dependent on the signal-to-noise ratio and this is a function of the particular tidal signal considered.

TABLE OF CONTENTS

NOTATION

Frequently used symbols are

Symbol	Meaning	§	Page
A_α	Azimuth of the ocean load from point of computation	5.2.2.2	47
a	Mean radius of the Earth	2.3.2	15
a_b	Semi-major axis of the disturbing body's orbit	2.1	9
a_s	Semi-major axis of the satellite orbit	7.2.1	90
c	A multiplying parameter	2.3.4	17
c_{lnm}	A parameter defining the ocean tide, related to amplitude	7.3	98
c_n	Multiplying parameter c of degree n	2.3.4	17
D_o	Undisturbed ocean depth	5.1.2	40
dm	An element of mass	2.3.2	15
dr	Radial displacement	2.4.1	18
$d\sigma$	An element of solid angle	2.3.2	15
E_s	Eccentric anomaly of the satellite	9.3.2	129
e_b	Eccentricity of the Disturbing body's orbit	7.2.2	95
e_s	Eccentricity of the satellite orbit	7.2.1	90
F_b	Disturbing function due to the disturbing body tide at satellite altitude	7.2.1	90
$F_{nmj}(i_s)$	Polynomial in terms of i_s	7.2.2	95
$F_{nmp}(i_b)$	Polynomial in terms of i_b	7.2.2	95
F_λ	Zonal component of the ocean bottom stress	5.1.2	40
F_ϕ	Meridional component of the ocean bottom stress	5.1.2	40
f	A Love number		
f_b	True anomaly of the disturbing body	7.2.1	89
f_e	Flattening of the Earth	2.3.3	16
f_s	True anomaly of the satellite	7.2.1	89
G	Gravitational constant	2.1	7
G_D	Doodson constant	2.1	9
$G_{njg}(e_s)$	Polynomial in terms of e_s	7.2.2	95
$G_{npq}(e_b)$	Polynomial in terms of e_b	7.2.2	95
g	Gravity at the Earth's surface	2.2	12
g'	Gravity at the tidal deformed Earth	2.4.2	19
H	Hour angle of the disturbing body	2.1	10
h	Mean longitude of the Sun	2.1	10
	Love number	2.4.1	18
	Height of a point on the Earth's surface	2.4.2	19
h_n	Love number h of degree n	2.4.1	18
h'_n	Load deformation coefficient of degree n	2.4.1	18
i_b	Inclination of the disturbing body's orbit	7.2.1	89
i_s	Inclination of the satellite, to the celestial equator	7.2.1	89
J_2	Second zonal harmonic of the Earth's potential	7.2.1	91
K_n	Multiplying parameter of degree n	5.2.3	53
k	Love number	2.3.2	16
k_n	Love number k of degree n	2.3.2	16
k'_n	Load deformation coefficient of degree n	2.3.4	17
L_b	Argument of latitude of the disturbing body	7.2.1	89
L_s	Argument of latitude of the satellite	7.2.1	89
l'_n	Load deformation coefficient of degree n	5.2.3	53
M( )	Global mean value of the enclosed quantity	-	

Symbol	Meaning	§	Page
M_b	Mean anomaly of the disturbing body	7.2.1	90
M_s	Mean anomaly of the satellite	7.2.1	90
m_b	Mass of the tide producing body	2.1	7
m_e	Mass of the Earth	7.2.1	89
N	Longitude of the ascending node of the Moon	2.1	10
n_b	Mean motion of the disturbing body	7.2.1	90
n_e	Earth's angular rate of rotation	5.1.2	40
n_s	Mean motion of the satellite	7.2.1	90
P_{no}	Legendre polynomial of degree n	2.1	7
p	Longitude of the lunar perigee	2.1	10
p_s	Longitude of perihelon	2.1	10
$\overline{P}_{nm}$	Normalised Legendre polynomial in n , m	5.2.2.4	51
R	Radius of the Earth	2.2	12
<R>	Modulus of the residual vector, obtained after ocean tidal solutions	9.2.4	125
R_b	Geocentric distance from the Earth to the disturbing body	2.1	7
R_p	Radius of the Earth at a point p	2.1	7
RA	Right ascension of disturbing body	Appendix A	143
r_b	Distance from a point on the Earth's surface to the disturbing body	2.1	7
r_s	Geocentric distance to the satellite	7.2.1	89
S_M	Unit surface mass	5.2.3	53
S_n	Surface harmonic of degree n	2.3.2	15
s	Mean longitude of the Moon	2.1	10
t	Mean solar time	-	
	A variable, = $\sin \frac{1}{2} \psi_0$	5.2.2.1	47
U	Deformation potential due to a load or external potential on the Earth's surface	2.3.2	15
U_1^o	Potential due to the ocean tide	7.3	98
U_n	Potential U of degree n	2.3.2	15
u	Eastward component of fluid velocity	5.1.2	40
V	Load potential due to a load on the Earth's surface	2.3.3	16
V_s	Potential due to redistribution of mass in Earth space due to loading at the Earth's surface	2.3.4	17
V''	Resulting potential due to deformation and stress	2.3.4	17
v	Northward component of fluid velocity	5.1.2	40
W_b	Tide producing potential	2.1	7
W_{ba}	Attractive potential due to the tide producing body	2.1	7
W_{br}	Potential causing a translational acceleration of the Earth	2.1	7
W_n	Tide producing potential of degree n	2.1	9
W_s^*	Potential of the tidally deformed Earth at satellite altitude due to the fictitious disturbing body	7.2.1	89
W'	Potential at the surface of the tidal deformed Earth	2.4.1	17
w_a	Speed of tidal wave	9.2.2	122
w_b	Argument of perigee of the disturbing body	7.2.1	89
w_s	Argument of perigee of the satellite	7.2.1	89
X_n	Function of ψ_0	5.2.2.1	47
X_α	Deflection of the vertical axes	2.4.2	20
Y_n	Function of ψ_0	5.2.2.2	48
α	Phase lag in relation to Earth tide results	4.3	32
α_a	Phase lag of the maximum tidal amplitude of the ocean tide, from cotidal charts	5.2.2.4	51

Symbol	Meaning	§	Page
α_n	Mean motion of the argument of the satellite Earth tide frequency	7.2.1	93
β	Mass of the disturbing body over the sum of masses of the disturbing body and the Earth	7.2.1	91
Γ	Potential of all tide generating forces with regard to ocean tides	5.1.2	40
γ	Diminishing factor in relation to Earth tide results	4.5	38
γ_{nmjg}	Function of the orbital elements of the satellite orbit	7.2.2	94
γ^b_{nmpq}	Function of the orbital elements of the disturbing body's orbit	7.2.2	94
Δt	Lag in the body tide	5.2.2.4	50
δ	Declination of the disturbing body	2.1	10
	Amplitude factor in relation to Earth tide results	4.3	32
δ_E	Geocentric solid Earth tide height	5.1.2	40
δg	Change in gravity due to Earth tides	2.4.2	19
δg_o	Change in gravity due to Earth tides and the outer zone contribution to the ocean loading effect	6.3	61
δl	Horizontal component of the surface displacement due to ocean tide loading	5.2.3	53
δN	Change in geoid height	2.4.3	19
δr	Vertical component of the surface displacement due to ocean tide loading	5.2.3	53
δW	Change in geopotential	2.4.1	18
δW_u	Change in geopotential at the undeformed surface due to ocean tide loading	5.2.3	53
δx	Earth tide perturbation in the orbital element x	7.2.1	92
δ_{om}	Kronecker delta	7.2.2	95
$\delta\xi_\alpha$	Change of the deflection of the vertical in the meridian and prime vertical components	2.4.3	19
$\delta\rho_T$	Change in density from a deformation	2.3.2	15
ε_{lnm}	Parameter defining the ocean tide, related to phase	7.3	99
ϵ_{nmpq}	Function of the time lag, Δt	7.2.2	95
ζ	Ocean tide height	2.3.3	16
ζ_a	Ocean tide amplitude, from corange charts	5.2.2.4	51
ζ_n	Ocean tide height of degree n	2.3.3	16
ζ_s	Ocean tide amplitude obtained by solution	9.2.4	124
$\zeta_{\alpha n1}$	Harmonic coefficient based on ζ	5.2.2.2	48
ζ'	Function of ζ	5.2.2.3	49
$\zeta'_{\alpha n1}$	Harmonic coefficient based on ζ'	5.2.2.3	50
$\overline{\zeta}$	Fictitious equilibrium tide	5.1.2	40
$\overline{\zeta}_\alpha(\theta)$	A sum of $\overline{\zeta}_{\alpha nm}$ and $\overline{\zeta}'_{\alpha nm}$	5.2.2.4	51
$\overline{\zeta}_{\alpha nm}$, $\zeta'_{\alpha nm}$	Surface spherical harmonics of the ocean tidal heights from cotidal-corange charts	5.2.2.4	51
θ	Sidereal time	2.1	10
θ_b	Reference meridian hour angle of the tide producing body	5.2.2.4	51
θ^*_b	$= \Omega_s - \Omega^*_b$	7.2.1	89
θ_G	Reference meridian sidereal time	5.2.2.4	50
λ	Longitude of a point on the Earth	-	
ν_{lnmjg}	Phase relationship for the ocean tidal effect on satellite orbits	7.3	98
ρ_e	Mean density of the Earth	2.3.3	16
ρ_w	Density of the ocean	2.3.3	16
σ	Sidereal rotation	7.3	98
σ_n	Surface density	5.2.3	53
τ	Mean lunar time	2.1	10

Symbol	Meaning	§	Page
$\Phi(\psi)$	Function of ψ	5.2.2.1	46
$\overline{\Phi}(\psi)$	Function of ψ	5.2.2.1	47
$\Phi_2(\psi)$	Function of ψ	5.2.2.2	48
$\overline{\Phi}_2(\psi)$	Function of ψ	5.2.2.2	48
ϕ	Latitude of a point on the Earth	2.1	10
ψ	Geocentric angle between a point on the Earth's surface and a load on the Earth's surface	2.1	7
ψ_b	Geocentric angle between a point on the Earth's surface and the disturbing body	2.1	7
ψ_b^*	Geocentric angle ψ_b, referred to the fictitious disturbing body	7.2.1	89
ψ_0	A particular angle for ψ, differentiating the inner and outer zones	5.2.2.1	46
Ω_b	Longitude of the ascending node of the disturbing body's orbit	7.2.1	90
Ω_s	Longitude of the ascending node of the satellite orbit	7.2.1	90
$\dot{\Omega}_s$	Secular motion of the satellite orbit node	7.2.1	91
$O\{\ \}$	Order of magnitude of the enclosed quantity		
$\dot{x}$	Mean motion of the orbital element x	7.2.1	93
N	Superscript: Newtonian part of the parameter	5.2.3	54
E	Superscript: Elastic part of the parameter	5.2.3	54
*	Superscript: Orbital element referred to the fictitious disturbing body	7.2.1	89

ABBREVIATIONS

ANU	Australian National University, Canberra
BMR	Bureau of Mineral Resources, Geology and Geophysics, Canberra
GEO	Geodynamics gravimeter
GMT	Greenwich Mean Time
ICET	International Centre for Earth Tides, Bruxelles
LCR	La Coste Romberg Gravimeter
LTE	Laplace Tidal Equations
MSL	Mean Sea Level
UNE	University of New England, Armidale
UNSW	University of New South Wales, Sydney
UT	Universal Time
UTAS	University of Tasmania, Hobart
UQ	University of Queensland

CONVENTIONS

A vector is represented in the form

$$\vec{R} = X_i \vec{i}$$

being a vector with components X_1, X_2 and X_3 along the rectangular co-ordinate axes which are represented by the unit vectors 1, 2 and 3.

A scalar product is defined as

$$\vec{X} \cdot \vec{Y} = X_i \; Y_i$$

$$= X_1 Y_1 + X_2 Y_2 + X_3 Y_3 \; .$$

While the operator $\vec{\nabla}$ is defined as

$$\vec{\nabla} = \frac{\partial}{\partial x_i} \vec{i} \; .$$

Thus,

$$\vec{\nabla} F = \frac{\partial F}{\partial x_i} \vec{i} \; .$$

INDEX OF FIGURES AND TABLES

FIGURES

TABLES

ACKNOWLEDGEMENTS

The author is indebted to Associate Professor R.S. Mather for supervision and assistance during the preparation of this thesis.

The Earth tide project in Australia was a cooperative program between the International Centre for Earth Tides (ICET), the Department of Geodesy at the University of New South Wales and the Government of Australia's Bureau of Mineral Resources, Geology and Geophysics, Canberra (BMR). Financial support for the activities of the Department of Geodesy was provided by the Australian Research Grants Committee.

Valuable assistance with regard to gravimeter operations was given by Messrs. B. Barlow and J. Van Son of the BMR and Dr. B. Ducarme and Professor P. Melchior of the ICET. The cooperation of the staff of the BMR, the Mines Branch of the Department of the Northern Territory, the Australian National University and the Universities of New South Wales (Department of Physics at Broken Hill), Queensland (Seismic Station, Charters Towers), New England (Cooney Geophysical Observatory) and Tasmania (Department of Geology) is appreciated during the project.

I am grateful for all members of staff and post-graduate students of the School of Surveying for their useful discussions and comments. Assistance with computing given by Messrs. B. Hirsch and W. Kent of the School of Surveying is acknowledged. I would also like to thank Mrs. Sue Kiriazis for typing the final draft and the tables.

In the final year the author held a DAAD Scholarship, and valuable supervision and assistance was obtained from the staff at the following institutions: Institut für Physikalische Geodäsie, Darmstadt, Institut für Theoretische Geodäsie, Hannover, Geodätisches Institut, Karlsruhe and the Institut für Theoretische Geodäsie, Bonn.

During the project, the author held a Commonwealth Postgraduate Research Award.

CHAPTER 1
INTRODUCTION

1.1 Significance of the Project

The gravitational attraction of the Moon and Sun causes periodic elastic deformations of the Earth. This response of the Earth appears as a small elongation of the Earth's shape in the Earth-Moon or Earth-Sun line. The perturbations and their instantaneous amplitudes can be calculated from the orbital elements of the Earth, Moon and Sun together with their masses. Such calculations assume a rigid Earth, which is not the case with radial deformations which reach amplitudes of 25 centimetres.

The effectsof the deformation include small periodic deviations of the vertical (approximately 0.02 arc seconds in amplitude), variations of the gravitational acceleration (amplitude of 200 μgals), variations in the radial distance to the centre of the Earth, variable internal strains and periodic volumetric expansions within the Earth. The radial deformation cannot be measured directly at present, but can be derived from gravity and tilt measurements.

The complex nature of the deformations can be simplified by representing the phenomena by spherical harmonic functions dependent on motion of the orbital elements of the Moon and Sun.

A comparison between the observed phenomenon and those calculated from an ideal rigid Earth model provides the basis of research in the Earth tide field. The amplitude ratios and phase differences for the major harmonic waves leads to much geophysical discussion.

The measurements of Earth tides at any site in the world generally does not represent the solid Earth deformation alone, but are contaminated by ocean tides, geological, tectonic and meteorological effects. The ocean tide effects usually dominate, but are complex and difficult to evaluate as the periods of the ocean tides are the same as those of the Earth tides. Of the Earth tide instruments, the gravimeter is less affected by local conditions than the tiltmeter and extensometer (strainmeter), thus representing a predominately global response.

One of the most important geodetic effects, the radial deformation is described by a Love number (see Section 2.4) which can be determined indirectly from a combination of gravimeter and horizontal pendulum data. The gravimeter measures changes in the gravitational attraction due to the variable luni-solar attraction. The instrument consists of a horizontal beam supported by a spring counterbalancing the gravitational attraction. Thus any change in the gravitational attraction causes a deflection of the beam which is amplified and measured. The horizontal pendulum, measuring tilts of the Earth's surface, consists of a pendulum suspended by two fine quartz threads and rotates around a nearly vertical axis under horizontal forces, in the case of Verbaandert-Melchior pendulums. Such data is also being recorded using vertical pendulums (MELCHIOR 1974).

Geodetic observations based on laser ranging to either the Moon or to orbiting satellites have an internal precision of less than 10 centimetres. Theoretical models for radial deformation, based on global data are not adequate for the geodetic reduction of these observations due to regional disturbances, departures of the Earth from a rigid body, interactions between the solid Earth and oceans, and also the effects of a liquid core. With the provision of both gravimeters and tiltmeters, the radial displacement can be adequately modelled, with a precision better than that of lunar laser ranging and satellite ranging.

Considerable advancements have been achieved in the Earth tide field in the last twenty years. Extensive Earth tide observations, particularly gravimeter measurements have been recorded over most of the Northern Hemisphere. The International Centre for Earth Tides (ICET) is currently involved in the Trans World Tidal Gravity Profile Program, where the main Earth tide constants (amplitude factor and phase) are determined at selected sites throughout the world. Profiles in the USA, Europe, through Asia to Australia and the western Pacific Islands have been completed. The observations in Australia and the neighbouring islands represent the first comprehensive program of tidal gravity measurements undertaken over a significant area in the Southern Hemisphere.

Recent research in Earth tides covers a number of fields including astronomy, space dynamics, gravimetry, oceanography, the Earth's interior and local deformation effects in tunnels and cavities. The relationship between the precession-nutation phenomena and Earth tides can be found in MELCHIOR (1971b, Vol. 4). Measurements with Earth tide instruments will lead to information on the liquid core in addition to precession and nutation.

The periodic and irregular variations in the rotation of the Earth, including polar motion, have a similar relationship to Earth tides (DJUROVIC & MELCHIOR 1972). The variations in time have produced a number of numerical results for the Love number k, which agree well with other geophysical determinations. In the immediate future, information on the secular retardation of the Earth's rotation and the dissipation of energy by internal friction should be obtained. The phase lag obtained from Earth tide gravimetric measurements of the semi-diurnal sectorial waves is a component of these factors. Ocean tides also produce a deceleration in the rotation, through friction on the ocean floor. Numerous attempts have been made to estimate the extent of this energy dissipation (see MELCHIOR 1974), based on ill defined data, although the calculations gave values with the same order of magnitude, between 1×10^{12} and 4×10^{12} watts. Further research in this field involves the correct evaluation and separation of the constituents of the dissipations.

The effects of the tidal potential on artifical satellite orbits has been evaluated by observations on various satellites, and can perturb the satellite by 50 metres. Investigations of such perturbations has lead to determinations of the Love number k_2. Recent research (LAMBECK ET AL 1974) has shown that these determinations were in error as much as 15% because the ocean tides were neglected. Research in this area is still continuing, together with attempts to solve the inverse problem where information on the ocean tides can be inferred from satellite perturbations (FELSENTREGER ET AL 1976, RUBINCAM 1976).

Laser distance measurements to the Moon and satellites could reach a precision of a few centimetres in the foreseeable future. Such accuracy needs an experimental determination of the tidal radial deformation for a reliable Earth model for the reduction of ranges from Earth stations to objects in space. This is especially important in the case of the lunar laser ranging system operating from Orroral near Canberra (DUCARME ET AL 1976).

The deformation measured by any Earth tide instrument is subject to the loading effects of ocean tides. Consequently, the sites in Australia were selected to provide a sampling of the response to the tide producing forces as a function of distance from the coastline. It was hoped that this information, along with the data collected using the Verbaandert-Melchior horizontal pendulums at Cooney Observatory, Armidale (BARLOW ET AL 1973) would provide a basis for quantifying the radial displacement of the Earth tide at any location on the Australian land mass at the 2 centimetre level. Information of this nature is important if systematic errors are to be avoided when using data from stations at different distances from the coastline for obtaining high precision geodetic information from quasi-radial range data to objects in Earth orbit.

Initial research into the oceanic effects on Earth tides involved the calculation of ocean loading from ocean tidal models and on the empirical separation of observed and theoretical Earth tide effects. Research has begun on solving the inverse problem, where ocean tidal models are improved from Earth tide measurements at selected global stations (JACHENS & KUO 1973).

The observations in Australia could provide valuable information for studying the short period variations in the heights of the sea surface topography. The data on sea surface topography was collected in the Coral Sea, while the gravimeters were operating in Australia, from satellite altimeter measurements as part of operations during the National Aeronautics and Space Administration's (NASA's) GEOS 3 mission. Improvements in the local ocean models could also be derived from this satellite altimeter data.

Research into tiltmeter observations has shown that perturbations can originate from the shape of the tunnel or cavity in which the instrument operates (HARRISON 1976). Further study should reveal optimum conditions for instrument location.

A fundamental objective in the study of Earth tides is the determination of the Love numbers, which will give information on the dynamical effects of the liquid core. Love numbers are not very sensitive to variations of the parameters describing various models of the Earth's overall internal structure. The discovery of free oscillations and their detailed analysis has led to progress in the construction of such models (LECOLAZET & MELCHIOR 1975). The determination of the tidal lag with respect to the acting potential should provide information on the Earth's viscosity.

The tidal results in Australia will be helpful in the reduction of high precision gravity measurements. The results will insure that no systematic errors can be introduced into the Australian gravity baselines through incorrect theoretical corrections.

Further conclusions and discussions in these fields will only be forecoming with an extension of the global coverage of the Earth tide observations.

1.2 Method of Analysis

The determination of Earth and ocean tide interactions can be obtained from both terrestial observations and satellite perturbations. Further discussion will primarily centre upon a model for the representation of the ocean loading effects on the Australian continent. Additional information, both on a regional and global basis can also be obtained from satellite studies. The tidal perturbations on satellites are discussed in Chapters 7 and 8, where an accurate model is needed for the ocean loading effect and for the tidal perturbations on the satellite orbit if high precision is required. The interaction between these two areas could lead to improvements in ocean tide models from satellite observations and land based observations. The study of the Earth's deformation due to the interaction of Earth and ocean tides involves a technique based on the use of truncation functions.

There are four constituent potentials which need to be considered in any Earth tide study at the Earth's surface, the tide producing potential, the deformation potential, the load potential and the stress potential. It is conventional to represent the tide producing and deformation potentials in terms of the source potential by the use of Love numbers and load deformation coefficients (see Section 2.4). The analytical function of these coefficients is the representation of the deformation and stress effects due to a complex loading at the Earth's surface. The Earth deformation effect on observations can be represented to better than 1% by a single parameter, when the deformation potential has a second degree structure (to 1%). In the case of the load due to ocean tides, the prevalent interpretation of the existence of several amphidromes suggests a complex nature. If the tidal deformation and the associated stress response due to the oceans are capable of representation by a finite set of parameters, the ocean effects can be solved with a truncation function procedure. Together with the surface integration procedures for local effects, the technique is a means for separating global influences from local contributions which produce significant signals especially in tilt measurements.

The geodetic parameter of interest when measuring ranges from the Earth's surface to reflectors or transmitters in Earth orbit, is the radial displacement due to the solid Earth tide and the ocean loading tide. High precision geodetic measurements and subsequent analyses should exclude positional variations which are shorter than an epoch of observation (say between 6 months and a year). This exclusion can be achieved by removing the effect of shorter period variations like Earth tides by modelling and making allowances for model improvement in solution procedures (MATHER 1974). The precision required is between ±5 cm and ±1 cm, preferably the latter. The influence of tidal effects on observations at a single site could possibly be characterised as random over long periods of time. The deduction of geodetic parameters from sites which are differently affected by ocean loading could be subject to bias of significant magnitude especially when interpreting results from data collected over limited periods of time.

The effect of tidal loading on gravity (approximately 10% of the observed tide in Australia) is mostly due to tidal loading patterns on a global scale. The influence of tiltmeter observations could be very large at coastal stations, due primarily to the local ocean tides. The loading on tiltmeter measurements reduces to about one tenth of its magnitude or less at inland sites in the major continental areas. The global analysis of the O_1 Earth tide suggests that the deformation potential and the radial body tide can each be separately represented to about 3% by the Love numbers k_2 and h_2 respectively (MELCHIOR 1973b). GROTEN (1970) showed that the nature of the ocean tidal load leads to a solution of a combination of quadratures methods and harmonic representation as a representation of the loading potential. This concept is reviewed (see Section 5.2), and extended by the use of truncation functions as a means of representing the stress potential, deformation potential and the radial displacement in the case of both gravity and tilt observations.

In addition, a development is outlined in Section 5.2.2.3 on the use of a finite set of parameters to characterise the Earth response to the ocean tidal loading. These parameters could provide an alternative to the conventionally used load deformation coefficients inview of the lack of convergence of the latter representation and the possibility that the Earth response can be characterised to the required 2% level by a limited set of parameters (see Section 5.2.2.3). The procedure proposed is based on a recognition of the nature of the ocean tidal loading, assumed to be known in the form of cotidal-corange information, as the dominant influence on the apparent complexity of the loading effects on gravity and tilt measurements.

The radial response at a point due to ocean tidal loading is a function of

a) the model adopted for the load,
b) the relation to the coastline, and
c) time.

It may be possible for the radial displacement due to loading in the case of an island like Australia to be usefully represented by a relation of the form

$$dr = \Phi_1(\psi) \quad \Phi_2(\alpha) \quad \Phi_3(\theta_G)$$

where ψ is the angular distance from the coast, α the azimuth from the land mass centroid and θ_G is Greenwich Sidereal Time. The exact nature of the function is the subject of investigations and probable forms are given in Section 5.2.

The experiment should provide an assessment of whether the global oceanic tidal models are of adequate precision for the representation of long wave (low degree) features of the oceans for use as a priori input data in the pre-processing of high energy mode satellite altimetry data collected from GEOS 3 off north-eastern Australia. The goal to be achieved is a model for the low degree harmonics with errors of less than 20%.

In an attempt to model ocean loading effects in Australia and Papua New Guinea, a simplified model of the crustal response is developed in Section 6.7 as an alternative to representation by the set of load deformation coefficients h'_n, k'_n. The objective was a model for the Earth response which can generate the ocean loading effect on tidal gravity at any point on the Australian mainland so that it is adequate for correcting quasi-radial distance measurements to extra-terrestrial sources in Earth orbit for the effect of Earth tides to ±2 cm in conjunction with adequate supplementary tiltmeter data.

Satellite altimeter measurements currently obtained from the GEOS 3 satellite contain information on the shape of the sea surface. If the altimetry is of sufficient precision there is a possibility of obtaining ocean tide models which could improve present cotidal-corange charts. A numerical estimate is given (see Section 9.2) on the possibility of determining these models from satellite altimetry, based on the signal-to-noise ratio. The degradation of the analysis is obtained by progressively adding specific levels of randomly distributed white noise, which simulates observational and orbital errors.

All geodetic measurements between the Earth's surface and the orbiting satellite are influenced by solid Earth tidal forces. Such forces perturb all orbital elements, although some only have short period durations. The ocean tides also perturb the satellite orbits, and there is a possibility of obtaining ocean tide models from the analysis of such perturbations. A formulation of both solid Earth and ocean tide perturbations is reviewed, and the resultant variations of the orbital elements is given in Sections 7.2 and 7.3. Satellite altimeter measurements are also influenced by Earth tide forces, although the magnitude of the perturbations have yet to be determined. The radial perturbations on the GEOS 3 satellite are determined, based on the formulation given in Chapter 7. Such determinations give an indication of the corrections necessary to obtain a precision at the one centimetre level.

1.3 Synopsis of Contents

The tidal theory is developed in Chapter 2, where the tidal potential is formulated for degrees two and three. A spherical harmonic representation of the potential produces four wave types, long period, diurnal, semi-diurnal and ter-diurnal tidal waves. These harmonic developments of the lunar and solar tide are given in Appendix A, where each tidal wave is expressed as a function of independent variables which have a linear response with time. The potential is differentiated in Section 2.2 to obtain the vertical and horizontal components of the tidal force. The elastic characteristics of the Earth generates further constituent potentials which need to be considered in the analysis of Earth tide measurements. The constituent potentials expressed in terms of Love numbers and load deformation coefficients, and referenced to the tide producing potential are formulated in Section 2.3. The corresponding changes in potential, gravity and deflection of the vertical are developed in Section 2.4.

In any study of geophysical data, it is important that the principles underlying the instrumentation be understood, together with its accuracy and limitations. The operation of gravimeters together with their optimum operating conditions are discussed in Chapter 3. In gravimetric tidal measurements, the recordings are effected by instrument drift. The causes of instrument drift are discussed and various methods of limiting, correcting and eliminating the drift outlined. A source of systematic error in all gravimetric measurements involves the correct calibration of the gravimeter. Various methods of calibrations are discussed together with the merits of each method.

An outline of the gravimetric observations in Australia can be found in Chapter 4. The reasons behind the site selections and their descriptions are discussed. Location sketches of the sites are presented in Appendix B. Instrumental difficulties and characteristics for the period of observations

are outlined, together with a presentation and interpretation of the final analyses.

The theoretical development for the use of truncation functions in Earth tide studies is given in Chapter 5. The characteristics of the functions and their relationship to conventional formula are discussed. Such developments are necessary due to the large ocean tide perturbations on any Earth tide measurements. All calculations for these perturbations are based on regional and global charts for ocean tides. Various researchers have produced global ocean models, which vary in their method of solution and limitations imposed. The differences between a number of models are discussed in this Chapter, together with a general introduction to ocean tides.

The formulation developed in Chapter 5 is utilised in ocean loading calculations in Australia, and shown in Chapter 6. The calculations are in two parts, the outer and inner zone effects, with conservation of mass being an important criteria for ocean tidal models. A comparison between the truncation function method and the Longman-Farrell method (see Section 6.6) is also given. A study of the radial deformation of the Earth tide by ocean tides with a view to providing data for modelling the tidal correction is discussed in Section 6.7.

In the study of satellite geodesy, corrections for Earth tides are necessary at the satellite altitude level. Chapter 7 presents theory for these perturbations, in both a simplified development of the main tidal waves and in a full general development. The formulation for the ocean tide perturbations on satellites is also outlined.

Chapter 8 presents the results of the theory developed in the previous Chapter on four satellites, BEC, GEOS 1, GEOS 2, and GEOS 3. The principal perturbations in the orbital elements are given in various tables, with the total perturbations presented in the form of graphs over a reasonable time span. A detailed study of GEOS 3 satellite is reported, consisting of both short and long period tidal perturbations.

Improvements in ocean tide models can possibly be obtained from satellite altimetry studies. Chapter 9 studies the effects of Earth tides on the satellite altimeter measurements, and determines the corrections, if necessary, to obtain accurate determinations. The magnitude of the corrections is dependent on the method of orbit determination. A preliminary study is also presented on the possibility of obtaining ocean tide signals from satellite altimetry measurements. This analysis is obtained by predicting an ocean height, and progressively increasing the noise level in subsequent analyses and determining the ability to recover the former at each noise level.

The conclusions and recommendations are presented in Chapter 10. This involves a discussion of the Australian results, with regard to ocean loading, and a comparison between various ocean tide models as to the best fit for the Australian results. The limitations and accuracy of the truncation function method is also discussed. The errors associated with Love number determinations from satellites is mentioned, including the effect of ocean tides on the determinations. Conclusions on the possibility of recovering ocean tide signals from satellite altimetry is also discussed.

CHAPTER 2

DEVELOPMENT OF TIDAL THEORY

2.1 Development of the Tidal Theory

In determining the oceanic perturbations on Earth tides, the appropriate tidal development should include ocean-Earth interactions in the theory.

This Chapter formulates both Earth tide and ocean tide potentials with their components. The presentation is developed in MATHER & BRETREGER (1975).

The tide producing potential, W_b can be represented by the equation

$$W_b = W_{ba} + W_{br} \tag{2.1}$$

where W_{ba} is the attractive potential due to the tide producing body B and W_{br} is the potential causing a translational acceleration of the Earth about the centre of mass of the Earth-Body system. W_{br} is evaluated by using the condition that the gravitational acceleration due to the tide producing body balances the centrifugal acceleration at the geocentre G (see Figure 2.1). Thus,

$$(\vec{\nabla} W_{ba})_G = - (\vec{\nabla} W_{br})_G \tag{2.2}$$

Assuming that the Earth's departures from rigidity are inconsequential for this purpose,

$$(\vec{\nabla} W_{br})_p = (\vec{\nabla} W_{br})_G \tag{2.3}$$

being independent of position for all points constituting the rigid Earth. Further,

$$\begin{aligned} (W_{br})_p - (W_{br})_G &= - (\vec{\nabla} W_{br} \cdot \vec{R}_p) \\ &= (\vec{\nabla} W_{ba})_G \cdot \vec{R}_p \end{aligned} \tag{2.4}$$

$\vec{R}_p$ being the position vector from the geocentre to P. W_{ba} can be represented as

$$\begin{aligned} (W_{ba})_p &= \frac{G m_b}{r_b} \\ &= \frac{G m_b}{R_b} \sum_{n=0}^{\infty} \left(\frac{R_p}{R_b}\right)^n P_{no} (\cos \psi_b) \end{aligned} \tag{2.5}$$

where G is the gravitational constant and m_b the mass of the tide producing body. The term $1/r_b$, being replaced by a Legendre polynomial, in degree n

$$\frac{1}{r_b} = \frac{1}{R_b} \sum_{n=0}^{\infty} \left(\frac{R_p}{R_b}\right)^n P_{no} (\cos \psi_b)$$

where R_b is the geocentric distance from the Earth to the disturbing body, and r_b is the distance from P to the disturbing body.

The total tide producing potential $(W_b)_p$ at P can be represented by

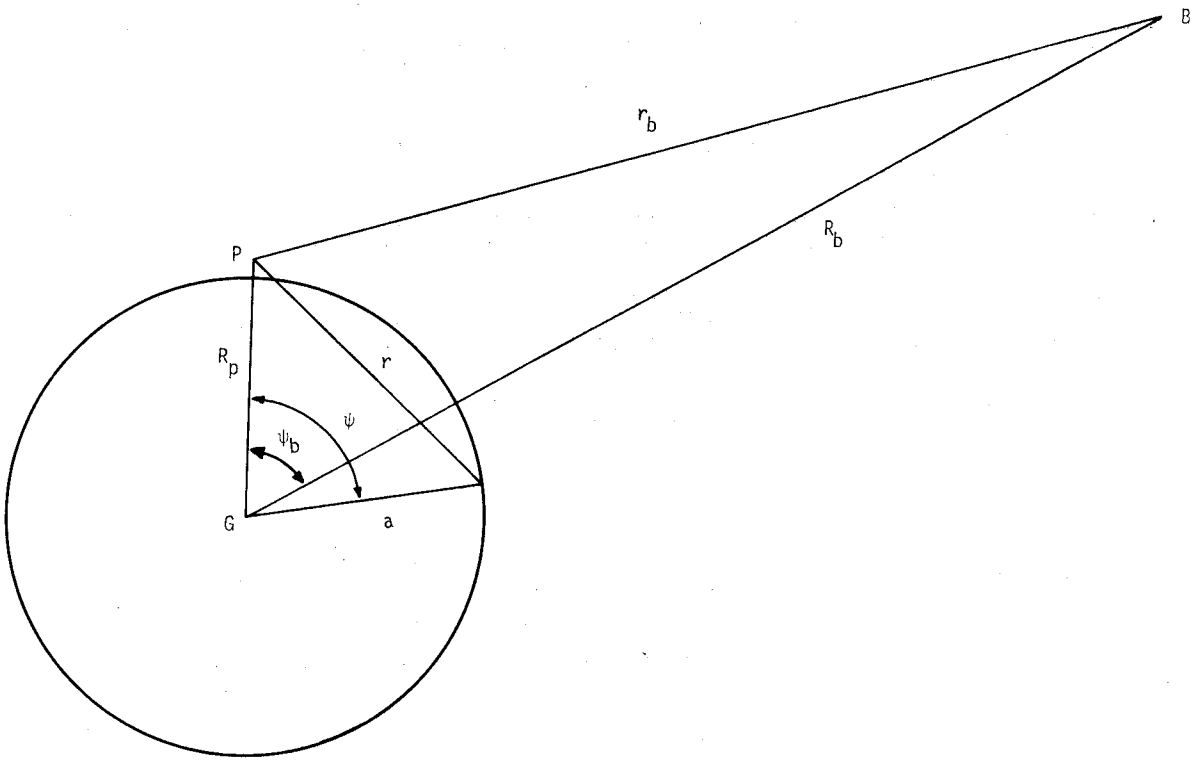

FIGURE 2.1
The Tide Producing Potential

$$(W_b)_p = (W_{ba})_p + (W_{br})_p$$

$$= (W_{ba})_p + (W_{br})_G + (\vec{\nabla}\ W_{ba})_G \cdot \vec{R}_p \qquad (2.6)$$

on using equations 2.1 and 2.4. The application of equation 2.5 gives

$$(\vec{\nabla}\ W_{ba})_G \cdot \vec{R}_p = - \frac{G\ m_b}{R_b^2}\ (1 + 0\ \{\ 10^{-2}\}\ )\ R_p \cos \psi_b \qquad (2.7)$$

which is numerically equal to the term of degree one in equation 2.5 to the stated order of precision.

As the tide producing potential at the geocentre is zero,

$$(W_{br})_G = - (W_{ba})_G$$

$$= - \frac{G\ m_b}{R_b} \qquad (2.8)$$

If $(R_p\ /\ R_b) \simeq 10^{-2}$, the third term in equation 2.5 is of order 10^{-6} and can be ignored in solutions correct to 1%. Using equations 2.7 and 2.8 in equation 2.6,

$$(W_b)_p = \frac{G\, m_b}{R_b} \left(\frac{R_p}{R_b}\right)^2 P_{20} (\cos \psi_b) \left[1 + 0 \{ 10^{-2} \} \right] \qquad (2.9)$$

It therefore follows that under the conditions above, the tide producing potential can be described by a zonal harmonic of the second degree to about 1%, the pole of the harmonic lying on the line joining the geocentre to the tide producing body.

The majority of the remaining 1% can be described by the addition of the third degree term.

The corresponding second and third degree representation of the potential, expressed in general terms are

$$W_2 = G_D \left(\frac{a_b}{R_b}\right)^3 (\cos 2\psi_b + 1) \qquad (2,10)$$

$$W_3 = G_D \left(\frac{a_b}{R_b}\right)^4 \left(\frac{R_p}{a_b}\right) (5 \cos^3 \psi_b - 3\cos \psi_b) \qquad (2.11)$$

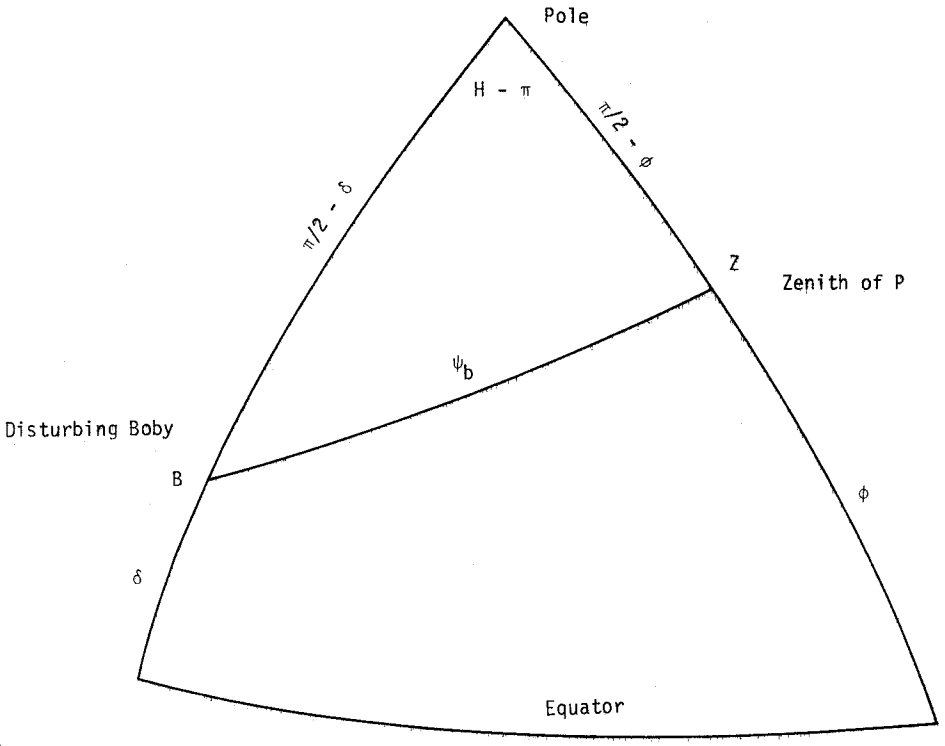

FIGURE 2.2
The Spherical Triangle

where a_b is the semi-major axis of the disturbing body's orbit, and G_D is the Doodson constant, and expressed as

$$G_D = \frac{3}{4} G\, m_b \frac{R_p^2}{a_b^3}$$

The potential, given by equations 2.10 and 2.11 is expressed in terms of the local coordinate ψ_b

of the perturbing body, and can be eliminated by the use of the spherical triangle, shown in Figure 2.2.

In the spherical triangle, ϕ is the latitude of the point of observation P, δ the declination of the disturbing body, and H the hour angle of the disturbing body.

By using the expression,

$$\cos \psi_b = \sin \phi \sin \delta + \cos \phi \cos \delta \cos (H - \pi)$$

equations 2.10 and 2.11 become

$$W_2 = G_D \left(\frac{a_b}{R_b}\right)^3 \left[3\left(\frac{1}{3} - \sin^2 \delta\right)\left(\frac{1}{3} - \sin^2 \phi\right) - \sin 2\phi \sin 2\delta \cos H + \cos^2\phi \cos^2\delta \cos 2H \right] \quad (2.12)$$

$$W_3 = G_D \left(\frac{a_b}{R_b}\right)^4 \left(\frac{R_p}{a_b}\right) \left[\frac{1}{3}(\sin \phi - 5\sin^3 \phi)(3\sin \delta - 5\sin^3 \delta) - \tfrac{1}{2}\cos \phi(1 - 5\sin^2 \phi) \cos \delta (1 - 5\sin^2 \delta) \cos H + 5\sin \phi \cos^2\phi \sin \delta \cos^2\delta \cos 2H - \frac{5}{6} \cos^3\phi \cos^3\delta \cos 3H \right] \quad (2.13)$$

The terms in equation 2.12 represent three types of surface spherical harmonic functions of the second order. The first, a long period term is a zonal function and is dependent only on latitude. The second, a tesseral function has diurnal characteristics, with the amplitude being maximum at latitudes of $\pm 45^\circ$ when the declination of the disturbing body is maximum. At the poles and the equator, the function is zero. The third term is a sectorial function, with semi-diurnal periods and the amplitude is maximum at the equator when the declination of the disturbing body is zero. The function is zero at the poles and also on the meridians located 45° on either side of the meridian beneath the perturbing body. These three types of spherical harmonics are illustrated in Figure 2.3.

The attractive force of other celestial bodies acting on the Earth also produces tide generating forces in addition to the Luni-solar constituents. These other celestial bodies are too distant from the Earth to exert any appreciable effects (MELCHIOR 1966).

The expressions for the potential given by equations 2.12 and 2.13 vary periodically, but are not suitable for tidal analysis due to the complex nature of the variables. The equations can be expressed by a finite series of harmonic terms with fixed maximum amplitudes and frequencies. The harmonic development is a function of six independent variables, which exhibit a linear response with time. These variables are

τ the mean lunar time,
s the mean longitude of the Moon,
h the mean longitude of the Sun,
p the longitude of the lunar perigee,
N the longitude of the ascending node of the Moon, and
p_s the longitude of perihelion,

a combination of these variables can define mean solar time t, and sidereal time θ.

The harmonic development of the potential for the Moon and Sun is conventionally expressed as

Long Period Waves:

$$\tfrac{1}{2}\, G_D\, (1 - 3\sin^2 \phi)\, A_i \cos (\alpha_i)$$

Diurnal Waves:

$$G_D \sin 2\phi\, A_i \sin (\alpha_i)$$

Semi-diurnal Waves:

$$G_D \cos^2\phi\, A_i \cos (\alpha_i)$$

Ter-diurnal Waves:

$$G_D \cos^3\phi\, A_i \cos (\alpha_i)$$

where A_i is the amplitude factor for a particular wave and α_i the argument, and are given in Table 2.1 for the major tidal waves. A harmonic development of the lunar and solar tides can be found in Appendix A.

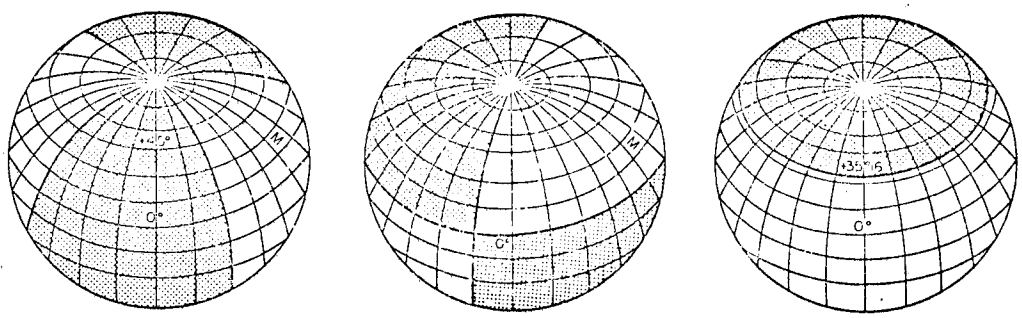

Sectorial Function Tesseral Function Zonal Function

FIGURE 2.3
Geometrical Characteristics of the Three Types of Tides
Source: MELCHIOR(1971b)

Tidal Symbol	Argument	Frequency (degrees)	Amplitude	Origin
		Diurnal components		
O_1	$\tau - s$	13.943	+0.376 89	Lunar, principal wave
P_1	$t - h$	14.959	+0.175 54	Solar, principal wave
S_1	$t - p_s$	15.000	-0.004 23	Solar, elliptic wave of $^sK_1$
$^mK_1$	θ	15.041	-0.362 33	Lunar, declinational wave
$^mK_1$	θ	15.041	-0.168 17	Solar, declinational wave
		Semi-diurnal components		
$2N_2$	$2\tau - 2s + 2p$	27.895	+0.023 01	Lunar, elliptic wave of M_2
N_2	$2\tau - s + p$	28.440	+0.173 87	Lunar, major elliptic wave of M_2
M_2	2τ	28.984	+0.908 12	Lunar, principal wave
S_2	$2t$	30.000	+0.422 86	Solar, principal wave
$^mK_2$	2θ	30.082	+0.078 58	Lunar, declinational wave
$^sK_2$	2θ	30.082	+0.036 48	Solar, declinational wave
		Ter-diurnal component		
M_3	3τ	43.476	-0.011 88	Lunar, principal wave

TABLE 2.1
Principal Tidal Waves

Each term of the harmonic series represents the tidal constituent of the equilibrium tide (or partial tide) at some particular point on the Earth's surface. The harmonic terms representing the observed tide will be of the same form, and comparing the observed tidal deformation of the Earth with the theoretically calculated equilibrium tidal deformation of the Earth yields the amplitude ratio and phase lag for each tidal constituent. The development of oceanic tides and atmospheric tides follows the same classic method.

2.2 Components of the Tidal Potential

The tidal force at the Earth's surface can be referred to three axes of a local reference system, there being a vertical component and two horizontal components. The vertical component directed towards the zenith measures changes in gravity. The two directions on the horizontal plane are defined as along the meridian towards the north, and the other the prime vertical direction towards the west. Three instruments can be used to measure these components on the Earth's surface, a gravimeter for the variation of gravity, and two pendulums directed on the two horizontal directions to measure tilt.

The components along these directions are obtained by taking the derivative of the potential with respect to the corresponding variables:

$$\text{vertical component} \qquad -\frac{\partial W}{\partial R} \ ,$$

$$\text{meridian component of tilt} \qquad -\frac{1}{Rg}\ \frac{\partial W}{\partial \phi} \ , \text{ and}$$

$$\text{prime vertical component of tilt} \qquad -\frac{1}{Rg}\ \frac{\partial W}{\cos\phi\, \partial \lambda} \ ,$$

where R is the radius of the Earth and g the value of gravity. The resultant expressions for the components are shown in Table 2.2.

Function	Potential and Vertical Component	North-South Component	East-West Component
Zonal	$3(\sin^2\phi - \frac{1}{3})(\sin^2\delta - \frac{1}{3})$	$-3 \sin 2\phi(\sin^2\delta - \frac{1}{3})$	0
Tesseral	$\sin 2\phi \sin 2\delta \cos H$	$-2 \cos 2\phi \sin 2\delta \cos H$	$2\sin\phi \sin 2\delta \sin H$
Sectional	$\cos^2\phi \cos^2\delta \cos 2H$	$\sin 2\phi \cos^2\delta \cos 2H$	$\cos\phi \cos^2\delta \sin 2H$

TABLE 2.2
Trigonometric Part of the Expression of the Different Species of Tides in the Three Local Components

In Table 2.2, ϕ is the latitude of a point on the globe, δ the declination of the disturbing body, and H is the hour angle of the disturbing body. A representation of the forces, as functions of latitude are given in Figures 2.4, 2.5 and 2.6 for the six major tidal waves M_2, S_2, N_2, P_1, O_1 and K_1.

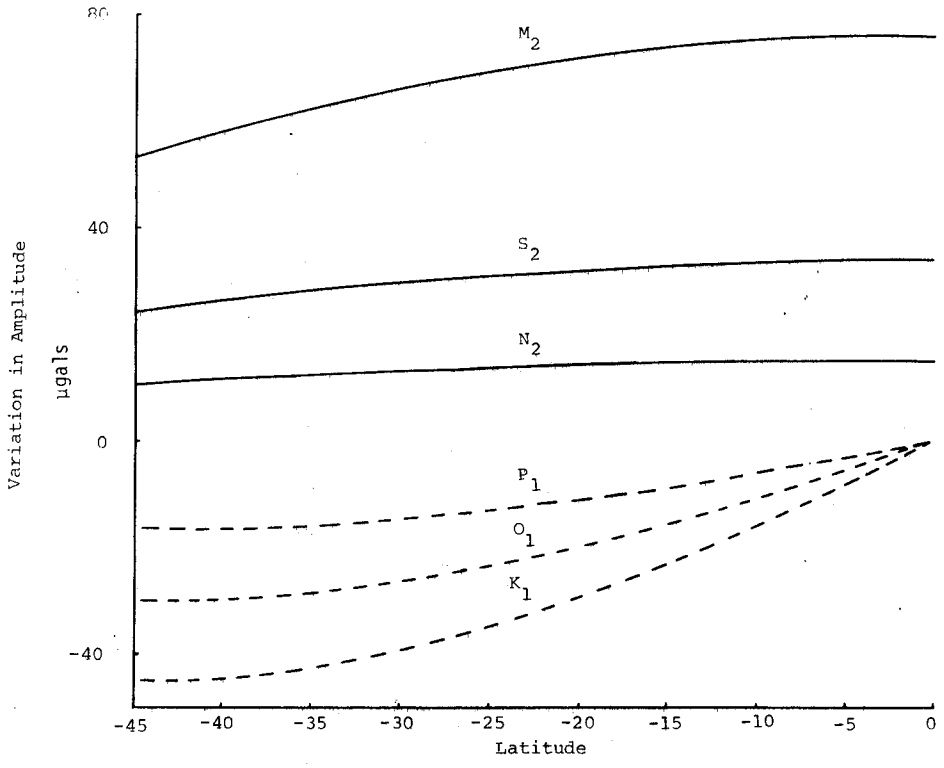

FIGURE 2.4
Amplitude Variation of the Principal Waves as a Function of Latitude for the Vertical Component of Tidal Force. (Australian Region).

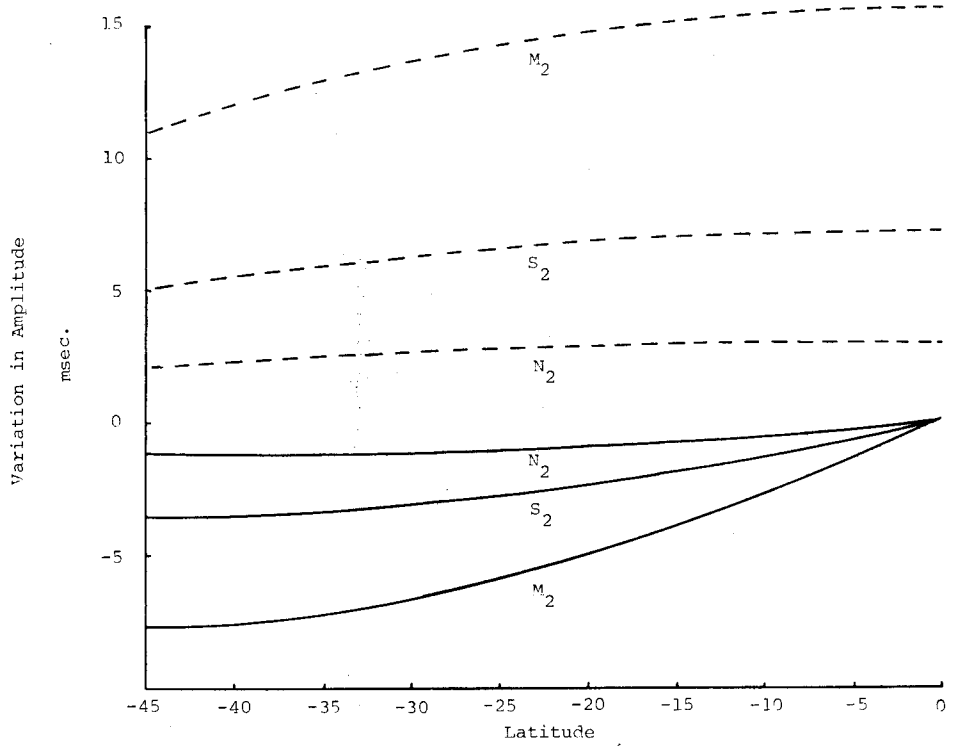

FIGURE 2.5

Amplitude Variation of the Principal Semi-diurnal Waves as a Function of Latitude for the Horizontal Components of the Tidal Force; EW Component: ----; NS Component: ——. (Australian Region).

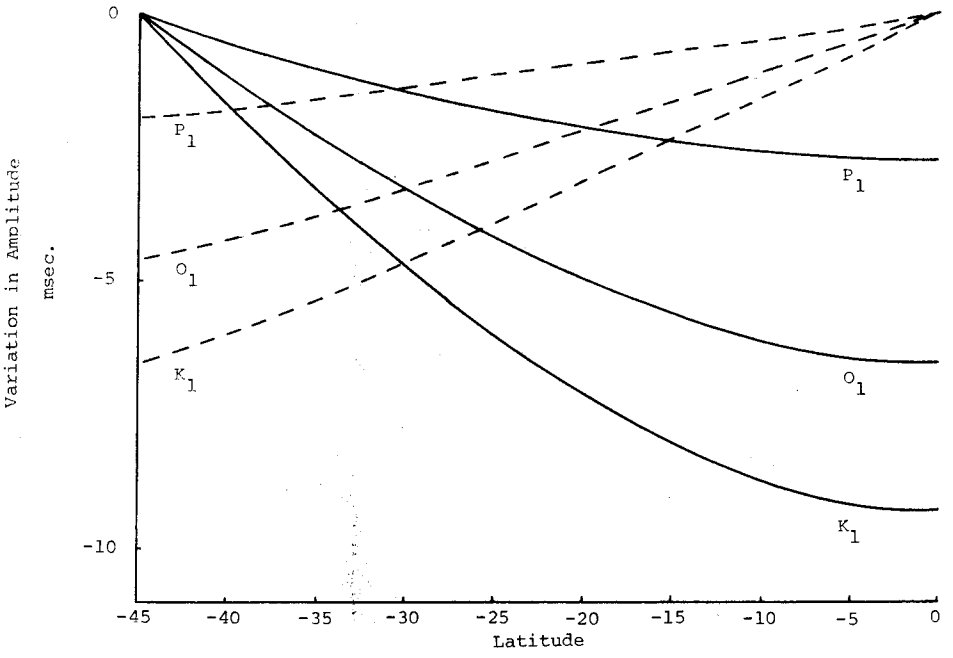

FIGURE 2.6

Amplitude Variation of the Principal Diurnal Waves as a Function of Latitude for the Horizontal Components of the Tidal Force; EW Component: ----; NS Component: ——. (Australian Region).

2.3 The Constituent Potentials

The previous discussion concerned only the tide producing potential of the Sun and the Moon. Due to the elastic characteristics of the Earth, this initial potential generates further constituent potentials, thus further complicating the deformation and loading properties on the Earth's surface.

The constituent potentials necessary to obtain a complete representation of the phenomena are,

(i) the tide producing potential,
(ii) the deformation potential,
(iii) the load potential, and
(iv) the stress potential.

The tide producing potential has been described in Section 2.1, the other three potentials will be described below, together with their dependence on Love numbers and load deformation coefficients.

2.3.1 The Tide Producing Potential

The tide producing potential was described and developed in Section 2.1, and from equation 2.9

$$(W_b)_p = \frac{G\, m_b}{R_b} \left(\frac{R_p}{R_b}\right)^2 P_{20}(\cos \psi_b) \left[1 + 0 \{ 10^{-2} \} \right]$$

which can be described by a zonal harmonic of the second degree to about 1%, the pole lying on the line joining the geocentre to the tide producing body.

2.3.2 The Deformation Potential

The Earth, being elastic, can be deformed by the application of either an external potential of the type described above or a load on the surface. The deformation potential in both cases can be described by

$$U_p = G \iiint \frac{dm}{r}$$

$$= \frac{G}{R_p} \iiint \delta\rho_T \sum_{n=0}^{\infty} \left(\frac{R}{R_p}\right)^n P_{no} (\cos \psi)\, R^2\, dR\, d\sigma \qquad (2.14)$$

where $\delta\rho_T$ is the change in density produced at the general location in the Earth's interior at a distance R from the geocentre (see Figure 2.1) resulting in the original mass element dm changing by δdm, with $d\sigma$ being the element of solid angle. As $U_p \to 0$ when $R_p \to \infty$ and is harmonic exterior to the Earth's surface of measurement, U_p can be represented by a set of spherical harmonics

$$U_p = \frac{G\, m_b}{R_p} \sum_{n=0}^{\infty} \left(\frac{a}{R_p}\right)^n S_n \qquad (2.15)$$

where a is the mean radius of the Earth, and S_n is a surface harmonic of degree n. The deformation potential due to a tide producing body is conventionally represented by the expression

$$U = \sum_{n=2}^{\infty} k_n W_{bn} \qquad (2.16)$$

where k_n is the n-th degree Love number and W_{bn} the harmonic of degree n in the representation of W_b. As the latter can be represented to 1% by a second degree harmonic, it is conventional to use

$$U = k_2 W_b$$

as a means of representing the deformation potential due to the tide. The Love number, k_n is conventionally described by the ratio of the additional potential of degree n generated by the deformation to the tide producing potential of degree n. At the Earth's surface, the value of gravity on the Earth-disturbing body direction decreases due to the disturbing body's attraction. Gravity is further diminished due to an increase in radial distance to the geocentre. The crust also inclines in the same direction as deviations of the vertical in an attempt to remain perpendicular to the vertical.

The analysis of the O_1 tide (the component least affected by ocean tidal loading in Europe) indicates that the use of a single parameter to represent the deformation effects on gravity and tilt tides is usually satisfactory at the 1% level (MELCHIOR 1973b).

2.3.3 The Load Potential

The loading effect of interest is that due to ocean tides. Let the ocean tides be represented by a set of surface spherical harmonics

$$\zeta = \sum_{n=1}^{\infty} \zeta_n \qquad (2.17)$$

The harmonic of zero degree is excluded on the assumption that conservation of mass is equivalent to a conservation of volume. No other acceptable assumption about the nature of the instantaneous ocean tides is possible in view of the probable irregular distribution of amphidromes (e.g. see HENDERSHOTT 1973). The load potential would have the same characteristics as the deformation potential if the load were not directly over the point of evaluation. This is so in the case of ocean loading and would apply to all space exterior to the surface of measurement. In this case,

$$V = G a \rho_w \iint \zeta \sum_{n=0}^{\infty} \left(\frac{R}{a}\right)^n P_{no} (\cos \psi) \, d\sigma \qquad (2.18)$$

for a spherical model of the Earth, with radius r and ρ_w is the density of the ocean. The combination of equations 2.17 and 2.18 on the surface of a sphere gives

$$V = 4\pi G a \rho_w \sum_{n=1}^{\infty} \frac{\zeta_n}{2n+1} \left(\frac{R}{a}\right)^n + 0 \{ f_e V \} \qquad (2.19)$$

where equation 2.17 applies to a representation of both oceanic and continential (ζ=0) areas. At the surface of the Earth, this equation could be written as

$$V = 3g \left(\frac{\rho_w}{\rho_e}\right) \sum_{n=1}^{\infty} \frac{\zeta_n}{2n+1} + 0 \{ f_e V \} \qquad (2.20)$$

where ρ_e is the mean density of the Earth. The equation is correct to the order of the Earth's flattening, f_e.

2.3.4 The Stress Potential

The loading at the Earth's surface described in Section 2.3.3 causes a compression of the Earth. The resulting redistribution of mass in Earth space changes the gravitational potential by V_s. The external characteristics of this potential are the same as those of the deformation potential. It is conventional to treat these two effects together because their external characteristics are not separable (e.g. see MUNK & MACDONALD 1960, p 29). Thus,

$$\begin{aligned} V'' &= V + V_s = \sum_{n=1}^{\infty} k'_n V_n \\ &= 4\pi G a \rho_w \sum_{n=1}^{\infty} \frac{\zeta_n}{2n+1} k'_n \left(\frac{a}{R_p}\right)^{n+1} + O\{f_e V''\} \\ &= 3g \left(\frac{\rho_w}{\rho_e}\right) \sum_{n=1}^{\infty} k'_n \frac{\zeta_n}{2n+1} + O\{f_e V''\} \end{aligned} \tag{2.21}$$

in the case of ocean loading at the surface of the Earth. V_n is the n-th degree harmonic in the representation of V in surface spherical harmonics and V'' is the resulting potential due to deformation and stress. k'_n are load deformation coefficients to degree n, and are defined as the ratio of additional potential of degree n due to the load deformation to the load potential to degree n.

Equation 2.21 can be interpreted as follows. Let the load $\rho_w \zeta$ at each point on the Earth's surface result in a nett compression such that the gravitational effect of the latter can be represented by a surface density of $\rho_w \, c \, \zeta$. Let the global distribution of $c\zeta$ be represented by

$$\zeta' = c\zeta = \sum_{n=1}^{\infty} c_n \zeta_n (\phi, \lambda) \tag{2.22}$$

where ζ_n is given by equation 2.17 and c_n is a multiplying parameter of degree n. Then

$$V'' = G \rho_w \iint \frac{c\zeta}{r} \, ds \tag{2.23}$$

On using the zonal harmonic representation of r^{-1} and equation 2.22, it can be shown that

$$V'' = 4\pi G a \rho_w \sum_{n=1}^{\infty} \frac{c_n \zeta_n}{2n+1} \left(\frac{a}{R_p}\right)^{n+1} \tag{2.24}$$

On comparing equations 2.21 and 2.24, it follows that

$$c_n = k'_n \tag{2.25}$$

This treatment is further developed in Section 5.2.2.

2.4 Variations in Potential and its Components

2.4.1 Change in Potential

The point P situated on the geop $(W = W_p)$ of the undeformed Earth is now situated on the geop $(W' = W'_p)$ of the deformed Earth, where (see Figure 2.7)

$$W'_p = W_p + dr \frac{\partial W}{\partial h} + W_2 + V''_t + V \tag{2.26}$$

W_2 being the tidal potential, V the load potential due to the ocean tides and V''_t the combined stress and deformation potential. The potential V''_t has two constituents due to

a) the deformation due to the tide $(k_2 W_2)$, and
b) the load deformation and stress potential given by equation 2.21. To the order of the flattening,

$$V''_t = k_2 W_2 + \sum_{n=1}^{\infty} k'_n V_n \tag{2.27}$$

Thus the change δW in geopotential at the observing station P due to the tide and load can be expressed as

$$\begin{aligned} \delta W &= W'_p - W_p \\ &= -gdr + (1 + k_2) W_2 + \sum_{n=1}^{\infty} (1 + k'_n) V_n \end{aligned} \tag{2.28}$$

where dr is the radial displacement.

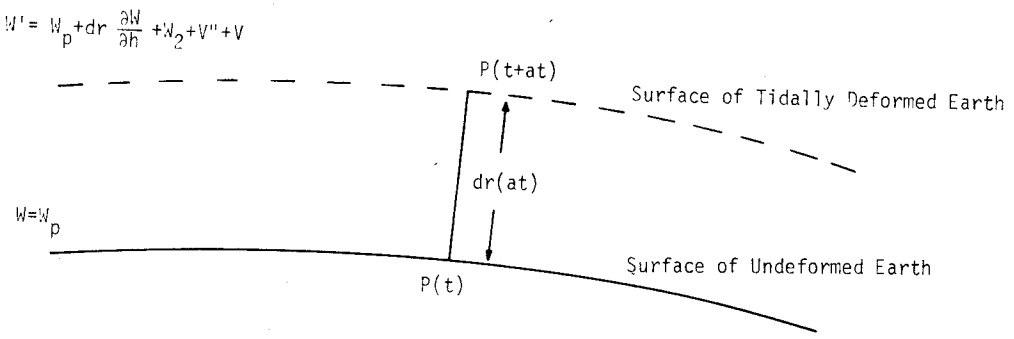

FIGURE 2.7
Change in Geopotential due to Tidal Interaction

The radial Earth tide can be expressed as

$$gdr = h_2 W_2 + \sum_{n=1}^{\infty} h'_n V_n \tag{2.29}$$

where h_2 is a Love number of degree 2 and h'_n is a load deformation coefficient of degree n. The Love number, h_n is conventionally defined as the ratio between the height of the Earth tide for degree n to the height of the corresponding static ocean tide at the surface for degree n. A load on the Earth's surface causes a deformation consisting of a normal stress which depresses the surface and a gravitational attraction which raises the surface. The resultant rise in the Earth's surface due to the load is defined as

$$h'_n V_n / g$$

Thus the change in geopotential becomes,

$$\delta W = (1 + k_2 - h_2) W_2 + \sum_{n=1}^{\infty} (1 + k'_n - h'_n) V_n \tag{2.30}$$

2.4.2 Change in Gravity

The change in gravity is obtained by differentiating equation 2.26 with respect to height (h),

$$-g' = -g + dr\,\frac{\partial^2 W}{\partial h^2} + \frac{\partial W_2}{\partial h} + \frac{\partial V}{\partial h} + \frac{\partial V_t''}{\partial h} \tag{2.31}$$

Using

$$\frac{\partial}{\partial h} = \frac{\partial}{\partial R_p} + 0\left\{ f_e \frac{\partial}{\partial h} \right\},$$

and equations 2.9, 2.15, 2.19, 2.21 and 2.27

$$\begin{aligned} \frac{\partial W_2}{\partial h} &= \frac{2W_2}{R_p} \\ \frac{\partial V}{\partial h} &= \sum_{n=1}^{\infty} \frac{nV_n}{R_p} \\ \frac{\partial V_t''}{\partial h} &= -\sum_{n=1}^{\infty} \frac{(n+1)\,k_n'\,V_n}{R_p} - \frac{3k_2 W_2}{R_p} \end{aligned} \tag{2.32}$$

all relations being correct to the order of the flattening. Also, to the same precision,

$$\frac{\partial^2 W}{\partial h^2} = -\frac{\partial g}{\partial h} = \frac{2g}{R_p} \quad .$$

Thus the change δg in gravity at the observing station P is given by

$$\begin{aligned} \delta g &= g' - g \\ &= -\frac{2g}{R_p}\,dr - \left(1 - \frac{3}{2}k_2\right)\frac{2W_2}{R_p} - \sum_{n=1}^{\infty} \left(n - (n+1)k_n'\right)\frac{V_n}{R_p} \end{aligned} \tag{2.33}$$

On using equation 2.29, the following relation is obtained

$$\delta g = -\left(1 + h_2 - \frac{3}{2}k_2\right)\frac{2W_2}{R_p} - \sum_{n=1}^{\infty} \left(\frac{n}{2} + h_n' - \frac{n+1}{2}\,k_n'\right)\frac{2V_n}{R_p} \tag{2.34}$$

The term $\left(1 + h_2 - \frac{3}{2}k_2\right)$ is conventionally expressed as δ_2, or δ.

2.4.3 Changes in the Deflection of the Vertical

As the potential at the Earth's surface changes according to equation 2.30, the resulting change in the geoid height (δN) is given by

$$\delta N = \frac{\delta W}{g} \quad .$$

The resulting changes $\delta\xi_\alpha$ in the meridian and prime vertical components of the deflection of the vertical are given by

$$\begin{aligned} \delta\xi_\alpha &= -\frac{\partial \delta N}{\partial X_\alpha} \\ &= -\frac{1}{g}\left(1 + k_2 - h_2\right)\frac{\partial W_2}{\partial X_\alpha} - \frac{1}{g}\sum_{n=1}^{\infty}\left(1 + k_n' - h_n'\right)\frac{\partial V_n}{\partial X_\alpha} \end{aligned} \tag{2.35}$$

where the X_1 axis is oriented north and the X_2 axis east. If the radial terms were separated using equation 2.29,

$$\delta\xi_\alpha = \frac{\partial dr}{\partial X_\alpha} - \frac{1}{g}(1 + k_2)\frac{\partial W_2}{\partial X_\alpha} - \frac{1}{g}\sum_{n=1}^{\infty}(1 + k_n')\frac{\partial V_n}{\partial X_\alpha} \tag{2.36}$$

Tiltmeters, which measure these components are insensitive to changes of zero degree in the radial tidal displacement.

The underlying principles of the geophysical instruments which measure Earth tides have to be understood so that a correct interpretation of the formula developed in this Chapter can be obtained. The following Chapter discusses the difficulties associated in obtaining accurate tidal observations and the limitations in present procedures.

CHAPTER 3
INSTRUMENTATION

3.1 Introduction

The effects of Earth tides described in the preceding Chapter have been predominantly observed with two types of instruments, changes in gravity by gravimeters and deflections of the vertical by tiltmeters. The principles underlying the instrumentation and accuracy of gravimeters are discussed with special reference to instruments used in the tidal gravity profiles of Australia.

The following principles regarding the installation of gravimeters and characteristics of instrumential drift are discussed in general terms, being applicable to most gravimeters. Where specific details are mentioned, only two types of gravimeters are discussed, the La Coste Romberg Gravimeter (LCR) Model G and the Tidal Recording Geodynamics Gravimeter (GEO). The observations in Australia were preformed using these instruments, with the La Coste Romberg Model G Gravimeters predominating.

A tidal gravimeter measures variations of gravity by producing a constant opposing force equal to a mean value of gravity. The opposing force is maintained by an elastic spring manufactured to high tolerances. A simplified diagram of the operation of a basic La Coste Romberg Gravimeter is shown in Figure 3.1. The following principle of operation is obtained from LA COSTE & ROMBERG(1973). The gravity response system consists of a weight on the end of a horizontal beam supported by a zero-length spring. The motion of the weight is balanced between an upper and lower stop. The opposing forces are the downward force of gravity on the weight and the restoring force of the spring. Slow changes in the gravitational force brought about by the changing positions of the Sun and the Moon with respect to the Earth cause the beam to move slowly between the stops. The shock eliminating springs which form a floating pivot eliminate friction in the moving system. The suspension of the response systems by springs diminishes most shocks and vibrations. The variations in the beam position are monitored by the use of the measuring screw. The measuring screw is connected to a micrometer, calibrated by both field measurements on a gravity calibration baseline and under laboratory conditions.

The Geodynamics Tidal Recording Gravimeter consists of a modified North American Gravimeter equiped with a capacitive transducer and uses the La Coste type zero length slant spring suspension (OBSERVATOIRE ROYAL DE BELGIQUE 1975). The gravimeter is mounted in a thermostatically controlled pressure tight case. The mass position is sensed by a capacitor plate system. Part of the mass, a plate at ground potential, is centered in the null position between two fixed plates. The beam position is adjusted by a driving motor on the gravimeter.

Originally, gravimeters were devised for field measurements, with the beam position controlled optically through a microscope. These instruments were later revised to obtain continuous recording devices.

Photographic registrations with cameras (LECOLAZET 1956) became the first attempt to obtain a recording gravimeter. Further development involved photocells, which received light reflected from a mirror fixed to the beam. The variations in light intensity cause a potential difference producing an electric current through a galvanometer coil, and a means for obtaining a continuous registration. Difficulties with instability in calibrations and high noise in the photocells lead to the development of the capacitive transducer (MELCHIOR 1977). The transducer detects the position of the plate attached to the oscillating mass of the gravimeter. This plate moves between two fixed plates and produces a direct measurement of the vertical displacement of the mass whereas the earlier methods involved angular measurements through optical devices (IBID).

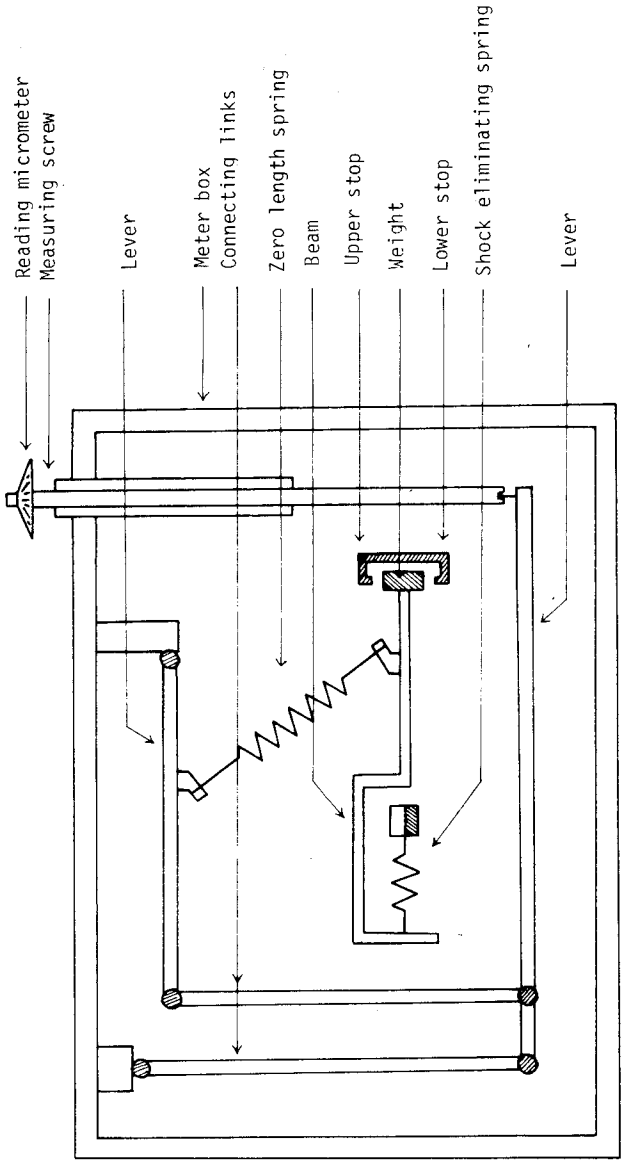

FIGURE 3.1

Gravimeter Operation

Source: LACOSTE ε ROMBERG (1973)

3.2 General Installation Aspects of Gravimeters

Practical experience has shown that horizontal pendulums and gravimeters perform well under different environmental conditions. Horizontal pendulums perform well when installed at reasonable depths below the surface and require suitable and stable rock or ground cover (MELCHIOR 1966). The initial installation being most critical. The observations are very susceptible to local perturbations and anomalies.

Gravimeters can be installed at the Earth's surface, provided the instrument has a firm and stable foundation, usually an observation pillar. The gravimeter electronics are more delicate than the pendulum electronics and thus more susceptible to high humidity and climatic changes. Such changes can lead to sensitivity changes in the gravimeter response and possible sensitivity changes in the gravimeter recording device.

The geological structure around the instrument also causes perturbations in the tidal observations. Horizontal pendulums require contact with a paleozoic base, while with gravimeters, the quality of the mounting pillar and foundations take precedence over the geological structure.

Experience, both in Australia and overseas, has shown that a constant electrical supply is also important. The voltage supply should be regulated, so as not to produce any diurnal or semi-diurnal variations, as these effects would be undetected in observations producing contaminated amplitudes and phases in the final analysis. Similar diurnal wavelength interferences could also originate from meteorological changes, such as temperature and air pressure. Diurnal influences can also be introduced by regular daily visits to the instrument site.

Together with the installation aspects for the location of gravimeters, consideration must also be given to the elimination of noise which will limit the recording accuracy of the gravimeter at any instant.

DIVIS & TOBYAS (1974) give several factors which are important in the study of noise. Increases in the amplitude of the noise occur with strong winds and when strong artifical sources of vibrations are present, such as power plants, traffic and heavy industry. The magnitude and frequency of the noise vibrations are determined by

(a) the output and spectrum of the source of the vibrations,
(b) the mechanism of transmission of the energy to the ground,
(c) the geological structure along the path of propagation, and
(d) the distance from the source.

Noise can be diminished by selecting a suitable site and by the introduction of filters between the gravimeter and the recording device.

Another important consideration in Earth tide measurements is the levelling of the instrument. An error in levelling produces a tilt which has the same effect as a change of gravity with the resultant effect amplified. To minimise any possible perturbations, the point of minimum sensitivity to tilt (a position where a known tilt produces the minimum effect on the tidal recordings) is determined for each particular instrument.

3.3 Instrumental Characteristics of Gravimeters

3.3.1 Gravimetric Drift

Earth tide recording instruments are susceptible to a large number of effects in addition to the Earth

tidal movements. Instrumental design has improved so as to reduce micro-climatic changes of the surroundings to tolerable limits. On a larger scale, however the meteorological changes produce both local and regional movements in the Earth's crust, which influences Earth tidal recordings. These influences cause slow changes in the Earth tide measurements and contribute to gravimetric drift.

The most delicate part of the gravimeter, the spring, provides the force opposing gravity. The force of the spring remains constant to very high tolerances through a thermostatically controlled environment. The metal spring is influenced by temperature, fatigue and elastic reactions, which cause drift in the gravimetric recordings.

MELCHIOR (1966, p 235) has given the following factors which contribute to gravimetric drift,

(a) External temperature variations, which produce temperature variations in the gravimeter. The effects of external temperature and the gravimetric recordings are not always conclusive, with a dependence on the thermostat characteristics.

(b) Variations of atmospheric pressure.

(c) Variations in the power supply to the thermostat, producing variations in internal temperature.

(d) The quality of the relays controlling the heating of the gravimeter. Past experience has shown that the quality of the relays can change during the duration of the observations.

(e) The contact thermometers, which control the heating of the gravimeter and occasionally show variations which affect the internal temperature.

(f) Alterations in the mechanical and elastic qualities of the measuring system, a hysteresis effect.

The variable drifts of a gravimeter are usually greatest during and after the transport of the instrument, due to the uncontrollable environment. Therefore, after transportation, a gravimeter is usually allowed to stablise it's internal heating. During the Australian observations, twelve hours was found to be sufficient for the stablisation. Results from MELCHIOR (1966, p 238) support the view that during the transport of a gravimeter from a controlled environment to an uncontrolled environment, a correlation exists between temperature variations and drift.

There is a close interrelationship between gravimeter drift and the variations of the gravimeter interior temperature. Thus a precondition for obtaining precise observations is good thermostatic control of the gravimeter.

As stated before, variations in atmospheric pressure cause deformations of the Earth. With a meteorological high pressure, the Earth's surface is depressed, thus theoretically increasing the gravity at that point. But in general the gravitational attraction of the air mass predominates, so that a meteorological high pressure system produces a reduction in the value of gravity in comparison with a depression. The amplitude and effects of these counteracting phenomena depends on the spatial extension of the air pressure fields. BREIN (1969) states an effect of -0.5 µgals/Torr for the sum of both gravity effects. The deformations of the Earth's surface by atmospheric pressure variations can be of a regional nature due to local differences in the elastic or quasi-elastic behaviour of the Earth. Also the gravimeter itself is affected by variations in the atmospheric pressure.

If the drift of the gravimeter has not been eliminated before a harmonic analysis is performed, the results of the analysis are systematically different from the analysis of the observations which had

been corrected for drift. The drift can be considered as a long period wave superimposed on the tidal curve, and can be eliminated through a suitable combination of ordinates. The choice of a particular combination of ordinates eliminates not only drifts of various orders, but certain long period Earth tide constituents.

Theoretically, the combination of ordinates used to eliminate the drift should separate as perfectly as possible the components corresponding to the diurnal and semi-diurnal tides. There are numerous possible combinations of ordinates for the elimination of drift, which vary from averaging of ordinates to the application of a parabolic drift correction. A popular method is the combination of ordinates devised by Doodson, and simplified by Pertsev (PERTSEV 1958). The method is easy to apply and provides good selectivity.

Pertsev's method involves the summation of the following fifteen hourly ordinates,

$$t_0,\ t_0 \pm 2h,\ t_0 \pm 3h,\ t_0 \pm 5h,\ t_0 \pm 8h,\ t_0 \pm 10h,\ t_0 \pm 13\ h,\ t_0 \pm 18h$$

where t_0 designates the hour at which the drift correction is required. The division of the above sum of the hourly ordinates by fifteen gives the drift at time t_0.

3.3.2 Calibration of Gravimeters

The calibration of gravimeters and their associated recording devices is an important source of systematic error. The calibration procedures with a La Coste Romberg Model G gravimeter involve the calibration of the recorded signal by movements of the measuring screw. Where the measuring screw is calibrated by artifically producing variations of gravity, this is achieved by changes in height or by the addition of mass.

There are several methods of calibrating gravimeters, involving relative procedures since absolute calibrations are difficult to perform, and then only under laboratory conditions.

If two fundamental stations are available where the gravity difference between the two are known, the gravity differential can be used in the calibrations. In this procedure, the gravimeter is alternately installed at the two fundamental stations, until a short tidal signal is obtained from discontinuous records at each station.

LENNON & BAKER (1973) raise a number of doubts regarding the validity of using such a procedure. They are the following:

(a) Gravimeters are designed for operation over long periods at a single station, so the implications of these repeated disturbances are unknown.

(b) The linear interpolation from the microgal range obtained from the tidal signal at one location, to the milligal range over a calibration range may not be justified.

(c) The method assumes that the tidal singal can be eliminated from the two records, usually by simple graphical processes, so as to produce two mean values appropriate to the two stations.

(d) The procedure assumes that the gravity differential between the two sites is known to a high precision. In fact, the differential was determined by less precise field gravimeters in an attempt to estimate spatial variations in gravity between the relatively few fundamental gravity stations where absolute values have been established.

Other attempts for a precise calibration procedure have involved vertical displacements with elevators and electrostatic platforms. These methods have the major objection that the local gravity differential is not known to sufficient accuracy. While other methods include the introduction of a large mass near the sensor, the addition of a small mass to the beam and the introduction of a known tilt to the sensor. The method of the introduction of a large mass to produce variations of gravity, produces a non-negligible flexion of the ground unless the mass is alternately operated above and beneath the instrument. These methods usually involve laboratory conditions, with the same limitations and doubts mentioned beforehand.

The above methods calibrate the micrometer of the gravimeter into units of milligals and microgals. Due to the difficulties associated with the procedures it is unpractical to carry out such calibrations regularly at the observation site. The doubts about the validity of the calibration procedures will only be dispelled when a calibration method produces artifically the phenomena the gravimeter has to measure.

VALLIANT (1973) introduced a technique for the precise calibration of continuously recording gravimeters which involved the application of an external sinusoidal vertical acceleration of tidal amplitude to the gravimeter. The method consists of comparing the gravimetric response with the applied acceleration which is computed by observing the amplitude and frequency of the gravimeter displacement. An alternate method is comparing the gravimeter displacement with the double integral of its response. In this method, the calibrator is both universal and reproducable, and an accuracy of 0.1% is claimed (IBID).

Calibration of the recording device, usually a chart recorder, is obtained through artifical variations of gravity by movement of the gravimetric micrometer which produces displacements on the recording device. The sensitivity of the gravimetric system varies non-linearly with time. Therefore it is necessary to repeat the calibration operations frequently, while ensuring that the tidal curve is not disturbed by this periodic interference. Through this procedure, a relationship is established between the micrometer of the gravimeter and the scale of the tidal range on the recording device.

This relationship is difficult to determine through separate shifts of an elastic system, due to the damping of the system, leading to time lags in the response of the system to any changes on the micrometer. The problem is overcome with successive shifts of the micrometer through some predetermined rotation, thus producing artifical variations in gravity and associated displacements on the tidal record. The amplitudes of the displacements are directly compared with the range of the micrometer settings of the gravimeter. The time lag in the response of the gravimeter to these artifical variations in gravity necessitates a waiting period before the gravimeter can be repositioned to a new equilibrium level. In addition to the shift of the system, the position of the beam has changed due to drift and the variation of gravity during this period of time between successive shifts.

GERSTENECKER & GROTEN (1976) have reported that the instrumental lag is not completely due to mechanical hysteresis, but partly due to non-linearities of the electronic output.

The effects of drift and gravity variations during calibrations can be diminished by performed calibrations when disturbances such as microseismic noise are least, and when the tidal curve is changing least with time, i.e. on the phases of quadrature of the Moon and the Sun. If the calibrations are preformed when the tide is changing least with time, the effect of drift and tidal variations are minimised.

The preceding discussion described gravimeters of similar construction to the La Coste Romberg Gravimeter. The other instrument involved in the Australian Tidal Gravity Profiles, the Geodynamics

Gravimeter, has its senstitivity controlled by introducing an artifical displacement of the beam by an electrostatic deflection of the mass.

The calibration of the Geodynamics Gravimeter involves applying a precise voltage to a calibration plate mounted over the beam in the gravimeter. The force exerted on the beam produces an artifical variation of gravity, displacing the beam by electrostatic attraction.

The discussion in this Chapter outlines some instrumental difficulties associated with the operation of tidal gravimeters. A preliminary knowledge of such information is important in the correct interpretation of the Australian tidal gravity results presented in Chapter 4, together with site descriptions and discussions.

CHAPTER 4
AUSTRALIAN TIDAL GRAVITY RESULTS

4.1 Introduction

Tidal gravity profiles were established in Australia-Papua New Guinea from September 1974 to May 1977. This study was a cooperative venture between The International Centre for Earth Tides (ICET), Bruxelles, the Government of Australia's Bureau of Mineral Resources, Geology and Geophysics (BMR), and the Department of Geodesy, University of New South Wales. Eight sites were located through Australia and one site is situated at Port Moresby, Papua New Guinea. The sites are shown in Figure 4.1, while the periods of occupation and site descriptions are found in Table 4.1. Location sketches of the nine sites can be found in Appendix B.

The site locations were influenced by logistical factors, leading to the selection of suitable existing observatories where the maintenance of the sensitive scientific instruments could be assured. Station locations were also influenced by lack of large centres of populations in the western half of Australia. A fundamental station was established at Canberra, where all instruments used in Australia were intercompared to ensure the normalisation of the net. Alice Springs being the centre of the continent, provides the most valuable site in the Australian network, such a inland site is of great value in solid Earth geophysics as it is relatively free

FIGURE 4.1
Earth Tide Sites in Australia Papua New Guinea 1974 to 1977

TABLE 4.1

Periods of Observations and Description of Australian Earth Tide Sites

Site	Latitude °N	Longitude °E	Height Above Sea Level(m)	Depth Below Ground Level(m)	Distance from Nearest Ocean (km)	Period of Observation	No. of Days of Obs.	Instrument Used	Site Description	Host Institution
Port Moresby	-9.455	147.154	70	2	5	Sept.1974 to Mar.1975	146	LCR 3	Seismic Vault	BMR
Canberra	-35.321	148.999	663	1	125	Mar.1975 to July 1975	78	LCR 3	Observatory Vault	BMR, ANU
"	"	"	"	"	"	Mar.1975 to July 1975	88	LCR 336	"	"
"	"	"	"	"	"	Mar.1975 to July 1975	86	GEO 84	"	"
"	"	"	"	"	"	July 1975 to Nov.1975	96	LCR 8	"	"
"	"	"	"	"	"	May 1976 to Nov. 1976	120	LCR 3	"	"
"	"	"	"	"	"	July 1976 to Dec.1976	72	LCR 398	"	"
Armidale	-30.579	151.893	650	140	135	July 1975 to Jan.1976	152	GEO 84	Geophysical Observatory (Abandoned Mine)	UNE
Broken Hill	-31.943	141.465	280	1	525	July 1975 to Dec.1975	86	LCR 3	Cellar	UNSW
Perth	-31.978	116.208	235	2	40	July 1975 to Nov.1975	98	LCR 336	Seismic Vault	BMR
Hobart	-42.910	147.320	132	1	1	Nov.1975 to April1976	130	LCR 8	"	UTAS
Darwin	-12.846	131.130	155	3	60	Nov.1975 to Mar. 1976	112	LCR 336	"	BMR
Charters Towers	-20.088	146.254	357	18	105	Dec.1975 to May 1976	114	LCR 3	Seismic Vault in Old Gold Mine	UQ
Alice Springs	-23.710	133.845	590	10	900	Feb.1976 to May 1977	266	GEO 84	Shallow Tunnel in Hill	BMR

Abbreviations:

BMR - Bureau of Mineral Resources
ANU - Australian National University
UNE - University of New England
UNSW - University of New South Wales
UTAS - University of Tasmania
UQ - University of Queensland

from ocean loading effects.

The following Section gives details on instrumentation and calibration of the gravimeters. The results of the series of observations obtained after analyses are given in Section 4.3, while an interpretation and discussion of the results are given in Sections 4.4 and 4.5 respectively.

4.2 Instrumental Properties

The nine sites were maintained by five astaticised gravimeters, as shown in Table 4.1, being four La Coste Romberg gravimeters (LCR 3, LCR 8, LCR 336 and LCR 398) and a North American gravimeter transformed by Geodynamics Inc. (GEO 84). A brief description of the instruments is given below, a full description can be found in DUCARME ET AL (1976).

Together with the gravimeter, each instrument site was completed with a potentiometric recorder and a quartz clock for provision of a time scale.

Displacements of the mass in the gravimeters are detected by a double capacitive transducer. The signal amplitude, thus detected is about 15 mV per μm for the Geodynamics instruments and about 100 mV per μm for the LCR meters. The resultant working sensitivity of the gravimeters becomes 0.1 μm for a gravity variation of one μgal. The microseismic noise is partially eliminated by a band reject filter for LCR meters or a low pass filter for the Geodynamics instrument.

The sensitivity of the (potentiometric) recorder scale expressed in μgal per mm was obtained by back and forth displacements of the recording pen, being equal in size to the observed Earth tide amplitude, for the LCR meter. The pen is moved by turning the dial of the gravimeter micrometer. Such calibration procedures were performed fortnightly. The Geodynamics instrument, having no micrometer, has its sensitivity controlled by an electrostatic calibration device. A fixed voltage is applied between the beam and the condenser plate producing a constant force equivalent to a calibrated gravity interval. This calibration procedure was performed bi-weekly using two different regulated voltage supplies (DUCARME ET AL 1976).

Instrumental stability in astaticised gravimeters is very dependent on the levelling. It is extremely important to position the gravimeter so that it has a minimum sensitivity to tilting because the instrument output exhibits a parabolic dependence on the extent of tilting. It was necessary to occasionally relevel the LCR instruments at each site producing a resultant discontinuity in the sensitivity of the meters. The Geodynamics instrument exhibited high stability with regard to levelling due to its large size and weight.

4.3 Results from Australian Stations

All computational results for the Australian stations were performed at the ICET. The computational procedure for the reduction of the tidal observations is outlined in DUCARME (1975b). Such computations are based on a least squares analysis, with preliminary application of Venedikov filters (VENEDIKOV 1966a, 1966b). The filtering eliminates the noise external to the tidal spectrum, thus accurately smoothing the tidal record. The process assumes there is no noise in the tidal frequencies.

The results obtained from the analyses of the observations are summarised in Table 4.2. A full harmonic analysis of all observations can be found in DUCARME ET AL(1976) and DUCARME & MELCHIOR (1977a, 1977b). The results are for analyses over a period of several months by a single gravimeter at one of the sites. The results for Canberra (the fundamental station) are for each of the five

gravimeters plus an additional recording period for LCR 3. The latter registration period acted as a check for the gravimeter.

The noise and stability of the tidal signal can be evaluated from comparisons of successive monthly analyses of the observations at each station. Such results show that the Geodynamics instrument and the La Coste Romberg instruments LCR 8 and LCR 336 have small variations in the amplitude factors (δ) for the O_1 and M_2 waves and their ratio. The LCR 3 instrument shows more variation than the others and thus less stability.

The stability of the signal can further be evaluated by calculating a root mean square error from the variations in the independent monthly analyses. These values, which indicate external perturbations on tidal data compared with mean square errors obtained from Venedikov filtering highlight any systematic trends. All the Australian stations showed acceptable standards of stability even at very noisy sites.

An estimate of the instrumental noise and reading error level can be obtained from mean square errors of different spectral bands. Such mean square errors from the Venedikov method, show insignificant contributions to the noise of the tidal bands, although some stations exhibit higher noise levels, and show that the LCR 3 meter has higher mean square errors than the other instruments.

The normalisation of the Australian stations is based on the Geodynamics instrument, which has recorded at Bruxelles (ICET) for approximately two years. All gravimeters were intercompared at Canberra with the amplitude factors for the O_1 wave obtained from the Geodynamics meter. All the La Coste Romberg instruments were normalised by fixing the value of the amplitude factor to that obtained by the Geodynamics instrument.

Preliminary analyses for the LCR 3 meter showed discontinuities in its micrometric calibration factors affecting the Port Moresby and Charters Towers observations. This being confirmed by a second registration period at Canberra. The results given for the former two stations were calibrated using the ter-diurnal wave M_3 which was adjusted to its normal value, and checked with results at Canberra.

4.4 Interpretation of Tidal Records

In the interpretation of the Earth tide results, namely the amplitude factors and phase lags, various geophysical phenomena and regional perturbations have to be considered to obtain the correct interpretation of the results. The parameters are effected by atmospheric tides, solar radiation, oceanic loading, oceanic attraction, thermic and barometric perturbations, and tectonic effects. Many of these perturbations are negligible or can be eliminated by careful selection of observational stations. The major perturbation is the oceanic effects, which effects all Earth tide results.

In the comparison of the observed phenomenon to that calculated for a rigid body for the diurnal frequencies, the resultant ratios of amplitudes and phase differences give information on the structure of the Earth. The relation of the elastic properties of the Earth and the density re-distributions associated with the tides can be modelled using the Love numbers, and are combined to give numerous theoretical terrestrial models. Such models are based on heterogeneous conditions, rigidity, compressibility, and boundary conditions between the interior layers of the Earth.

The existence of a liquid core causes tidal resonance due to movements in the liquid core. This resonance is noticeable on the Earth tide amplitude factors and phase lags, the subsequent periods being very near to a sidereal day. In addition, the diurnal waves are very important in astronomy and geophysics. The waves have the same originating forces as the Earth tides, for example, the main diurnal waves K_1, P_1 and O_1 have the following association with astronomical precession and nutation,

TABLE 4.2

Summary of Results for Australian Tidal Stations

Station	Instrument	Semi-Diurnal Amplitude Factors(δ)				Semi-Diurnal Phase Factors (α)				Diurnal Amplitude Factors (δ)				Diurnal Phase Factors (α)				Mean Observed M_2 Amplitude	Mean Observed O_1 Amplitude
		M_2	N_2	S_2	K_2	M_2	N_2	S_2	K_2	K_1	P_1	O_1	Q_1	K_1	P_1	O_1	Q_1	(μgal)	(μgal)
Port Moresby	LCR 3	1.226	1.246	1.268	1.300	-0.3	-3.1	0.8	-4.1	0.942	0.966	1.064	1.032	7.5	3.1	0.0	-7.3	91	10
Canberra	LCR 3	1.225	1.244	1.219		-2.2	-0.9	1.2		1.157		1.194	1.309	-1.0		-1.0	3.4	62	32
	LCR 336	1.206	1.203	1.191		-2.2	-3.7	-0.2		1.154		1.194	1.233	-0.6		-1.0	-2.4	62	32
	GEO 84	1.210	1.217	1.196		-2.2	-2.0	-0.6		1.164		1.194	1.164	-0.4		-1.0	2.6	62	32
	LCR 8	1.204	1.234	1.179		-2.2	-3.3	-1.0		1.151		1.194	1.304	-1.6		-1.0	-2.3	62	32
	LCR 3	1.195	1.189	1.189		-2.2	-2.9	0.7		1.137		1.194	1.193	0.0		-1.0	0.7	62	30
	LCR 398	1.231	1.233	1.211		-2.2	-2.9	-0.4		1.170		1.194	1.215	-0.5		-1.0	2.0	64	29
Armidale	GEO 84	1.201	1.219	1.162	1.179	-2.4	-1.9	-0.6	0.1	1.106	1.150	1.158	1.179	0.3	-0.8	-0.9	-2.3	68	28
Broken Hill	LCR 3	1.159	1.235	1.187		-0.1	-0.6	-0.4		1.131		1.149	1.223	-0.4		-0.2	-1.3	64	29
Perth	LCR 336	1.237	1.224	1.222		0.4	1.0	-0.3		1.242		1.241	1.292	2.3		2.5	3.6	68	31
Hobart	LCR 8	1.203	1.238	1.178		-4.1	-6.9	0.1		1.210		1.252	1.277	-2.9		-2.2	-2.7	50	34
Darwin	LCR 336	1.204	1.186	1.243		0.9	-0.4	-1.3		1.231		1.273	1.323	-8.4		-1.6	3.1	88	15
Charters Towers	LCR 3	1.195	1.210	1.210		-2.4	-1.5	-2.2		1.103		1.164	1.206	-0.4		-1.5	-0.6	81	20
Alice Springs	GEO 84	1.167	1.170	1.164	1.154	-0.3	-0.9	0.7	2.8	1.137	1.174	1.164	1.218	0.3	0.7	0.9	2.1	76	23

where δ is defined as the observed tide amplitude divided by the theoretical tide amplitude,

α the phase lag is defined as the phase of the observed tide minus the phase of the theoretical tide.

K_1 wave is associated with precession,
P_1 wave is associated with semi-annual nutation, and
O_1 wave is associated with fortnightly nutation

The O_1 wave frequency is usually considered as representing a pure static deformation because of its separation from resonance frequency. The fundamental parameter determining the resonance frequency is the flattening of the core which determines the possible movements with respect to the mantle (MELCHIOR 1973b). In addition the period of the O_1 wave was distant from that of the other strong diurnal waves, and can thus be derived with a high precision by harmonic analysis.

The amplitude factor, δ according to theoretical models of the Earth with a liquid core is calculated to be 1.161 or 1.164 after Molodensky's models (MELCHIOR ET AL 1976). The corresponding phase lag is near zero on the globe. In regions of low diurnal ocean tides, the amplitude factors for the O_1 wave would be expected to approach the theoretical values. Such a case occurs in Western Europe (MELCHIOR ET AL 1976).

The semi-diurnal waves are strongly influenced by the oceanic tides. The amplitude factors and phase lags would be expected to be correlated with position. Any departure of the amplitude factors and phase lags from the theoretical values obtained at a site would be expected to be primarily due to ocean loading. This subject is discussed in more detail in Chapters 5 and 6.

4.5 Discussion of Results

In discussions of Earth tide results, two waves, M_2 and O_1 are of greatest interest and produce most of the research on Earth tides and ocean loading in the past. The positional variations of these tidal parameters are illustrated in Figures 4.2 and 4.3.

The amplitude factors $\delta(M_2)$ for the M_2 tide approach the theoretical estimates for $\delta(O_1)$ of 1.163 (see Section 4.4) at the inland sites of Alice Springs and Broken Hill, with a zero phase lag also occurring near this region. The larger discrepancies occur at the coastal sites with all stations presenting amplitude factors greater than 1.20, being primarily due to ocean loading effects. The phase lags appear to be correlated with position with the negative values occurring on the eastern Australian sites and positive at the north western sites.

The results for the diurnal wave O_1, although still position depend are not as obvious as the M_2 results. The amplitude factors approach the theoretical at the inland sites, with the phase lags also having a zero around the inland sites.

Phasor plots (ZÜRN ET AL 1976) for the results of the M_2 and O_1 waves can be seen in Figures 4.4 and 4.5 respectively.

The large diurnal ocean tides in the Pacific and Indian Oceans can be seen to have large effects on the amplitude factors, especially on the coastal sites. At some of the sites there is the possibility that a part of some regional perturbation has been absorbed into the observations.

The results for the diurnal waves for the close equatorial stations should be viewed with caution because of the low Earth tide amplitudes at low latitudes, and are thus poorly determined. Any ocean tide pertrubation, although similar in amplitude compared with other global sites can be relatively large compared to the Earth tide amplitude. The semi-diurnal waves for the Australian region are well determined, the M_2 wave for example has a range of 50-100 µgals over Australia.

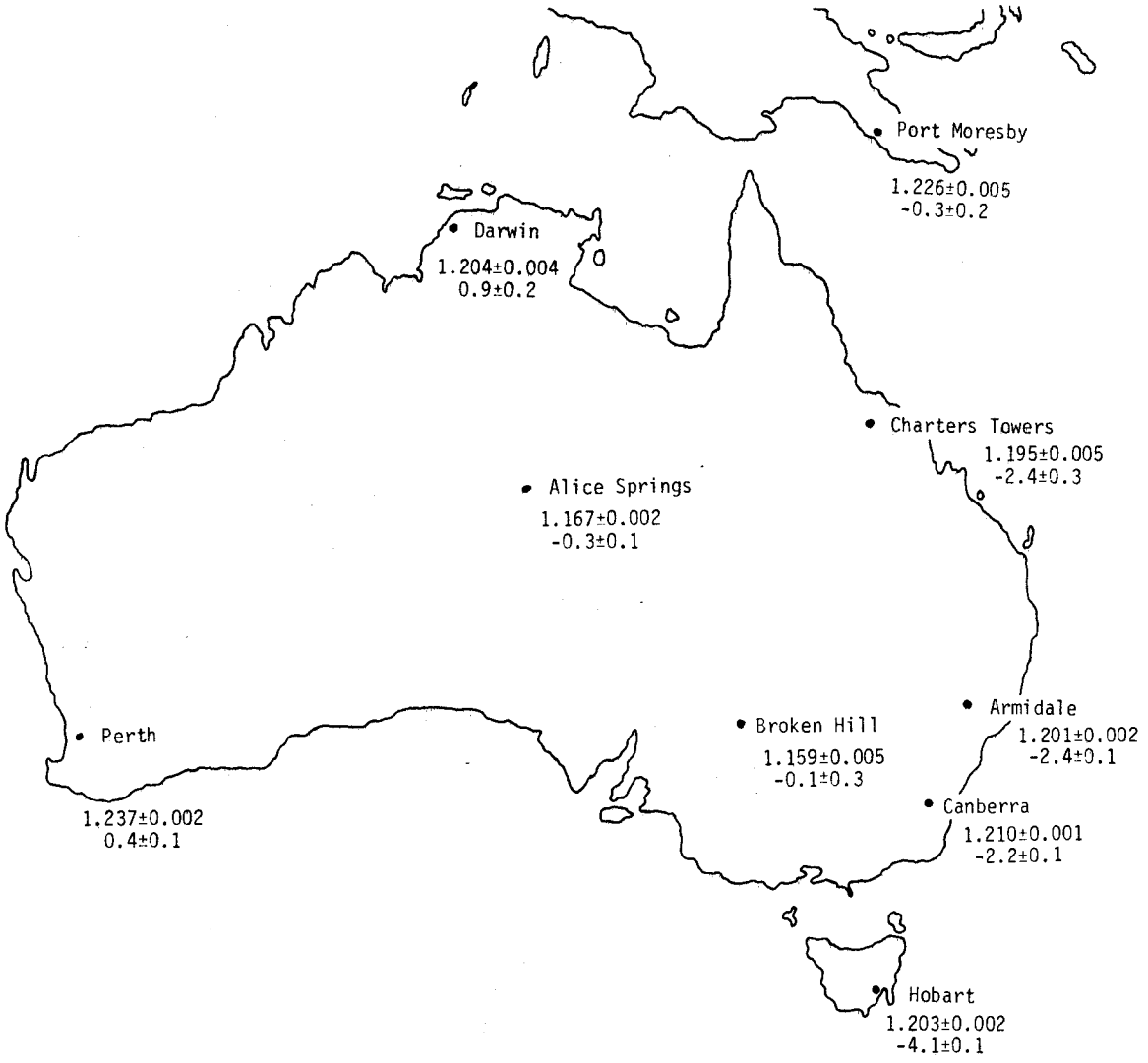

FIGURE 4.2

Tidal Parameters for M_2 as a Function of Position

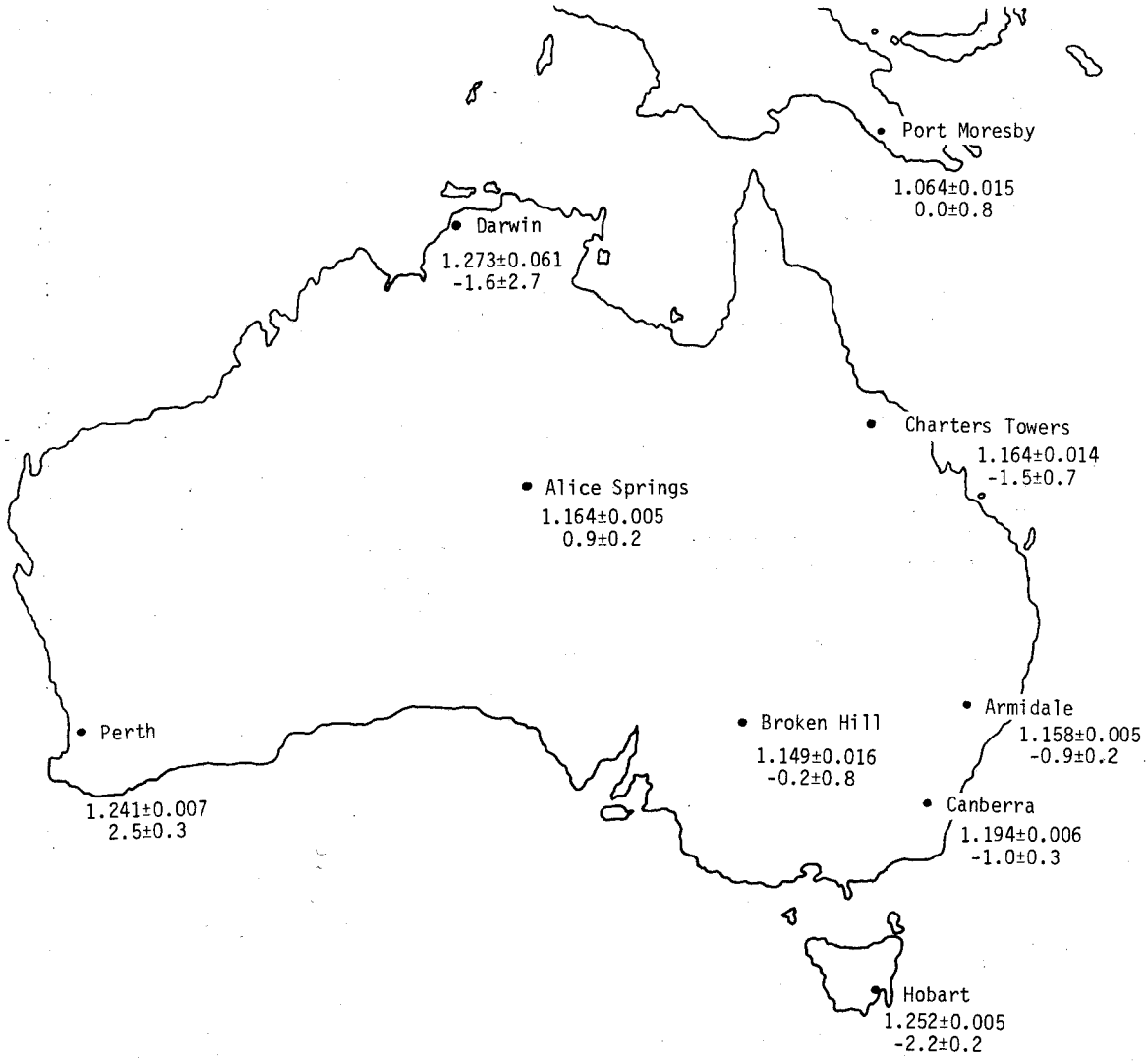

FIGURE 4.3
Tidal Parameters for O_1 as a Function of Position

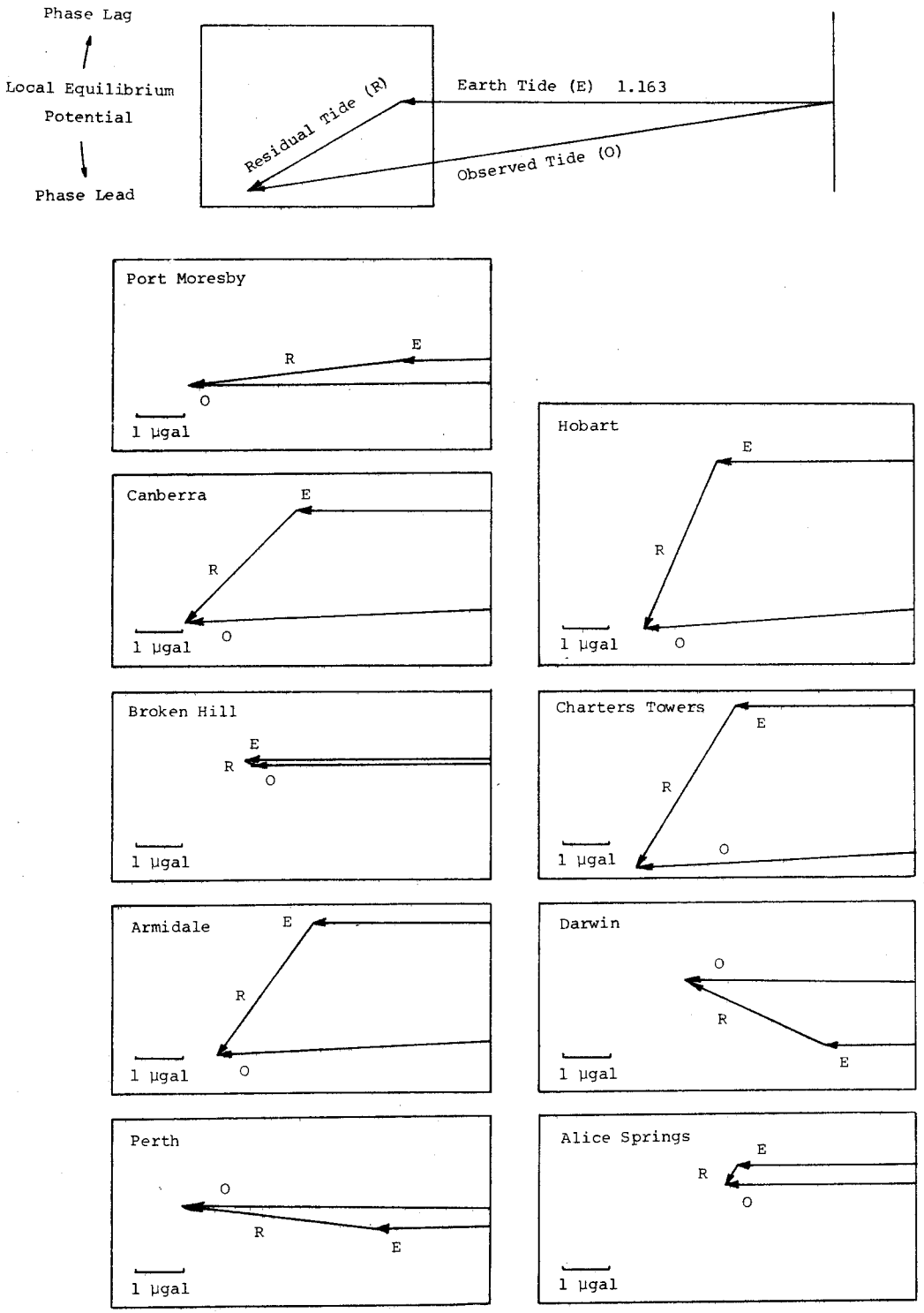

FIGURE 4.4

Phasor Plots for M_2

Phasor plots comparing the observed gravity phasor O with the theoretically calculated gravity phasor E. The theoretical phasor assumes a phase lag of zero and δ=1.163. The phasor R is the gravity residual between the two phasors. The phasor is a vector with length representing the amplitude of the tide (in µgal) and angle (referenced to the horizontal axis) representing phase (local phase is measured counterclockwise). In the detailed plots, only the boxed regions at the ends of the phasors on the upper diagram are shown.

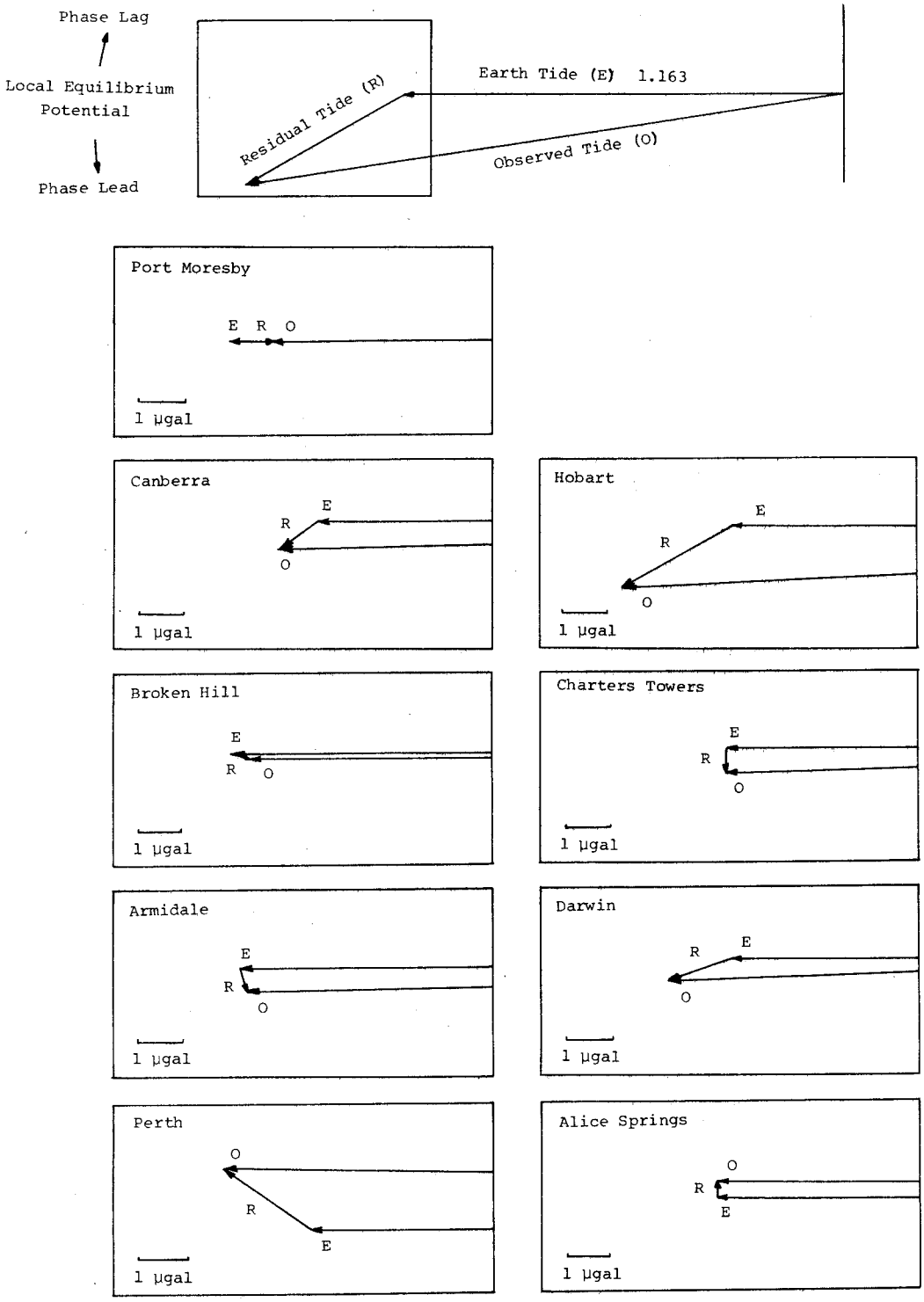

FIGURE 4.5

Phasor Plots for O_1

Phasor plots comparing the observed gravity phasor O with the theoretically calculated gravity phasor E. (See Figure 4.4).

As outlined in Chapter 1, it was hoped to supplement the gravimetric Earth tide results with data collected from the Verbaandert - Melchior horizontal pendulums in operation at Cooney Observatory, Armidale. The use of both types of data would provide a basis of quantifying the radial displacement of the Earth tide at any location in Australia. Cooney Observatory operate two pendulums measuring tilt in the azimuths 54.9° and 144.0°. The records obtained from both pendulums highlighted many non-tidal effects which adversely disturbed the readings. The perturbations included drift, small offsets in the records, possible thermal disturbances, teleseismic noise, microseismic noise and discordant noise (BARLOW ET AL 1973). Subsequent analysis of available data by the ICET provided results which were considered unsuitable for inclusion in any solutions. The diminishing factors (γ) and the phase lags (κ) for all major tidal waves did not yield the expected theoretical values ($\gamma = 0.69$ and $\kappa = 0^{\circ}$). The results for the M_2 tide gave (TANAKA & SYDENHAM 1977)

$$\text{N } 54.9^{\circ}\text{ E} : \gamma = 1.091 \pm 0.006 \quad , \quad \kappa = 12.6^{\circ} \pm 0.3^{\circ}$$
$$\text{E } 54.0^{\circ}\text{ S} : \gamma = 1.365 \pm 0.009 \quad , \quad \kappa = -11.6^{\circ} \pm 0.4^{\circ}.$$

Preliminary calculations for the oceanic effect for the Armidale site indicate that the perturbations are large, although the corrections do not fully account for the disturbances. TANAKA & SYDENHAM(1977) showed that the topography around the Cooney Observatory does effect the tilt measurements to a limited extent. Recent research into the location of the pendulums at Cooney Observatory indicates that the niche excavated in the end wall of the tunnel for the instruments is not an ideal site due to unequal stress relief parallel and transverse to the axis of the tunnel (BARLOW ET AL 1973, HARRISON 1976). However, the disturbances could originate from a number of error sources, such as, calibrations, a deflection of the pendulum from the assigned direction or possible thermic perturbations.

The results obtained for the pendulums and the unfavourable location of the instruments leads to a high degree of uncertainty in the analysis of the horizontal pendulums and thus were not considered in any further discussions or calculations. Attempts for modelling any oceanic loading for Australia thus centred only on the gravimetric results.

The perturbations represented by the gravity residual phasors in Figures 4.4 and 4.5 are predominantly due to ocean tides. The appropriate formulation is developed in the next Chapter, where an introduction to ocean tides is also presented. A discussion based on various ocean tide model effects on Earth tide results can be found in Chapter 6.

CHAPTER 5

OCEANIC PERTURBATIONS ON EARTH TIDES

5.1 Modelling of Ocean Tides

An introduction to ocean tide modelling is presented in this Section, where global ocean tide models are compared. Formulae for the calculation of tidal loading are developed in Section 5.2.

5.1.1 Ocean Tides

Ocean tides are usually measured with standard tide gauges, which consist of a float in a vertical well. They are typically located at the mouths of harbours, or rivers for which predictions are required. The position of the tide gauges are most likely to exert anomalous effects on the phase and amplitude of the tides due to coastal features. HENDERSHOTT & MUNK (1970) have expressed the influences of such locations as 'recording some process through a series of filters, each with a different time constant than the others, and having in common only that none of them are known'. The introduction of deep sea tide gauges has done much to alleviate this problem. These instruments are pressure/temperature sensitive, containing recording devices which can be placed almost anywhere on the ocean floor and later recovered by acoustic commands from surface vessels. MUNK ET AL (1970) have developed the tidal pattern in the northeast Pacific Ocean on the basis of six capsule drops. Such measurements have found to be at least comparable in quality to the best land observations, due to a favourable temperature environment and the absence of low-frequency noise.

Given regular records of tidal heights at a point, future tidal heights can be predicted by extracting the various frequencies of the tidal response. A harmonic development of the tide producing forces relates the frequencies of the ocean tide constituents to the motion of the Sun and the Moon. This harmonic tidal analysis groups the tidal components into three types of waves; long period, diurnal and semi-diurnal.

Global tidal charts have been constructed for the main tidal components from both empirical and numerical methods. The tidal charts are of two types, corange charts and cotidal charts, or a combination of the two. The cotidal chart shows the time of maximum amplitude of each tidal wave, expressed in hours (or degrees) after the Moon's transit through Greenwich in the case of the M_2 wave. The corange chart show lines of equal vertical range. Cotidal lines radiate from points of zero range, called amphidromes.

In open oceans, the tidal range measured at isolated island stations most closely approximates the theoretical tide, but in narrow seas, in estuaries and within broad continential shelves, the amplication of the range usually occurs. There are two main factors (FAIRBRIDGE 1966, p 919)

(i) in shallow water or funnel-shaped channels the tidal range rises approximately inversely to the fourth root of the water depth and the square root of the width, and

(ii) resonance occurs when the free period of the water mass approaches the period of the tide.

5.1.2 The Laplace Tidal Equations

The prediction of the response of the oceans to the tide generating forces is solved by the

the integration of Newton's dynamical equations, and approximated by attempting to solve Laplace's Tidal Equation (LTE), which in the following form include yielding of the solid Earth to the tide generating forces (HENDERSHOTT 1972, p 389),

$$\frac{\partial u}{\partial t} - (2n_e \sin\phi)v = -\frac{g}{a\cos\phi}\frac{\partial(\zeta - \Gamma/g)}{\partial\lambda} + \frac{F_\lambda}{\rho_w D_o} \tag{5.1}$$

$$\frac{\partial v}{\partial t} + (2n_e \sin\phi)u = -\frac{g}{a}\frac{\partial(\zeta - \Gamma/g)}{\partial\phi} + \frac{F_\phi}{\rho_w D_o} \tag{5.2}$$

$$\frac{1}{a\cos\phi}\left(\frac{\partial(uD_o)}{\partial\lambda} + \frac{\partial(v D_o \cos\phi)}{\partial\phi}\right) + \frac{\partial\zeta}{\partial t} - \frac{\partial\delta_E}{\partial t} = 0 \tag{5.3}$$

where (ϕ,λ) are the latitude and longitude with the corresponding northward and eastward components (v, u) of fluid velocity. The Earth's mean spherical radius is denoted by a, the Earth's angular rate of rotation by n_e, the undisturbed ocean depth by $D_o(\phi,\lambda)$, and the deviation of the sea surface from its undisturbed level by ζ. The geocentric solid Earth tide height is denoted by δ_E. $F\lambda$ and $F\phi$ are the zonal and meridional components of the bottom stress, while g is the downward acceleration of gravity at the spherical Earth's surface.

The potential Γ of all the tide generating forces comprises the astronomical contribution W and its motion relative to the Earth, plus the yielding of the solid Earth and the ocean. The potential W is expressed in terms of the fictitious equilibrium tide, $\overline{\zeta}$

$$\overline{\zeta} \equiv W/g \ .$$

Due to the integro-differential character of the above LTE, they are very difficult to solve. Various simplifications have been introduced to solve the LTE, one of the most important being the neglect of all effects of ocean self-attraction and solid Earth yielding. All published solutions for the global tide in realistically shaped oceans except the *Hendershott* 1972 model neglected these factors.

The LTE, after making the simplification $\Gamma = W$, i.e. neglecting self attraction and solid Earth yielding become, (HENDERSHOTT & MUNK 1970, p 210),

$$\frac{\partial u}{\partial t} - (2n_e \sin\phi)v = -\frac{g}{a\cos\phi}\frac{\partial(\zeta - \overline{\zeta})}{\partial\lambda} \tag{5.4}$$

$$\frac{\partial v}{\partial t} + (2n_e \sin\phi)u = -\frac{g}{a}\frac{\partial(\zeta - \overline{\zeta})}{\partial\phi} \tag{5.5}$$

and

$$\frac{\partial\zeta}{\partial t} + \frac{1}{a\cos\phi}\left(\frac{\partial(uD_o)}{\partial\lambda} + \frac{\partial(v D_o \cos\phi)}{\partial\phi}\right) = 0 \tag{5.6}$$

In both sets of LTE, the first two equations are obtained from the Navier-Stokes equations of momentum conservation for a homogeneous fluid. It neglects all dissipative terms, non-linear terms, variations in the effective gravity and in the geocentric radius of fluid particles, and assumes the pressure field is hydrostatic. The third Laplace Tidal Equation is a conservation relationship, obtained by integrating the conditions of continuity and mass conservation, combined for a homogeneous and incompressible fluid, from the sea floor to the free ocean surface.

The horizontal components of fluid velocity become depth independent due to the hydrostatic assumption, subject to the neglect of local vertical fluid accelerations, of buoyancy forces, and of the radial component of the Coriolis force. The extreme aspect ratio (width to depth) of the oceans or the great static stability of the oceans are factors which have been used to justify the hydrostatic assumption. For the approximate equations to conserve energy, the corresponding zonal component of the Coriolis force associated with the tangential component of the Earth's rotation must be neglected.

Some of the factors associated with the LTE are discussed below, a full description is found in HENDERSHOTT & MUNK(1970).

The hydrostatic assumption excludes certain free inertial ($\sigma < 2n_e$) oscillations of a homogeneous fluid. A large aspect ratio effectively eliminates such oscillations as major components of the astronomically forced tide except possibly in the case of inertial oscillations near the equator and the poles. The assumptions for the homogeneous and hydrostatic approximations in the LTE still need careful examination.

Sea water density greatly effects the ocean tides. Very slight variations, for example a few parts per thousand in a depth of 4 km produces noticeable effects in the ocean tides. The density relationship is dependent on the stability frequency N_f as compared to the rotation n_e, with N_f^2 considerably greater than n_e^2 over most of the water column. Some solutions for the LTE include buoyancy forces, with the Coriolis forces associated with the tangential component of the Earth's rotation. Barotropic solutions to the resulting equations are similar with the corresponding LTE solutions.

The presence of lateral boundaries and ocean-floor roughness introduces complications into the LTE. In many solutions, these conditions are usually taken as constants or completely neglected.

From the LTE, the known tidal potential and ocean floor topography, it should be theoretically possible to determine the ocean tide at any point on the globe, without having any reference to tidal observations.

Allowing for the many simplifications mentioned above, the LTE are difficult to solve. This is primarily due to the introduction of the rotation coupling the different spherical harmonics in an expansion of the ocean tide height recorded by conventional or deep-sea gauges.

The inclusion of ocean self attraction and solid Earth yielding have been solved only in the unrealistic case of a non-rotating Earth.

5.1.3 Cotidal-Corange Charts

Preliminary global cotidal-corange charts were drawn empirically by interpolating coastal and island measurements without taking into account any theoretical considerations. Such procedures usually entailed the division of the oceans into simple shaped regions whose free oscillations were assumed to dominate the tidal spectrum. The first global charts constructed were for the dominant M_2 wave. Charts have also been constructed for the S_2, K_1 and O_1 waves (e.g. TIRON ET AL 1967, BOGDANOV & MAGARIK 1967, 1969, ZAHEL 1973). Further cotidal-corange charts were influenced by known solutions to the LTE regarding amphidromic systems, free oscillations, and Kelvin waves in the major oceans. HENDERSHOTT & MUNK (1970) describe these charts as crude integrations of LTE with tidal elevations specified at the boundaries.

Semi-empirical cotidal-corange charts involve the numerical treatment of a model for the oceans. Many of these involved one-dimensional computations neglecting Coriolis forces. This was partly be remedied by basing the calculations on a plane rectangular basin so that Kelvin and Poincaré waves could be included in the solutions (IBID).

Numerical charts produced by solving LTE involve the application of the method of finite differences by an elimination procedure. The motion of the oceans is assumed to be harmonic in time with the frequency of a major tidal constituent. The solving of the LTE, fully or after eliminating one or two dependent variables, involves applying some of the following conditions (HENDERSHOTT & MUNK 1970, p 219)

(i) zero normal velocity at coastlines,
(ii) observed values of the constituent at coastal stations and at selected islands (e.g. *Bogandov* model) or at coastal stations only (e.g. *Hendershott* model),
(iii) observed values of the constituent at selected coastal and island stations plus zero normal velocity at the remaining coastal boundary points (e.g. *Tiron* models), or
(iv) a specified albedo (HENDERSHOTT & MUNK 1970, p. 219) at coastlines or continental shelves.

Numerical models of the global tides are very sensitive to the computational grid and the associated boundary representations. In many global solutions, some regional results are very sensitive to the computational representation of topography and boundaries. Thus a slight change in any one of these factors can produce large variations in corange results. This situation is frequently referred to as near basin resonance.

In trying to obtain solutions less sensitive to details of boundaries and grids, some models have attempted to include known large energy dissipations. Various estimates for the tidal dissipation are unable to distinguish between the numerous contributions to the dissipation and to the rates of dissipation. Current research is attempting to determine if the majority of the tidal dissipation occurs at the major ocean basin edges and to investigate the possibility of tidal energy being scattered into internal waves by ocean floor roughness.

Due to the complexity of the dissipation, numerous parametric representations have been attempted (HENDERSHOTT & MUNK 1970). These have included the introduction of an artificial frictional term which leads to limited dissipation near coastal regions. Coastal and island tidal observations are frequently used as boundary values in the solutions. In *Hendershott's* models coastal tidal heights have been used, together with predicted island tides and interpoled coastal tides. Both the *Tiron* models and the *Bogdanov & Magarik* models include island observations as specified boundary values. These boundary conditions have two assumptions (HENDERSHOTT & MUNK 1970):

(i) coastal and island values are directly representative of adjoining deep-water values, and
(ii) the regions of dissipation are concentrated near the coasts or boundaries.

In the numerical calculations to solve the LTE it is necessary to represent the ocean topography. Numerous investigators have found that the bottom relief can greatly influence the computational stability of the solution and influences directly the representation of the deep-sea tides. This is particularly important at continental shelves where smoothing of the ocean floor is usually undertaken.

The various global numerical models, some of which are outlined in Table 5.1, differ primarily in the inclusion of dissipation and solid Earth tide effects, and with the treatment of coastal boundary conditions. Dissipation has been treated in several ways, by directly including bottom-drag dissipation and having impermeable coastlines or by treating the dissipation as a coastal process and allow energy to flow out of the computational boundaries.

In the global numerical models to date, there is a tendency for the semi-diurnal tide to resonant at many places. PEKERIS & ACCAD (1969) found in their dissipationless global ocean models that slight changes in the coastlines or refinements in the finite difference mesh caused large amplitude changes at many places.

The *Pekeris & Accad* models were based on purely theoretical calculations. Such conditions make the LTE very difficult to solve, so simplifications were made in the solution. The force of friction on the bottom of the ocean was assumed to be represented by a quantity proportional to the first power of the current velocity, whereas a second power would have been more appropriate. Another assumption was a constant depth of one kilometre assigned at the boundaries of the ocean, thus

Model	Type of Model	Boundary Condition	Dissipation	Earth Tide	Reference
Zahel	Global M_2, K_1	Impermeable coast	Bottom stress in shallow water	None	KUZNETSOV (1972), ZAHEL (1973)
Pekeris & Accad	Global M_2	Impermeable coast	Linearised artifical bottom stress in shallow water	None	PEKERIS & ACCAD (1969)
Hendershott	Global M_2	Coastal elevation specified	At coast only	Both ocean self-attraction and tidal loading in latter model	HENDERSHOTT & MUNK (1970), HENDERSHOTT (1972)
Bogdanov & Magarik	Global M_2, S_2, K_1, O_1	Coastal elevation specified	At coast only	None	BOGDANOV & MAGARIK (1967) BOGDANOV & MAGARIK (1969)
Tiron	Global M_2, S_2, K_1, O_1	Coastal elevation specified where data exists, otherwise impermeable coast	At coast only	None	TIRON ET AL (1967)

TABLE 5.1

Summary of Major Ocean Tide Models
Source: HENDERSHOTT(1973)

neglecting any shelf and marginal seas.

The investigations also found that the neglect of tidal friction lead to a slow numerical convergence and generally lead to over estimates of the tidal parameters with the solution being sensitive to the coastal configuration. This was a practical study based on various models with ranging frictional forces and computation configuration. When tidal solutions were obtained with friction included, the following results were obtained (PEKERIS & ACCAD 1969):

(i) the solution was insensitive to the computational grid,
(ii) solutions are insensitive to moderate changes in the configuration of the coastline,
(iii) tidal amplitudes are of the same magnitude as observed values,
(iv) tidal phases are slightly advanced relative to the observed values, and
(v) the rate of tidal dissipation by friction in the ocean was 6TJ/s (6×10^{19}erg).

The *Zahel* models were also based on theoretical calculations employing the solution of a system of differential equations for a hydrodynamic model of the oceans. The frictional force was assumed to be proportional to the second power of the current velocity.

The *Bogdanov & Magarik* models solved the LTE by dividing the surface of the ocean into $5^{\circ} \times 5^{\circ}$ blocks of latitude and longitude, whereas the *Pekeris & Accad* models used block sizes down to $1^{\circ} \times 1^{\circ}$. Each block obtained an average value for the harmonic tidal amplitude and phase, filtered to correct for any abnormal data, such as at near-shore points. Together with this tidal data at each block, the average depth was calculated. Boundary conditions were imposed using observed values of the constituents at coastal stations and at selected islands.

The basic difference between the *Hendershott 1972* model and the previously mentioned tidal models is the inclusion of ocean self attraction and solid Earth yielding. Hendershott derived this model by firstly numerically solving the LTE without bottom stress and neglecting ocean self-attraction and tidal loading, obtaining the *Hendershott 1970* model. The LTE (in a integro-differential form) were differentiated to obtain an equation based on the departure of the geocentric ocean tide from the equilbrium tide corresponding to the total tide generating potential. This equation is solved with boundary values derived from coastal harmonic analysis. The cotidal-corange chart thus produced was used to evaluate the contributions of ocean self-attraction and of tidal loading. A cotidal-corange chart corrected for these two factors has been obtained (HENDERSHOTT 1972) and the magnitudes of the values obtained indicates their importance in global solutions.

5.2 Ocean Loading

5.2.1 Introduction to Ocean Load Modelling

Surface loads from varying ocean tides around the globe produce deformations in the Earth's crust at any observational site. These tides produce the same frequencies as the solid Earth tides, due to both being derived from the same astronomical forces.

The tidal loading at a point is primarily dependant on the global pattern of the ocean tides and the regional ocean tidal layout. Such ocean tide patterns become very irregular due to the land masses and varying ocean depths.

The largest contribution to the ocean loading is from the water closest to the observation site. However, a total global calculation has to be preformed as all oceans contribute to the ocean loading.

An estimate of the tidal loading effect at a point can be obtained by subtracting the predicted solid Earth tide from the observed Earth tide at that point. This assumes that the perturbations such as atmospheric tides, geological structure, solar radiation, tectonic effects, and departures from radial symmetry are negligible. The loading effects on gravity, strain and tilt measurements can account for a significant portion of the observed Earth tide at a point.

The oceanic load response is dependent on the local variable properties of the crust and mantle. Thus the difference between the predicted solid Earth tide and observed Earth tide will give significant information on the local ocean tides. On the other hand, the Earth's global deformation properties influence the solid Earth tides more than the regional properties.

A review of the calculations on the loading effect can be found in FARRELL (1972a). A brief outline will be given below.

The periodically varying ocean tide loads produce three effects on the Earth tide measurements. These are the direct (or Newtonian) attraction of the moving water masses, the deformation of the Earth under the loading, and the redistribution of mass due to the deformation.

The evaluation of the Newtonian acceleration and the elastic acceleration (the latter comprises the deformation and redistribution components) have involved both flat and spherical models (MEONS 1976a).

The Newtonian acceleration based on a flat Earth model produces zero for the vertical component. The horizontal component produces a simple relationship between the water mass and the distance to the load. A spherical model for the vertical and horizontal components involves a numerical summation of all global ocean data. In this calculation a correction is made to take account of the altitude of the station.

The calculation of the elastic component for a flat Earth model initially involved an infinite and homogeneous half-plane. The displacements were functions of Lamé elastic parameters of the crust with point loads. KUO (1969) improved this by developing stratified models. Such flat Earth models were unsuitable for global calculations due to the planar approximations.

Spherical models were used by CAPUTO (1961) to calculate deformations under spherical caps. This assumed symmetrical distribution of the load with respect to the equator. This model is too restrictive for global determinations. Spherical models based on a Gutenburg-Bullen type Earth were developed by LONGMAN (1962, 1963) and FARRELL (1972a). These models assumed spherical symmetry (radial stratification), a non-rotating Earth, elastic deformations according to Hooke's law and isotropy. A method for evaluating the ocean tide loading effect using truncation functions is given in Section 5.2.2, while the Longman-Farrell method is outlined in Section 5.2.3.

5.2.2 Mathematical Formulation of Trunction Function Method

This method based on the formulation of Chapter 2 was developed in MATHER & BRETREGER (1975).

5.2.2.1 Gravity Variations

The conventional relation for the variation of gravity at a point on the Earth's surface is (equation 2.34)

$$\delta g = -(1 + h_2 - \frac{3}{2} k_2) \frac{2W_2}{R_p} - \sum_{n=1}^{\infty} (\frac{n}{2} + h'_n - \frac{n+1}{2} k'_n) \frac{2V_n}{R_p} \qquad (5.7)$$

The term

$$(1 + h_2 - \frac{3}{2} k_2) \frac{2W_2}{R_p}$$

is the response due to the solid Earth tide effect, and

$$\sum_{n=1}^{\infty} n V_n/R_p$$

is the gravitational effect due to the attraction of the re-distributed tidal water masses. The loading effect of the latter on the Earth's crust produces a change in potential

$$\sum_{n=1}^{\infty} (n+1) k'_n V_n/R_p ,$$

while

$$\sum_{n=1}^{\infty} 2h'_n V_n/R_p$$

is the gravitational effect due to the corresponding radial displacement.

Equation 5.7 can be rewritten as

$$\delta g = -(1 + h_2 - \tfrac{3}{2}k_2) \frac{2W_2}{R_p} - \frac{\partial V}{\partial h} - \sum_{n=1}^{\infty} (h'_n - \frac{n+1}{2} k'_n) \frac{2V_n}{R_p} \qquad (5.8)$$

where V is given by equation 2.18 as

$$V = Ga^2\rho_w \iint \frac{\zeta}{r} d\sigma \qquad (5.9)$$

and all other terms being defined in Section 2.5.

Thus

$$\frac{\partial V}{\partial h} = Ga^2\rho_w \iint \frac{\zeta}{2ar} d\sigma + 0 \{ f_e \frac{\partial V}{\partial h} \} \qquad (5.10)$$

as

$$\frac{\partial}{\partial h} (\frac{1}{r}) = \frac{\partial}{\partial R_p} (\frac{1}{r})$$

$$= - \frac{1}{2ar} + 0 \{f_e \frac{\partial}{\partial h} (\frac{1}{r})\} .$$

The evaluation of equation 5.10 in practice is best effected by resorting to truncation functions adopting procedures similar to those outlined by MOLODENSKII ET AL (1962, p 147). See GROTEN (1970) for an application of this technique to ocean tides. This enables the relatively large contributions of those close areas within some limiting angular distance ψ_0 to be evaluated by surface integration assuming that sufficient tidal information were available. The problems associated with defining the higher harmonics of the global ocean tide with a minimal accuracy is circumvented in this manner. It is estimated that the distant zone effects could be represented without significant error to 1 part in 10^2 by a discrete set of error free surface spherical harmonics. To achieve suitable working expressions, equation 5.10 is written as

$$\frac{\partial V}{\partial h} = - \frac{1}{4} G\rho_w \int_0^{\psi_0}\int_0^{2\pi} \zeta \Phi(\psi) d\sigma - \frac{1}{4} G\rho_w \iint \zeta \overline{\Phi}(\psi) d\sigma \qquad (5.11)$$

where

$$\Phi(\psi) = \text{cosec } \tfrac{1}{2}\psi,$$

and

$$\overline{\Phi}(\psi) = \begin{cases} 0 & 0 \leqslant \psi < \psi_0 \\ \operatorname{cosec} \tfrac{1}{2}\psi & \psi_0 \leqslant \psi \leqslant \pi \end{cases} \tag{5.12}$$

Defining

$$\overline{\Phi}(\psi) = \sum_{n=0}^{\infty} \frac{2n+1}{2} X_n P_{no}(\cos \psi) \tag{5.13}$$

where X_n is a function of ψ_0, given by

$$\begin{aligned} X_n (\cos \psi_0) &= \int_{-1}^{1} \overline{\Phi}(\psi) P_{no}(\cos \psi) \, d(\cos \psi) \\ &= \int_{-1}^{\cos\psi_0} \Phi(\psi) P_{no}(\cos \psi) \, d(\cos \psi) \end{aligned} \tag{5.14}$$

On using the orthogonal properties of surface spherical harmonics, equation 5.11 can be written as

$$\frac{\partial V}{\partial h} = -\frac{1}{4} G\rho_w \int_0^{\psi_0} \int_0^{2\pi} \zeta \operatorname{cosec}\tfrac{1}{2}\psi \, d\sigma - \tfrac{1}{2} G\rho_w \pi \sum_{n=1}^{\infty} X_n \zeta_n \tag{5.15}$$

This equation assumes that the surface harmonic expansion of ζ represents both oceans and land ($\zeta=0$). The X_n's are evaluated by using equation 5.14 and the fact that $X_n(\cos \pi) = 0$. On changing the variable to $t = \sin \frac{1}{2}\psi_0$, equation 5.14 can be interpreted as

$$\frac{dX_n}{dt} = -4 P_{no}(1 - 2t^2) \tag{5.16}$$

5.2.2.2 Variations in the Deflection of the Vertical

The changes in the deflection of the vertical are given by equation 2.35,

$$\delta\xi_\alpha = -\frac{1}{g}(1 + k_2 - h_2) \frac{\partial W_2}{\partial X_\alpha} - \frac{1}{g} \sum_{n=1}^{\infty} (1 + k_n' - h_n') \frac{\partial V_n}{\partial X_\alpha} \tag{5.17}$$

with similar responses due to the solid Earth tide effect and ocean loading as the variations in gravity.

Measurements of the deflections of the vertical can be used to separate the effects of the radial deformation on the change in potential from the contributions due to deformation and stress. A problem of some consequence is the numerical evaluation of $\partial V/\partial X_\alpha$ especially in coastal areas where the ocean tide may be adequately known for the evaluation of V but not of $\partial V/\partial X_\alpha$.

Proceeding on lines similar to those used in deriving expressions for deflections of the vertical (e.g. HEISKANEN & MORITZ 1967, p 112), the consideration of equation 5.9 gives

$$\begin{aligned} \frac{\partial V}{\partial X_\alpha} &= \sum_{n=1}^{\infty} \frac{\partial V_n}{\partial X_\alpha} \\ &= \tfrac{1}{4} G\rho_w \iint \zeta \operatorname{cosec}^2 \tfrac{1}{2}\psi \cos \tfrac{1}{2}\psi \cos A_\alpha \, d\sigma \end{aligned} \tag{5.18}$$

where A_1 is the azimuth of $d\sigma$ from the point of computation and $A_2 = \frac{1}{2}\pi - A_1$. A comparison of the structures of equations 5.11 and 5.18 indicates the degree to which tiltmeter observations are more susceptible to local effects of tidal loading than gravimeters. Since the kernel function of equations 5.11 and 5.18 converge towards the same limits as equivalent expressions in gravimetric geodesy when $\psi \to 0$, experience with latter type of calculation would appear to indicate that a significant proportion of the signal from ocean loading on tiltmeters (even up to 90% in coastal areas

with large tidal ranges) should come from tidal effects within about 200 km of the tiltmeter location.

It is convenient to use truncation functions in the evaluation of equation 5.18, in view of the limited effect of outer zones on tiltmeter observations. The appropriate kernel function can be used with a procedure initially devised by COOK (1950). Introducing

$$\bar{\Phi}_2(\cos\psi) = \begin{cases} 0 & 0 \leq \psi < \psi_0 \\ \Phi_2(\cos\psi) & \psi_0 \leq \psi \leq \pi \end{cases} \tag{5.19}$$

where

$$\Phi_2(\cos\psi) = \operatorname{cosec}^2 \tfrac{1}{2}\psi - \cos\tfrac{1}{2}\psi \tag{5.20}$$

Defining

$$\bar{\Phi}_2(\cos\psi) = \sum_{n=0}^{\infty} \frac{2n+1}{2n(n+1)} Y_n P_{n1}(\cos\psi) \tag{5.21}$$

the use of orthogonal properties of surface harmonics gives

$$\begin{aligned} Y_n &= \int_{-1}^{\cos\psi_0} \Phi_2(\cos\psi) P_{n1}(\cos\psi)\, d(\cos\psi) \\ &= \int_{-1}^{1} \bar{\Phi}_2(\cos\psi) P_{n1}(\cos\psi)\, d(\cos\psi) \end{aligned} \tag{5.22}$$

Thus equation 5.18 can be written as

$$\begin{aligned} \frac{\partial V}{\partial X_\alpha} = \frac{1}{4} G\rho_w \int_0^{\psi_0}\int_0^{2\pi} \zeta \operatorname{cosec}^2 \tfrac{1}{2}\psi \cos\tfrac{1}{2}\psi \cos A_\alpha \, d\sigma \\ + \frac{1}{4} G\rho_w \pi \sum_{n=1}^{\infty} \zeta_{\alpha n1} Y_n \end{aligned} \tag{5.23}$$

where

$$\zeta_{\alpha n1} = \frac{2n+1}{2\pi n(n+1)} \iint \zeta_n(\psi, \alpha) P_{n1}(\cos\psi) \cos A_\alpha \, d\sigma \tag{5.24}$$

Numerical values of Y_n can be obtained by using the same technique adopted for the evaluation of X_n in equation 5.16, on applying equation 5.22

$$\frac{dY_n}{dt} = -4(1 - t^2)^{\frac{1}{2}} t^{-1} P_{n1}(1 - 2t^2) \tag{5.25}$$

5.2.2.3 The Combination of the Elastic Components of the Potential

The effect of the stress and deformation potentials on gravity and the direction of the vertical are conventionally represented by the use of the load deformation coefficients k'_n, the relevant formulation being given by equations 2.34 and 2.35. An approach based on a multiple linear regression (in lieu of harmonic) analysis has also been proposed (LAMBERT 1974). The treatment of loading effects using the load deformation coefficients needs the use of a large number of parameters (e.g. FARRELL 1972a, p 791) along with higher degree harmonics of the load which in the case of ocean tides, are not reliably known. The treatment would be warranted only if the stress and deformation potential bear little direct relation to the nature of the load. A measure of the static response of the Earth to the basic tide producing forces can be obtained from the analysis of the O_1 tide, and this shows the deformation potential due to the body tide can be represented to 3% by a single parameter k_2 (MELCHIOR 1973b). In this context, re-examination of the framework in which the ocean tidal data is numerical evaluated in the loading problem is

necessary. Presently available cotidal-corange charts are not reliable in the open oceans, and it is hoped that satellite altimetry data which is expected to be available in the next decade will improve the global ocean tide models. A discussion of such a study is outlined in Chapter 9.

The development with the truncation function method indicates that the effect of the load potential on both gravimeter and tiltmeter observations can be adequately described by:

(a) the use of discrete low degree surface spherical harmonic representations of the loading function for distant zone effects, and
(b) the surface integration of the loading function (assumed to be known) for the evaluation of local effects.

The limit of surface integration should vary from about 500 km for tiltmeter data analysis to about 2000 km in the case of gravity data if experience in the use of similarly structured kernel functions in other geodetic computations is an appropriate measure for comparisons. Large tidal ranges in restricted but distant areas which depart significantly from the global tidal model as implied in surface harmonic representations of low degree, have little effect on computed values of V and $\partial V/\partial h$.

The problem then devolves into the choice of the most effective model for describing the deformation and stress potentials due to the tidal loading, noting that:

(i) a minimum number of parameters is desirable,
(ii) the deformation response of the Earth to the body tide appears to be effectively described at the 3% level by a single parameter k_2,
(iii) local anomalies apart, the change in parameters describing the Earth model within the framework of accepted concepts, does not significantly change the value of k_2 (FARRELL 1972a, Table A1),
(iv) for ocean tidal loading, the load, stress and deformation potentials are harmonic exterior to the Earth and down to the surface of measurement.

One procedure which is described in the literature (e.g. GROTEN 1970, HENDERSHOTT 1973) treats the load potential V and the stress and deformation potential V'' due to the load, as the potential

$$\sum_{n=1}^{\infty} (1 + k_n') V_n ,$$

which in turn, can be expressed in terms of harmonics in the global representation of the ocean tide as described in equation 2.21. Thus,

$$\sum_{n=1}^{\infty} (1 + k_n') V_n = G\rho_w \iint \frac{(1+c)\zeta}{r} \, ds \tag{5.26}$$

where

$$(1+c)\zeta = \sum_{n=1}^{\infty} (1 + k_n') \zeta_n \tag{5.27}$$

An alternate approach when representing the Earth's stress and deformation response to the load, is the following. Assume that only a few coefficients are required to describe the stress and deformation potential globally at the level of 1% of the body tide. Thus,

$$c = \sum_{n=0}^{n_m} c_n (\phi, \lambda) \tag{5.28}$$

where n_m is finite. Let

$$\zeta' = (1 + c)\zeta = \sum_{n=1}^{\infty} \zeta_n' \tag{5.29}$$

Equations 5.7 and 5.17 can be rewritten as

$$\delta g = -\frac{2g}{R_p}\, dr - (1 - \frac{3}{2} k_2)\, \frac{2W_2}{R_p} - \frac{1}{4} G\rho_w \int_0^{\psi_0}\int_0^{2\pi} \zeta' \operatorname{cosec} \tfrac{1}{2}\psi \, d\sigma - \tfrac{1}{2} G\rho_w \pi \sum_{n=1}^{\infty} X_n \zeta'_n \qquad (5.30)$$

and

$$\delta\xi_\alpha = \frac{\partial dr}{\partial X_\alpha} - \frac{1}{g}(1 + k_2)\, \frac{\partial W_2}{\partial X_\alpha} - \frac{G\rho_w}{4g} \int_0^{\psi}\int_0^{2\pi} \zeta' \operatorname{cosec}^2 \tfrac{1}{2}\psi \cos \tfrac{1}{2}\psi \cos A_\alpha \, d\sigma - \frac{G\rho_w \pi}{4g} \sum_{n=1}^{\infty} \zeta'_{\alpha n1} Y_n \qquad (5.31)$$

where X_n, Y_n and $\zeta'_{\alpha n1}$ are defined by equations 5.14, 5.22 and 5.24, with ζ replaced by ζ'.

An iterative procedure could be used in the numerical evaluations. In such a procedure, c is not known for the surface integration. An approximation can be obtained by assuming a constant value c_t and then assume $\zeta' = (1 + c_t)\zeta$ for the evaluation of the inner zone by quadratures. The observation equations obtained from equations 5.30 and 5.31 could then be solved after application to data from co-located gravimeters and tiltmeters. To obtain a meaningful solution a global coverage of data is needed. The solution could be further improved by analysing the values of the harmonic coefficients $\zeta'_{\alpha nm}$ obtained along with the values of c_t and the global ocean tide coefficients $\zeta_{\alpha nm}$, noting that

$$\zeta'(\phi,\lambda) = [1 + \sum_{n=0}^{n_m} c_n (\phi,\lambda)]\ \zeta (\phi,\lambda) \qquad (5.32)$$

The resulting values of c_n could be used in a second integration as multiplying coefficients for the surface integration contributions. Only a finite number of terms constituting the surface spherical harmonic series in equations 5.30 and 5.31 need to be evaluated in practice. The exact degree to which terms should be included in solutions would be a function of ψ_0. For the variation in gravity, adequate representation should be obtained by considering terms to degree 8 if $\psi_0 = 20^{\circ}$ (2000 km).

5.2.2.4 Representation of the Ocean Loading Effects on the Radial Deformation

The radial tide dr, like the stress and deformation potentials, cannot be uniquely represented without recourse to an appropriate set of parameters to characterise the Earth's response. The radial tide can be expressed as

$$dr = dr_{\text{body tide}} + dr_{\text{tidal loading}} .$$

The effect of the body tide is obtained from equations 2.9 and 2.29 as

$$dr_{\text{body tide}} = \frac{h_2 W_2}{g} = \frac{h_2 G m_b}{R_b} \left(\frac{R}{R_b}\right)^2 P_{20} (\cos [\ \psi_b + d\psi\ ]) \qquad (5.33)$$

where $d\psi$ is the apparent change in ψ_b (see Figure 2.1) due to the lag Δt in the body tide. This can be written as

$$dr_{\text{body tide}} = \frac{h_2 W_2}{g} [1 - \frac{P_{21}(\cos\psi)}{P_{20}(\cos\psi)}\ d\psi\ ] = \frac{h_2 W_2}{g} [1 - \frac{P_{21}(\cos\psi)}{P_{20}(\cos\psi)}\ \frac{\cos\phi \cos\delta \sin t}{\sin\psi}\ \Delta t\ ] \qquad (5.34)$$

where

$$t = RA - \theta_G - \lambda ,$$

(ϕ,λ) being coordinates of the station, θ_G the reference meridian sidereal time and (RA, δ) the celestial coordinates of the tide producing body B.

The two parameters $(h_2, \Delta t)$ appear to represent the body tide to 3%, thus showing a possibility that a finite number of parameters are needed in conjunction with the load representation, to adequately model the deformation of the radial response to the tide producing forces. Following the same procedures used in the derivations of equations 5.26 and 5.27,

$$dr = \frac{h_2 W_2}{g} \left[1 - \frac{P_{21}(\cos\psi)}{P_{20}(\cos\psi)} \frac{\cos\phi \cos\delta \sin t}{\sin\psi} \Delta t\right] + \frac{G\rho_w a}{2g} \iint \zeta'' \operatorname{cosec}^2 \tfrac{1}{2}\psi \, d\sigma \qquad (5.35)$$

where

$$\zeta'' = c'\zeta = \sum_{n=1}^{\infty} h'_n \zeta_n \text{ , and}$$

$$c' = \sum_{n=1}^{n'_m} c'_n (\phi,\lambda) \text{ ,}$$

Similarly,

$$\frac{\partial dr}{\partial X_\alpha} = -\frac{h_2}{ag} \frac{\partial W_2}{\partial \psi} \cos A_\alpha + \frac{G\rho_w a}{4g} \iint \zeta'' \operatorname{cosec}^2 \tfrac{1}{2}\psi \cos \tfrac{1}{2}\psi \cos A_\alpha \, d\sigma \qquad (5.36)$$

The representation of the radial deformation by a set of parameters defining c' could possibly be obtained through the analysis of gravimeter and tiltmeter data by using equations 5.30, 5.31, 5.35 and 5.36 on a global basis. This set would be finite in number if, as in the case of the body tide, the deformation could be characterised as a response which is more a function of load than of position.

The tidal information on a global scale is usually given in the form of cotidal-corange charts. The ocean tide height ζ_b at a point $G(\phi,\lambda)$ is given by

$$\zeta_b(\phi,\lambda,\theta_b) = \sum\sum \bar{P}_{nm} (\sin\phi) \left[\bar{\zeta}_1(\theta_b) \cos m\lambda + \bar{\zeta}_2(\theta_b) \sin m\lambda\right] \qquad (5.37)$$

where

$$\bar{\zeta}_1(\theta_b) = \bar{\zeta}_{1nm} \cos\theta_b + \bar{\zeta}'_{1nm} \sin\theta_b$$

and

$$\bar{\zeta}_2(\theta_b) = \bar{\zeta}_{2nm} \cos\theta_b + \bar{\zeta}'_{2nm} \sin\theta_b \qquad (5.38)$$

θ_b being the reference meridian hour angle of the tide producing body. The coefficients $\bar{\zeta}_{\alpha nm}$ and $\bar{\zeta}_{\alpha nm}$ are obtained by the global analysis of tidal information from the relations

$$\zeta_a \cos\alpha_a = \sum\sum \bar{P}_{nm} (\sin\phi)\left[\bar{\zeta}_{1nm} \cos m\lambda + \bar{\zeta}_{2nm} \sin m\lambda\right]$$

and (5.39)

$$\zeta_a \sin\alpha_a = \sum\sum \bar{P}_{nm} (\sin\phi) \left[\bar{\zeta}'_{1nm} \cos m\lambda + \bar{\zeta}'_{2nm} \sin m\lambda\right]$$

where ζ_a is the tidal amplitude and α_a the phase lag at (ϕ,λ) in relation to the lag-free tide on the reference meridian.

In trying to represent the effect of ocean loading on the radial deformation of the body tide with reference to Australia, the following remarks can be made.

The boundary of a vaguely circular land mass can be economically described by a set of wavelength doubled zonal harmonics with the pole at the centroid $G(\phi_c, \lambda_c)$ of the land mass. The geographical

coordinates of the centroid representing the mean value, $M\{\ \}$ of geographical coordinates of the coastline, denoted by $(\phi_q,\ \lambda_q)$ for a general point Q, are

$$\phi_c = M\{\phi_q\} \quad ; \quad \lambda_c = M\{\lambda_q\} \tag{5.40}$$

The angular distance ψ' from the centroid to the coastline is defined by

$$\psi' = \cos^{-1}(\sin\phi_q \sin\phi_c + \cos\phi_q \cos\phi_c \cos\delta\lambda) \tag{5.41}$$

where

$$\delta\lambda = \lambda_q - \lambda_c \tag{5.42}$$

The coastline can be represented by the relation

$$\psi'_j = \sum_{i=0}^{n'} c_{\psi i} P_{io}(\cos\tfrac{1}{2}\alpha_j) \tag{5.43}$$

where

$$\alpha = \sin^{-1}(\sin\psi' \cos\phi_q \operatorname{cosec}\delta\lambda)$$

$$= \cos^{-1}[(\sin\phi_q - \cos\psi' \sin\phi_c)/(\sin\psi' \cos\phi_c)] \tag{5.44}$$

and $c_{\psi i}$ being the appropriate harmonic coefficients. The radial deformation $dr_{\text{tidal loading}}$ at $P(\phi,\lambda)$ can be expressed at any time t by a relation of the form

$$dr_{\text{tidal loading}} = dr(\phi, \lambda, t)$$

$$= dr_1(\psi_c)\, dr_2(\alpha_c)\, dr_3(t) \tag{5.45}$$

ψ_c being the angular distance from the coastline and α_c the azimuth of P from C.

A possible computational sequence for the definitive parameters is the following. ψ'_p is obtained from equation 5.41 using the coordinates of P instead of Q. α_c is obtained from equation 5.44, using parameters related to P instead of Q.

$$\psi_c = \psi' - \psi'_p \tag{5.46}$$

ψ' being computed from equation 5.43 for the specified value of α_c.

Calculations for the ocean loading effect have recently been performed using a method developed by Longman and Farrell. An outline of the method is given below, with results of the method compared with results from the truncation function method of evaluating the ocean loading effect.

5.2.3 Outline of Longman-Farrell Method for Calculation of Oceanic Perturbations

This method for the calculation for ocean loading perturbations is formulated from a development by LONGMAN (1962, 1963). The development was adapted from a presentation by PEKERIS & JAROSCH (1958) and ALTERMAN ET AL (1959). The formulae given by LONGMAN (1963) involve infinite summations of load deformation coefficients which in turn are evaluated by FARRELL (1972) to obtain a practical method for the calculation of oceanic perturbations. This development and evaluation will be expressed as the Longman-Farrell method, and is outlined below.

The response of the Earth is obtained from solving the equations of equilibrium of the deformed Earth, developed in terms of displacements from the Earth's centre and changes in potential. The equations were initially obtained from equations of free oscillations of the Earth (see PEKERIS & JAROSCH 1958, ALTERMAN ET AL 1959).

Assuming a mass distribution of surface density, σ_n proportional to the Legendre polynomial $P_n(\cos \psi)$,

$$\sigma_n = K_n P_n (\cos \psi) \tag{5.47}$$

the solutions of the equations of equilibrium are of the form

$$\delta r = A(r) P_n(\cos \psi) \tag{5.48}$$

$$\delta l = B(r) \frac{\partial P}{\partial \psi} (\cos \psi) \tag{5.49}$$

$$\delta W_u = C(r) P_n (\cos \psi) \tag{5.50}$$

where δr and δl are the vertical and horizontal components of the surface displacements due to the ocean tide loading. δW_u is the change in potential at the undeformed surface, ψ is the angular distance between the point mass and the computation point, and r the distance from the Earth's centre.

A unit surface mass can be expressed as

$$S_M = \sum_{n=0}^{\infty} K_n P_n (\cos \psi) \tag{5.51}$$

where

$$K_n = \frac{[P_{n-1} (\cos \alpha_r) - P_{n+1} (\cos \alpha_r)]}{4\pi a^2 (1 - \cos \alpha_r)} \quad , \quad n > 0$$

$$K_o = 1 / 4 \pi a^2 \qquad n = 0$$

where the unit mass is uniformly distributed across a disk of radius α_r.

To obtain a solution for the displacements, the equations of equilibrium are altered by using the equilibrium of the core. The equations of equilibrium are numerically solved by using estimates of the Lamé elastic constants and the density distribution, subject to boundary conditions.

Using the method of ALTERMAN ET AL (1959) the equations of motion are numerical integrated. These transformed equations (see LONGMAN 1963, p 486) are solved subject to boundary conditions determined by the mass distribution of the load on the surface and internal properties. The boundary conditions consist of three conditions to be satisfied at the Earth's surface and conditions of continuity at internal discontinuities and at the core boundary.

Load deformation coefficients (see MUNK & MACDONALD 1960, p 29) are introduced directly from the solution of boundary conditions at the Earth's surface (see LONGMAN 1963). Thus a solution in terms of load deformation coefficients (h'_n, k'_n, l'_n), the surface displacements and change in potential (at the undeformed surface) is

$$\delta r = \frac{1}{m_e} a h'_n P_n (\cos \psi) \tag{5.52}$$

$$\delta l = \frac{1}{m_e} a\, l'_n \frac{\partial P_n}{\partial \psi} (\cos \psi) \tag{5.53}$$

$$\delta W_u = \frac{1}{m_e} a\, g\, (1 + k'_n)\, P_n (\cos \psi) \tag{5.54}$$

for unit mass load, where m_e is the mass of the Earth, g is gravity at the Earth's surface, and a is the Earth's mean radius.

At the deformed surface, the change in potential is

$$\delta W = \frac{ag}{m_e} \sum_{n=0}^{\infty} (1 + k'_n - h'_n)\, P_n (\cos \psi) \tag{5.55}$$

The change in gravity at the deformed surface becomes (LONGMAN 1963, p 489, FARRELL 1972, p 782)

$$\delta g = \frac{g}{m_e} \sum_{n=0}^{\infty} (n + 2h'_n - (n+1)\, k'_n)\, P_n (\cos \psi) \tag{5.56}$$

and the tilt at the deformed surface is

$$\delta \xi = -\frac{1}{m_e} \sum_{n=0}^{\infty} (1 + k'_n - h'_n) \frac{\partial P_n}{\partial \psi} (\cos \psi) \tag{5.57}$$

In order to improve the convergence of the above summations, Farrell introduced scale shifts and transformations. The latter two equations are divided into a Newtonian and an elastic acceleration in the form

$$\delta g = \delta g^N + \delta g^E \tag{5.58}$$

$$\delta \xi = \delta \xi^N + \delta \xi^E \tag{5.59}$$

where

$$\delta g^N = \frac{-g}{4 m_e \sin (\psi/2)} \tag{5.60}$$

$$\delta \xi^N = \frac{\cos (\psi/2)}{4 m_e \sin^2 (\psi/2)} \tag{5.61}$$

The elastic terms, which consist of all but the first term in the summations of equations 5.56 and 5.57, are summed by Farrell up to n = 10,000 for a unit mass at varying geocentric distances. The calculations are presented in tabular form for various Earth models (see FARRELL 1972, Tables A3 to A5).

The formulation developed and outlined in this Chapter is utilised in the following Chapter to calculate ocean loading effects in Australia. Various ocean model calculations are compared, as are comparisons between the truncation function approach and the Longman-Farrell method.

CHAPTER 6
COMPUTATIONAL RESULTS FOR TIDAL LOADING FOR AUSTRALIA

6.1 Introduction

The major contribution to the ocean tide effect on gravity comes from the water closest to the observation site. However, the outer zone contributions of the global ocean tide cannot be neglected irrespective of the distance of the gravimeter site from the oceans.

The truncation function method, outlined in Section 5.2.2 has been used to estimate the effect of the ocean loading of the outer zone on tidal gravity, and the results are presented in Section 6.2. The calculations are estimated for all Australian stations and use all the models described in Table 5.1. As a comparison, the Longman-Farrell method which was outlined in Section 5.2.3, based on response functions is used and the results are given in Section 6.4. The latter method was limited to the same global surface area as the truncation function method, five degrees from the computation point. In Section 6.6 a model is developed for the Earth response which can generate the ocean loading effect on tidal gravity for adequately correcting quasi-radial distance measurements to extra-terrestrial sources in Earth orbit.

The evaluation of the ocean loading effects on gravity, as expressed by equation 5.7, conventionally entails numerical summation of surface elements over the entire globe. The summation needs a harmonic representation of the surface element ocean load with appropriate multiplication by local deformation coefficients. The Longman-Farrell method uses this approach, where predetermined ocean loading effects are given in tabular form for a point mass load at varying distances from the computation point.

In the truncation function approach, the gravitational effect due to the attraction of the re-distributed tidal water mass is directly calculated through equation 5.15. To evaluate the other two contributions, as described by equation 5.8, a numerical summation similar to the one described above is needed. The numerical summation is eliminated by relating the attraction term to the load potential. The evaluation of the total ocean loading effect is thus reduced to calculating the attraction term for individual values of degree n, and then applying the load deformation coefficients. A description of this method is found in Section 6.2.

The tidal data within five degrees of the Australian coastline was obtained from local cotidal-corange data (EASTON 1970). Thus providing a more realistic model of local oceans for the inner zone calculations, whereas the global models would in many cases provide little or no data on the continental shelves. The inner zone calculations are best evaluated by using the first term of equation 5.15, which determines only the attraction of the water masses directly from the ocean height. However, the evaluation of the total inner zone effect requires a harmonic representation of the local ocean tide. A harmonic representation of local oceans is both unpractical and unreliable, as it will be unable to model local conditions to sufficient accuracy. To overcome this limitation, the inner zone calculations were preformed using the Longman-Farrell method, which requires no harmonic development of the local ocean. Due to the unreliability of all the global ocean tide harmonic models and the lack of local ocean models, the inner zone calculations were limited only to the M_2 constituent.

6.2 Computational Procedures for Truncation Function Method

The tidal information for the calculation of the outer zone effects must provide a global coverage. This can be obtained from cotidal-corange charts where the ocean tide height is given by equation 5.37,

$$\zeta_b\ (\phi,\ \lambda,\ \theta_b) \ = \ \sum_n \ \sum_m \bar{P}_{nm}(\sin\ \phi)\ [\ \bar{\zeta}_1(\theta_b)\ \cos\ m\lambda \ + \bar{\zeta}_2\ (\theta_b)\ \sin\ m\lambda\ ]\ .$$

Charts showing the global ocean tides were analysed using surface spherical harmonics to (20,20) by data sampling on a five degree equal area grid according to equation 5.39. The load deformation coefficients were obtained from LONGMAN(1966) and are shown in Table 6.1.

Equation 5.8 can be rewritten as

$$\delta g \ = \ -(1 + h_2 - \frac{3}{2} k_2)\ \frac{2W_2}{R_p} - \sum_{n=1}^{\infty}\ (1 + \frac{2}{n} h'_n - \frac{n+1}{n} k'_n)\ \frac{\partial V_n}{\partial h} \qquad (6.1)$$

by use of the relation,

$$\frac{\partial V}{\partial h} \ = \ \sum_{n=1}^{\infty}\ \frac{nV_n}{R_p} \ = \ \sum_{n=1}^{\infty}\ \frac{\partial V_n}{\partial h} \qquad (6.2)$$

The results obtained for the Australian sites, by the use of the load deformation coefficients in equation 6.1 are shown in Tables 6.2, 6.3 and 6.4.

Table 6.2 shows the amplitudes in μgals and the local phase in degrees of the ocean tide effects on gravity using three global M_2 ocean tide models, *Hendershott* model 1 and 2, and the *Zahel* model. The properties of these models and other models used in this Chapter are outlined in Section 5.1 and Table 5.1. The phases shown in Table 6.2 represent twice the hour angle of the Moon when the ocean tide amplitude is a maximum. The results for each site are set out in four rows, referenced a, b, c and d. The results in row a represents the gravitational attraction of the water masses. Those in row b give the tidal loading effect, while the results in row c are the effect on gravity of the apparent variation of the potential field at the observing station and can also be expressed as the radial displacement term. The total effect of the ocean tide loading on gravity is given in row d. The results of Table 6.2 represent only the outer zone effect beyond an angular distance of five degrees from the computation point and have been computed by the use of the truncation function procedure described in Sections 5.2.2.1 and 6.1. The attraction of the re-distributed tidal water mass is evaluated for degree n by the second term of equation 5.15. The attraction term evaluated for degree n, is then used in equation 6.1 together with load deformation coefficients to obtain the ocean tide loading for degree n. A summation for all n provides the total outer zone tidal loading effect.

Table 6.3 represents a summary of the total outer zone ocean tide loading on gravity at Australian sites using seven different M_2 wave models. Table 6.4 summaries the total outer zone ocean tide loading on gravity using different O_1, K_1 and S_2 ocean tide waves. Both Tables show the amplitude of the tidal loading in μgals and the local phase in degrees.

The results given in the last two Tables show variations in amplitudes and phases on each row when using several models at the same site. However, the variations between sites for the same tidal model are similar for the constituents, being dependent on longitude and/or time. Overall the diurnal wave models show less variations in phase between sites for the same tidal model.

The differences between the models are primarily due to the method of solution used and the conditions applied in each case when solving the Laplace Tidal Equation. ROBINSON(1974) has reported similar discrepancies between various ocean tide models at sites in the south-eastern United States.

n	h'	k'	l'	h'	k'	l'	h'	k'	l'	h'	k'	l'
	(LONGMAN 1966)			(KAULA 1963)			(TAKEUCHI ET AL 1962)			(FARRELL 1972a)		
0	-0.134			-	-		-	-				
1										-0.290	0	0.113
2	-1.007	-0.310	0.030	-0.981	-0.303	0.027	-1.034	-0.312	-	-1.001	-0.308	0.030
3	-1.059	-0.197	0.075	-1.050	-0.197	0.073	-1.078	-0.191	-	-1.052	-0.195	0.074
4	-1.059	-0.133	0.062	-1.058	-0.134	0.062	-1.083	-0.126	-	-1.053	-0.132	0.062
5	-1.093	-0.104	0.049	-1.093	-0.105	0.049	-1.121	-0.096	-	-1.088	-0.103	0.049
6	-1.152	-0.090	0.041	-1.153	-0.090	0.041	-1.185	-0.071	-	-1.147	-0.089	0.041
7	-1.223	-0.082	0.037	-1.223	-0.082	0.037	-1.260	-0.072	-	-	-	-
8	-1.296	-0.076	0.034	-1.297	-0.076	0.034	-1.338	-0.066	-	-1.291	-0.076	0.034
9	-1.369	-0.072	0.032	-1.369	-0.072	0.032	-	-	-	-	-	-
10	-1.439	-0.069	0.030	-1.439	-0.069	0.030	-1.486	-0.058	-	-1.433	-0.068	0.030
11	-1.506	-0.066	0.029	-	-	-	-	-	-	-	-	-
12	-1.572	-0.064	0.028	-1.571	-0.064	0.028	-1.622	-0.052	-	-	-	-
13	-1.631	-0.062	0.027	-	-	-	-	-	-	-	-	-
14	-1.691	-0.060	0.027	-1.691	-0.060	0.027	-1.750	-0.048	-	-	-	-
15	-1.747	-0.058	0.026	-	-	-	-	-	-	-	-	-
16	-1.798	-0.056	0.026	-1.801	-0.056	0.026	-1.872	-0.045	-	-	-	-
17	-1.852	-0.055	0.025	-	-	-	-	-	-	-	-	-
18	-1.902	-0.054	0.025	-	-	-	-	-	-	-1.893	-0.053	0.025
19	-1.949	-0.052	0.025	-	-	-	-	-	-	-	-	-
20	-1.994	-0.051	0.025	-	-	-	-	-	-	-	-	-
21	-2.037	-0.050	0.024	-	-	-	-	-	-	-	-	-
22	-2.078	-0.049	0.024	-	-	-	-	-	-	-	-	-
23	-2.117	-0.048	0.024	-	-	-	-	-	-	-	-	-
24	-2.156	-0.047	0.023	-	-	-	-	-	-	-	-	-
25	-2.194	-0.046	0.023	-	-	-	-	-	-	-	-	-

TABLE 6.1
Load Deformation Coefficients Determined by Various Authors

TABLE 6.2

Amplitudes and Phases of the Outer Zone Effect due to the M_2 Tide on Gravity Measurements Using Selected Ocean Tide Models

(Truncation Function Method)

Site	Hendershott Model 1		Hendershott Model 2		Zahel Model		Reference
	Amplitude (μgal)	Local Phase (degrees)	Amplitude (μgal)	Local Phase (degrees)	Amplitude (μgal)	Local Phase (degrees)	
Port Moresby	0.983	-30.1	2.125	-26.1	1.244	61.8	a
	0.086	-161.4	0.537	165.1	0.469	-101.3	b
	0.111	168.2	1.157	160.2	1.016	-108.7	c
	0.935	-28.3	1.503	-27.0	0.692	59.1	d
Canberra	0.990	-46.8	1.794	-30.2	1.014	8.0	a
	0.121	162.1	0.609	167.1	0.340	-123.3	b
	0.171	126.6	1.181	164.1	0.743	-142.3	c
	0.930	-42.0	1.236	-35.3	0.604	-2.8	d
Broken Hill	0.982	-24.5	1.329	-11.2	0.804	42.6	a
	0.155	163.2	0.463	-176.3	0.333	-113.3	b
	0.226	131.3	0.836	179.8	0.718	-126.5	c
	0.937	-17.7	0.957	-13.7	0.404	42.6	d
Armidale	1.060	-47.8	2.269	-33.4	1.385	10.3	a
	0.126	177.1	0.692	161.4	0.405	-122.4	b
	0.181	155.2	1.425	158.8	0.910	-140.5	c
	0.983	-46.8	1.551	-38.1	0.879	0.7	d
Perth	2.134	45.1	0.720	130.0	0.409	152.9	a
	0.468	-148.5	0.152	-24.3	0.207	-100.9	b
	0.898	-150.6	0.395	-4.5	0.379	-97.6	c
	1.730	49.4	0.618	109.5	0.376	177.8	d
Hobart	0.832	-53.6	1.281	-29.5	0.618	-11.8	a
	0.114	145.4	0.522	171.0	0.248	-127.0	b
	0.187	93.9	0.928	168.2	0.505	-149.5	c
	0.793	-43.6	0.891	-35.9	0.370	-30.5	d
Charters Towers	0.984	-31.3	2.005	-21.0	1.214	41.6	a
	0.111	-179.1	0.575	170.8	0.435	-109.6	b
	0.142	153.9	1.179	166.9	0.955	-121.7	c
	0.938	-28.4	1.401	-22.8	0.683	36.1	d
Darwin	1.037	12.4	1.111	9.5	0.589	80.7	a
	0.182	164.7	0.296	-170.4	0.329	-107.9	b
	0.277	140.9	0.558	179.6	0.670	-113.8	c
	1.034	19.9	0.864	16.3	0.291	104.9	d
Alice Springs	0.992	4.5	1.055	10.1	0.653	76.9	a
	0.193	171.1	0.325	-162.7	0.325	-106.0	b
	0.265	147.5	0.553	-169.2	0.676	-113.4	c
	0.974	11.2	0.825	12.4	0.327	95.1	d

Key

a = Attraction Term

b = Loading Term

c = Radial Displacement

d = a - b + c

Site	Hendershott Model 1		Hendershott Model 2		Zahel		Bogdanov		Tiron		Pekeris & Accad 2^{o} non-diss.		Pekeris & Accad 1^{o} diss.	
	Amplitude	Phase	Amplitude	Phase	Amplitude	Phase	Amplitude	Phase	Amplitude	Phase	Amplitude	Phase	Amplitude	Phase
Port Moresby	0.935	-28.3	1.503	-27.0	0.692	59.1	0.169	46.2	0.275	175.7	1.384	72.5	1.180	20.2
Canberra	0.930	-42.0	1.236	-35.3	0.604	-2.8	0.660	-150.5	0.533	-150.2	1.519	129.5	1.054	17.0
Broken Hill	0.937	-17.7	0.957	-13.7	0.404	42.6	0.652	-139.9	0.694	-151.2	1.208	125.8	0.756	35.8
Armidale	0.983	-46.8	1.551	-38.1	0.879	0.7	0.451	-141.1	0.355	-134.3	1.525	124.1	1.512	12.6
Perth	1.730	49.4	0.618	109.5	0.376	177.8	0.786	-99.2	1.406	-106.7	0.715	144.1	0.129	130.1
Hobart	0.793	-43.6	0.891	-35.9	0.370	-30.5	0.871	-154.5	0.697	-158.2	1.430	131.2	0.741	3.1
Charters Towers	0.938	-28.4	1.401	-22.8	0.683	36.1	0.218	-128.6	0.369	-162.0	1.192	100.9	1.377	16.8
Darwin	1.034	19.9	0.864	16.3	0.291	104.9	0.396	-115.2	0.809	-135.7	1.040	-170.5	0.110	75.5
Alice Springs	0.974	11.2	0.825	12.4	0.327	95.1	0.548	-127.7	0.837	143.9	0.790	142.0	0.422	57.1

TABLE 6.3

Amplitudesand Phases of the Outer Zone Effects due to Various M_2 Ocean Tide Models on Gravity Using Truncation Function Method

Note: Amplitudes in μgals
Phases are local phases in degrees

Site	Bogdanov S_2		Tiron S_2		Bogdanov O_1		Tiron O_1		Bogdanov K_1		Tiron K_1		Zahel K_1	
	Amplitude	Phase	Amplitude	Phase	Amplitude	Phase	Amplitude	Phase	Amplitude	Phase	Amplitude	Phase	Amplitude	Phase
Port Moresby	0.269	23.6	0.210	34.6	0.146	68.4	0.214	-27.3	0.317	2.3	0.470	-80.0	0.346	-62.0
Canberra	0.052	-150.0	0.086	74.2	0.351	121.4	0.168	-33.1	0.269	89.4	0.303	-76.5	0.294	-90.2
Broken Hill	0.058	167.1	0.162	111.6	0.322	130.8	0.165	-16.7	0.228	101.9	0.299	-65.5	0.287	-94.6
Armidale	0.084	-75.4	0.107	-2.8	0.317	110.1	0.161	-24.5	0.248	60.8	0.337	-73.2	0.299	-72.8
Perth	0.214	-164.5	0.504	-169.0	0.396	176.9	0.227	45.7	0.274	-178.0	0.330	-5.7	0.493	-93.0
Hobart	0.106	178.7	0.145	115.4	0.394	133.5	0.217	-44.4	0.332	113.9	0.316	-80.9	0.374	-106.0
Charters Towers	0.108	10.2	0.139	35.2	0.207	99.7	0.186	-8.0	0.213	25.9	0.386	-67.2	0.301	-70.4
Darwin	0.087	122.7	0.301	147.7	0.155	127.0	0.111	42.3	0.089	53.8	0.241	-45.8	0.399	-90.6
Alice Springs	0.085	146.1	0.275	140.5	0.236	137.0	0.145	19.1	0.120	99.7	0.271	-47.7	0.341	-94.0

TABLE 6.4

Amplitudes and Phases of the Outer Zone Effects due to Various S_2, O_1 and K_1 Ocean Tide Models on Gravity Using Truncation Function Method

Note: Amplitudes in μgals

Phases are local phases in degrees

6.3 A Method of Representing the Ocean Tide Deformation with Truncation Functions

The initial development and calculations in this Section were obtained from BRETREGER & MATHER (1976). The results in Table 6.2, calculated from Longman's load deformation coefficients, show an approximate tendency for the loading term to be related to the radial deformation term for a given tidal model. It is not unreasonable to postulate that the complex nature of the ocean tidal loading effect on observed gravity is more a function of the tidal model rather than any unrelated response of the elastic Earth to the complex load. The conventional method requires the use of load deformation coefficients together with surface spherical harmonic representations of the ocean tide to a very high degree. This requires a very large number of parameters (load deformation coefficients) to model the Earth response to the ocean tide load. Furthermore, the higher degree harmonics of the global ocean tide are not reliably known at the present time.

In view of the approximate relationships reported in Table 6.2, it would appear that a few coefficients c_n may be able to provide a representation equivalent to that obtained by the less economic procedure based on higher harmonic representations of the global ocean tide and numerous load deformation coefficients.

Equation 6.1 can then be rewritten for the outer zone contribution (δg_o) to the ocean loading effect on gravity as

$$\delta g_o = - (1 + h_2 - \tfrac{3}{2} k_2) \frac{2W_2}{R_p} - c \left(\frac{\partial V}{\partial h}\right)_o \qquad (6.3)$$

where

$$c = \sum_{n=1}^{n_{max}} c_n (\phi,\lambda) \qquad (6.4)$$

$$\left(\frac{\partial V}{\partial h}\right)_o = - \tfrac{1}{2} G \rho_w \pi \sum_{n=1}^{\infty} X_n \zeta_n \qquad (6.5)$$

and δg_o represents the solid Earth tide in addition to the outer zone contribution of the ocean tidal loading effect on gravity. This is a modified form of the approach suggested in Section 5.2.2.4. The form of the functions $c_n(\phi,\lambda)$ can only be reliably determined from a study of the gravity tidal loading effects on a global basis. As the data available at the present time was confined to the Australian region, it was decided to evaluate c in the case when n_{max} is equal to 1 in equation 6.4. Such a procedure was felt to be warranted as the phase angle differences between the attraction and total loading terms in Table 6.2 appear to be correlated with position and did not vary excessively over the test region.

As shown in Table 6.5, these estimates of c_1 at Australian stations, computed on the basis of rows a and d in Table 6.2 have mean values $\bar{c}_1$ for the region as shown at the foot of the table referred to earlier. The value obtained for $\bar{c}_1$ using *Hendershott's* M_2 model 1 is 0.94 ± 0.05, *Hendershott's* M_2 model 2 is 0.74 ± 0.06, while that obtained using *Zahel's* M_2 model is 0.60 ± 0.13. The significance of these numbers is more clearly illustrated by considering the results in columns (3 & 4), (6 & 7) and (9 & 10) in Table 6.5 which represent [(d - $\bar{c}_1$a) / d] expressed both as a percentage and in μgal, for each of the ocean tide models studied. The largest discrepancy in the case of *Hendershott's* M_2 model 1 occurs at Perth. This is probably due to the intermediate zone effects being evaluated using significantly different areas of the oceans as it is located on the west coast of Australia. The largest percentage change obtained on using both the *Zahel* M_2 model and *Hendershott's* M_2 model 2 is again at Perth though the numerical change in μgal is no larger than at other sites which lie in more westerly longitudes (Broken Hill, Alice Springs and Darwin).

Comparison with the results from Earth tide observations in Australia (see Figure 4.2) shows a relationship between the variations in the c_1 parameter and variations in the tidal parameters. The amplitude factors are high along the coast, and the phase lags being positive on the west coast

Site	Hendershott M_2 Model 1 Ocean Tide $(d - \bar{c}_1 a)/d$			Hendershott M_2 Model 2 Ocean Tide $(d - \bar{c}_1 a)/d$			Zahel M_2 Ocean Tide $(d - \bar{c}_1 a)/d$		
	c	%	µgal	c	%	µgal	c	%	µgal
Port Moresby	0.95	1.1	0.01	0.71	-4.6	-0.07	0.56	-7.1	-0.09
Canberra	0.94	-0.2	-0.00	0.69	-7.4	-0.09	0.60	-0.1	-0.00
Broken Hill	0.95	1.4	0.01	0.72	-2.8	-0.03	0.50	-18.6	-0.15
Armidale	0.93	-1.5	-0.02	0.68	-8.3	-0.13	0.63	6.1	0.08
Perth	0.81	-16.1	-0.34	0.86	13.8	-0.09	0.92	35.2	0.14
Hobart	0.95	1.3	0.01	0.70	-6.4	-0.06	0.60	0.5	0.00
Charters Towers	0.95	1.3	0.01	0.70	-5.9	-0.08	0.56	-5.9	-0.07
Darwin	0.98	5.6	0.06	0.78	4.8	0.04	0.49	-20.6	-0.12
Alice Springs	0.98	4.2	0.04	0.82	5.4	0.04	0.50	-19.0	-0.12
Mean	0.94			0.74			0.60		

TABLE 6.5
Values of the Coefficient c_1 at Instrument Sites in Australia and Papua New Guinea

and negative on the east coast. These two characteristics show the differing effects of the Indian and Pacific Oceans respectively. This trend can also be noticed in the results for the c_1 values for each Australian station. The range in c_1 is greatest at Perth for all ocean models, while the eastern sites show small variations in c_1 between each site. Such variations show that the global response for Australia cannot be simplified with one parameter due to the different nature of the Indian and Pacific Oceans near the Australian continent.

In conclusion, it would appear that the similarities in the values of c_1 obtained for tidal gravity stations on the eastern littoral of Australia are not unexpected in view of the limited surface area sampled. It should be noted that the results only represent outer zone effects.

All calculations presented so far in this Chapter represent only the truncation function method for the ocean loading effect, the following Sections represent calculations by the Longman-Farrell method.

6.4 Calculation of Outer Zone Effects by Longman-Farrell Method

In the evaluation of equations 5.58 and 5.59 in Section 5.2.3, FARRELL (1972a) has tabulated the effects of a point mass load for a number of Earth models expressed in terms of the angular distance from the computation point. Such a table for the elastic part of the gravity loading is illustrated in Figure 6.1, where the amplitudes are gravity perturbations arising from a 1 kg point load on the Earth's surface. The Newtonian part of the response can be calculated by the use of equation 5.60 in Section 5.2.3.

The load at a point in the ocean was calculated by obtaining the amplitude and phase values on a 5° grid for all the ocean tide models mentioned in Section 5.1.3. The ocean load is calculated at each $5^\circ \times 5^\circ$ block and then multiplied by the appropriate response value obtained from Figure 6.1. All the squares are then summed to provide a global value for the outer zone effect of the tidal loading. All calculations, as with the truncation function method are limited to the zone beyond five degrees from the computation point.

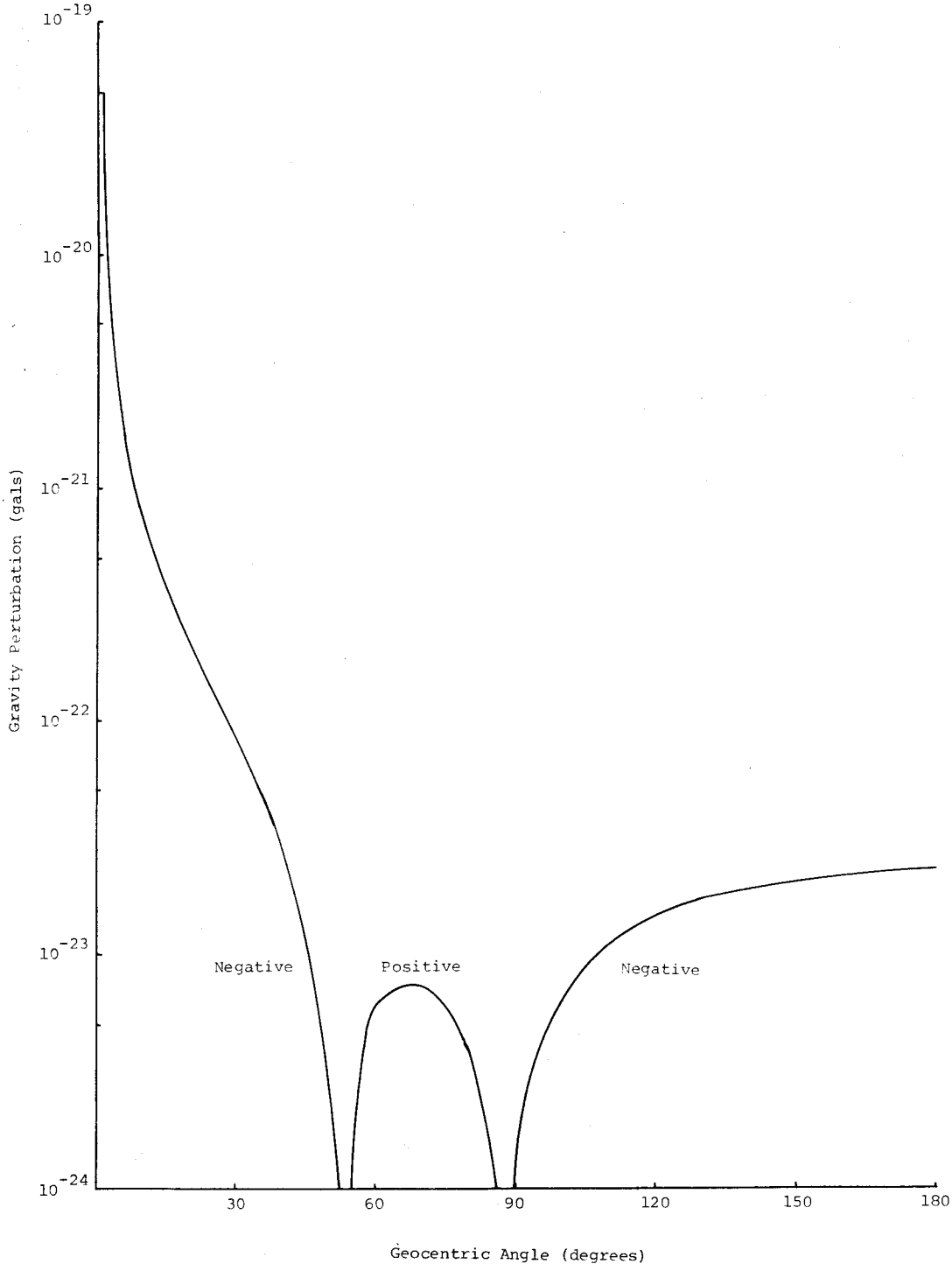

FIGURE 6.1

Gravimetric Response Function for Solid Earth (Continental-Shield Mantle on G-B Nucleus). Amplitude Indicates Gravity Perturbation Arising from a 1 kg Point Load on the Surface.

The results of these calculations are shown in Tables 6.6 and 6.7. The Tables show the amplitudes in μgals and phase in degrees of the total gravimetric tidal loading at each Australian site. These initial computations come directly from the digitised ocean tidal models and thus have not been corrected for mass conservation. The semi-diurnal M_2 tidal models are shown in Table 6.6, while the S_2, O_1 and K_1 tide models are shown in Table 6.7. In all cases the amplitudes and phases have the same definitions as in Sections 6.2 and 6.3.

The sensitivity of using a $5^o \times 5^o$ block was checked using the *Zahel* M_2 tide model. The check method consisted of using geocentric annular rings which were dependent on the rate of change of the gravity response with the geocentric angle. The ocean tide height at a point on the globe was calculated by interpolation from the values on a $5^o \times 5^o$ block. This method takes a considerably longer execution time than the $5^o \times 5^o$ block method. The results for all sites show differences of less than 10% in amplitude and less than 6 degrees in phase. Considering the numerous approximations and other assumptions the block method is considered to be appropriate for the calculations.

These calculations were based on the initial digitisation of the ocean tidal models, additional calculations showed that the tidal models did not conserve mass. All models were subsequently modified by applying a correction (expressed in centimetres and a phase) proportional to the amplitude of the oceanic tide. This being a simple and convenient method to obtain conservation of mass. The amount to which each tidal model does not conserve mass is very dependent on the method of digitisation of the ocean tidal charts, in addition to the actual ocean tide charts obtained through solving the LTE. FARRELL (1972b) reported the necessity for ocean tides to conserve mass in his study of tidal loading.

The tidal loading effects after correction for conservation of mass are presented in Tables 6.8 and 6.9. Table 6.8 gives the results for the M_2 ocean tide models while Table 6.9 shows the results for the S_2, O_1 and K_1 ocean tide models. The results show considerable differences to those calculated without conservation of mass, and signifies the importance of this correction in any tidal loading calculations. It can be seen that for all Australian sites, even the continental site of Alice Springs, the results can reverse the phase and alter the amplitudes considerably. MELCHIOR ET AL (1976) have shown similar large variations after correcting for mass conservation in European sites.

The Longman-Farrell method is also used to calculate the inner zone effects for the tidal loading. The results obtained for the Australian sites are presented in the following Section.

6.5 Inner Zone Calculations Using Longman-Farrell Method

The inner zone ocean tidal loading, limited to within 5 degrees of the computation point, produces a significant effect on tidal gravity measurements. The truncation function procedure for the inner zone consists of solving the first term in equation 5.15. This expression evaluates the gravitational effect due to the attraction of the re-distributed tidal water masses and is equivalent to the Newtonian acceleration in the Longman-Farrell method, given by equation 5.60. However, the other components of the tidal loading require the harmonic representation of the local tide to a high degree to obtain sufficient resolution, which is not available on global ocean tide models. Also the accuracy of local data on the global models is open to controversy. Thus, any harmonic representation method is unsuitable for inner zone calculations and is usually replaced by the Longman-Farrell method which overcomes the harmonic representation by predetermining the response for point mass ocean loads. For the above reasons local tidal models were adopted for the inner zone calculations. The calculations were limited only to the principal ocean tide, M_2 obtained from EASTON (1970), and solved using the Longman-Farrell method.

The results for these calculations are shown in Table 6.10, where the amplitudes are expressed in

Site	Hendershott Model 1		Hendershott Model 2		Zahel		Bogdanov		Tiron		Pekeris & Accad 2^{δ} non-diss.		Pekeris & Accad 1^{δ} diss.	
	Amplitude	Phase	Amplitude	Phase	Amplitude	Phase	Amplitude	Phase	Amplitude	Phase	Amplitude	Phase	Amplitude	Phase
Port Moresby	2.760	-16.9	2.263	-8.2	3.353	48.6	4.217	37.2	1.634	-13.2	6.026	71.1	6.645	6.0
Canberra	2.380	-34.9	1.248	1.4	3.139	-2.5	0.844	63.0	2.041	-74.6	7.485	136.9	5.133	6.7
Broken Hill	2.119	-8.7	0.976	94.6	2.084	32.8	1.105	70.7	1.243	-65.8	4.923	129.6	3.628	18.6
Armidale	2.882	-35.4	2.666	-12.7	4.056	2.5	1.549	22.3	2.399	-58.2	7.119	134.0	6.890	5.2
Perth	5.081	51.5	4.164	-179.7	1.048	170.3	0.974	142.0	1.903	-85.1	3.206	129.9	0.620	21.9
Hobart	1.766	-40.1	0.695	105.5	2.207	-23.4	1.080	136.4	1.740	-100.0	7.059	140.2	4.180	-5.7
Charters Towers	2.443	-23.8	1.996	9.1	3.321	30.0	2.679	33.1	1.721	-38.4	5.089	103.1	6.977	7.5
Darwin	2.335	44.5	0.935	132.9	1.124	78.8	1.953	62.9	0.969	-23.3	3.986	-163.0	1.091	-23.8
Alice Springs	2.242	19.7	1.323	129.0	1.391	66.8	1.407	74.8	0.864	-53.6	3.426	147.7	2.314	23.2

TABLE 6.6

Amplitudes and Phases of the Outer Zone Effects due to Various M_2 Ocean Tide Models on Gravity Using the Longman-Farrell Method without Mass Conservation

Note: Amplitudes in μgals
Phases are local phases in degrees

Site	Bogdanov S_2		Tiron S_2		Bogdanov O_1		Tiron O_1		Bogdanov K_1		Tiron K_1		Zahel K_1	
	Amplitude	Phase	Amplitude	Phase	Amplitude	Phase	Amplitude	Phase	Amplitude	Phase	Amplitude	Phase	Amplitude	Phase
Port Moresby	1.552	23.8	0.396	62.3	0.831	17.6	1.579	-40.1	2.114	-14.9	2.333	-78.2	1.848	-58.2
Canberra	0.222	25.5	0.366	153.2	1.355	125.0	1.106	-47.9	1.091	84.5	1.300	-71.6	0.703	-111.0
Broken Hill	0.335	51.3	0.704	151.4	1.072	139.2	1.164	-36.5	0.764	105.0	1.424	-65.8	0.910	-122.4
Armidale	0.462	-14.9	0.140	-122.7	1.177	105.1	1.015	-39.5	1.124	47.5	1.426	-65.4	0.813	-70.7
Perth	0.505	136.0	1.939	-155.5	1.790	-161.3	1.316	10.0	1.625	-155.7	1.705	-22.5	2.329	-123.3
Hobart	0.239	105.8	0.719	149.0	1.751	139.8	1.371	-53.5	1.609	115.3	1.383	-80.0	1.168	-141.0
Charters Towers	0.858	16.3	0.042	23.9	0.643	75.1	1.283	-20.1	1.270	2.0	1.898	-66.3	1.189	-65.6
Darwin	0.614	58.7	1.372	171.3	0.080	107.8	0.892	-16.9	0.550	-28.8	1.366	-58.1	2.068	-102.3
Alice Springs	0.481	70.1	1.012	166.7	0.659	154.7	1.036	-20.7	0.100	105.4	1.402	-55.3	1.303	-113.6

TABLE 6.7

Amplitudes and Phases of the Outer Zone Effects due to Various S_2, O_1 and K_1 Ocean Tide Models on Gravity Using the Longman-Farrell Method without Mass Conservation.

Note: Amplitudes in μgals
Phases are local phases in degrees

Site	Hendershott Model 1		Hendershott Model 2		Zahel		Bogdanov		Tiron		Pekeris & Accad 2^{o} non-diss.		Pekeris & Accad 1^{o} diss.	
	Amplitude	Phase	Amplitude	Phase	Amplitude	Phase	Amplitude	Phase	Amplitude	Phase	Amplitude	Phase	Amplitude	Phase
Port Moresby	2.016	-34.3	3.819	-26.3	3.404	47.0	2.878	32.6	0.868	-29.7	5.810	69.2	6.703	4.6
Canberra	1.898	-58.8	2.831	-31.9	3.242	-3.0	0.683	-161.5	1.997	-99.2	7.229	138.0	5.177	4.9
Broken Hill	1.506	-32.1	1.328	-5.0	2.168	31.2	0.338	-166.4	1.371	-101.1	4.651	129.9	3.680	16.2
Armidale	2.282	-53.4	4.214	-31.6	4.152	1.9	0.411	-42.5	1.998	-78.2	6.873	135.2	6.921	3.8
Perth	4.223	44.7	2.344	170.4	0.994	165.0	0.803	-112.8	2.692	-94.1	3.003	126.0	0.779	16.5
Hobart	1.511	-75.7	1.391	-37.4	2.317	-23.0	1.819	-169.8	2.133	-123.9	6.794	141.4	4.272	-7.8
Charters Towers	1.877	-45.0	3.299	-17.1	3.397	28.8	1.446	18.8	1.272	-64.7	4.818	102.5	7.032	6.2
Darwin	1.366	39.9	0.881	14.7	1.176	74.4	0.878	41.0	0.864	-69.5	3.828	-159.8	1.251	-25.0
Alice Springs	1.472	4.0	0.781	31.0	1.450	63.7	0.167	84.0	1.087	-97.2	3.169	148.4	2.390	19.9

TABLE 6.8

Amplitudes and Phases of the Outer Zone Effects due to Various M_2 Ocean Tide Models on Gravity Using the Longman-Farrell Method with Mass Conservation.

Note: Amplitudes in μgals
Phases are local phases in degrees

Site	Bogdanov S_2		Tiron S_2		Bogdanov O_1		Tiron O_1		Bogdanov K_1		Tiron K_1		Zahel K_1	
	Amplitude	Phase	Amplitude	Phase	Amplitude	Phase	Amplitude	Phase	Amplitude	Phase	Amplitude	Phase	Amplitude	Phase
Port Moresby	1.292	23.9	0.655	9.5	0.915	18.6	0.972	-35.4	2.084	-10.9	1.813	-77.7	1.749	-61.6
Canberra	0.054	173.3	0.172	-41.6	1.347	121.3	0.484	-46.1	1.241	84.7	0.789	-64.8	0.740	-122.4
Broken Hill	0.118	89.3	0.242	125.3	1.055	134.9	0.581	-31.2	0.903	103.3	0.937	-61.3	0.982	-129.6
Armidale	0.259	-44.7	0.561	-51.5	1.195	100.9	0.424	-20.4	1.251	51.6	0.942	-54.8	0.740	-80.1
Perth	0.396	167.5	1.415	-159.1	1.727	-163.2	0.811	29.8	1.645	-160.9	1.260	-11.9	2.453	-125.4
Hobart	0.346	159.5	0.170	139.3	1.722	137.0	0.732	-58.7	1.750	112.9	0.835	-80.1	1.271	-146.2
Charters Towers	0.613	12.9	0.531	-22.3	0.704	70.3	0.735	-17.0	1.284	8.3	1.418	-61.9	1.115	-71.7
Darwin	0.391	60.8	0.930	164.9	0.131	78.4	0.392	3.2	0.472	-17.4	0.924	-55.4	2.116	-105.9
Alice Springs	0.275	87.3	0.567	156.8	0.635	148.4	0.522	-6.7	0.231	103.3	0.960	-49.9	1.369	-118.7

TABLE 6.9

Amplitudes and Phases of the Outer Zone Effects due to Various S_2, O_1 and K_1 Ocean Tide Models on Gravity Using the Longman-Farrell Method with Mass Conservation.

Note: Amplitudes in μgals
Phases are local phases in degrees

μgals and phase in degrees. The sites of Broken Hill and Alice Springs have no inner zone contributions due to their continental location.

Site	Elastic Acceleration		Newtonian Acceleration		Total Acceleration	
	Amplitude (μgal)	Local Phase (degrees)	Amplitude (μgal)	Local Phase (degrees)	Amplitude (μgal)	Local Phase (degrees)
Port Moresby	1.944	-133.5	0.440	-135.3	2.384	-133.9
Canberra	0.723	-72.2	0.218	-73.9	0.941	-72.6
Broken Hill	-	-	-	-	-	-
Armidale	0.859	-74.4	0.261	-74.2	1.120	-74.3
Perth	0.146	-133.1	0.040	-134.1	0.187	-133.3
Hobart	0.927	-93.7	0.239	-95.8	1.166	-94.1
Charters Towers	1.132	-112.3	0.344	-112.2	1.476	-122.3
Darwin	2.879	39.9	0.698	43.0	3.576	40.5
Alice Springs	-	-	-	-	-	-

TABLE 6.10
Amplitudes and Phases of the Inner Zone Effects due to the M_2 Tide on Gravity Using the Longman-Farrell Method.

6.6 Comparison Between Different Methods

A comparison between the various methods and models can be obtained by correcting the observed amplitude factors and phase lags for the ocean loading effects. The correct values should then approach the theoretical values of 1.163 for the amplitude factor and zero phase lag. The results for the M_2 and O_1 waves are found in Tables 6.11 to 6.14. The methods used in the calculations were the truncation function method and the Longman-Farrell method with and without conservation of mass. The corrected M_2 results represent both the outer and inner zone effects, the latter being calculated by the Longman-Farrell method. Due to the lack of a local O_1 ocean tide model, the results for O_1 represent corrections for only the outer zone effect.

A comparison of these results for each tidal model exhibit many discrepancies, which in turn must be related to the nature of the assumptions made in the tidal model. Many assumptions are involved, including the solving of LTE, the method of solution and the quality of the ocean tide data. The former assumption being discussed in Section 5.1, while the latter two being discussed in Chapters 5, 6, and 10.

The differences between the various models and methods do show some similarities between various sites for a particular model, but it is difficult to establish the best ocean tide model for Australia on the whole. The poor modelling of both the Indian and Pacific Oceans is obvious by the variations in each model for a particular site. The *Hendershott* models and the *Zahel* model for M_2 have the best representation in the Pacific, where some sites in eastern Australia agree well between models and with theory. The poorly modelled Indian Ocean is represented in the Perth results, where the amplitude factor remains high after correction. The M_2 values for Darwin and Alice Springs approach the theoretical values more than any other site. The results for Port Moresby (see row 1, Tables 6.11 to 6.14) suggest there is some unmodelled perturbation in the recordings. A similar pattern occurs in Perth, where the high amplitude factors are still present. The results for Port Moresby should be viewed with some caution, as the instrument used at the site exhibited sensitivity changes (see Section 4.3).

Site	Observed		Hendershott Model 1		Hendershott Model 2		Zahel		Bogdanov		Tiron		Pekeris & Accad 2^0 non-diss.		Pekeris & Accad 1^0 diss.	
	Amp. Factor	Phase Lag(^{0})	Amp. Factor	Phase Lag(^{0})	Amp. Factor	Phase Lag(^{0})	Amp. Factor	Phase Lag(^{0})	Amp. Factor	Phase Lag(^{0})	Amp. Factor	Phase Lag(^{0})	Amp. Factor	Phase Lag(^{0})	Amp. Factor	Phase Lag(^{0})
Port Moresby	1.226	-0.3	1.237	1.0	1.231	1.2	1.243	0.4	1.247	0.7	1.252	0.8	1.243	0.0	1.233	0.5
Canberra	1.210	-2.2	1.190	-0.8	1.184	-0.7	1.192	-1.4	1.215	-1.1	1.213	-1.1	1.224	-2.4	1.184	-1.7
Broken Hill	1.159	-0.1	1.143	0.1	1.142	0.1	1.154	-0.3	1.168	0.3	1.170	0.2	1.172	-1.0	1.148	-0.5
Armidale	1.201	-2.4	1.182	-0.9	1.172	-0.7	1.179	-1.5	1.200	-1.3	1.198	-1.3	1.210	-2.5	1.168	-1.8
Perth	1.237	0.4	1.220	-0.6	1.244	0.0	1.247	0.5	1.243	1.2	1.248	1.6	1.251	0.2	1.242	0.4
Hobart	1.203	-4.1	1.189	-2.2	1.186	-2.2	1.195	-2.6	1.222	-2.3	1.219	-2.4	1.228	-3.9	1.186	-2.8
Charters Towers	1.195	-2.4	1.190	1.1	1.183	1.1	1.195	1.7	1.205	1.3	1.208	1.3	1.206	2.2	1.183	1.7
Darwin	1.204	0.9	1.154	-0.8	1.156	-0.7	1.168	-0.7	1.169	-0.3	1.175	-0.1	1.181	-0.4	1.167	-0.6
Alice Springs	1.167	-0.3	1.152	-0.4	1.155	-0.4	1.167	-0.5	1.172	0.0	1.177	0.1	1.177	-0.7	1.164	-0.6

TABLE 6.11

Corrected Values for Amplitude Factors and Phase Lags for M_2 Using Several Oceanic Models - Truncation Function Method

Site	Observed		Hendershott Model 1		Hendershott Model 2		Zahel		Bogdanov		Tiron		Pekeris & Accad 2^{o} non-diss.		Pekeris & Accad 1^{o} diss.	
	Amp. Factor	Phase Lag(^{o})	Amp. Factor	Phase Lag(^{o})	Amp. Factor	Phase Lag(^{o})	Amp. Factor	Phase Lag(^{o})	Amp. Factor	Phase Lag(^{o})	Amp. Factor	Phase Lag(^{o})	Amp. Factor	Phase Lag(^{o})	Amp. Factor	Phase Lag(^{o})
Port Moresby	1.226	-0.3	1.213	1.3	1.218	1.0	1.218	-0.8	1.203	-0.8	1.227	1.0	1.223	-2.8	1.159	0.4
Canberra	1.210	-2.2	1.165	-0.1	1.719	-1.4	1.142	-1.3	1.197	-2.1	1.193	0.5	1.317	-5.6	1.104	-2.1
Broken Hill	1.159	-0.1	1.121	0.2	1.161	-1.0	1.127	-1.1	1.153	-1.0	1.150	0.8	1.218	-3.4	1.097	-1.3
Armidale	1.201	-2.4	1.152	-0.1	1.148	-1.0	1.123	-1.8	1.169	-2.0	1.171	0.2	1.286	-5.4	1.074	-2.3
Perth	1.237	0.4	1.185	-3.0	1.316	0.5	1.259	0.4	1.254	0.1	1.238	2.1	1.278	-1.5	1.230	0.3
Hobart	1.203	-4.1	1.170	-1.5	1.209	-3.5	1.154	-1.8	1.223	-3.6	1.209	-0.8	1.344	-7.1	1.102	-2.5
Charters Towers	1.195	-2.4	1.169	-0.8	1.174	-1.7	1.161	-2.7	1.170	-2.5	1.182	-0.7	1.224	-4.8	1.101	-2.3
Darwin	1.204	0.9	1.145	-1.7	1.176	-1.0	1.164	-1.3	1.155	-1.7	1.155	-0.3	1.219	0.2	1.153	-0.2
Alice Springs	1.167	-0.3	1.135	-0.9	1.180	-1.1	1.159	-1.3	1.162	-1.3	1.159	0.2	1.212	-1.6	1.134	-1.0

TABLE 6.12

Corrected Values for Amplitude Factors and Phase Lags for M_2 Using Several Oceanic Models - Longman-Farrell Method without Mass Conservation

Site	Observed		Hendershott Model 1		Hendershott Model 2		Zahel		Bogdanov		Tiron		Pekeris & Accad 2^0 non-diss.		Pekeris & Accad 1^0 diss.	
	Amp. Factor	Phase Lag(^{0})	Amp. Factor	Phase Lag(^{0})	Amp. Factor	Phase Lag(^{0})	Amp. Factor	Phase Lag(^{0})	Amp. Factor	Phase Lag(^{0})	Amp. Factor	Phase Lag(^{0})	Amp. Factor	Phase Lag(^{0})	Amp. Factor	Phase Lag(^{0})
Port Moresby	1.226	-0.3	1.226	1.5	1.203	1.9	1.217	-0.8	1.216	-0.2	1.238	1.0	1.222	-2.7	1.158	0.5
Canberra	1.210	-2.2	1.184	0.1	1.157	0.0	1.141	-1.3	1.191	-1.6	1.210	0.5	1.315	-5.4	1.103	-1.9
Broken Hill	1.159	-0.1	1.136	0.6	1.135	0.0	1.126	-1.1	1.165	0.0	1.164	1.1	1.215	-3.2	1.095	-1.1
Armidale	1.201	-2.4	1.170	0.0	1.131	0.4	1.121	-1.7	1.189	-1.3	1.186	0.1	1.285	-5.2	1.073	-2.1
Perth	1.237	0.4	1.187	-2.1	1.282	0.2	1.258	0.3	1.246	1.1	1.245	2.8	1.273	-1.5	1.227	0.3
Hobart	1.203	-4.1	1.193	-1.1	1.176	-1.8	1.151	-1.8	1.246	-2.3	1.231	-0.7	1.340	-6.8	1.101	-2.3
Charters Towers	1.195	-2.4	1.183	-0.5	1.156	-0.8	1.160	-2.7	1.183	-1.8	1.194	-0.6	1.222	-4.7	1.100	-2.1
Darwin	1.204	0.9	1.153	-1.1	1.155	-0.7	1.163	-1.3	1.158	-0.9	1.163	0.0	1.216	0.3	1.151	-0.2
Alice Springs	1.167	-0.3	1.144	-0.4	1.157	-0.6	1.157	-1.3	1.167	0.4	1.168	0.5	1.209	-1.5	1.133	-0.9

TABLE 6.13

Corrected Values for Amplitude Factors and Phase Lags for M_2 Using Several Oceanic Models - Longman-Farrell Method with Mass Conservation

Site	Observed		Truncation Function Method				Longman-Farrell Method without Mass Conservation				Longman-Farrell Method with Mass Conservation			
			Bogdanov Model		Tiron Model		Bogdanov Model		Tiron Model		Bogdanov Model		Tiron Model	
	Amp. Factor	Phase Lag(°)	Amp. Factor	Phase Lag(°)	Amp. Factor	Phase Lag(°)	Amp. Factor	Phase Lag(°)	Amp. Factor	Phase Lag(°)	Amp. Factor	Phase Lag(°)	Amp. Factor	Phase Lag(°)
Port Moresby	1.064	0.0	1.058	-0.7	1.044	0.6	0.982	-1.5	0.944	6.5	0.974	-1.8	0.983	3.4
Canberra	1.194	-1.0	1.201	-1.5	1.189	-0.8	1.224	-2.9	1.167	0.4	1.221	-3.0	1.182	-0.4
Broken Hill	1.149	-0.2	1.158	-0.7	1.143	-0.1	1.182	-1.6	1.112	1.2	1.180	-1.7	1.129	0.4
Armidale	1.158	-0.9	1.163	-1.5	1.152	-0.8	1.172	-3.2	1.126	0.4	1.169	-3.3	1.142	-0.6
Perth	1.241	2.5	1.257	2.4	1.234	2.2	1.311	3.4	1.188	2.2	1.309	3.2	1.212	1.8
Hobart	1.252	-2.2	1.262	-2.7	1.246	-1.9	1.303	-3.9	1.221	-0.4	1.300	-4.0	1.237	-1.2
Charters Towers	1.164	-1.5	1.166	-2.1	1.153	-1.4	1.156	-3.3	1.094	-0.3	1.152	-3.4	1.123	-0.9
Darwin	1.273	-1.6	1.281	-2.0	1.266	-1.9	1.276	-1.9	1.201	-0.7	1.271	-2.1	1.241	-1.7
Alice Springs	1.164	0.9	1.173	0.5	1.157	0.8	1.195	0.2	1.114	2.0	1.192	0.1	1.137	1.1

TABLE 6.14

Corrected Values for Amplitude Factors and Phase Lags for O_1 Using Several Oceanic Models for Outer Zone only

The effect of mass conservation can be observed in Tables 6.12 and 6.13, where generally the condition of mass conservation does improve the results.

The results for O_1 are not conclusive, as no inner zone calculations have been included in the corrections. However, the truncation function approach does look promising.

A theoretical comparison between the two methods is discussed in Chapter 10.

The truncation function approach is used in the following Section in an attempt to model for the Earth response for the ocean loading effect on tidal gravity at any point on the Australian mainland so that it is adequate for correcting quasi-radial distance measurements to extra-terrestrial sources in Earth orbit for the effect of Earth tides to ±2 cm.

6.7 Modelling Ocean Loading Effects in Australia

The presentation in this Section was developed in BRETREGER & MATHER (1977) using preliminary data.

6.7.1 Introduction

The analysis of the principal tidal constituents presented in Chapter 4 showed that the amplitudes and phases of the major tidal waves varied as a function of position across the region investigated. These variations in the case of the M_2 and O_1 constituents are summarised in Figures 6.2 to 6.5. The M_2 and O_1 waves contribute at least 40% of the tidal gravity signal in Australia and approximately 50% of the tilt singal as recorded at Cooney Observatory, Armidale by a set of Verbaandert-Melchior pendulums.

In the case of the gravity tide, the variation of the amplitude factor δ with position was found to be as large as 15% of its expected value. The variation of the amplitude factors with time as computed for monthly data spans, was significantly smaller, being about 2-5% of the expected value at each site. The exception being the Port Moresby site where variations as large as 10% were recorded (DUCARME ET AL 1976, p 30). Tidal gravity recordings at European sites over periods longer than the 4-6 month observation period used in the Australian measurements, indicate that time variations in the amplitude factor are small enough to permit the use of values of δ deduced from the shorter recording period, as being representative of the recording site (e.g. MELCHIOR & PAQUET 1966, PARIISKII ET AL 1967).

This following investigation is based on the assumption that the tidal parameters extracted from the analysis of the 4-6 month sequence of tidal gravity recordings at each of the nine stations in Australia and Papua New Guinea could be treated as representing a field which are functions of position alone and not of time, even though the recordings were not made simultaneously in all cases. As the resulting uncertainty is estimated to be less than 5% of the total tidal spectrum, it is expected that the data available and the procedures used can provide data of use in modelling the radial tide at the ±1 cm level.

Section 6.7.2 outlines the methods of analysis used in evaluating the ocean loading effects, while Section 6.7.3 summarises the computations based on these methods.

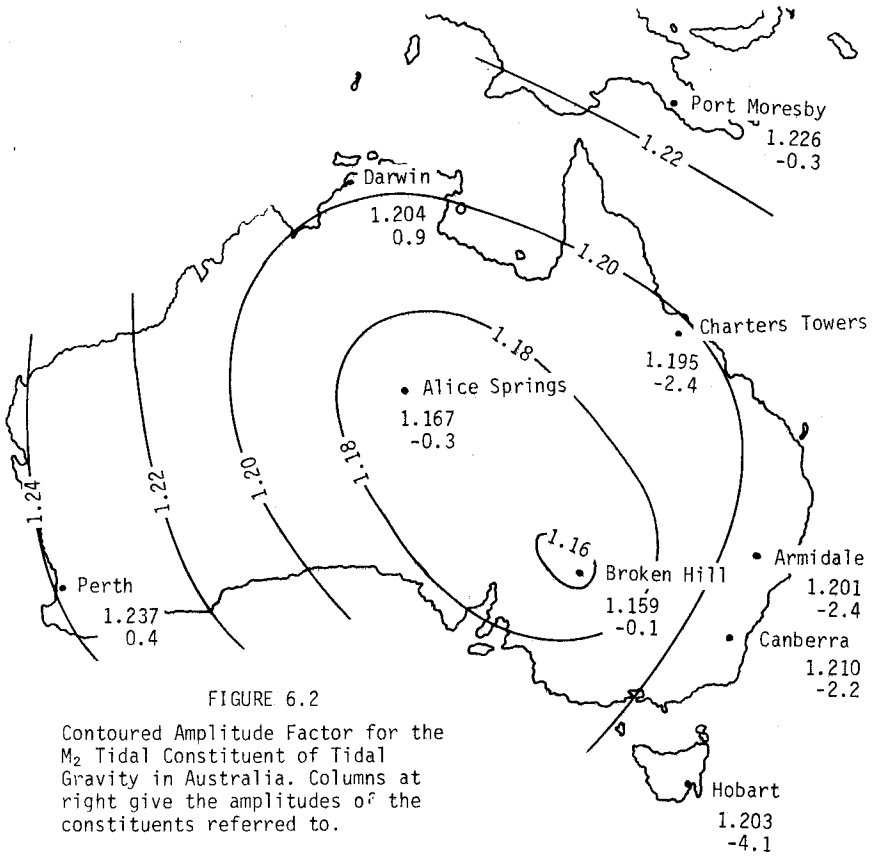

Semi-diurnal Signal µgal	M_2 Signal µgal	Total Signal µgal	% M_2 to Total Signal
170	91	202	45
151	88	200	44
155	84	210	40
139	77	205	38
125	68	220	31
121	64	195	33
127	68	207	33
97	62	196	32
86	50	184	27

FIGURE 6.2

Contoured Amplitude Factor for the M_2 Tidal Constituent of Tidal Gravity in Australia. Columns at right give the amplitudes of the constituents referred to.

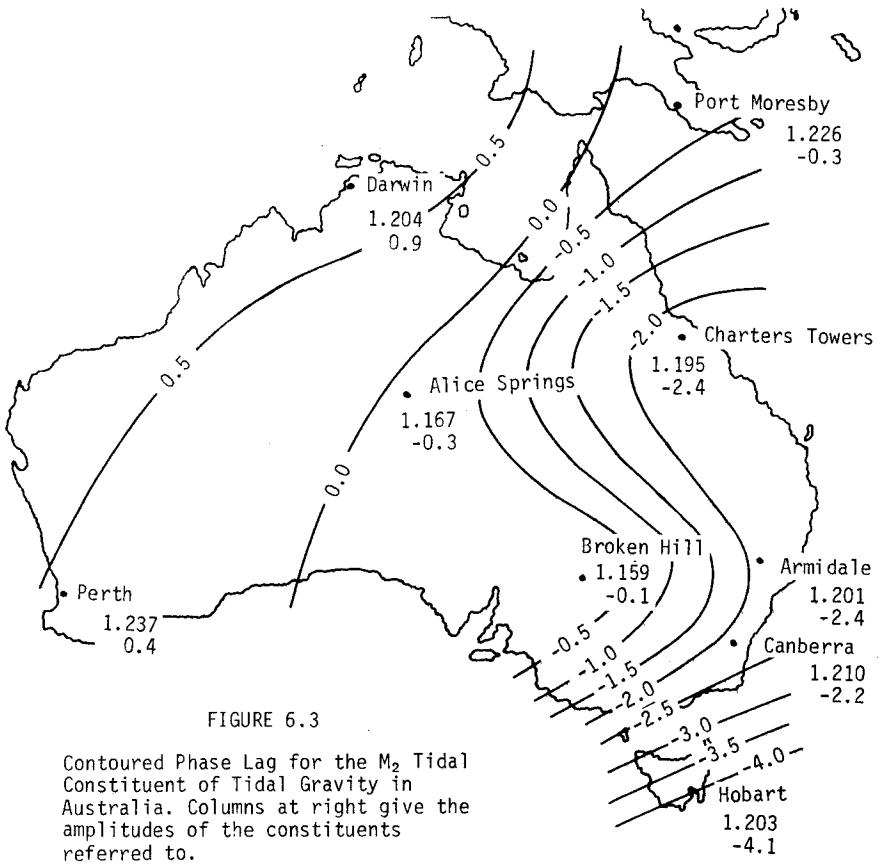

Semi-diurnal Signal µgal	M_2 Signal µgal	Total Signal µgal	% M_2 to Total Signal
170	91	202	45
151	88	200	44
155	84	210	40
139	77	205	38
125	68	220	31
121	64	195	33
127	68	207	33
97	62	196	32
86	50	184	27

FIGURE 6.3

Contoured Phase Lag for the M_2 Tidal Constituent of Tidal Gravity in Australia. Columns at right give the amplitudes of the constituents referred to.

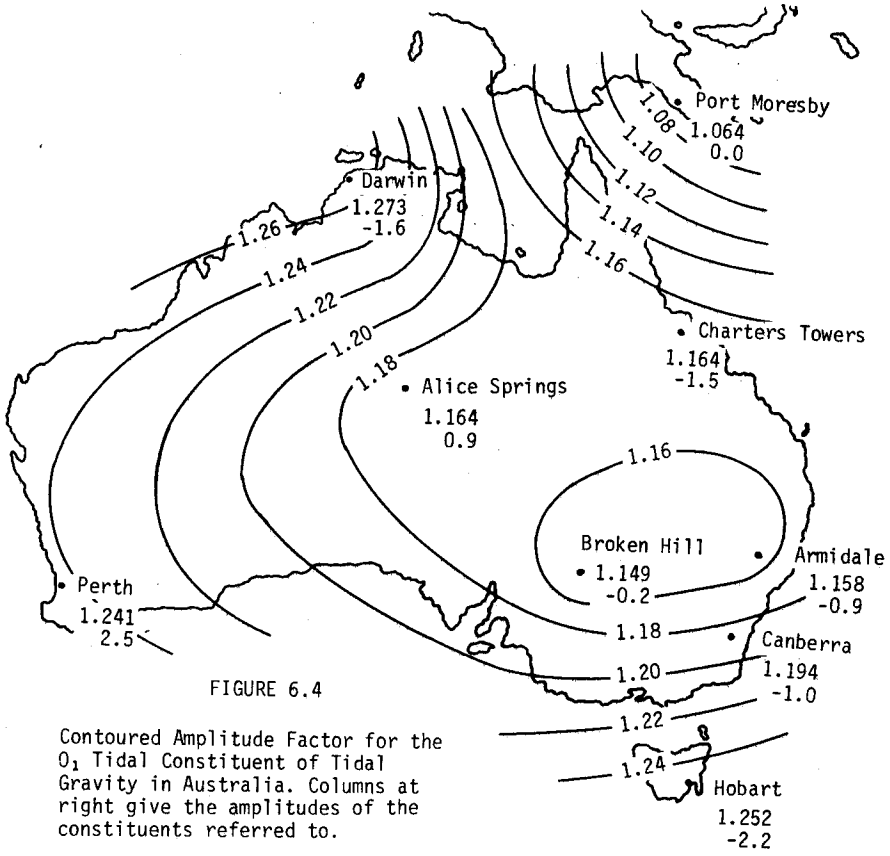

FIGURE 6.4

Contoured Amplitude Factor for the O_1 Tidal Constituent of Tidal Gravity in Australia. Columns at right give the amplitudes of the constituents referred to.

Diurnal Signal µgal	O_1 Signal µgal	Total Signal µgal	% O_1 to Total Signal
32	10	202	5
49	15	200	8
55	21	210	10
66	23	205	11
95	28	220	13
74	28	195	14
80	31	207	15
99	33	196	17
98	34	184	18

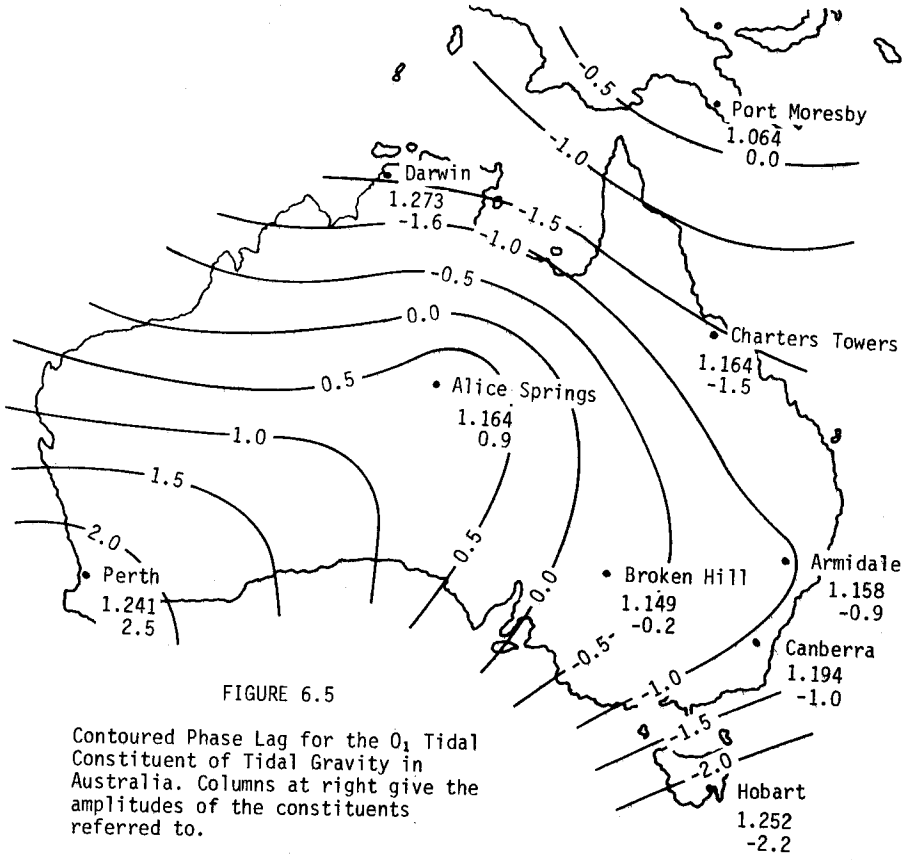

FIGURE 6.5

Contoured Phase Lag for the O_1 Tidal Constituent of Tidal Gravity in Australia. Columns at right give the amplitudes of the constituents referred to.

Diurnal Signal µgal	O_1 Signal µgal	Total Signal µgal	% O_1 to Total Signal
32	10	202	5
49	15	200	8
55	21	210	10
66	23	205	11
95	28	220	13
74	28	195	14
80	31	207	15
99	33	196	17
98	34	184	18

6.7.2 Method of Analysis

The gravity tide δg at any point can be represented by the relation

$$\delta g = -\frac{2}{R}\,\delta \sum_i W_{2i}\,(\theta_{bi}) + \delta g_l \qquad (6.6)$$

where W_{2i} is the i-th constituent of the tide producing potential, θ_{bi} the hour angle of the tide producing body for the i-th tidal wave, and δg_l is the effect of ocean loading on tidal gravity.

The method of analysis used by DUCARME ET AL (1976) can be interpreted as producing observation equations of the form

$$\delta g = -\frac{2}{R} \sum_i \delta_i\, W_{2i}\,(\theta_{bi} + \alpha_i) \qquad (6.7)$$

where δ_i is the amplitude factor obtained for the i-th wave and α_i is the related phase lag. On comparing equations 6.6 and 6.7,

$$\delta g_l = \sum_i \delta g_{li} = -\frac{2}{R}\{\sum_i (\delta_i - \delta)\, W_{2i}\,(\theta_{bi}) + \delta_i[\, W_{2i}(\theta_{bi} + \alpha_i) - W_{2i}(\theta_{bi})]\} \qquad (6.8)$$

The ocean loading effect on tidal gravity can also be defined as follows (see Section 2.4.2) in the case of the i-th constituent of the ocean tide

$$\delta g_{li} = -\left(\frac{\partial V}{\partial R}\, i + \frac{\partial V''}{\partial R}\, i\right) - 2g\,\frac{\delta dr}{R} \qquad (6.9)$$

where V_i is the load potential generated by the i-th wave and V_i'' is the resulting deformation potential, δdr being the deformation in the radial displacement due to the load and gravity. Expressions for V_i and $\partial V_i/\partial R$ can be found in Sections 2.3.3 and 5.2.2.1, involving spherical harmonics.

On adopting a truncation function representation, (see Section 5.2.2.1),

$$\frac{\partial V}{\partial R}\, i\,(\theta_{bi}) = -\tfrac{1}{4}\, G\,\rho_w \int_0^{\psi_0}\int_0^{2\pi} \zeta_i(\theta_{bi})\ \mathrm{cosec}\ \tfrac{1}{2}\psi\ d\sigma$$

$$-\tfrac{1}{2}\, G\,\rho_w\,\pi \sum_{n=1}^{\infty} X_n\ \zeta_{ni}\,(\theta_{bi}) \qquad (6.10)$$

An alternative means of modelling the ocean tide loading effect on tidal gravity is possible by using the set of load deformation coefficients h_n', k_n' of degree n using a representation of the form

$$2g\,\frac{\delta dr}{R} + \frac{\partial V''}{\partial R}\, i = \sum_{n=1}^{\infty} \left(h_n' - \frac{n+1}{2}\, k_n'\right) \frac{2V_n}{R}\, i \qquad (6.11)$$

where V_{ni} is the n-th degree surface harmonic in the global representation of V_i. This type of approach which has been widely used, requires the incorporation of a large number of such load deformation coefficients for the successful modelling of ocean tide loading as the model characteristics are based on global rather than regional considerations. Convolution procedures can be used to obtain values of h_n', k_n' consistent with the average physical characteristics of the Earth (e.g. LONGMAN 1966).

This investigation examines the intuitive appreciation that the complexity of the ocean tide loading is due to that in the global tide rather than in the Earth's response to the tidal loading. Furthermore, assuming that reliable models of the ocean tide have been obtained from satellite altimetry, it would appear that it would be more reliable to use equation 6.10 rather than equation 6.11 in the representation of $\partial V_i/\partial R$ as the reliability of harmonic models of V_i can be expected to diminish with increase of n. In the case of a simple Earth response to a complex load, the deformation $\delta\zeta_i(\theta_{bi})$ produced by the tide $\zeta_i(\theta_{bi})$ could be represented by an equation of the form

$$\delta\zeta_i\ (\theta_{bi}) \;=\; c\ (\phi,\lambda)\ \zeta_i\ (\theta_{bi}) \tag{6.12}$$

where $c(\phi,\lambda)$ is a slowly varying function of position on the Earth's surface. $c(\phi,\lambda)$ can be represented in regional studies like the present investigations for Australia, by a two dimensional representation of the form

$$c(\phi,\lambda) \;=\; \sum_j c_j\ F_j\ (\phi,\lambda) \tag{6.13}$$

where c_j are a set of constants independent of both position and time within the region and $F_j(\phi,\lambda)$ is a regional surface harmonic function. In the present study, $F_j(\phi,\lambda)$ were functions of the Fourier type given by

$$F_j(\phi,\lambda) \;=\; \cos\ (m\ \Delta\phi + n\ \Delta\lambda) \tag{6.14}$$

where n, m are parameters controlling the wavelength of the harmonic function and $\Delta\phi$, $\Delta\lambda$ are differences in latitude and longitude with respect to a convenient point of reference. On adopting this model, it follows that

$$\frac{\partial V}{\partial R}\,i \;+\; \frac{\partial V''}{\partial R}\,i \;=\; \frac{\partial V}{\partial R}\,i\ [1 + c(\phi,\lambda)] \tag{6.15}$$

From equations 6.9 and 6.15, δg_{1i} is defined by

$$\delta g_{1i} \;=\; -\frac{\partial V}{\partial R}\,i\ [1 + c(\phi,\lambda)] \;-\; 2g\,\frac{\delta dr}{R} \tag{6.16}$$

δdr being the deformation of the radial Earth tide dr, given by

$$dr \;=\; h_2 \sum_i \frac{W_2}{g}\,i \tag{6.17}$$

due to ocean tides.

While the effect $\delta\xi_{1\alpha}$ of ocean loading on measurements of tilt $\delta\xi_\alpha$ in the direction X_α is given by (see Section 2.4.3)

$$\delta\xi_{1\alpha} \;=\; \delta\xi_\alpha \;+\; \frac{\gamma}{g} \sum_i \frac{\partial W_2}{\partial X_\alpha}\,i\ (\theta_{bi}) \tag{6.18}$$

where W_{2i} has the same significance as in equation 6.6, and γ is defined as $1 + k_2 - h_2$.

If conventional analysis has been carried out on tiltmeter data on lines similar to those described in equations 6.7 and 6.8, it follows that

$$\delta\xi_{1\alpha} \;=\; -\frac{1}{g} \sum_i \left\{ \frac{\partial W_2}{\partial X_\alpha}\,i\ (\theta_{bi})[\,\gamma_i - \gamma] + \gamma_i \left[\frac{\partial W_2}{\partial X_\alpha}\,i\ (\theta_{bi} + \alpha_i) - \frac{\partial W_2}{\partial X_\alpha}\,i\ (\theta_{bi}) \right] \right\} \tag{6.19}$$

where γ is the value adopted for the Earth model by averaging all estimates available.

$\delta\xi_{1\alpha}$ can therefore be written as

$$\delta\xi_{1\alpha} \;=\; \frac{\partial \delta dr}{\partial X_\alpha} \;-\; \frac{1}{g} \sum_i \frac{\partial V}{\partial X_\alpha}\,i\ (1 + c(\phi,\lambda)) \tag{6.20}$$

with $\partial V_i/\partial X_\alpha$ being defined by equation 5.23.

The set of parameters c_j defining the model for $c(\phi,\lambda)$ in equation 6.13 are equally applicable to both equations 6.16 and 6.20. A combination of these two equations provides a basis for the determination of both the set of coefficients c_j in equation 6.13 and δdr in equation 6.16 and

its horizontal derivatives in equation 6.20. For simplicity, it is preferable to adopt a model of the form

$$g\ \delta dr\ (\theta_{bi}) = c_r\ (\phi,\lambda)\ \sum_i W_{2i}\ (\theta_{bi}) \qquad (6.21)$$

where $c_r(\phi,\lambda)$ is defined by an equation similar to equation 6.13. δdr can also be expressed in terms of the ocean tide model ζ (see Section 5.2.2.4). Equation 6.21 is easier to use in practice as the radial deformation is expressed as a function of the ephemerides of the Sun and Moon, rather than in terms of the ocean tide model. However, the use of different ocean tide models can be expected to give different values for the set of coefficients c_j as illustrated in Table 6.17.

The final equations which can be used in the data analysis take the form

$$\delta g_l = - \sum_i \{ [1 + c(\phi,\lambda)] \frac{\partial V}{\partial R} i + \frac{2}{R} c_r\ (\phi,\lambda)\ W_{2i} \} \qquad (6.22)$$

and

$$\delta \xi_{l\alpha} = - \frac{1}{g} \sum_i \{ [1 + c(\phi,\lambda)\ ] \frac{\partial V}{\partial X_\alpha} i - c_r\ (\phi,\lambda) \frac{\partial W_2}{\partial X_\alpha} i \} \qquad (6.23)$$

at any given instant of time.

The recovery of solutions in practice using the principles outlined is described in Section 6.7.3

6.7.3 Analysis of Australian Results

Preliminary computations using the type of approach described in Section 6.7.2 were carried out at the nine sites in Australia and Papua New Guinea for the loading effect of the M_2 tide on gravity using only the zero degree term in the representation of c (Section 6.3). The ocean tide models used in the calculations were those of *Zahel* (KUZNETZOV 1972) and *Hendershott* (HENDERSHOTT 1972). The basic data was in the form of cotidal-corange charts prepared from numerical solutions of Laplace's Tidal Equations. Neither the solid Earth deformation nor self attraction were considered in the preparation of the *Zahel* model, but allowance was made for bottom stress in shallow water with the imposition of the boundary condition of an impermable coastline. The *Hendershott* model made allowance for both solid Earth deformation and coastal dissipation.

The quantity $\partial V/\partial R$ for the M_2 tide in this study was approximated by the outer zone representation at equation 6.10. In addition, the loading effect on tidal gravity, as represented by the relation

$$\delta g_l = - c' \frac{\partial V}{\partial R} \qquad (6.24)$$

where

$$c' = 1 + c_o + 2g \left(\frac{\delta dr}{R}\right) / (\partial V/\partial R) \qquad (6.25)$$

in terms of equation 6.13, c_o being independent of position, in lieu of the formulation based on the load deformation coefficients implied by equation 6.11

$$\delta g_l = - \sum_{n=1}^{\infty} \left[\frac{n}{2} + h'_n - \frac{n+1}{2} k'_n \right] \frac{2V}{R} \text{ in} \qquad (6.26)$$

for $n \leq 20$, produced agreement in the computed values of δg_l to better than ±0.35 μgal. This disagreement between values of δg_l computed from equations 6.24 and 6.26 improved to better than ±0.15 μgal if the station Perth on the western seaboard of Australia were excluded in the case of computations with all models of the M_2 tide.

While the values of c' for each model were in significant disagreement, the variation in values of c' with position as computed at each of the eight sites in Figure 6.2 excluding Perth, were less than 8% (±0.13 μgal) for the *Hendershott* models and less than 21% (±0.12 μgal) for the *Zahel* model. Discrepancies obtained in the values of c' as computed from equation 6.24 using equation 6.26, as a function of position for the same model, arise due to the use of truncated spherical surface harmonic series in both equations 6.24 and 6.26. In the former case, the inner zone region ($\psi_0 < 5^o$) was excluded from computations. Evaluations using equation 6.26 excluded the effect of all harmonics greater than degree 20.

The principles underlying the procedure used in the present study are as follows. On suppressing the subscript i, $\delta g_{1j}\ (\theta_b)$ as computed at the station P_j (coordinates ϕ_j, λ_j) using ocean loading $(\partial V/\partial R)_j$ at P_j at the same instance using the second term in equation 6.10, being given by

$$\left[\frac{\partial V}{\partial R}\ (\theta_b) \right]_j = \sum_i \left[\frac{\partial V}{\partial R}\ i\ (\theta_b) \right]_j \tag{6.27}$$

using observation equations of the form

$$\begin{aligned} v_{gj}\ (\theta_b) = &- \{ \sum_1 c_1\ F_{1j}\ \sum_i \left[\frac{\partial V}{\partial R}\ i\ (\theta_b) \right]_j \\ &+ \sum_{1'} \frac{2}{R}\ c_{r1'}\ F_{1'j}\ \sum_i [W_{2i}\ (\theta_b)]_j \} - \sum_i \left[\frac{\partial V}{\partial R}\ i\ (\theta_b) \right]_j \\ &- \delta g_{1j}\ (\theta_b) \end{aligned} \tag{6.28}$$

at time θ_b, $v_{gj}\ (\theta_b)$ being the residual. The equivalent equation for tilt measurement is

$$\begin{aligned} v_{1\alpha j} = &- \frac{1}{g} \{ \sum_1 c_1\ F_{1j}\ \sum_i \left[\frac{\partial V}{\partial X_\alpha} i\ (\theta_b) \right]_j - \sum_{1'} c_{r1'}\ F_{1'j}\ \sum_i \left[\frac{\partial W_2}{\partial X_\alpha} i (\theta_b) \right]_j \} \\ &- \frac{1}{g}\ \sum_i \left[\frac{\partial V}{\partial X_\alpha} i\ (\theta_b) \right]_j - \delta \xi_{1\alpha j}\ (\theta_b) \end{aligned} \tag{6.29}$$

on using equations 6.22 and 6.23.

The model used for F_{1j} in the present study is of the form

$$F_{1j} = \cos(a_{\phi j}\ \pi 1) \quad \text{or} \quad \sin\ (a_{\lambda j}\ \pi 1) \tag{6.30}$$

where

$$a_{\phi j} = (\phi_j - \phi_o) / (\phi_m - \phi_o)$$

and

$$a_{\lambda j} = (\lambda_j - \lambda_o) / (\lambda_m - \lambda_o) \tag{6.31}$$

(ϕ_o, λ_o) being the south-west corner of the region and (ϕ_m, λ_m) its north-east corner.

As tiltmeter observations of proven quality were only available at the Cooney Observatory site at Armidale (BARLOW ET AL 1974), sufficient data were not available to separate the effects to be modelled by the parameters c_1 on the one hand and c'_r on the other. The tidal gravity observations summarised in Figures 6.2 to 6.5 were available for the generation of observation equations from equation 6.28. This equation could be written in the form

$$v_{gj} = - \sum_1 c_{c1}\ F_{1j}\ \sum_i \left[\frac{\partial V}{\partial R}\ i\ (\theta_b) \right]_j - \sum_i \left[\frac{\partial V}{\partial R}\ i\ (\theta_b) \right]_j - \delta g_{1j}\ (\theta_b) \tag{6.32}$$

where the parameters c_{c1} represent the combined effects of the first two terms on the right of equation 6.28.

The observational data used in equation 6.32 was that presented in Chapter 4, the results being summarised for the M_2 and O_1 tidal constituents in Figures 6.2 to 6.5. The contours are based solely on the data points shown in the figures. For more information on the uncertainties quoted, see (DUCARME ET AL 1976). The variation of the computed amplitude factors δ_j at P_j from the model value ($\delta = 1.163$) and the phase lag α_j from zero is influenced by ocean loading. The vector difference between the observed values and the model can be represented by an amplitude and a local phase lag (observed phase minus model phase) and is called the tidal gravity residual. Values of this residual are listed in Table 6.15 for the M_2 constituent of the ocean tide at the nine sites in Figure 6.2. A graphical representation is given in Figures 4.4.

TABLE 6.15
Amplitude and Local Phase Lag of the Observed Tidal Gravity Residual for the M_2 Tidal Constituent

Site	Amplitude (μgal)	Local Phase Lag (^{o})
Port Moresby	4.48	-6.1
Canberra	3.34	-45.2
Broken Hill	0.25	-153.2
Armidale	3.55	-53.7
Perth	4.11	6.7
Hobart	3.87	-66.8
Charters Towers	4.00	-58.3
Darwin	3.30	24.8
Alice Springs	0.47	-56.9

Investigations were restricted to the M_2 tide as this is the best modelled of the tidal constituents and its loading effect on tidal gravity is well defined over the short observing periods at each station (between 4 and 6 months). Thus $i=1$ in equation 6.32. The gravitational effect of the M_2 tide (the term $\partial V_1(\theta) / \partial R$ in the equation) was computed using equation 6.10 as a combination of an inner zone and an outer zone contribution, the limiting angular distance ψ_0 in this series of calculations being 5^o.

The global ocean tide coverage used for computing the outer zone effect was in the form of a surface spherical harmonic representation to (20, 20) as outlined in Section 6.2. The harmonic models used were *Hendershott's* model 1 (1970), *Hendershott's* model 2 (1972) and *Zahel's* model.

The initial set of calculations shown in Table 6.16 represent only the outer zone effects ($\psi > 5^o$). As there were only nine tidal gravity sites at which data were available, it was decided to attempt a solution for 9 parameters c_{cl} in the first instance using 24 observation equations at each station. The resulting solutions for the three M_2 tidal models referred to above are shown in Table 6.17, the values of the coefficients c_{cl} being listed for each Fourier function as specified, a_ϕ and a_λ being defined by equation 6.31. The resulting model of the tidal loading effect of gravity is valid only within the region

$$\phi_0 < \phi < \phi_m \quad ; \quad \lambda_0 < \lambda < \lambda_m$$

with $\phi_0 = -45^o$, $\lambda_0 = 115^o$, $\phi_m = -5^o$ and $\lambda_m = 155^o$ for the present study.

TABLE 6.16

Amplitude and Phase of the Ocean Attraction Effect (Outer Zone only) on Tidal Gravity at Australian Sites due to Three Models of the M_2 Tide

Site	Hendershott Model 1		Hendershott Model 2		Zahel Model	
	Amplitude (μgal)	Local Phase Lag (^{o})	Amplitude (μgal)	Local Phase Lag (^{o})	Amplitude (μgal)	Local Phase Lag (^{o})
Port Moresby	0.98	-30.1	2.12	-26.1	1.24	61.8
Canberra	0.99	-46.8	1.79	-30.2	1.01	8.0
Broken Hill	0.98	-24.5	1.33	-11.2	0.80	42.6
Armidale	1.06	-47.8	2.27	-33.4	1.39	10.3
Perth	2.13	45.1	0.72	130.0	0.41	152.9
Hobart	0.83	-53.6	1.28	-29.5	0.62	-12.1
Charters Towers	0.98	-31.1	2.01	-21.0	1.21	41.6
Darwin	1.04	12.4	1.11	9.5	0.59	80.7
Alice Springs	0.99	4.5	1.06	10.1	0.65	76.9

TABLE 6.17

The Coefficients c_{cl} Modelling the Earth Response in the Australian Region for Three Models of the M_2 Tide (Outer Zone Effects Only)

The Argument F	Hendershott Model 1	Hendershott Model 2	Zahel Model
1	-4.31	-5.01	-4.32
$\sin(a_\phi \pi)$	5.58	12.28	15.55
$\cos(a_\phi \pi)$	1.62	2.10	3.34
$\sin(a_\lambda \pi)$	3.91	-4.87	-10.94
$\cos(a_\lambda \pi)$	-1.36	-3.23	-6.82
$\sin(2a_\phi \pi)$	-2.38	-2.53	-2.83
$\cos(2a_\phi \pi)$	3.03	5.89	8.56
$\sin(2a_\lambda \pi)$	1.41	1.54	3.24
$\cos(2a_\lambda \pi)$	3.47	-2.32	-6.55

The values obtained for the coefficients c_{cl} vary with the tidal model used. The maximum residual in μgal between the observed quantity δg_{lj} and that generated from the deformation model described in equation 6.32 is shown for each tidal model at all nine sites in Table 6.18. The best agreement was obtained between the *Hendershott* model 1 and the observations with three sites (Port Moresby, Perth and Charters Towers) having residuals in excess of ±1 μgal. No special significance is attached to the other residuals in view of the statistical estimates associated with the determination of parameters from the Australian tidal gravity profiles (DUCARME ET AL 1976, pp 35-47). These figures assume that only the M_2 tide contributed to the residuals δg_{lj} in equation 6.32. The residuals provide a measure of the contribution of the other constituents of the ocean tide to loading effects on tidal gravity along with the effects of local perturbations and/or instrumental uncertainties.

TABLE 6.18
Maximum Residuals at Each Tidal Gravity Site on Fitting Models at Table 6.17 against Observational Data

Site	Hendershott Model 1 Maximum Residual (± μgal)	Hendershott Model 2 Maximum Residual (± μgal)	Zahel Model Maximum Residual (± μgal)
Port Moresby	1.8	1.5	4.1
Canberra	0.1	0.9	2.7
Broken Hill	0.2	0.1	0.1
Armidale	0.4	1.2	3.2
Perth	2.5	3.4	2.3
Hobart	0.9	2.3	3.2
Charters Towers	1.8	2.4	3.9
Darwin	0.7	0.9	2.7
Alice Springs	0.4	0.4	0.3

Neither the exclusion of stations which exhibited large residuals nor an increase in the number of parameters modelling the deformation produced by the load, improved the residual of fit. Variations in the limits of the test area were also found to influence the coefficients c_{cl} but not the residual of fit. The values obtained for the parameters c_{cl} are also a function of the data acquisition period as the signal-to-noise ratio in the case of the ocean loading effect on tidal gravity is not markedly different from unity. However, the residuals of fit in all instances are only marginally changed from the values given in Table 6.18.

A second series of computations was performed in which the effect of the inner cap $(\psi < 5^{\circ})$ was also included. This effect was computed using the first term on the right in equation 6.10 using regional M_2 tidal models (EASTON 1970). The results for the nine tidal gravimeter sites are listed in Table 6.10.

The combined inner and outer zone effects for the three M_2 tidal models tested are given in Table 6.19 while the maximum residuals obtained at each site for the combined effects is given in Table 6.20. These tables are equivalent to Tables 6.17 and 6.18 respectively which list results for the model of the ocean load based on outer zone effects alone. It cannot be claimed that the results presented in Table 6.20 are an improvement on those in Table 6.18.

TABLE 6.19
The Coefficients c_{cl} Modelling the Earth Response in the Australian Region for Three Models of the M_2 Tide (including Inner Zone Effects)

The Argument F	Representation of Outer Zone From		
	Hendershott Model 1	Hendershott Model 2	Zahel Model
1	-5.97	-6.20	-5.78
$\sin(a_\phi \pi)$	4.19	5.56	9.86
$\cos(a_\phi \pi)$	1.78	1.44	3.65
$\sin(a_\lambda \pi)$	7.07	3.66	-2.74
$\cos(a_\lambda \pi)$	-0.63	-2.85	-6.71
$\sin(2a_\phi \pi)$	-2.33	-1.74	-2.76
$\cos(2a_\phi \pi)$	1.79	2.78	5.87
$\sin(2a_\lambda \pi)$	0.91	1.74	3.56
$\cos(2a_\lambda \pi)$	4.75	1.38	-2.79

TABLE 6.20
Maximum Residuals at Each Tidal Gravity Site on Fitting Models at Table 6.19 Against Observational Data

Site	Representation of Outer Zone From Hendershott Model 1 (± μgal)	Hendershott Model 2 (± μgal)	Zahel Model (± μgal)
Port Moresby	3.4	2.3	4.4
Canberra	0.4	0.6	2.2
Broken Hill	0.2	0.1	0.1
Armidale	0.1	1.0	2.9
Perth	2.5	3.3	2.0
Hobart	0.3	1.8	2.2
Charters Towers	0.6	1.8	4.0
Darwin	0.0	0.1	1.9
Alice Springs	0.4	0.4	0.3

The quality of prediction was investigated in the next series of tests. Each of the nine stations were excluded in turn as a source of observational data when forming the observation equations using the relation at equation 6.32 with $(\partial V_1(\theta_b) / \partial R)$ being represented by outer zone effects only. The results are given in Table 6.21. It was observed that the residuals of fit were distorted by the differential variation in phase between the term $(\partial V_1(\theta_b) / \partial R)$ for the M_2 tide across Australia and that in the observed ocean loading of the gravity tide $\delta g_1 (\theta_b)$ (Table 6.15) in equation 6.32. If the precision desired in the modelling is ±1 μgal, it follows that discrepancies in phase of $\pm 20^{\circ}$ are not significant. It can therefore be stated that the goal in the modelling process is the representation of at least 80% of the tidal gravity residual δg_1.

TABLE 6.21
Prediction of the Amplitude of the Tidal Gravity Residual Using a Nine Parameter Model at Each Australian Site from Data at the Eight Other Sites Based on Equation 6.32 and the Hendershott Model 1 for the M_2 Tide.

Site	Predicted Value (μgal)	Observed Value (μgal)
Port Moresby	4.36	4.48
Canberra	2.37	3.34
Broken Hill	0.55	0.25
Armidale	2.51	3.55
Perth	-548.	4.11
Hobart	7.02	3.87
Charters Towers	3.10	4.00
Darwin	2.98	3.30
Alice Springs	0.35	0.47

It was therefore decided to model the amplitude and the phase of the tidal gravity residual separately on the basis of equation 6.8, using the following modified forms of equation 6.32

$$v_{g\delta j} = -\sum_l c_{c\delta l} F_{lj} \sum_i \{\frac{\partial V}{\partial R} i (\theta_b)\}_j - \sum_i \{\frac{\partial V}{\partial R} i (\theta_b)\}_j - \delta g_{\delta lj}(\theta_b) \quad (6.33)$$

where

$$\delta g_{\delta lj}(\theta_b) = -\frac{2}{R} \sum_i (\delta_i - \delta) \{ W_{2i} (\theta_b) \}_j \quad (6.34)$$

for amplitude, and

$$v_{g\alpha j} = -\sum_l c_{c\alpha l} F_{lj} \sum_i \{ \frac{\partial V}{\partial R} i(\theta_b) \}_j - \sum_i \{ \frac{\partial V}{\partial R} i (\theta_b) \}_j - \delta g_{\alpha lj}(\theta_b) \quad (6.35)$$

where

$$\delta g_{\alpha lj}(\theta_b) = -\frac{2}{R} \sum_i \delta_i \{ W_{2i} (\theta_b + \alpha_i) - W_{2i} (\theta_b) \} \quad (6.36)$$

for phase.

On repeating the solutions summarised in Table 6.21 using this modified form of analysis using five parameters in each of the sets of coefficients $c_{c\delta l}$ and $c_{c\alpha l}$, the residuals obtained were those set out in Table 6.22. These results indicate that a loss in resolution occurs when the predictions are the results of extrapolation over distances in excess of 10^3 km. The loss in resolution is particularly evident when predicting the Perth values, where the variations are considerable in both Tables 6,21 and 6.22.

TABLE 6.22

Prediction of the Amplitude and Phase Lag of the Tidal Gravity Residual at Each Australian Site from Data at the Eight Other Sites using a Ten Parameter Model Based on Equations 6.33 & 6.35 and the M_2 Tide based on the Hendershott Model 1 (including Inner Zone Effects)

Site	Predicted Values		Observed Values	
	Amplitude (μgal)	Phase Lag (^{o})	Amplitude (μgal)	Phase Lag (^{o})
Port Moresby	5.20	159.7	4.48	-6.1
Canberra	3.20	-86.8	3.34	-45.2
Broken Hill	1.24	-38.0	0.25	-153.2
Armidale	4.87	-13.3	3.55	-53.7
Perth	0.04	-118.5	4.11	6.7
Hobart	2.09	-99.5	3.87	-66.8
Charters Towers	2.32	-103.2	4.00	-58.3
Darwin	4.06	60.2	3.30	24.8
Alice Springs	0.21	16.9	0.47	-56.9

The ten parameter model for the tidal deformation due to the M_2 tide as described in Table 6.23 should be adequate for the description of the tidal loading effect on gravity at all eastern Australian sites with a standard error of ± 2 μgal (i.e., ±1 cm in the appropriate contribution to the radial displacement).

TABLE 6.23

The Coefficients c_{cl} Modelling the Earth Response in the Australian Region using Equations 6.33 & 6.35 for Three M_2 Tide Models (including Inner Zone Effects)

The Argument F	Representation of Outer Zone From Hendershott Model 1	Hendershott Model 2	Zahel Model
Amplitude δ			
1	4.84	4.42	9.32
sin $(a_\phi \pi)$	-2.55	-1.82	-4.46
cos $(a_\phi \pi)$	-1.07	-0.24	-0.76
sin $(a_\lambda \pi)$	-3.02	-2.89	-5.52
cos $(a_\lambda \pi)$	-0.89	1.16	1.28
Phase Lag α			
1	-3.34	-2.78	1.25
sin $(a_\phi \pi)$	1.89	1.65	-4.24
cos $(a_\phi \pi)$	0.88	1.09	0.03
sin $(a_\lambda \pi)$	3.99	3.24	0.56
cos $(a_\lambda \pi)$	-0.04	-0.46	1.36

6.7.4 Conclusions on the Modelling Method

The computations described in Section 6.7.3 show that it is possible to model the deformation of the gravity tide due to the loading of ocean tides over a finite area of the globe using a set of ten regional deformation coefficients c_l with a precision adequate for representing radial corrections for Earth tides in quasi-radial range measurements. Such a representation is an attractive alternative to the use of a much larger number of load deformation coefficients h'_n, k'_n which have global rather than regional significance. However, such modelling is designed solely for regional geodetic rather than geophysical considerations.

The validity of the model for the Australian region described in Table 6.23 is subject to certain conditions being satisfied. The observations used to generate this model were not recorded simultaneously during the period 1974-1977. As the variations in the response of the Earth to the tide producing forces as a function of position are at least three times greater than those at a point over periods of up to one year, it is probable that the relevance of this model is assured for at least five years.

Tests on the model for the ocean loading described in Section 6.7.3 indicate that the effect on the gravity tide can be represented at the ±1 μgal level in eastern Australia using the *Hendershott* model 1 for the M_2 tide. The precision is somewhat inferior on the west coast which is represented by the single site at Perth. Tests based on the selective exclusion of stations indicate that the model is reliable at the stated level except when extrapolation is involved over distances greater than 10^3 km. The validity of the model over period of time in excess of five years has still to be established.

Discussion to this stage has centred only on geodetic measurements on the Earth's surface, the next three Chapters will deal with Earth and ocean tide effects on satellites. The next Chapter develops the theory of tidal perturbations in satellites.

CHAPTER 7

TIDAL PERTURBATION THEORY ON SATELLITES

7.1 Introduction

The following Chapters present theory and calculations for tidal perturbations on satellites. This Chapter develops the theory for both solid Earth and ocean tide perturbations.

The Sun and Moon deform the Earth by their tidal forces, these deformations cause temporal variations in the gravitational potential that in turn induce perturbations in the motion of close Earth satellites. Preliminary work in the formulation of these effects was developed by KAULA(1964), KOZAI(1965) and NEWTON(1965). All these developments were in terms of instantaneous Keplerian elements, while in recent studies, MUSEN & ESTES(1972) and MUSEN & FELSENTREGER(1973) introduce Brown-Hill variables, which facilitate integration over long time periods due to their linear motion.

Expressing the tidal potential in a similar manner to the tides on the Earth, the principal satellite perturbations group around the principal terms in the lunar and solar motion. The lunar semi-diurnal M_2 tide will give perturbations with a period of approximately 14 days, while the solar S_2 tide has a period of a few months. Since the satellite measures the integral effect of the tidal potential, the longer the period of the perturbation, the larger will be its amplitude. The significance of this can be observed with the M_2 and S_2 waves. On the Earth's crust the amplitude of S_2 is less than half of M_2, but at satellite altitude the S_2 perturbation is about ten times larger than that due to M_2.

Preliminary attempts at obtaining orbital estimations of the Love number k_2 were by KOZAI(1968) and NEWTON(1968). KAULA(1969) introduced latitude dependent parameters into his theory to explain the variations in the numerical estimates of k_2. Recent studies give estimates as low as 0.25 (SMITH ET AL 1973), as against terrestial observations of 0.30. LAMBECK & CAZENAVE(1973) put forward the theory of ocean tide perturbations and stated that neglecting these tidal perturbations introduced errors in the Love number determinations of up to 15% and in the phase of several degrees depending on both the ocean tide component and the satellite orbit.

Recent research in the ocean tide field has centred on obtaining ocean tide models from satellite mean element variations assuming solid Earth tide parameters (FELSENTREGER ET AL 1976, RUBINCAM 1976, and GOAD & DOUGLAS 1977). The results show good agreement with observed data. This is further discussed in Chapter 10.

The development of solid Earth tidal perturbation theory will be shown in Section 7.2, together with the ocean tide perturbation theory in Section 7.3. The formulae thus derived are used to obtain numerical estimates of the tidal perturbations on four satellites, BEC, GEOS1, GEOS2, and GEOS3.

7.2 Tidal Perturbation Theory

The solid Earth tide perturbation theory will be discussed in two developments. In the first development only the principal tidal terms of degree two will be considered, with the effects of higher degrees being negligible.

In addition, at satellite altitude, the potential decreases rapidly with increasing degree due to the term $(\frac{R}{r_s})^{2n+1}$. Such a development can be easily understood and visualised on the orbital plane.

The following Section, 7.2.2 gives a generalised development due to KAULA(1964). This includes all long period and short period terms for all orbital elements.

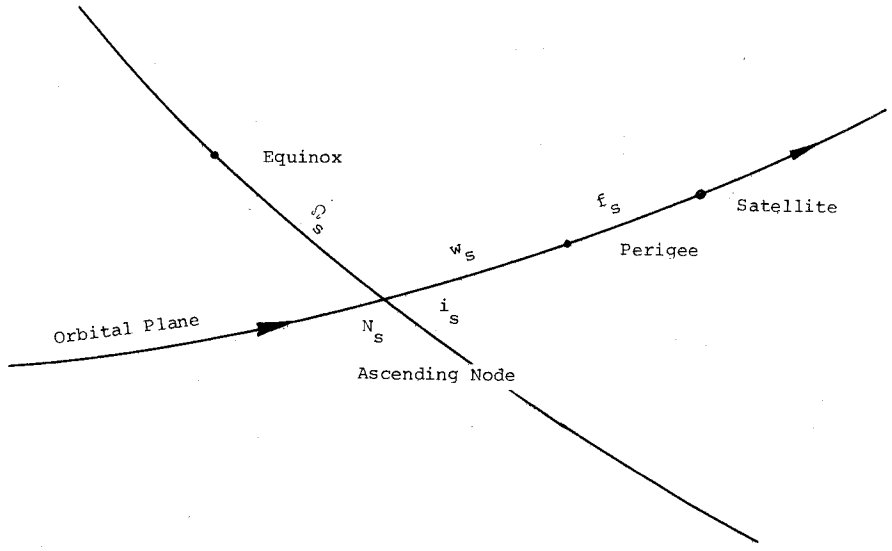

Figure 7.1
Orbital Plane of the Satellite and the Equator

7.2.1 Simplified Tidal Perturbation Theory

The development closely follows KOZAI(1965), with only the principal terms being considered.

The tidal perturbation on the Earth, due to the disturbing body (Moon or Sun), can be expressed by

$$W_b = \frac{Gm_b}{R_b^3} R^2 \left[P_2(\cos \psi_b) + \frac{R}{R_b} P_3 (\cos \psi_b) + \ldots\right] \qquad (7.1)$$

where
- G is the gravitational constant,
- m_b is the mass of the disturbing body,
- R_b is the geocentric distance to the disturbing body,
- R is the radius of the Earth,
- ψ_b is the angular distance of the radius vector of the object to the direction of the disturbing body (direction cosine), and
- $P_n(\cos \psi_b)$ are Legendre Polynomials with

$$P_2(X) = \tfrac{1}{2}(3X^2 - 1), \text{ and}$$

$$P_3(X) = \tfrac{1}{2}(5X^3 - 3X).$$

The tidal attractions of the Moon and Sun cause the Earth to be deformed by an amount

$$\frac{R^2 W_b}{G m_e}$$

where m_e is the mass of the Earth, the amplitude of the deformations being reduced by the Love number k. Also, lags are associated with these deformations, the tide is displaced by an amount $n_e \Delta t$ in the direction of the rotation of the Earth, where n_e is the rotational angular velocity of the Earth, and Δt is the time lag of the tide. The tidal friction can be included into the orbital elements by shifting the ascending node (by $n_e \Delta t$) and introducing 'fictitious' disturbing bodies, whose argument of latitude on the shifted plane is equal to that of the real disturbing body at time $t - \Delta t$. The effect of shifting the ascending node displaces the disturbing body's orbital plane. These new orbital elements are denoted by a superscript*.

Thus the tidal deformation of the Earth is

$$\frac{m_b}{m_e} \frac{R^4}{R_b^{*3}} \{ k_2 P_2(\cos \psi_b^*) + k_3 \frac{R}{R_b^*} P_3(\cos \psi_b^*) + \ldots \} \tag{7.2}$$

and the potential of the tidally deformed Earth at satellite altitude is

$$W_s^* = \frac{G m_b}{r_s} \frac{R^5}{R_b^{*3}} \{ k_2 P_2(\cos \psi_b^*) + k_3 \frac{R}{r_s R_b^*} P_3(\cos \psi_b^*) + \ldots \} \tag{7.3}$$

where r_s is the geocentric distance to the satellite, ψ_b^* the geocentric angle to the fictitious disturbing body, and k_n is a Love number of degree n, being the ratio of the tidal deformed potential to the tide rising potential.

The direction cosine, $\cos \psi_b^*$ can be expressed as

$$\begin{aligned} \cos \psi_b^* = {} & \cos(L_s - L_b^* + \theta_b^*) - 2\sin^2 \frac{i_s}{2} \sin L_s \sin(L_b^* - \theta_b^*) \\ & - 2 \sin^2 \frac{i_b}{2} \sin L_b^* \sin(L_s + \theta_b^*) \\ & + 4 \sin^2 \frac{i_s}{2} \sin^2 \frac{i_b}{2} \sin L_s \sin L_b^* \cos \theta_b^* \\ & + \sin i_s \sin i_b \sin L_s \sin L_b^* \end{aligned} \tag{7.4}$$

where
- $L_s = f_s + w_s$ = argument of latitude of satellite,
- L_b = argument of latitude of disturbing body,
- f_s = true anomaly of satellite,
- f_b = true anomaly of disturbing body,
- w_s = argument of perigee of satellite,
- w_b = argument of perigee of disturbing body,
- i_s = inclination of the satellite, to the celestial equator, and
- i_b = inclination of the disturbing body.

Also

$$\theta_b^* = \Omega_s - \Omega_b^* \tag{7.5}$$

where Ω_s is the longitude of the ascending node of the satellite orbit, measured from the equinox, and Ω_b^* is the longitude of the ascending node of the fictitious disturbing body.

The fictitious orbital elements are related to the real elements by

$$M_b^* = M_b - n_b \Delta t \tag{7.6}$$

and

$$\Omega_b^* = \Omega_b + n_e \Delta t \tag{7.7}$$

(for the Sun, $\Omega_b^* = n_e \Delta t$),

where M_s is the mean anomaly of the satellite,
M_b is the mean anomaly of the disturbing body, and
n_b is the mean motion of the disturbing body.

Since the tidal effects are minor, those of short-period are eliminated. Also, by Kepler's third law

$$n_s^2 a_s^3 = G m_e \tag{7.8}$$

where n_s is the mean motion of the satellite, and a_s is the semi-major axis of the satellite orbit.

Also,

$$n_b^2 a_b^3 = G(m_e + m_b) \tag{7.9}$$

where a_b is the semi-major axis of the disturbing body's orbit.

Hence

$$\frac{m_b}{m_e} \left(\frac{a_s}{a_b}\right)^3 = \frac{m_b}{m_e + m_b} \left(\frac{n_b}{n_s}\right)^2 \tag{7.10}$$

For the Sun,

$$n_b^2 a_b^3 = G m_b .$$

Also using the relations (KOZAI 1965, KOZAI 1973)

$$\frac{1}{2\pi} \int_0^{2\pi} \left(\frac{a_s}{r_s}\right)^3 dM = (1 - e_s^2)^{-3/2} \tag{7.11}$$

$$\frac{1}{2\pi} \int_0^{2\pi} \left(\frac{a_s}{r_s}\right)^3 \begin{Bmatrix}\cos\\ \sin\end{Bmatrix} 2f_s \, dM = 0 \tag{7.12}$$

where e_s is the eccentricity of the satellite orbit, with equations 7.8 to 7.10, the disturbing function due to a perturbing body tide is

$$F_b = \beta n_b^2 \left(\frac{a_b}{r_b^*}\right)^3 \frac{R^5}{a_s^3} k_2 (1 - e_s^2)^{-3/2} S_b \tag{7.13}$$

where

$$
\begin{aligned}
S_b = {} & \tfrac{1}{4}\left(1 - \tfrac{3}{2}\sin^2 i_s\right)\left(1 - \tfrac{3}{2}\sin^2 i_b\right) \\
& + \frac{3}{16}\sin 2i_s \sin 2i_b \cos\theta_b^* \\
& + \frac{3}{16}\sin^2 i_s \sin^2 i_b \cos 2\theta_b^* \\
& + \frac{3}{8}\sin^2 i_b \left(1 - \frac{3}{2}\sin^2 i_s\right)\cos 2\left(f_b^* + w_b\right) \\
& + \frac{3}{8}\sin^2 i_s \cos^4\frac{i_b}{2} \cos 2\left(f_b^* + w_b - \theta_b^*\right) \\
& - \frac{3}{8}\sin 2i_s \sin i_b \cos^2\frac{i_b}{2} \cos\left(2f_b^* + 2w_b - \theta_b^*\right) \\
& + \frac{3}{8}\sin^2 i_s \sin^4\frac{i_b}{2} \cos 2\left(f_b^* + w_b + \theta_b^*\right) \\
& + \frac{3}{8}\sin 2i_s \sin i_b \sin^2\frac{i_b}{2} \cos\left(2f_b^* + 2w_b + \theta_b^*\right)
\end{aligned}
\tag{7.14}
$$

where

$$\beta = \frac{m_b}{m_e + m_b} \tag{7.15}$$

and $\beta = 1$ for the Sun.

For small eccentricities of the Moon and Sun

$$\lambda_b^* = f_b^* + w_b = M_b^* + w_b = \lambda_b - n_b \Delta t \tag{7.16}$$

and

$$\frac{a_b}{r_b^*} = 1 \tag{7.17}$$

In equation 7.16, $n_b \ll n_e$ and therefore can be neglected $(n_e \Delta t < 5^o)$.

The variations of the orbital elements are obtained from the formulae

$$
\begin{aligned}
\frac{d\delta i}{dt} &= \frac{-1}{n_s a_s^2 (1 - e_s^2)^{\frac{1}{2}} \sin i_s} \frac{\partial F_b}{\partial \Omega_s} \\
\frac{d\delta\Omega}{dt} &= \frac{1}{n_s a_s^2 (1 - e_s^2)^{\frac{1}{2}} \sin i_s} \frac{\partial F_b}{\partial i_s} \\
\frac{d\delta w}{dt} &= \frac{-\cos i_s}{n_s a_s^2 (1 - e_s^2)^{\frac{1}{2}} \sin i_s} \frac{\partial F_b}{\partial i_s} + \frac{(1-e_s^2)^{\frac{1}{2}}}{n_s a_s^2 e_s} \frac{\partial F_b}{\partial e_s} \\
\frac{d\delta M}{dt} &= \frac{-(1-e_s^2)}{n_s a_s^2 e_s} \frac{\partial F_b}{\partial e_s} - \frac{2}{n_s a_s} \frac{\partial F_b}{\partial a_s}
\end{aligned}
\tag{7.18}
$$

with both $\frac{d\delta a}{dt}$ and $\frac{d\delta e}{dt}$ equal to zero. Secondary effects through the secular perturbations due to the oblateness of the Earth have to be taken into account. The secular motion of the node, due to the oblateness is

$$\dot{\Omega}_s = -\frac{3}{2} \frac{R^2 J_2}{a_s^2 (1 - e_s^2)^2} n_s \cos i_s \tag{7.19}$$

where J_2 is the second zonal harmonic of the Earth's potential.

Indirect effects due to the secular variations of the inclination are (KOZAI 1959)

$$\frac{d\delta\Omega}{dt} = -\dot{\Omega}_s \tan i_s \, \delta i \tag{7.20}$$

$$\frac{d\delta w}{dt} = 5\dot{\Omega}_s \sin i_s \, \delta i \tag{7.21}$$

$$\frac{d\delta M}{dt} = 3\dot{\Omega}_s \sin i_s (1 - e_s^2)^{\frac{1}{2}} \, \delta i \tag{7.22}$$

Addition of these to equations 7.18 give equations 7.23.

$$\begin{aligned}
\delta i = F \Big[& -\frac{3}{8} \cos i_s \sin 2i_b \cos \theta_b^* / \alpha_1 \\
& - \frac{3}{8} \sin i_s \sin^2 i_b \cos 2\theta_b^* / \alpha_2 \\
& + \frac{3}{4} \sin i_s \cos^4 \frac{i_b}{2} \cos 2(f_b^* + w_b - \theta_b^*) / \alpha_4 \\
& - \frac{3}{4} \cos i_s \sin i_b \cos^2 \frac{i_b}{2} \cos (2f_b^* + 2w_b - \theta_b^*) / \alpha_5 \\
& - \frac{3}{4} \sin i_s \sin^4 \frac{i_b}{2} \cos 2(f_b^* + w_b + \theta_b^*) / \alpha_6 \\
& - \frac{3}{4} \cos i_s \sin i_b \sin^2 \frac{i_b}{2} \cos (2f_b^* + 2w_b + \theta_b^*) / \alpha_7 \Big]
\end{aligned}$$

$$\begin{aligned}
\delta\Omega = F \Big[& -\frac{3}{4} \cos i_s \left(1 - \frac{3}{2} \sin^2 i_b\right) t \\
& + \frac{3}{8} \sin 2i_b \sin \theta_b^* \left(\frac{\cos 2i_s}{\sin i_s} + \frac{\dot{\Omega}_s}{\alpha_1} \sin i_s\right) \frac{1}{\alpha_1} \\
& + \frac{3}{8} \sin^2 i_b \sin 2\theta_b^* \left(\cos i_s + \frac{\dot{\Omega}_s}{\alpha_2} \tan i_s \sin i_s\right) \frac{1}{\alpha_2} \\
& - \frac{9}{8} \sin^2 i_b \cos i_s \sin 2(f_b^* + w_b) \frac{1}{\alpha_3} \\
& + \frac{3}{4} \cos^4 \frac{i_b}{2} \sin 2(f_b^* + w_b - \theta_b^*) \left\{ \cos i_s - \frac{\dot{\Omega}_s}{\alpha_4} \tan i_s \sin i_s \right\} \frac{1}{\alpha_4} \\
& + \frac{3}{4} \sin i_b \cos^2 \frac{i_b}{2} \sin(2f_b^* + 2w_b - \theta_b^*) \left\{ \frac{-\cos 2i_s}{\sin i_s} + \frac{\dot{\Omega}_s}{\alpha_5} \sin i_s \right\} \frac{1}{\alpha_5} \\
& + \frac{3}{4} \sin \frac{i_b}{2} \sin 2(f_b^* + w_b + \theta_b^*) \left\{ \cos i_s + \frac{\dot{\Omega}_s}{\alpha_6} \tan i_s \sin i_s \right\} \frac{1}{\alpha_6} \\
& + \frac{3}{4} \sin i_b \sin^2 \frac{i_b}{2} \sin(2f_b^* + 2w_b + \theta_b^*) \left\{ \frac{\cos 2i_s}{\sin i_s} + \frac{\dot{\Omega}_s}{\alpha_7} \sin i_s \right\} \frac{1}{\alpha_7} \Big]
\end{aligned}$$

$$\delta w = F \Big[\frac{3}{4}(1 - \frac{3}{2}\sin^2 i_b)(2 - \frac{5}{2}\sin^2 i_s)\, t$$
$$+ \frac{3}{8}\sin 2i_b \sin\theta_b^* \{\sin 2i_s (\frac{3}{2} - \frac{5}{2}\frac{\dot\Omega_s}{\alpha_1}) - \cot i_s \cos 2i_s\} \frac{1}{\alpha_1}$$
$$+ \frac{3}{8}\sin^2 i_b \sin 2\theta_b^* \{\sin^2 i_s (\frac{5}{2} - 5\frac{\dot\Omega_s}{\alpha_2}) - 1\} \frac{1}{\alpha_2}$$
$$+ \frac{9}{8}\sin^2 i_b \sin 2(f_b^* + w_b) \{2 - \frac{5}{2}\sin^2 i_s\} \frac{1}{\alpha_3}$$
$$+ \frac{3}{4}\cos^4\frac{i_b}{2} \sin 2(f_b^* + w_b - \theta_b^*) \{\sin^2 i_s (\frac{5}{2} + 5\frac{\dot\Omega_s}{\alpha_4}) - 1\} \frac{1}{\alpha_4}$$
$$+ \frac{3}{4}\sin i_b \cos^2\frac{i_b}{2} \sin(2f_b^* + 2w_b - \theta_b^*) \{-\sin 2i_s (\frac{3}{2} + \frac{5}{2}\frac{\dot\Omega_s}{\alpha_5})$$
$$+ \cot i_s \cos 2i_s\} \frac{1}{\alpha_5}$$
$$+ \frac{3}{4}\sin^4\frac{i_b}{2} \sin 2(f_b^* + w_b + \theta_b^*) \{\sin^2 i_s (\frac{5}{2} - 5\frac{\dot\Omega_s}{\alpha_6}) - 1\} \frac{1}{\alpha_6}$$
$$+ \frac{3}{4}\sin i_b \sin^2\frac{i_b}{2} \sin(2f_b^* + 2w_b + \theta_b^*) \{\sin 2i_s (\frac{3}{2} - \frac{5}{2}\frac{\dot\Omega_s}{\alpha_7})$$
$$- \cos 2i_s \cot i_s\} \frac{1}{\alpha_7} \Big]$$

$$\delta M = F(1 - e_s^2)^{\frac{1}{2}} \Big[\frac{3}{4}(1 - \frac{3}{2}\sin^2 i_s)(1 - \frac{3}{2}\sin^2 i_b)\, t$$
$$+ \frac{9}{16}\sin 2i_s \sin 2i_b \sin\theta_b^* (1 - \frac{\dot\Omega_s}{\alpha_1}) \frac{1}{\alpha_1}$$
$$+ \frac{9}{16}\sin^2 i_s \sin^2 i_b \sin 2\theta_b^* (1 - 2\frac{\dot\Omega_s}{\alpha_2}) \frac{1}{\alpha_2}$$
$$+ \frac{9}{8}\sin^2 i_b (1 - \frac{3}{2}\sin^2 i_s) \sin 2(f_b^* + w_b) \frac{1}{\alpha_3}$$
$$+ \frac{9}{8}\sin^2 i_s \cos^4\frac{i_b}{2} (1 + 2\frac{\dot\Omega_s}{\alpha_4}) \sin 2(f_b^* + w_b - \theta_b^*) \frac{1}{\alpha_4}$$
$$- \frac{9}{8}\sin 2i_s \cos^2\frac{i_b}{2} \sin i_b \sin(2f_b^* + 2w_b - \theta_b^*) (1 + \frac{\dot\Omega_s}{\alpha_5}) \frac{1}{\alpha_5}$$
$$+ \frac{9}{8}\sin^2 i_s \sin^4\frac{i_b}{2} (1 - 2\frac{\dot\Omega_s}{\alpha_6}) \sin 2(f_b^* + w_b + \theta_b^*) \frac{1}{\alpha_6}$$
$$+ \frac{9}{8}\sin 2i_s \sin i_b \sin^2\frac{i_b}{2} (1 - \frac{\dot\Omega_s}{\alpha_7}) \sin(2f_b^* + 2w_b + \theta_b^*) \frac{1}{\alpha_7} \Big] \qquad (7.23)$$

where
$$F = \frac{n_b^2}{n_s}\beta (\frac{a_b}{r_b^*})^3 (\frac{R}{a_s})^5 k_2 (1 - e_s^2)^{-2} \qquad (7.24)$$

and
$$\alpha_1 = \dot\theta_b^*$$
$$\alpha_2 = 2\dot\theta_b^*$$
$$\alpha_3 = 2\dot f_b^* + 2\dot w_b$$
$$\alpha_4 = 2\dot f_b^* + 2\dot w_b - 2\dot\theta_b^*$$
$$\alpha_5 = 2\dot f_b^* + 2\dot w_b - \dot\theta_b^*$$
$$\alpha_6 = 2\dot f_b^* + 2\dot w_b + 2\dot\theta_b^*$$
$$\alpha_7 = 2\dot f_b^* + 2\dot w_b + \dot\theta_b^*$$

which refer to the mean motions of the orbital elements.

The first term in S_b is a secular term, and cannot be distinguished from other secular terms due to the oblateness of the Earth. Therefore it is not included in any calculations for tidal perturbations. The frequencies of the satellite perturbations, related to Earth tide periods can be found in Table 7.1.

TABLE 7.1
Relation between Orbital Expansion and
Principal Tidal Terms

Indices in Orbital Development						Wave Symbol	Argument
n	m	p	q	j	g		
				Lunar Tides			
2	1	0	0	1	0	O_1	$2w_b + 2M_b + \Omega_b - \Omega_s$
2	2	0	0	1	0	M_2	$2w_b + 2M_b + 2\Omega_b - 2\Omega_s$
2	2	1	0	1	0	K_2^m	$2\Omega_b - 2\Omega_s$
2	1	1	0	1	0	K_1^m	$\Omega_b - \Omega_s$
				Solar Tides			
2	1	1	0	1	0	K_1^s	$\Omega_b - \Omega_s$
2	2	1	0	1	0	K_2^s	$2\Omega_b - 2\Omega_s$
2	2	0	0	1	0	S_2	$2w_b + 2M_b + 2\Omega_b - 2\Omega_s$
2	1	0	0	1	0	P_1	$2w_b + 2M_b + \Omega_b - \Omega_s$

7.2.2 General Development of Earth Tide Perturbation Theory

The formulation given here follows KAULA(1964), KAULA(1969), and LAMBECK ET AL(1974). The development is expanded to include all tidal periods for any degree n.

Following the development in the previous Section, the potential due to the deformation at a position beyond the Earth is

$$\Delta U(r) = \frac{Gm_b}{r_b^*} \sum_{n=2}^{\infty} k_n \left(\frac{R}{r_b^*}\right)^n \left(\frac{R}{r_s}\right)^{n+1} P_{no}(\cos \psi_b^*) \tag{7.25}$$

Expressing ψ_b^*, r_b^* and r_s in terms of Keplerian elements of the perturbing body and of the satellite, with the appropriate transformations (LAMBECK ET AL 1974, KAULA 1964, 1969) the perturbing potential is

$$\begin{aligned} \Delta U(r) = & \sum_{n=2}^{\infty} \sum_{m=0}^{n} \sum_{p=0}^{n} \sum_{q=-\infty}^{\infty} \sum_{j=0}^{n} \sum_{g=-\infty}^{\infty} k_n \left(\frac{R}{a_b}\right)^n \frac{Gm_b}{a_b} \\ & \frac{(n-m)!}{(n+m)!} (2 - \delta_{om}) F_{nmp}(i_b) G_{npq}(e_b) \\ & \left(\frac{R}{a_s}\right)^{n+1} F_{nmj}(i_s) G_{njg}(e_s) \\ & \cos(\gamma^b_{nmpq} - \gamma_{nmjg} + \varepsilon_{nmpq}) \end{aligned} \tag{7.26}$$

with

$$\gamma_{nmjg} = (n-2j) w_s + (n-2j+g) M_s + m \Omega_s ,$$

$$\gamma^b_{nmpq} = (n-2p) w_b + (n-2p+q) M_b + m \Omega_b ,$$

where e_b is the eccentricity of the disturbing body's orbit and the phase ε is related to the time lag Δt by

$$\varepsilon_{nmpq} = -(n-2p+q)\, n_b\, \Delta t + m n_e \Delta t \,.$$

The polynomials $F_{nmp}(i_b)$ and $G_{npq}(e_b)$ are terms in $\sin i_b$ and e_b respectively and are given below (KAULA 1966).

$$F_{nmp}(i_b) = \sum_{t=0}^{t_{max}} \frac{(2n-2t)!}{t!(n-t)!(n-m-2t)!\,2^{2n-2t}} \sin^{n-m-2t} i_b \sum_{S=0}^{m} \binom{m}{s} \cos^{s} i_b \sum_{c} \binom{n-m-2t+s}{c} \binom{m-s}{p-t-c} (-1)^{c-k}$$

where

$$t_{max} = \left\{ \begin{matrix} k = \text{Integer } \left(\frac{n-m}{2}\right) \\ p \end{matrix} \right\} \quad \begin{matrix} \text{whichever} \\ \text{is less} \end{matrix} .$$

The range of c is

$$\left\{ \begin{matrix} 0 \\ p-t-m+s \end{matrix} \right\} \leq c \leq \left\{ \begin{matrix} n-m-2t+s \\ p-t \end{matrix} \right. ,$$

commencing at the greater of the lower indices and ending at the smaller of the upper values.

Also, $\binom{x}{y}$ is defined as

$$\binom{x}{y} = \frac{x!}{y!(x-y)!} .$$

The function $G_{npq}(e_b)$ is expressed as

$$G_{npq}(e_b) = (-1)^{|q|} (1+B^2)^{n} B^{|q|} \sum_{k=0}^{\infty} P_{npqk}\, Q_{npqk}\, B^{2k} ,$$

where

$$B = \frac{e_b}{1+(1-e_b^2)^{\frac{1}{2}}} ,$$

$$P_{npqk} = \sum_{r=0}^{h} \binom{2p-2n}{n-r} \frac{(-1)^r}{r!} \left(\frac{(n-2p'+q')e_b}{2B}\right)^r$$

$$h = k + q' \quad \text{for} \quad q' > 0 ,$$

$$h = k \quad \text{for} \quad q' < 0 ;$$

and

$$Q_{npqk} = \sum_{r=0}^{h} \binom{-2p'}{h-r} \frac{1}{r!} \left(\frac{(n-2p'+q')e_b}{2B}\right)^r$$

$$h = k \quad \text{for} \quad q' > 0 ,$$

$$h = k - q \quad \text{for} \quad q' < 0 ;$$

if $p \leq n/2$, then $p' = p$ and $q' = q$, and

if $p > n/2$, then $p' = n-p$ and $q' = -q$.

Similarly, $F_{nmj}(i_s)$ and $G_{njg}(e_s)$ are functions of i_s and e_s, and the Kronecker delta δ_{om} is equal to 1 for $m = 0$ and 0 for $m \neq 0$.

To obtain the variations of the orbital elements, Legrange's equations, given by equations 7.18 are solved. The equations expressed previously are developed only for long period perturbations,

the revised equations for all periods become

$$\frac{d\delta a}{dt} = \frac{2}{n_s a_s} \frac{\partial(\Delta U)}{\partial M_s}$$

$$\frac{d\delta e}{dt} = \frac{(1-e_s^2)}{n_s a_s^2 e_s} \frac{\partial(\Delta U)}{\partial M_s} - \frac{(1-e_s^2)^{\frac{1}{2}}}{n_s a_s^2 e_s} \frac{\partial(\Delta U)}{\partial w_s}$$

$$\frac{d\delta i}{dt} = \frac{\cos i_s}{n_s a_s^2 (1-e_s^2)^{\frac{1}{2}} \sin i_s} \frac{\partial(\Delta U)}{\partial w_s} - \frac{1}{n_s a_s^2 (1-e_s^2)^{\frac{1}{2}} \sin i_s} \frac{\partial(\Delta U)}{\partial i_s}$$

$$\frac{d\delta W}{dt} = \frac{-\cos i}{n_s a_s^2 (1-e_s^2)^{\frac{1}{2}} \sin i_s} \frac{\partial(\Delta U)}{\partial i_s} + \frac{(1-e_s^2)^{\frac{1}{2}}}{n_s a_s^2 e_s} \frac{\partial(\Delta U)}{\partial e_s}$$

$$\frac{d\delta \Omega}{dt} = \frac{1}{n_s a_s^2 (1-e_s^2)^{\frac{1}{2}} \sin i_s} \frac{\partial(\Delta U)}{\partial i_s}$$

$$\frac{d\delta M}{dt} = \frac{-(1-e_s^2)}{n_s a_s e_s} \frac{\partial(\Delta U)}{\partial e_s} - \frac{2}{n_s a_s} \frac{\partial(\Delta U)}{\partial a_s} \qquad (7.27)$$

When solving for major long period perturbations,

$$\frac{d\delta a}{dt} = 0 \quad \text{and} \quad \frac{d\delta e}{dt} = 0$$

and any differential in terms of the mean anomaly is zero for long period terms.

The complete differentation, including short period terms, for each orbital element becomes

$$\frac{d\delta a}{dt}(n,m,p,q,j,g) = \frac{2}{n_s a_s} k_n \left(\frac{R}{a_b}\right)^n \frac{Gm_b}{a_b} \frac{(n-m)!}{(n+m)!} (2-\delta_{om})$$
$$F_{nmp}(i_b)\, G_{npq}(e_b) \left(\frac{R}{a_s}\right)^{n+1} F_{nmj}(i_s)\, G_{njg}(e_s)$$
$$(n-2j+g) \sin(\gamma^b_{nmpq} - \gamma_{nmjg} + \varepsilon_{nmpq})$$

$$\frac{d\delta e}{dt}(n,m,p,q,j,g) = \frac{(1-e_s^2)}{n_s a_s^2 e_s} k_n \left(\frac{R}{a_b}\right)^n \frac{Gm_b}{a_b} \frac{(n-m)!}{(n+m)!} (2-\delta_{om})$$
$$F_{nmp}(i_b)\, G_{npq}(e_b) \left(\frac{R}{a_s}\right)^{n+1} F_{nmj}(i_s)\, G_{njg}(e_s)$$
$$(n-2j+g) \sin(\gamma^b_{nmpq} - \gamma_{nmjg} + \varepsilon_{nmpq})$$
$$- \frac{(1-e_s^2)^{\frac{1}{2}}}{n_s a_s^2 e_s} k_n \left(\frac{R}{a_b}\right)^n \frac{Gm_b}{a_b} \frac{(n-m)!}{(n+m)!} (2-\delta_{om})$$
$$F_{nmp}(i_b)\, G_{npq}(e_b) \left(\frac{R}{a_s}\right)^{n+1} F_{nmj}(i_s)\, G_{njg}(e_s)$$
$$(n-2j) \sin(\gamma^b_{nmpq} - \gamma_{nmjg} + \varepsilon_{nmpq})$$

$$\frac{d\delta \Omega}{dt}(n,m,p,q,j,g) = \frac{1}{n_s a_s^2 (1-e_s^2)^{\frac{1}{2}} \sin i_s} k_n \left(\frac{R}{a_b}\right)^n \frac{Gm_b}{a_b} \frac{(n-m)!}{(n+m)!} (2-\delta_{om})$$
$$F_{nmp}(i_b)\, G_{npq}(e_b) \left(\frac{R}{a_s}\right)^{n+1} F'_{nmj}(i_s)\, G_{njg}(e_s)$$
$$\cos(\gamma^b_{nmpq} - \gamma_{nmjg} + \varepsilon_{nmpq})$$

$$\frac{d\delta M}{dt}(n,m,p,q,j,g) = \frac{-(1-e^2)}{n_s a_s^2 e_s} k_n \left(\frac{R}{a_b}\right)^n \frac{Gm_b}{a_b} \frac{(n-m)!}{(n+m)!} (2 - \delta_{om})$$
$$F_{nmp}(i_b)\, G_{npq}(e_b) \left(\frac{R}{a_s}\right)^{n+1} F_{nmj}(i_s)\, G'_{njg}(e_s)$$
$$\cos\left(\gamma^b_{nmpq} - \gamma_{nmjg} + \varepsilon_{nmpq}\right)$$
$$+ \frac{2}{n_s a_s} k_n \left(\frac{R}{a_b}\right)^n \frac{Gm_b}{a_b} \frac{(n-m)!}{(n+m)!} (2 - \delta_{om}) \frac{(n+1)}{a_s}$$
$$F_{nmp}(i_b)\, G_{npq}(e_b) \left(\frac{R}{a_s}\right)^{n+1} F_{nmj}(i_s)\, G_{njg}(e_s)$$
$$\cos\left(\gamma^b_{nmpq} - \gamma_{nmjg} + \varepsilon_{nmpq}\right)$$

$$\frac{d\delta i}{dt}(n,m,p,q,j,g) = \frac{\cos i_s}{n_s a_s^2 (1-e_s^2)^{\frac{1}{2}} \sin i_s} k_n \left(\frac{R}{a_b}\right)^n \frac{Gm_b}{a_b} \frac{(n-m)!}{(n+m)!} (2 - \delta_{om})$$
$$F_{nmp}(i_b)\, G_{npq}(e_b) \left(\frac{R}{a_s}\right)^{n+1} F_{nmj}(i_s)\, G_{njg}(e_s)$$
$$(n-2j) \cos\left(\gamma^b_{nmpq} - \gamma_{nmjg} + \varepsilon_{nmpq}\right)$$
$$- \frac{1}{n_s a_s^2 (1-e_s^2)^{\frac{1}{2}} \sin i_s} k_n \left(\frac{R}{a_b}\right)^n \frac{Gm_b}{a_b} \frac{(n-m)!}{(n+m)!} (2 - \delta_{om})\, m$$
$$F_{nmp}(i_b)\, G_{npq}(e_b) \left(\frac{R}{a_s}\right)^{n+1} F_{nmj}(i_s)\, G_{njg}(e_s)$$
$$\sin\left(\gamma^b_{nmpq} - \gamma_{nmjg} + \varepsilon_{nmpq}\right)$$

$$\frac{d\delta w}{dt}(n,m,p,q,j,g) = \frac{-\cos i_s}{n_s a_s^2 (1-e_s^2)^{\frac{1}{2}} \sin i_s} k_n \left(\frac{R}{a_b}\right)^n \frac{Gm_b}{a_b} \frac{(n-m)!}{(n+m)!} (2 - \delta_{om})$$
$$F_{nmp}(i_b)\, G_{npq}(e_b) \left(\frac{R}{a_s}\right)^{n+1} F'_{nmj}(i_s)\, G_{njg}(e_s)$$
$$\cos\left(\gamma^b_{nmpq} - \gamma_{nmjg} + \varepsilon_{nmpq}\right)$$
$$+ \frac{(1-e_s^2)^{\frac{1}{2}}}{n_s a_s^2 e_s} k_n \left(\frac{R}{a_b}\right)^n \frac{Gm_b}{a_b} \frac{(n-m)!}{(n+m)!} (2 - \delta_{om})$$
$$F_{nmp}(i_b)\, G_{npq}(e_b) \left(\frac{R}{a_s}\right)^{n+1} F_{nmj}(i_s)\, G'_{njg}(e_s)$$
$$\cos\left(\gamma^b_{nmpq} - \gamma_{nmjg} + \varepsilon_{nmpq}\right) \qquad (7.28)$$

The total tidal perturbation for any orbital element involves a summation in n,m,p,q,j and g, as given in equation 7.26. The notation $F'_{nmj}(i_s)$ is the differential of $F_{nmj}(i_s)$ with respect to i_s, while $G'_{njg}(e_s)$ is the differential of $G_{njg}(e_s)$ with respect to e_s.

Long period terms arise when $(n-2j+g) = 0$, and the principal terms when $g = 0$. If $g \neq 0$, long period terms do arise but their amplitudes are very small, due to the nature of the power series in the satellite eccentricity comprising the function $G_{njg}(e_s)$. The long period terms in the satellite eccentricity can be assumed to be negligible.

The expressions for the secular variations of the satellite inclination (equations 7.20, 7.21 and 7.22) still have to be included in these formulae.

Kozai's formulae can be obtained by appropriate simplifications and the gravitational constant can be eliminated by using equations 7.8 to 7.10.

The relationships between various formulations can be found in Table 7.1.

If the mean motions of the argument of the frequencies (denoted by α) approaches zero, very long period perturbations occur. Thus very small tides on the Earth could produce large perturbations to a satellite, because the satellite measures the integrated effect of the tides.

7.3 Ocean Tide Perturbations

The development is taken from LAMBECK & CAZENAVE(1973) and LAMBECK ET AL(1974).

The potential at the Earth's surface due to the ocean tides is

$$U_l^o(R) = 4\pi GR \sum_n \sum_m C_{lnm}\, \rho_w\, P_{nm}(\sin\phi)\, \frac{1}{2n+1} \sin(lt + m\lambda + \varepsilon_{lnm}) \tag{7.29}$$

For a non-rigid Earth, the potential external to R is (LAMBECK & CAZENAVE 1973)

$$U_l^o(r) = \sum_n \sum_m (1 + k_n')\, \frac{4\pi}{2n+1}\, \frac{GR^2}{a_s}\, C_{lnm}\, \rho_w\, \left(\frac{R}{a_s}\right)^n \sum_j F_{nmj}(i_s) \sum_g G_{njg}(e_s) \begin{bmatrix} \sin \\ -\cos \end{bmatrix}^{\text{n-m even}}_{\text{n-m odd}} \nu_{lnmjg} \tag{7.30}$$

with

$$\nu_{lnmjg} = [(n-2j)\, w_s + (n-2j+g)\, M_s + m(\Omega_s - \sigma) + 2\pi lfT + \varepsilon_{lnm}] ,$$

and k_n' are the load deformation coefficients,
ρ_w is the density of the oceans,
C_{lnm} and ε_{lnm} are parameters related to amplitude and phase, defining the ocean tide,
σ is the sidereal rotation, and
the argument $2\pi lfT$ varies for particular waves and is given by LAMBECK ET AL(1974).

The summations in n,m,j and g follow the same limits as defined in Section 7.2.2.

The long period perturbations in i_s and Ω_s become

$$\Delta i_{(lnmjg)} = (1+k_n')\, \frac{4\pi}{2n+1}\, \frac{GR^2}{a_s}\, \rho_w\, C_{lnm} \left(\frac{R}{a_s}\right)^n F_{nmj}(i_s)\, G_{njg}(e_s) \frac{[-m + (n-2j)\cos i_s]}{[n_s a_s^2 (1-e_s^2)^{\frac{1}{2}} \sin i_s]}\, \frac{1}{\dot{\nu}_{lnmjg}} \begin{bmatrix} \sin \\ -\cos \end{bmatrix}^{\text{n-m even}}_{\text{n-m odd}} \nu_{lnmjg} \tag{7.31}$$

$$\Delta\Omega_{(lnmjg)} = (1+k_n')\, \frac{4\pi}{2n+1}\, \frac{GR^2}{a_s}\, \rho_w\, C_{lnm} \left(\frac{R}{a_s}\right)^n F_{nmj}'(i_s)\, G_{njg}(e_s) \frac{1}{[n_s a_s^2 (1-e_s^2)^{\frac{1}{2}} \sin i_s]}\, \frac{1}{\dot{\nu}_{lnmjg}} \begin{bmatrix} -\cos \\ -\sin \end{bmatrix}^{\text{n-m even}}_{\text{n-m odd}} \nu_{lnmjg} \tag{7.32}$$

The total perturbations for the orbital elements involve summations in n,m,j and g, where $\dot{X}$ is the mean rate of change of X. A term for the indirect effect of the Earth's oblateness should also be included in equation 7.32.

The values of C_{lnm} and ε_{lnm} can be found in LAMBECK ET AL(1974) for various ocean tide models.

The theory developed and outlined in this Chapter for tidal perturbations on satellites is used in the next Chapter to predict and comment on the tidal perturbations on four satellites, BEC, GEOS1, GEOS2, and GEOS3.

CHAPTER 8

TIDAL EFFECTS ON VARIOUS SATELLITES

8.1 Introduction

The basic response of the Earth to the gravitational attraction of the Moon or Sun appears as a small elongation of the Earth's shape in the Earth-Moon or Earth-Sun line. To a satellite, the tides appear as a distortion of the gravitational field arising from this tidal bulge. The tidal perturbations of a satellite are thus primarily determined by the motion of the Moon and Sun rather than the motion of the Earth.

The satellites studied are BEC, GEOS1, GEOS2, and GEOS3. The orbital parameters of these satellites, together with a value of the right ascension of the ascending node of the satellite orbit, at a given epoch are shown in Table 8.1.

TABLE 8.1
Orbital Parameters of Satellites

	BEC	GEOS 1	GEOS 2	GEOS 3
a_s	7400 000 m	8073 000 m	7705 000 m	7207 000 m
e_s	0.025	0.07	0.03	0.0025
i_s	41^o	59^o	106^o	115^o
$\dot{\Omega}_s$	-4.5^o/day	-2.2^o/day	1.4^o/day	2.7^o/day
Ω_s	15.5^o	58.3^o	20.8^o	97.1^o
epoch	4.5.70	25.11.65	5.2.70	29.6.75

The periods and amplitudes of tidal perturbations, are given in two Sections. Section 8.2 will deal only with perturbations in the inclination of the satellite, and is limited to only the dominant tidal waves for both the solid Earth tide effects and the ocean tide effects. Section 8.3 will cover a detailed Earth tide study of the GEOS3 satellite. This will include numerous second degree harmonic waves for all the orbital elements.

8.2 Major Tidal Perturbations in Inclination

The amplitudes and periods of the tides on the four satellites BEC, GEOS1, GEOS2, and GEOS3 are shown in Table 8.2. The Earth tide results are obtained from equations 7.23, while the ocean tide perturbations are obtained from equation 7.31. The inclination is examined because it is usually the easiest and most accurately determined of the orbital elements during tracking. For this reason estimates of Love's numbers are usually based on the inclination residuals.

TABLE 8.2

Tidal Perturbations in Inclination

	M_2	S_2	K_2	O_1	P_1	K_1
			Earth Tide Perturbations			
BEC						
Period(days)	10.3	34.4	42.3	11.7	57.9	84.7
Amplitude(secs)	.16	.24	.09	.09	.18	.87
GEOS 1						
Period	11.7	55.7	80.1	12.6	85.3	160.2
Amplitude	.18	.39	.16	.05	.14	.87
GEOS 2						
Period	15.3	431.2	128.3	144.4	633.6	256.6
Amplitude	.31	3.99	.34	.03	.65	.87
GEOS 3						
Period	17.2	102.3	65.6	15.2	465.4	131.2
Amplitude	.42	1.12	.21	.07	.94	.87
			Ocean Tide Perturbations(Amplitudes)			
BEC						
2nd Harmonic	.025	.027		.006		.077
4th Harmonic	.017	.009		.001		.008
GEOS 1						
2nd Harmonic	.029	.044		.003		.077
4th Harmonic	.005	.004		.001		.009
GEOS 2						
2nd Harmonic	.050	.445		.002		.077
4th Harmonic	.005	.024		.001		.021
GEOS 3						
2nd Harmonic	.067	.126		.005		.077
4th Harmonic	.004	.004		.002		.017

The combined effects of the Earth tides are shown in Figures 8.1, which include only the M_2, S_2, K_2, K_1, O_1 and P_1 Earth tides. The graphs were plotted from values obtained at 00UT on every fourth day from the epoch using the results of Table 8.2 and adopting a k_2 value of 0.30.

The solid Earth tide perturbations in inclination on BEC are shown in Figure 8.1a. Over the 400 day interval sampled, there is a range of approximately 2.5 seconds, and the dominate wave present is the K_1 term having a period of 80 days. The variations in GEOS1 (Figure 8.1b) also have a range of 2.5 seconds, and the dominate wave being K_1 with a period of 160 days. The perturbations on GEOS2 (Figure 8.1c) has a greater range, approximately 8.5 seconds with the dominate wave being S_2 with a period of 430 days. Lastly, GEOS3 (Figure 8.1d) has no single dominate term, but the main waves are K_1, S_2 and P_1. The range of inclination being about 4 seconds. The magnitude of the tidal perturbations is dependent on the orbital characteristics of the satellite.

In all cases the main long period waves are K_1, S_2 and P_1, and if any single wave does dominate, it is the wave with the longest period.

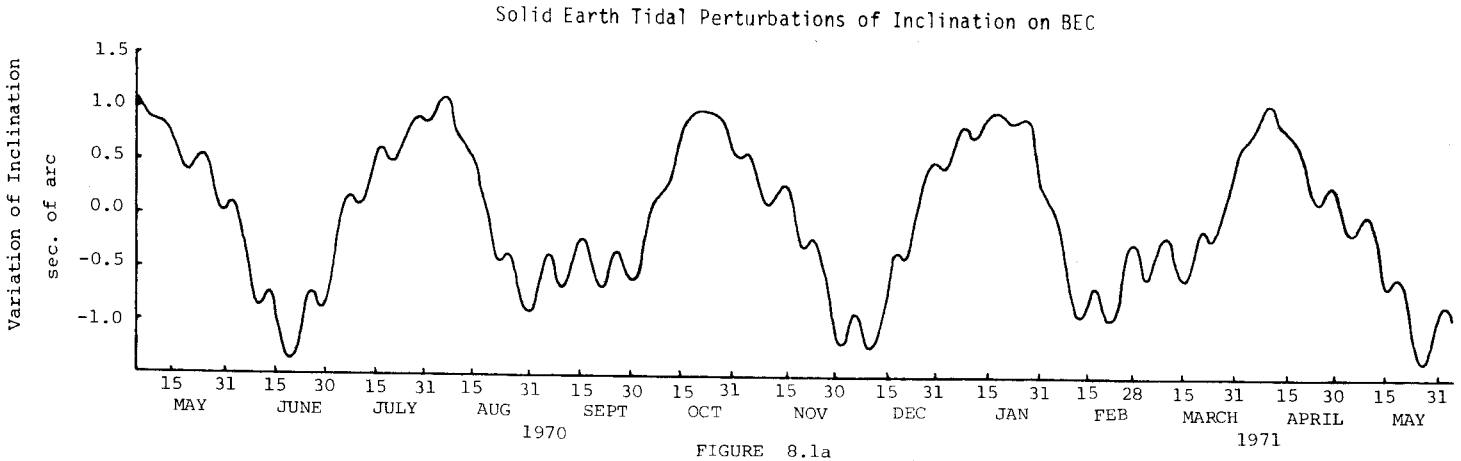

FIGURE 8.1a

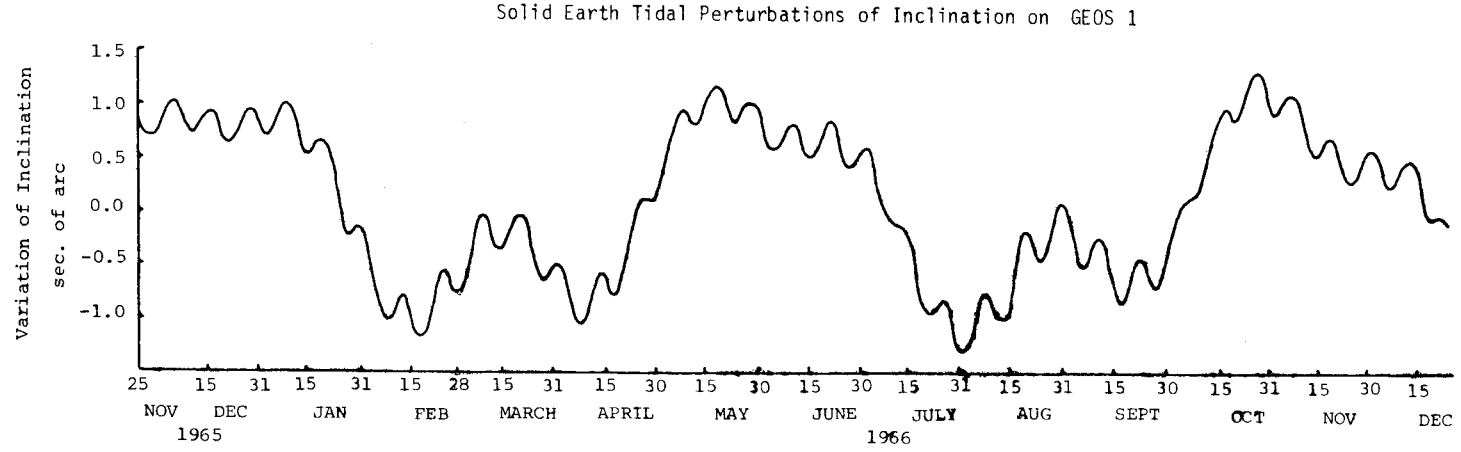

FIGURE 8.1b

Solid Earth Tidal Perturbations of Inclination on GEOS 2

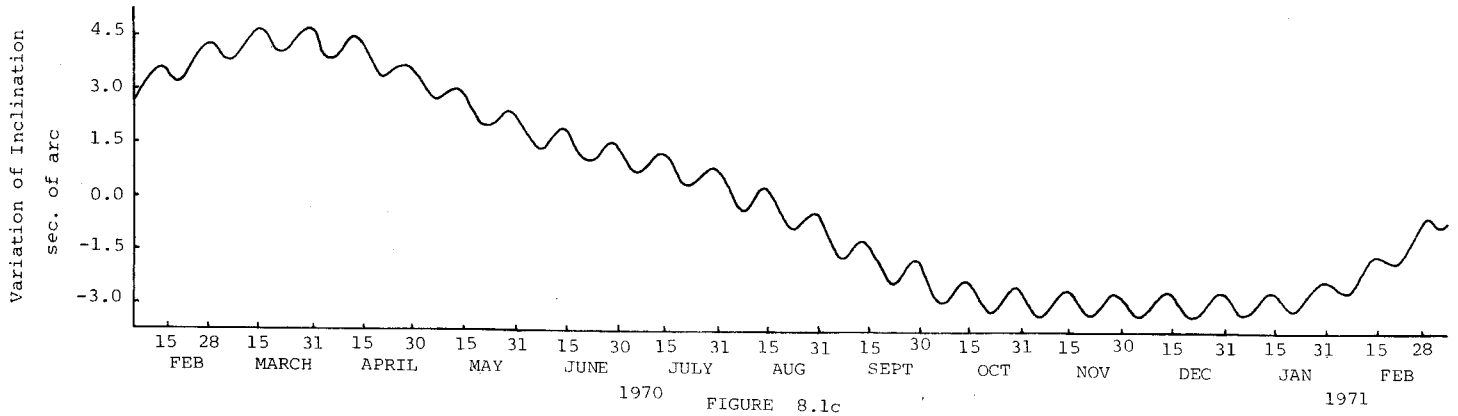

FIGURE 8.1c

Solid Earth Tidal Perturbations of Inclination on GEOS 3

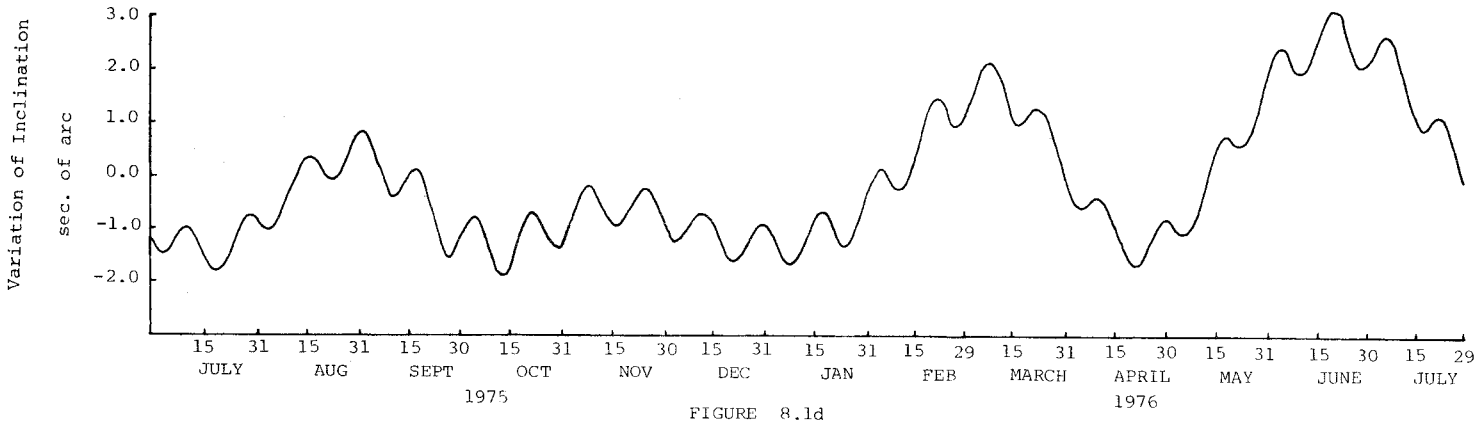

FIGURE 8.1d

The results for the variations in inclination for the oceanic waves M_2, S_2, K_1 and O_1 are presented in Table 8.2 and in Figures 8.2a to 8.2d. Although the amplitudes (less than 0.4 arc seconds) are smaller, the graphs exhibit the same characteristics as the solid Earth tide perturbations (Figures 8.1a to 8.1d). The method of evaluation is the same as the solid Earth tide effect and are based on the results in Table 8.2. The combined effect of the ocean tides and solid Earth tides is shown in Figures 8.3a to 8.3d. The graphs are very similar to the solid Earth tide perturbations graphs, with the exception of slight changes in amplitude. The amplitudes of the tidal perturbations are effected by up to 15% due to the ocean tide effects. The periods of the ocean tide perturbations are the same as the Earth tide perturbations, but have a phase difference.

The dominant ocean tide perturbations are related to the dominant Earth tide perturbations of each satellite, with the M_2 tide never being dominant in the four satellites examined. The fourth degree term has been included, because of its importance in low inclination satellites.

The graph for the perturbations of the inclination on the BEC satellite are magnified in Figure 8.4. This shows the difference between the combined tidal perturbations (with $k_2 = 0.3$) and the Earth tide perturbations with a k_2 value of 0.245, which was determined by SMITH ET AL(1973). In this figure, the unbroken line represents the solid Earth tide perturbations using $k_2 = 0.3$, the broken line represents the combined ocean tide-Earth tide perturbations using $k_2 = 0.3$, while the chained line represents the Earth tide perturbations using $k_2 = 0.245$. Assuming that the present day tracking procedures are adequate and that the solid Earth tide perturbations are correctly modelled.

The various figures in this Section show the similarities between the ocean tide and Earth tide perturbations, and show the need for each effect to be modelled in all satellite studies. The results for BEC perturbations in inclination (Figure 8.4) show the differences between the Earth tide and Earth-ocean tide perturbations. The Love number determined by SMITH ET AL(1973) of 0.245 for this satellite does not agree with calculations using a Love number of 0.3 with ocean tides included. This would suggest unreliability of present ocean tide models and the possibility of unmodelled perturbations influencing the results. There is a possibility that a Love number determined from particular satellite is dependent on the orbital path of the satellite and might not represent a true global value.

The results for GEOS3 are presented in more detail in the following Section, where all orbital elements are examined.

8.3 Solid Earth Tidal Perturbations on GEOS3

The results presented in this Section are determined by equations 7.20 to 7.22, and 7.28, with the wave type expressed as in Kaula's representation. Both the short and long period terms for each of the orbital elements are examined on the GEOS3 satellite. Short period terms have the property that their periods are less than the revolution of the satellite, for the GEOS3 the period of revolution of the satellite is approximately 101 minutes. GEOS3 is chosen because of its geodetic expectations in satellite altimetry.

The determination of short period tidal perturbations are necessary to obtain the instantaneous position of the satellite in altimetry analyses. The accuracy of the analyses are dependent on the orbit determination which is solved using short arc measurements (see Section 9.3.3). Such a orbit determination models long period tidal perturbations but is unable to model short period perturbations.

The dominant short and long period terms for each orbital element are shown in Tables 8.3 to 8.8. In these Tables, the wave types are expressed in the n,m,p,q,j,g notation (see Section 7.2.2) with the amplitudes expressed in seconds of arc in the case of the elements i_s, Ω_s, M_s and w_s. The

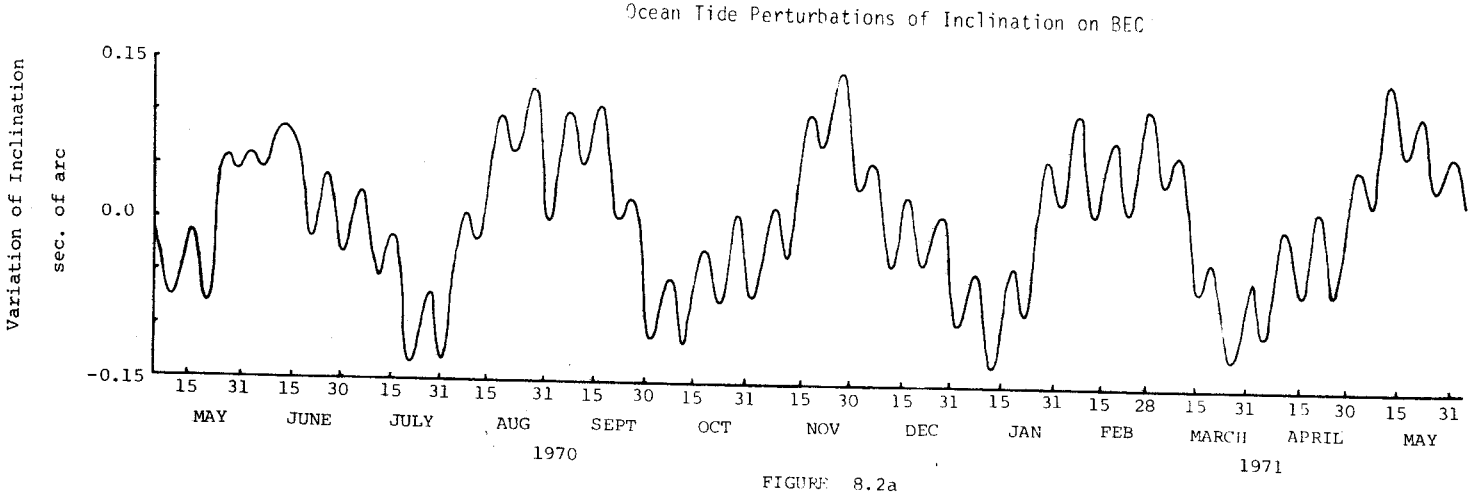

FIGURE 8.2a

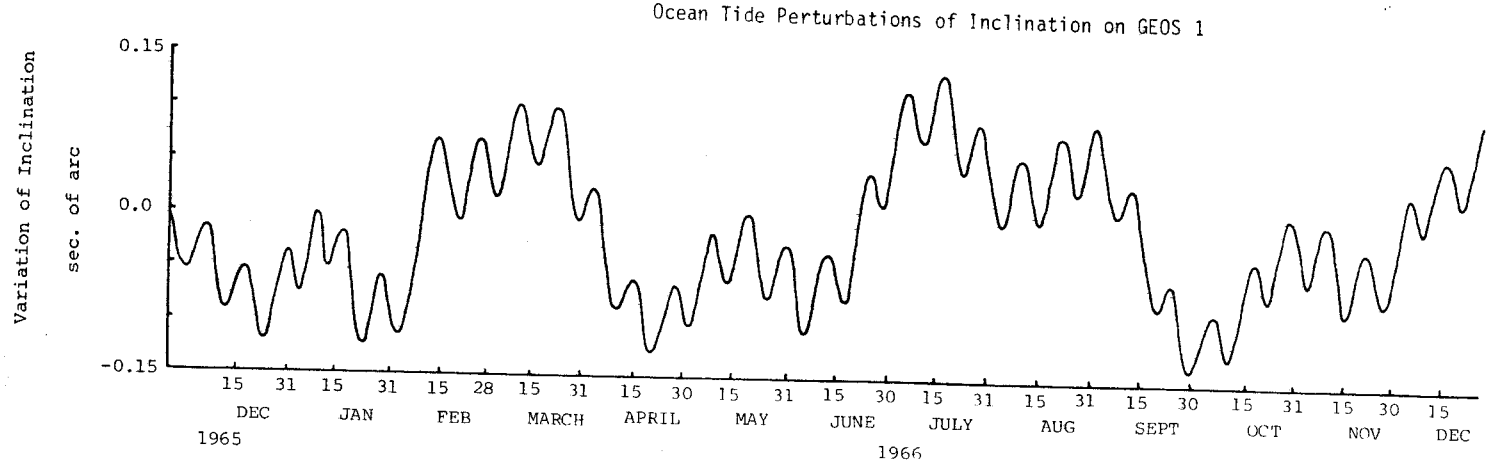

FIGURE 8.2b

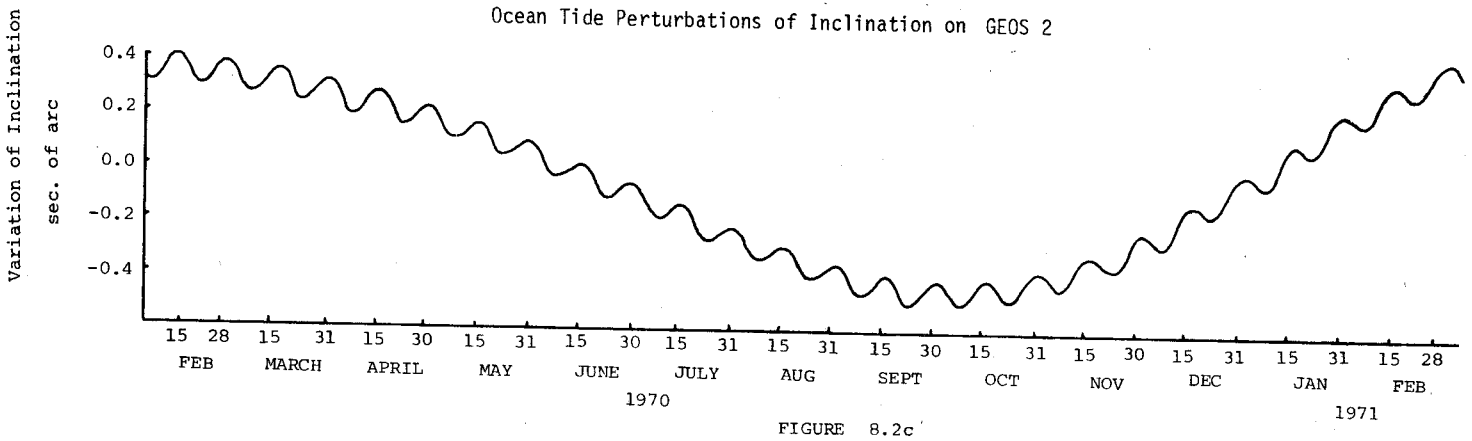

FIGURE 8.2c

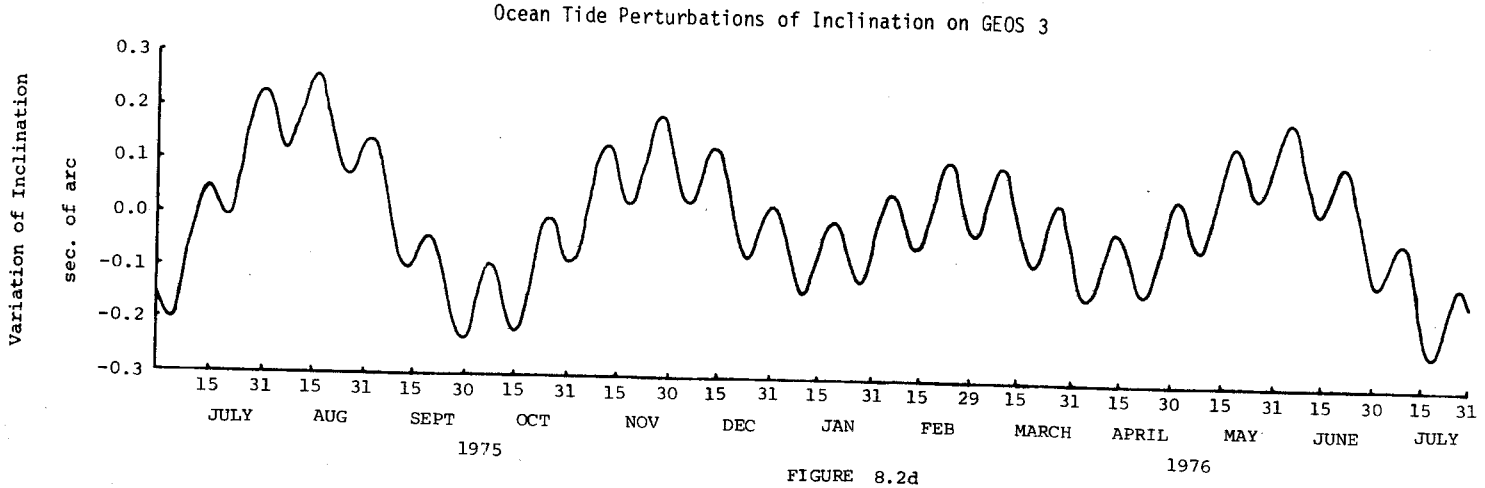

FIGURE 8.2d

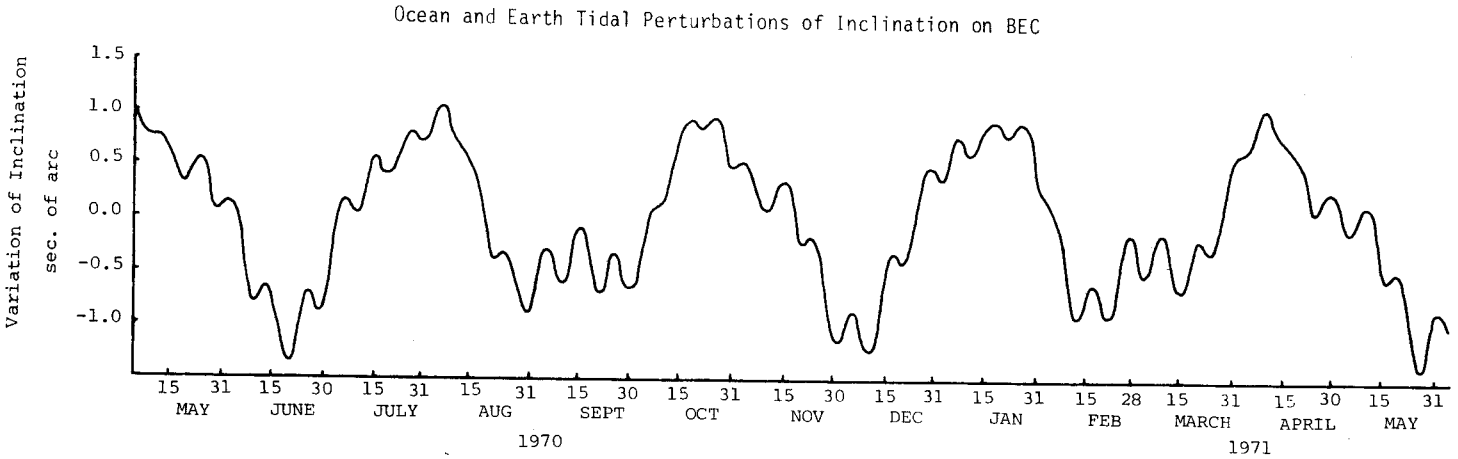

FIGURE 8.3a

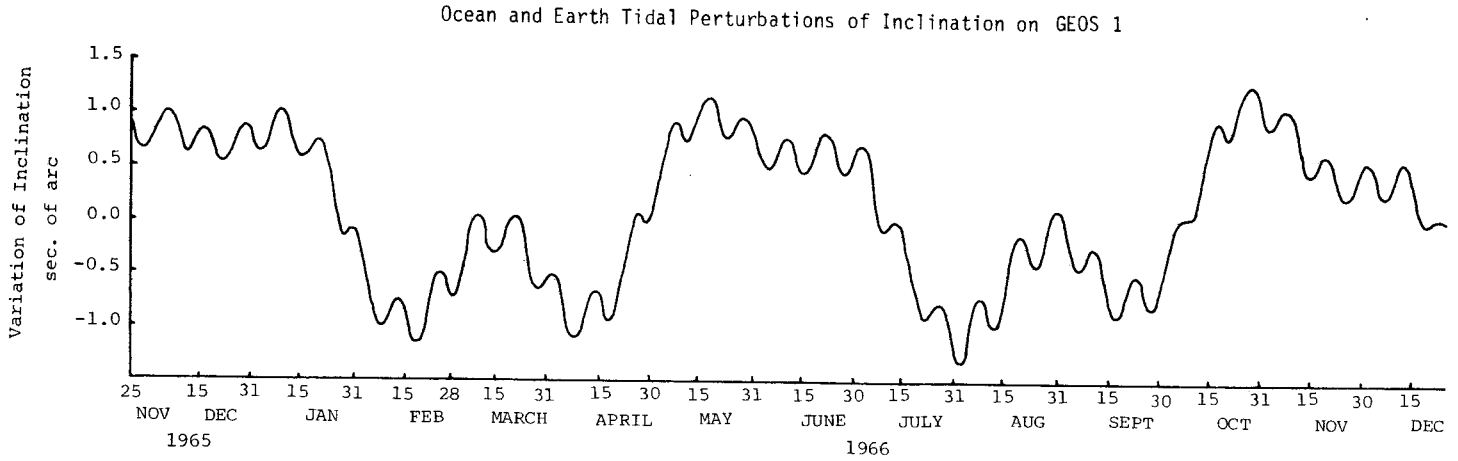

FIGURE 8.3b

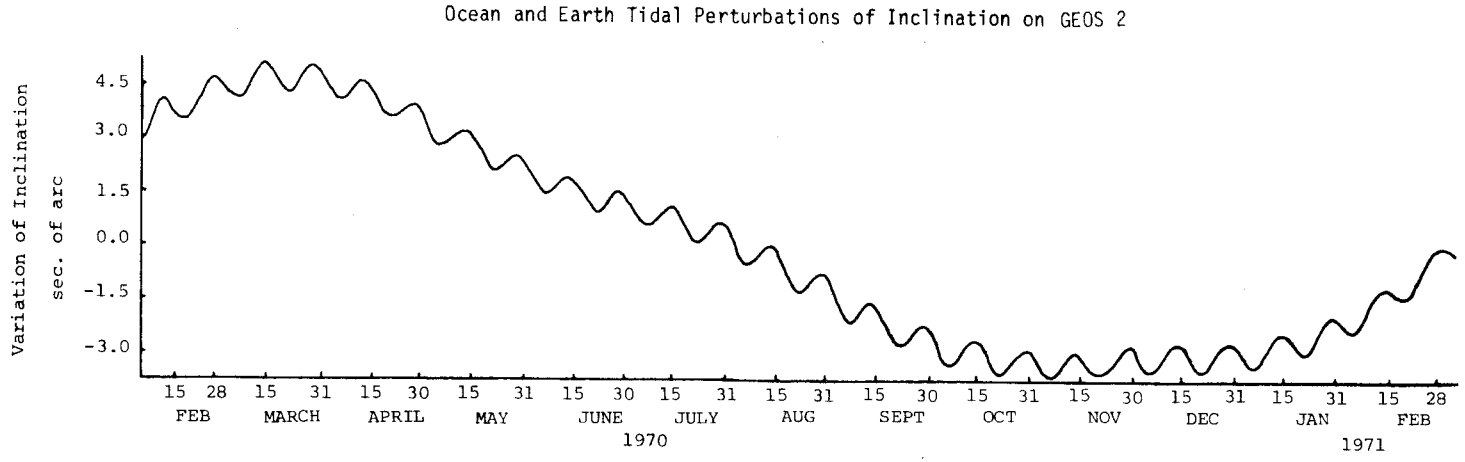

FIGURE 8.3c

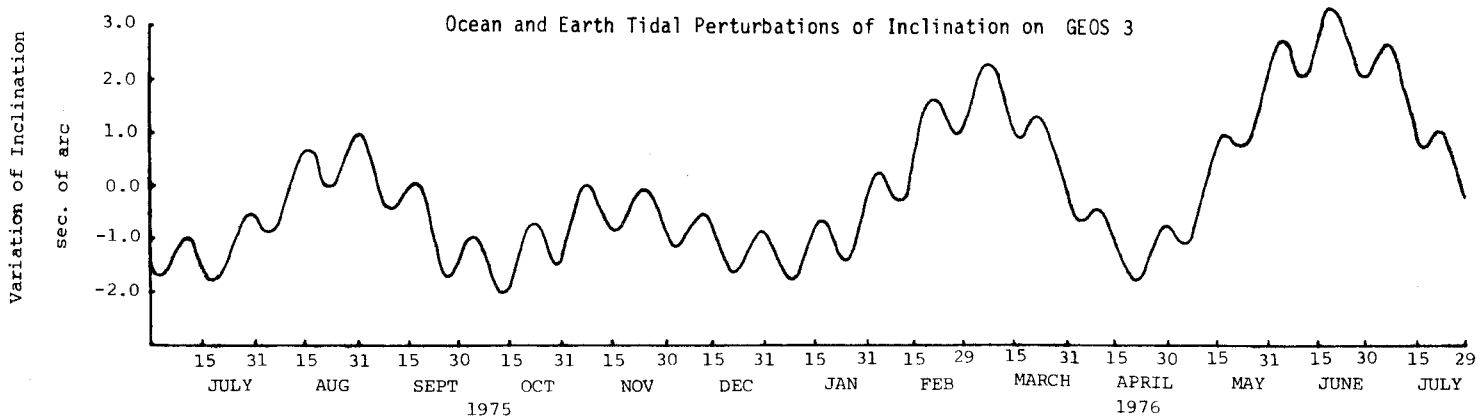

FIGURE 8.3d

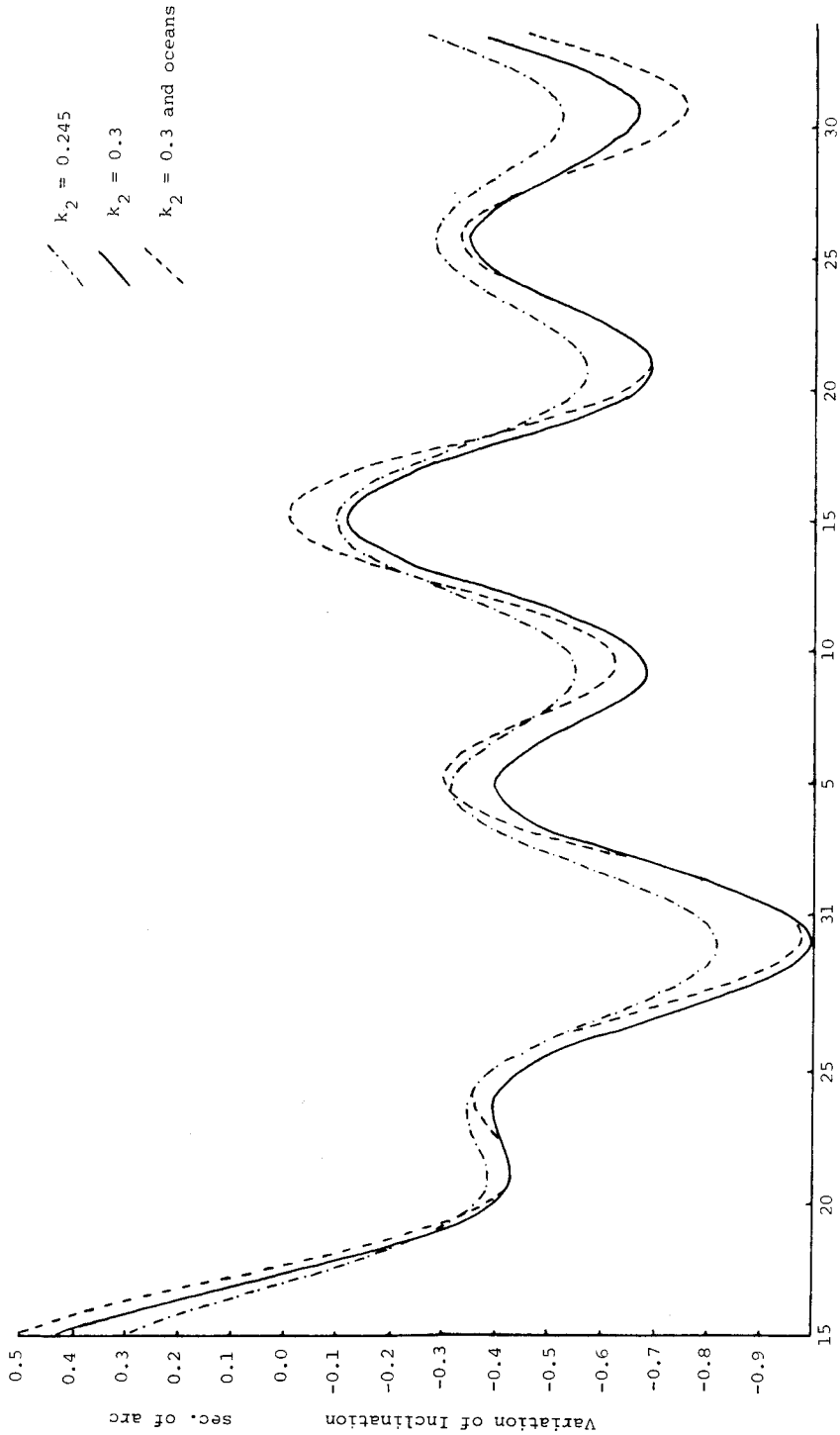
Effect of Variation in Love Number, k_2 on Tidal Perturbations of BEC
k_2 = 0.245
k_2 = 0.3
k_2 = 0.3 and oceans
Variation of Inclination
sec. of arc
0.5
0.4
0.3
0.2
0.1
0.0
-0.1
-0.2
-0.3
-0.4
-0.5
-0.6
-0.7
-0.8
-0.9
15
20
25
31
5
10
15
20
25
30
AUGUST
1970
SEPTEMBER

FIGURE 8.4

eccentricity is expressed in terms of the eccentricity changes, while the semi-major axis is expressed in centimetres. The periods of the tidal waves are either expressed in days or minutes of time.

TABLE 8.3a

Principal Long Period Perturbations in i_s GEOS 3

Lunar Waves			Solar Waves		
Wave Type n m p q j g	Amplitude (arc seconds)	Period (days)	Wave Type n m p q j g	Amplitude (arc seconds)	Period (days)
2 1 0 0 1 0	0.0700	15.2	2 1 0 0 1 0	-0.9991	468.5
2 1 1 0 1 0	0.5870	131.4	2 1 0 1 1 0	0.2073	1657.7
2 2 0-1 1 0	-0.0300	45.5	2 1 1 0 1 0	0.2685	131.4
2 2 0 0 1 0	0.4088	17.2	2 2 0 0 1 0	-1.1311	102.6
2 2 0 1 1 0	0.0484	10.6	2 2 0 1 1 0	-0.0922	142.7
2 2 1 0 1 0	-0.1365	65.7	2 2 1 0 1 0	-0.0624	65.7

TABLE 8.3b

Principal Short Period Perturbations in i_s GEOS 3

Lunar Waves			Solar Waves		
Wave Type n m p q j g	Amplitude (10^{-4} arc secs)	Period (mins)	Wave Type n m p q j g	Amplitude (10^{-4} arc secs)	Period (mins)
2 0 1 0 0 0	-0.1468	50.02	2 2 0 0 0 0	-0.1104	50.00
2 0 1 0 2 0	-0.1468	50.02	2 2 0 0 2 0	0.2723	50.04
2 1 0 0 0 0	-0.2024	50.13			
2 1 1 0 0 0	0.1955	50.01			
2 2 0 0 0 0	-0.2394	50.12			
2 2 0 0 2 0	0.5874	49.92			
2 2 0 1 2 0	0.1128	49.85			

TABLE 8.4a

Principal Long Period Perturbations in Ω_s GEOS 3

Lunar Waves			Solar Waves		
Wave Type n m p q j g	Amplitude (arc seconds)	Period (days)	Wave Type n m p q j g	Amplitude (arc seconds)	Period (days)
2 0 0 0 1 0	0.0195	13.6	2 0 0 0 1 0	0.1213	182.6
2 0 1-1 1 0	-0.0211	27.6	2 0 1-1 1 0	-0.0391	365.3
2 0 1 1 1 0	0.0211	27.6	2 0 1 1 1 0	0.0391	365.3
2 0 2 0 1 0	-0.0195	13.6	2 0 2 0 1 0	-0.1213	182.6
2 1 0 0 1 0	0.1348	15.2	2 1 0 0 1 0	5.962	468.5
2 1 0 1 1 0	0.0160	9.8	2 1 0 1 1 0	5.956	1657.7
2 1 1 0 1 0	-0.2737	131.4	2 1 1 0 1 0	-0.1252	131.4
2 1 1 1 1 0	-0.0288	34.9	2 2 0 0 1 0	2.421	102.6
2 2 0 0 1 0	-0.0761	17.2	2 2 0 1 1 0	0.2577	142.7
2 2 1 0 1 0	0.2100	65.7	2 2 1 0 1 0	0.0961	65.7

TABLE 8.4b

Principal Short Period Perturbations in Ω_s GEOS 3

Lunar Waves			Solar Waves		
Wave Type	Amplitude	Period	Wave Type	Amplitude	Period
n m p q j g	(10^{-4} arc secs)	(mins)	n m p q j g	(10^{-4} arc secs)	(mins)
2 0 1 0 0 0	0.1621	50.02	2 1 0 0 0 0	0.1031	50.01
2 0 1 0 2 0	-0.1621	50.02	2 2 0 0 0 0	0.1219	50.00
2 1 0 0 0 0	0.2234	50.13	2 2 0 0 2 0	0.3006	50.04
2 1 1 0 0 0	-0.2158	50.01			
2 2 0 0 0 0	0.2643	50.12			
2 2 0 0 2 0	0.6485	49.92			
2 2 0 1 2 0	0.1245	49.85			

TABLE 8.5a

Principal Long Period Perturbations in M_s GEOS 3

Lunar Waves			Solar Waves		
Wave Type	Amplitude	Period	Wave Type	Amplitude	Period
n m p q j g	(arc seconds)	(days)	n m p q j g	(arc seconds)	(days)
2 1 0 0 1 0	0.2123	15.2	2 0 0 0 1 0	-0.0666	182.6
2 1 0 1 1 0	0.0254	9.8	2 0 2 0 1 0	0.0666	182.6
2 1 1-1 1 0	0.0188	22.8	2 1 0 0 1 0	6.9682	468.5
2 1 1 1 1 0	-0.0441	34.9	2 1 0 1 1 0	7.6734	1657.7
2 2 0-1 1 0	-0.0689	45.5	2 2 0 0 1 0	0.8636	102.6
2 2 0 0 1 0	0.7009	17.2	2 2 0 1 1 0	0.1469	142.7
2 2 0 1 1 0	0.0765	10.6			
2 2 1 1 1 0	0.0190	47.5			

TABLE 8.5b

Principal Short Period Perturbations in M_s GEOS 3

Lunar Waves			Solar Waves		
Wave Type	Amplitude	Period	Wave Type	Amplitude	Period
n m p q j g	(arc seconds)	(mins)	n m p q j g	(arc seconds)	(mins)
2 1 0 0 1-1	-0.1734	99.57	2 1 0 0 1-1	-0.0806	100.04
2 1 0 0 1 1	0.1750	100.49	2 1 0 0 1 1	0.0805	100.01
2 1 0 0 2-1	0.2277	33.29	2 1 0 0 2-1	0.1055	33.35
2 1 1 0 1-1	0.1688	100.08	2 1 1 0 2-1	-0.1010	33.35
2 1 1 0 1 1	-0.1686	99.98	2 2 0 0 1-1	-0.2082	100.10
2 1 1 0 2-1	-0.2209	33.35	2 2 0 0 1 1	0.2079	99.96
2 2 0 0 1-1	-0.4481	99.63	2 2 0 0 2-1	-0.1994	33.35
2 2 0 0 1 1	0.4518	100.44	2 2 0 0 2 1	0.0855	100.11
2 2 0 0 2-1	-0.4306	33.30			
2 2 0 0 2 1	0.1841	99.64			

TABLE 8.6a

Principal Long Period Perturbations in w_s GEOS 3

Lunar Waves			Solar Waves		
Wave Type	Amplitude	Period	Wave Type	Amplitude	Period
n m p q j g	(arc seconds)	(days)	n m p q j g	(arc seconds)	(days)
2 1 0 0 1 0	0.2766	15.2	2 1 0 0 1 0	12.7160	468.5
2 1 1 0 1 0	-0.6477	131.4	2 1 0 1 1 0	12.5603	1657.7
2 1 1 1 1 0	-0.0593	34.9	2 1 1 0 1 0	-0.2962	131.4
2 2 0-1 1 0	-0.0818	45.5	2 2 0 0 1 0	2.6867	102.6
2 2 0 0 1 0	0.7171	17.2	2 2 0 1 1 0	0.3466	142.7
2 2 0 1 1 0	0.0740	10.6	2 2 1 0 1 0	0.0689	65.7
2 2 1 0 1 0	0.1506	65.7			

TABLE 8.6b

Principal Short Period Perturbations in w_s GEOS 3

Lunar Waves			Solar Waves		
Wave Type	Amplitude	Period	Wave Type	Amplitude	Period
n m p q j g	(arc seconds)	(mins)	n m p q j g	(arc seconds)	(mins)
2 0 1 0 1 0	-0.1469	33.34	2 1 0 0 2-1	-0.1055	33.35
2 0 1 0 2-1	0.1469	33.34	2 1 1 0 2-1	0.1010	33.35
2 1 0 0 1-1	0.1734	99.57	2 2 0 0 1-1	0.2082	100.10
2 1 0 0 1 1	-0.1750	100.49	2 2 0 0 1 1	-0.2079	99.96
2 1 0 0 2-1	-0.2277	33.29	2 2 0 0 2-1	0.1994	33.35
2 1 1 0 1-1	-0.1688	100.08	2 2 0 0 2 1	0.0855	100.11
2 1 1 0 1 1	0.1686	99.98			
2 1 1 0 2-1	0.2209	33.35			
2 2 0 0 1-1	0.4481	99.63			
2 2 0 0 1 1	-0.4518	100.44			
2 2 0 0 2-1	0.4306	33.30			
2 2 0 0 2 1	-0.1841	99.64			

TABLE 8.7

Principal Perturbations in e_s GEOS 3

Lunar Waves			Solar Waves		
Wave Type	Amplitude	Period	Wave Type	Amplitude	Period
n m p q j g	($\times 10^{-8}$)	(mins)	n m p q j g	($\times 10^{-8}$)	(mins)
2 1 0 0 1-1	0.2102	99.57	2 2 0 0 1-1	0.2524	100.10
2 1 0 0 1 1	0.2121	100.49	2 2 0 0 1 1	0.2520	99.96
2 1 0 0 2-1	-0.2760	33.29	2 2 0 0 2-1	0.2417	33.35
2 1 1 0 1-1	-0.2046	100.08			
2 1 1 0 1 1	-0.2044	99.98			
2 1 1 0 2-1	0.2678	33.35			
2 2 0 0 1-1	0.5432	99.63			
2 2 0 0 1 1	0.5476	100.44			
2 2 0 0 2-1	0.5219	33.30			
2 2 0 0 2 1	0.2231	99.64			

TABLE 8.8

Principal Perturbations in a_e GEOS 3

Lunar Waves			Solar Waves		
Wave Type n m p q j g	Amplitude (cms)	Period (mins)	Wave Type n m p q j g	Amplitude (cms)	Period (mins)
2 0 1 0 0 0	2.2002	50.02	2 0 1 0 0 0	1.0063	50.02
2 0 1 0 2 0	2.2002	50.02	2 0 1 0 2 0	1.0063	50.02
2 1 0 0 0 0	1.3893	50.13	2 1 0 0 2 0	-1.5793	50.02
2 1 0 0 2 0	-3.4074	49.90	2 1 1 0 2 0	1.5132	50.03
2 1 1 0 0 0	-1.3421	50.01	2 2 0 0 2 0	2.9866	50.04
2 1 1 0 2 0	3.3087	50.03			
2 2 0 0 0 0	1.0657	50.12			
2 2 0 0 2 0	6.4437	49.92			
2 2 0 1 2 0	1.2377	49.85			

The main short period terms in the mean anomaly cancel with corresponding short period terms in the argument of perigee. Thus the position of the satellite from the ascending node of the satellite orbit has only slight perturbations due to the short period tidal terms.

Summing the corresponding short period terms for both the Sun and Moon, the tidal perturbations are shown in Figures 8.5. The graphs for these tidal perturbation calculations have the following orbital parameters,

$$a_s = 7207\ 000\ m$$
$$e_s = 0.0025$$
$$i_s = 115^o$$
$$\dot{\Omega}_s = 2.74^o/day$$
$$\Omega_s = 97.7^o$$
$$M_s = 149.4^o$$
$$w_s = 325.85^o$$
$$\text{epoch} = 0518\ UT\ \ 29.6.75$$

and the graphs are evaluated at 1½ minute intervals.

Figure 8.5a, which shows the short period effects in inclination and right ascension of the node have amplitudes of 0.8×10^{-3} arc seconds. While for the argument of perigee and mean anomaly, the maximum amplitude for this time span is approximately one arc second. The large amplitudes of the latter two orbital elements as compared to other short period elements is due to the term $G'_{njg}(e_s)$ in the tidal perturbation equations, being the derivative of $G_{njg}(e_s)$ with respect to e_s. Figure 8.5b shows graphs of short period terms for w_s and M_s, where the combination of the two will largely cancel the effects. These two elements have a complex nature consisting of a number of frequencies,whereas the elements i_s and Ω_s consist of one dominant wave. The graph for semi-major axis short period perturbations (Figure 8.5c) shows an amplitude of approximately 10 cm, and has a wave pattern similar to both the w_s and M_s elements. The eccentricity perturbation has been scaled by the semi-major axis, to show amplitudes of $a_s\ \delta\ e_s$.

The combination of short period and long period terms for the orbital elements i_s, Ω_s, w_s and M_s are shown in Figures 8.6 to 8.9 respectively. The perturbation in the inclination (Figure 8.6) has

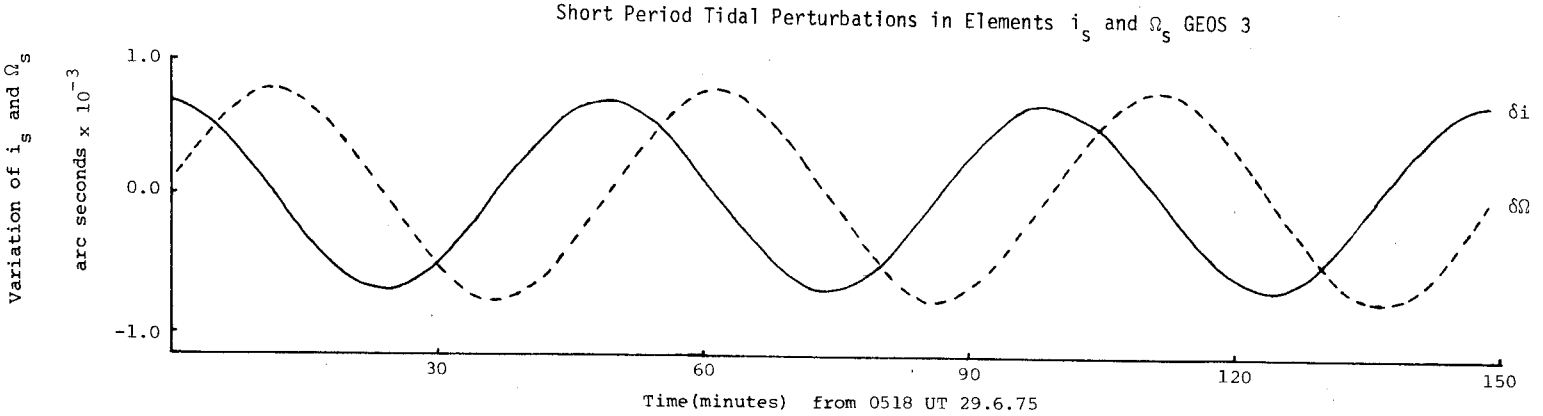

FIGURE 8.5a

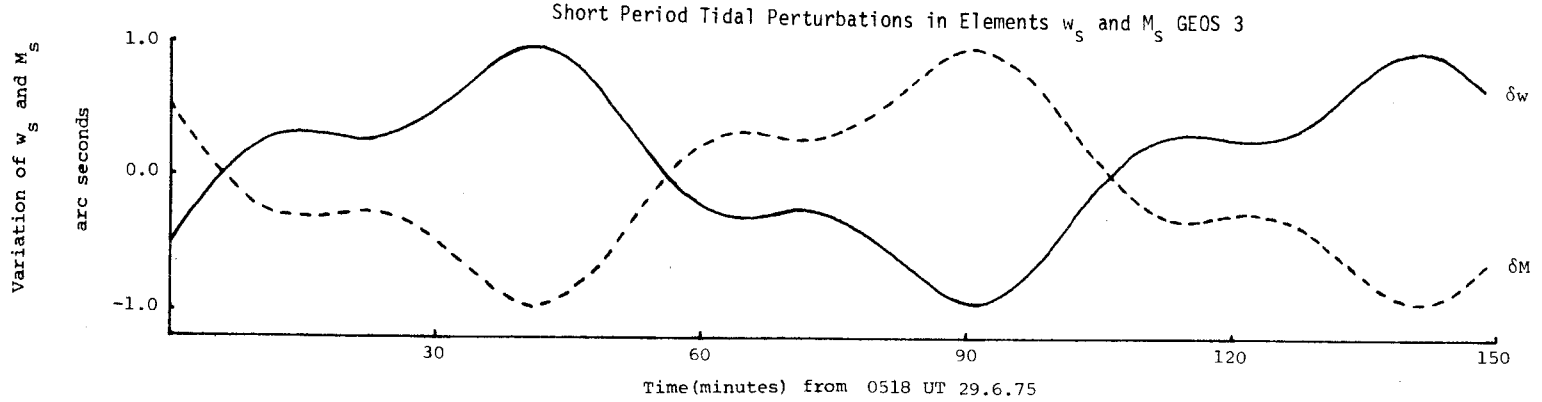

FIGURE 8.5b

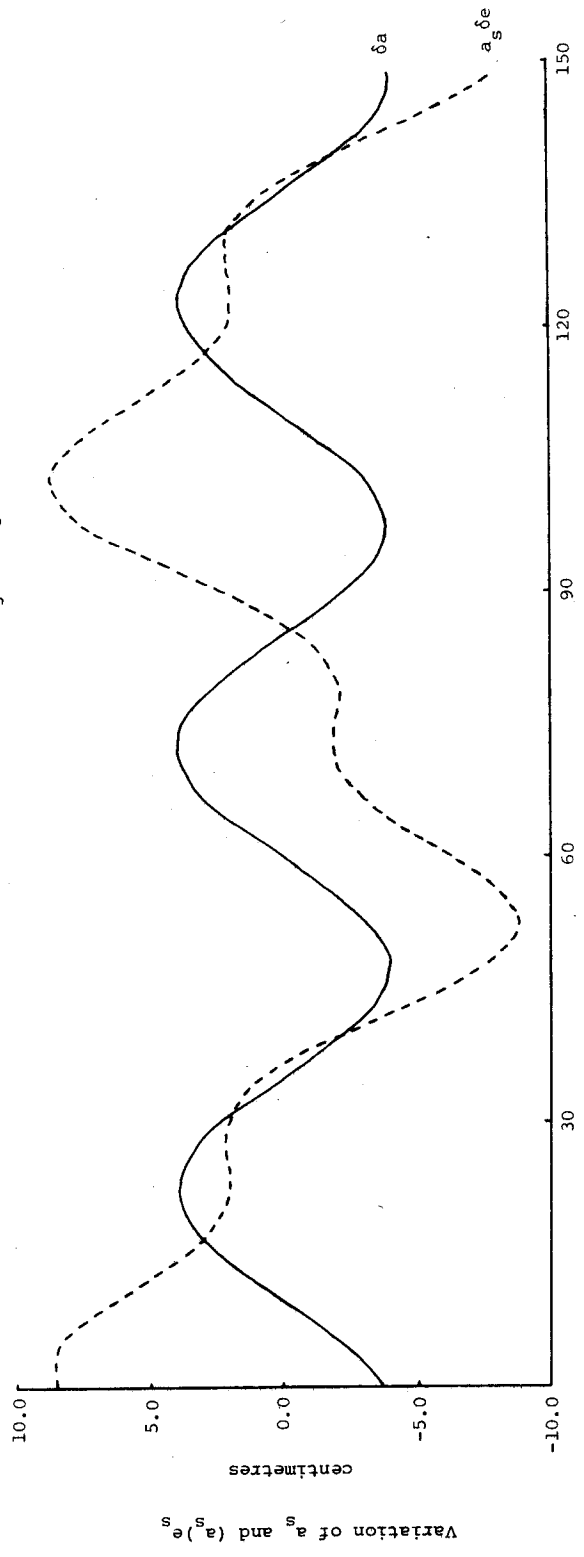

FIGURE 8.5c

Note: Variation of e_s scaled by semi-major axis a_s, to provide variations of $a_s \delta e$.

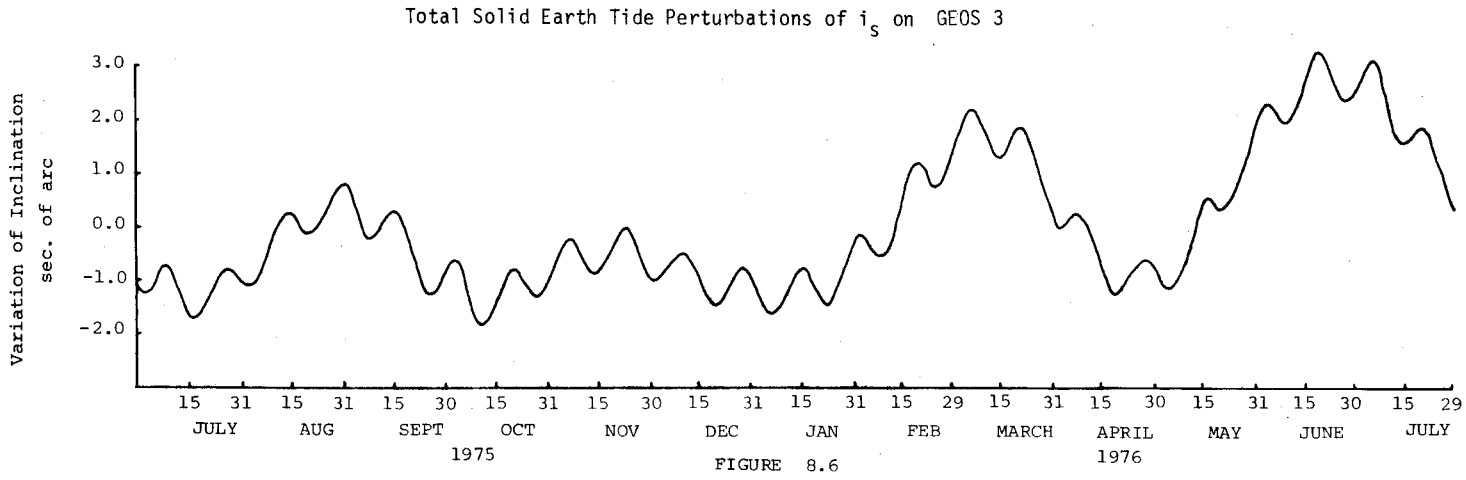

FIGURE 8.6

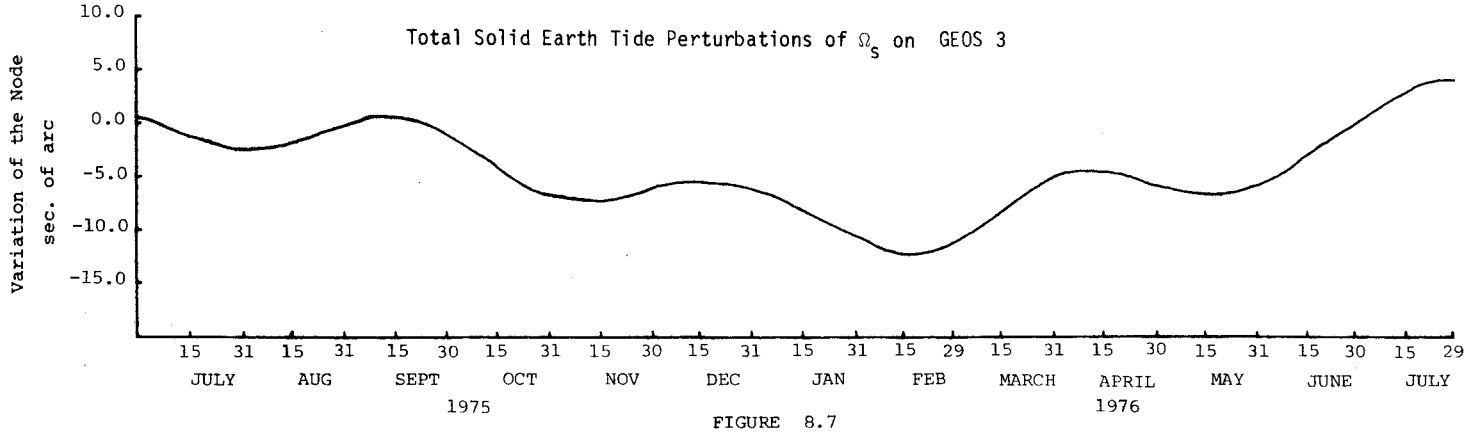

FIGURE 8.7

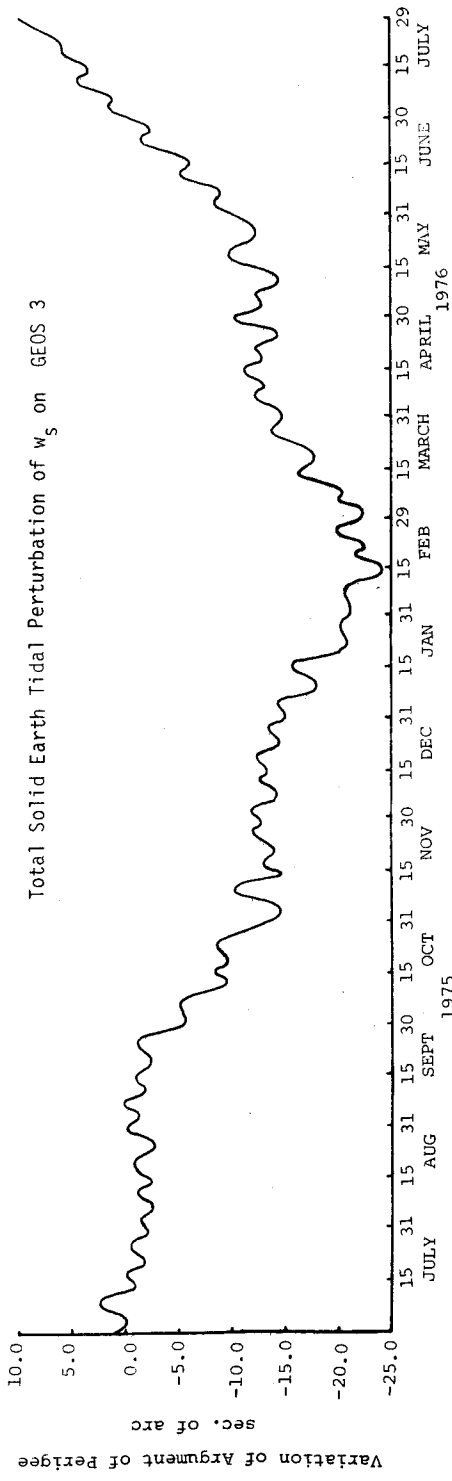

FIGURE 8.8

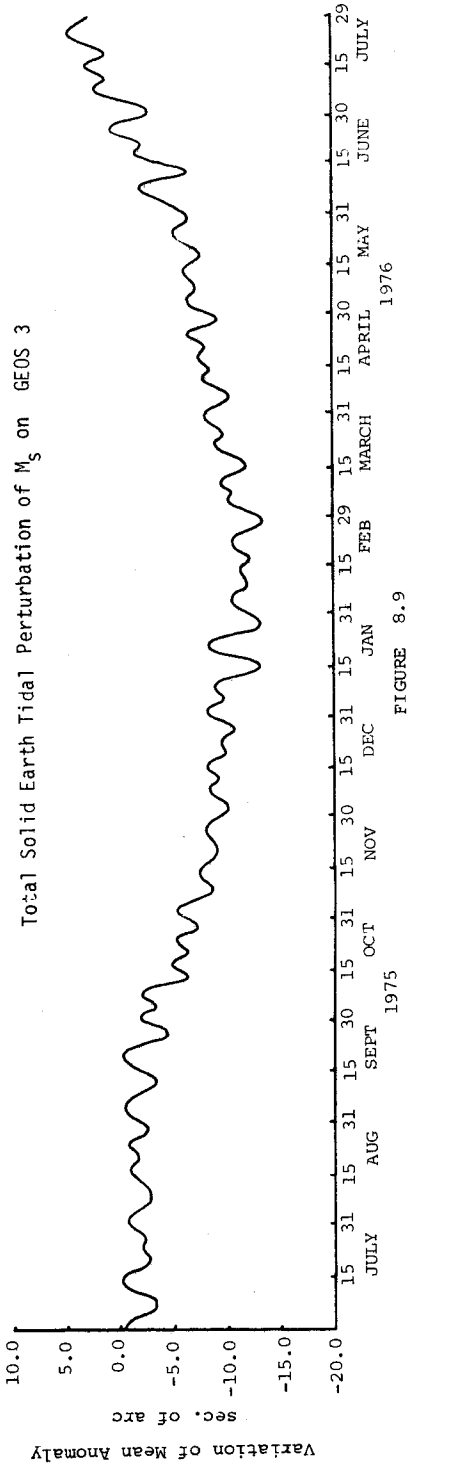

FIGURE 8.9

the same form as Figure 8.1d, and shows that the majority of the perturbation can be expressed by the six main tidal waves (see Table 8.2). The variation of the ascending node (Figure 8.7) shows a domination of a few frequencies of large amplitude. The perturbations in perigee and the mean anomaly (Figures 8.8 and 8.9 respectively) show a very complex pattern, due to the many long and short period terms influencing the instantaneous perturbation evaluations.

The results presented in this Section confirm that short period tidal terms need not be included in any Earth tide models for satellite perturbations. Perturbations in inclination and right ascension of the node for GEOS 3 have magnitudes of only milliseconds of arc, which are well within observational noise levels. Similarly, the perturbation in the eccentricity is small and the perturbation in the semi-major axis reaches a magnitude of 5 centimetres. However, a study on the orbital elements of the argument of perigee or mean anomaly does require the inclusion of short period tidal effects which have a magnitude of one arc second. Nevertheless, the position of the satellite along the orbital plane is only slightly perturbed due to the latter two orbital element perturbations.

This study of the GEOS 3 satellite shows the magnitude of tidal perturbations expected on the satellite. The latter study on the short period terms will be of importance in the following Chapter which discusses satellite altimetry measurements. This requires the instantaneous position of the satellite to be known, thus requiring short period effects to be studied. Satellite altimetry measurements are directly influenced by radial distance perturbations which are short period functions of the orbital elements: the eccentricity, semi-major axis and mean anomaly. The expected radial distance perturbations are discussed in the next Chapter.

In addition to these discussions, Chapter 9 contains information on the recoverability of the ocean tide signal from satellite altimetry, with the view of improving present ocean tide models for improved ocean loading calculations.

CHAPTER 9

SATELLITE ALTIMETRY STUDIES

9.1 Introduction

Current research in developing techniques for the Earth space position of the sea surface from satellite altimetry measurements, raises the possibility of obtaining useful information on the ocean tide signal on a global basis. Any improvements in the ocean tide model will not only give more reliable calculations of ocean loading on surface Earth tide measurements but also lead to more accurate satellite orbital perturbation calculations. The possibility of recovering the ocean tide signal from satellite altimetry is discussed in Section 9.2.

The ocean tide height can be recovered only if the accuracy of the radial component of the satellite orbit provides an acceptable signal-to-noise ratio. The Earth tide effects on various satellite parameters has been discussed in Chapters 7 and 8. The altimeter measurements give the radial distance from the satellite to the instantaneous sea surface, and thus would include Earth tide perturbations in the measurement. Such determinations will be discussed in Section 9.3.

Calculations presented in this Chapter are based on the GEOS 3 satellite, which has collected altimetry data since April 1975 over a large area of oceans between the parallels 65^{o}N and 65^{o}S.

9.2 Ocean Tide Models from Satellite Altimetry

9.2.1 Introduction

The possibility of obtaining information on the global ocean tide signal is dependent on the frequency and quality of altimetry measurements. If these conditions are met the ocean tide signals can be used to obtain regional and global models of the oceans, in areas where conventional tide gauges cannot be placed. This will possibly give a more realistic representation of the world's oceans, than that obtained from the conventional tidal models from coastal recordings. Such determinations will also be a useful supplement to pressure sensor data collected at the sea floor (SNODGRASS 1968).

The work in the following sections numerically investigates the possibility of recovering ocean tide models successfully from satellite altimetry measurements over a specific region of the ocean and from a limited number of satellite passes. Due to the scarcity of data at the present time from the GEOS 3 mission, no practical analysis has yet been carried out. However conclusions can be drawn concerning the reliability of analyses based on such data sets using criteria for acceptable levels of the signal-to-noise ratio. This ratio is a function of the magnitude and nature of errors in the satellite altimeter and satellite orbit. Such errors are a major contribution to the noise in the satellite altimetry measurements.

A similar study based on the problem of recovering the tidal signal from satellite altimetry was undertaken by ZETLER & MAUL(1971) using coastal tidal data for a region around the United States. This study will deal with an area within the Coral Sea, north-east of Australia. This area is chosen because it is the site of an experiment on the present GEOS 3 mission which should finish a number of high energy mode satellite altimetry passes in the region. The area is also interesting with regard to sea surface topography research, and other investigations involving Earth tides in the surrounding areas (see LEPPERT ET AL 1975).

The method of analysis involves a satellite - borne altimeter transiting a particular oceanic area and obtaining altimeter measurements to the instantaneous sea surface. The sea surface height above the reference ellipsoid can be obtained after correcting for the biases and for the satellite height above the reference ellipsoid. The geometry of such a transit is seen in Figure 9.1. The distribution of altimetry measurements from the satellite for this specified region is determined by the orbital characteristics of the satellite and the duration of the altimeter measurements. The sea surface heights of the same area as obtained from several such passes, can be analysed for the major harmonic constituents of the ocean tides. The data sampling rate in conventional tidal analyses is one per hour. In the case of the recovery of tidal signal from GEOS 3 satellite altimetry data, the sampling rate is one per several days.

To estimate the viability of such a process, the ocean tide amplitudes of the main harmonic constituents at a specific point in the Coral Sea region where obtained from cotidal-corange charts. Thus a good estimate of the tidal height can be obtained at any instant. The tidal height is then degraded by progressively adding levels of white noise and the data is re-analysed at each noise level. The recoverability at each noise level is then compared with the signal-to-noise ratio and thus provides an estimate of the amount of noise tolerable for the successful recovery of ocean tide signals. A discussion of the errors associated with satellite altimeter measurements is found in Section 9.2.3.

9.2.2 Analysis of Altimeter Measurements

Due to the orbital characteristics of the GEOS 3 satellite and the limited duration of the altimeter measurements in the Coral Sea, it was decided to consider a $5^{o} \times 5^{o}$ ocean square, for the analysis. Thus whenever an altimeter measurement is taken within a specified $5^{o} \times 5^{o}$ ocean square, it constitutes an observation.

The consecutive observations are obtained after a lapse of 5 days for south-north or north-south passes, or $2\frac{1}{2}$ days for either type of pass. The observations themselves have noise associated with them, and are largely due to errors in the orbit determinations. There is also the high probability that the errors for a north-south pass are different from those for a south-north pass due to errors in both the tracking station coordinates as well as the gravity field model held fixed during the orbit integration. These conditions will provide approximately 20 north-south and 20 south-north altimeter measurements for each $5^{o} \times 5^{o}$ block that is used in the analysis over a period of 3 months.

In a harmonic development of the ocean tide at a point in the ocean, 95% of the total tidal energy can be expressed by five constituents. These are M_2 and S_2 in the semi-diurnal waves and K_1, O_1 and P_1 in the diurnal waves. The amplitudes and phases for these five principal waves in the ocean tide were extracted from cotidal-corange charts of the Coral Sea and are expressed in Table 9.1.

Wave	Amplitude (cm)	Phase (degrees)	Percentage of wave amplitude to total tidal amplitude	Model and Source
M_2	100	240	70%	Zahel (KUZENTSOV 1972)
S_2	10	290	7%	Tiron (TIRON ET AL 1967)
K_1	15	50	11%	Zahel (ZAHEL 1973)
O_1	10	10	7%	Tiron (TIRON ET AL 1967)
P_1	7	90	5%	Estimate

TABLE 9.1
Wave Amplitudes and Phases from Cotidal-Corange Charts
of a Point in the Coral Sea
(Location: ϕ - 15^{o}N, λ 160^{o}E)

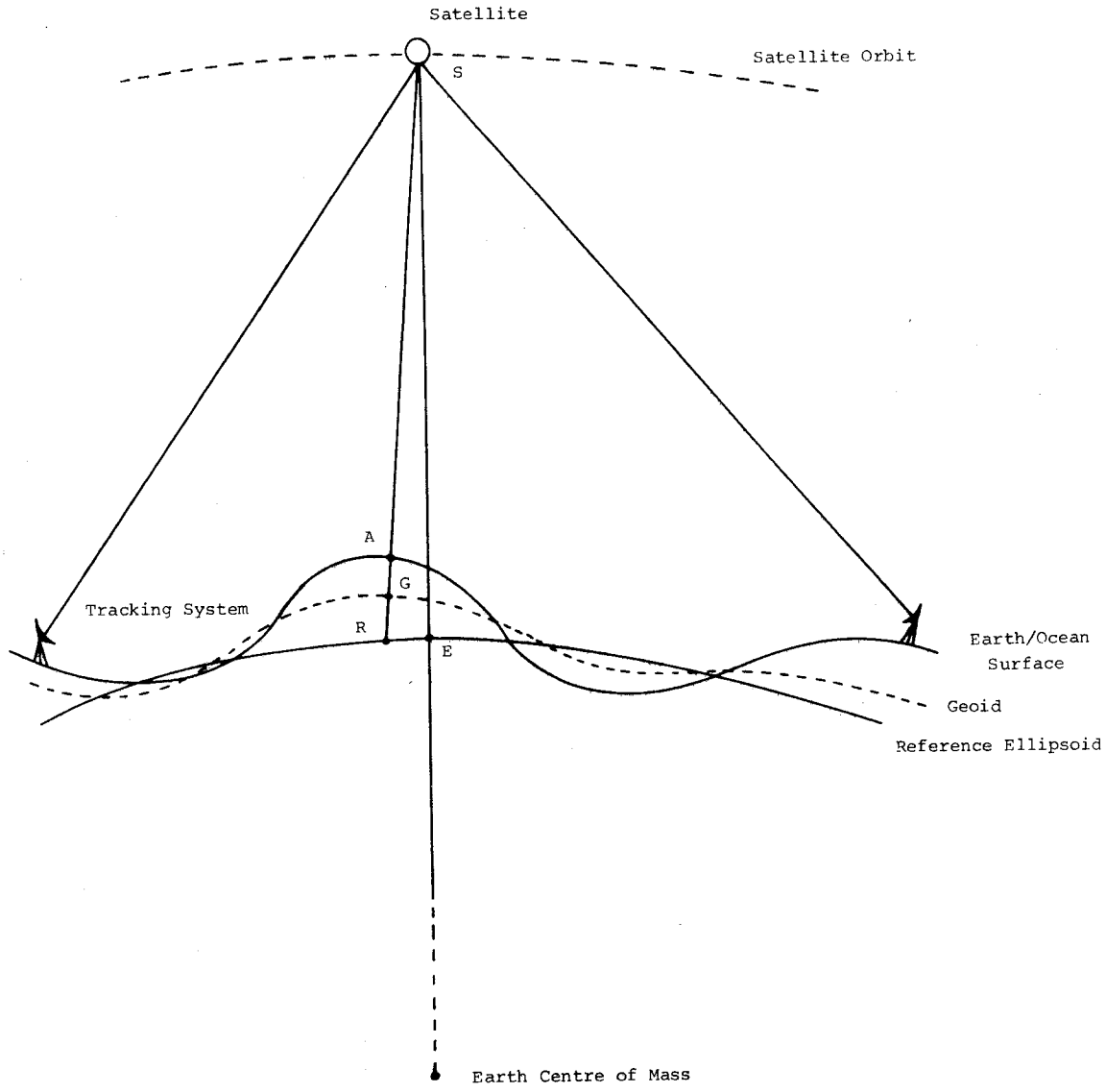

FIGURE 9.1

The Relationship between Satellite Altitude Measurements

where SE is the satellite height above a reference ellipsoid, obtained from the satellite orbit determined from tracking data,

SA is the satellite altitude measured by the altimeter,

AG is the dynamic ocean effect of tides, winds and currents (or tide height),

GR is the geoid height, and

AR is the sea surface height.

These waves, then give a maximum tidal range of 284 centimetres. In the Coral Sea, the M_2 wave accounts for a half to three-quarters of the tidal range while the other four constituents average approximately 10% each.

Any ocean tide constituent can be expressed as

$$A \cos (w_a t - \alpha_a) \tag{9.1}$$

where A is the amplitude, t is the time, w_a is the speed of the wave, and α_a is the phase lag. The above equation can also be expressed as

$$X \cos w_a t + Y \sin w_a t \tag{9.2}$$

where $X = A \cos \alpha_a$,
$Y = A \sin \alpha_a$,
$A^2 = X^2 + Y^2$, and
$\tan \alpha_a = Y/X$.

Thus, the ocean height ζ obtained from altimeter measurements can be expressed as

$$\zeta = \sum_{i=1}^{n} (X_i \cos w_{ai} t + Y_i \cos w_{ai} t) + C \tag{9.3}$$

where C is the sum of all errors and any zero degree terms in the ocean height measurements. In this study, n is limited to 5.

To commence the investigation, twenty 'error-free' observations of ζ were produced over a 3 month period corresponding to the GEOS 3 orbit. The ocean height was calculated from values of amplitude and phases in Table 9.1.

In the initial analysis the observations were not contaminated with noise. A zero degree term was included so that all altimeter determined ocean heights were large positive values. In successive analyses the amplitudes and phases of the five waves were determined from the X_i and Y_i values given the ocean heights.

The level of the noise is then increased by systematically adding controlled amounts of white noise which simulates observational and orbital errors to the altimeter ranges. The signal-to-noise ratio is decreased, thereby degrading the quality of the values obtained for the tidal amplitudes and phases on analyses. The noise levels vary from 0% to 100% of the total tidal range of 284 centimetres (see Section 9.2.4).

The white noise was generated by a random number program, ranging from zero to a preset maximum which was determined by the percentage of noise to the tidal range required. Ten analyses were completed at each noise level in order to obtain an unbiased indication from the random number process.

9.2.3 Error Sources in Satellite Altimetry

Due to the relationship between the radial satellite height and the sea surface height as seen in Figure 9.1, any radial orbit errors will propagate directly into errors in the sea surface heights and thus the tide heights and geoid heights. In the analysis, the observational data used will be the sea surface height, with the geoid height unknown, and will be treated as constant over a small area and thus a zero degree term. Therefore for the analysis and evaluation of any altimeter data it is necessary to obtain the most accurate orbit possible from the available tracking data.

The error sources in the altimetry can be divided into a number of classifications and sources (McGOOGAN ET AL 1975), being errors due to instrumentation factors, pointing, ocean surface, atmospheric causes, and orbit uncertainties. Only a brief description will be given here of the errors. A full description of altimeter operations and characteristics, in addition to error sources can be found in McGOOGAN ET AL (1974) and McGOOGAN ET AL (1975).

A summary of the error sources and their magnitudes can be found in Table 9.2.

	Uncorrected Magnitude	Error Source	Corrected Data Residuals
Instrument Errors Systematic	Up to 50 m	Zero set error, discriminator drift, servo unbalance, operating parameter changes	<10 m (Correcting for operating parameters only)
	1 cm	Timing errors	1 cm (No correction)
	30 cm	Transit Time Error	<1 cm
	Up to 40 cm	Dynamic Lag Error	<10 cm (Using waveform analysis during high dynamic conditions)
	1 cm	Scaling Factor . Oscillator Frequency Error . Velocity of Light Error	1 cm (No correction)
Random	Up to 70 cm	Height Thermal Noise	30 cm (Where features permit more averaging can be applied)
	1 to 5 cm	Quantising Error	
Pointing	Up to 30 cm	Off Nadir Pointing	<1 m (If trailing edge is used to generate off nadir position)
Ocean Surface	Up to 75 cm	Electromagnetic MSL vs MSL	<10 cm (If waveheight is known to 25%)
Atmosphere	Up to 2 m	Atmospheric refraction path delay	<10 cm (If temp., pressure and humidity are known)

TABLE 9.2

Typical System Error Model and Residuals

Source: McGOOGAN ET AL(1975)

9.2.3.1 Instrumental Errors

These include instrument bias, timing bias, transit time corrections, dynamic lag error, and random errors.

One of the largest instrumental errors is bias. This is a zero set error or initial alignment error and is a fixed bias, and can usually be eliminated by field calibration. The bias errors change if the operating parameters change, but the changes can be recognised and corrected. The zero set error can also change slowly due to any system drift, but are usually small and can be easily eliminated.

Timing bias errors are mostly a consequence of time lag in relation to true Greenwich Mean Time (GMT) and the altimeter processor time delays. The time lag error is the bias between the satellite time system and GMT. The altimeter processer time delay correction is largely due to the delay characteristics of the on-board averaging operation.

Transit time errors are errors due to "measure time" lags with the altimeter pulse arriving at the Earth's surface, and is small in amplitude.

Dynamic lag error is the error associated with the satellite altimeter in following the relative motion of the ocean surface undulations and the satellite height variations. These errors can be corrected for and are usually small.

Finally, random errors are primarily made up of a quantising error and the thermal noise of the satellite altimeter.

9.2.3.2 Other Errors

Pointing errors in the altimeter arise when the altimeter is not pointing to the nadir. For small angles, it affects the altitude bias, but can be corrected. For GEOS 3 the angle is ±1 degree. If the pointing errors are large, the signal has to be filtered.

Ocean surface errors are biases caused by the difference between the true mean sea level and the mean point that the altimeter measures. Also atmospheric errors arise from the refraction in the atmosphere, but can be modelled.

In addition to errors associated with the altimeter, there are inherent errors due to the orbit fit, because the orbit is a reference for the altimeter measurements. This is one of the largest sources of error and has in the past been estimated to be under ten metres. This figure is considered to be optimistic in regions where no direct tracking is available.

9.2.4 Results on the Recovery of Ocean Models

To represent the residual amplitude and phase (see last paragraph Section 9.2.2) from the 'true' amplitude and phase, the modulus of the residual vector was computed for each solution and normalised by dividing by the amplitude obtained from corange charts. The modulus of the residual vector is denoted by $\langle R \rangle$, the corange amplitude by ζ_a, and the amplitude obtained by each solution ζ_s. These conventions can be seen in Figure 9.2, while the means and standard deviations of the normalised residuals are presented in Table 9.3 and in Figure 9.3.

In the analysis, the M_2 constituent proved to be the most reliably determined, due to its dominant tidal amplitude. The phase of M_2 could be recovered to ±10 degrees if the noise level was 20% of the tidal signal and to ±20 degrees at a noise level of 40%. The amplitude of the M_2 tide was recoverable with an error of 20% if the noise was at the 40% level. This meant the noise level was approximately equal to the amplitude of the M_2 constituent.

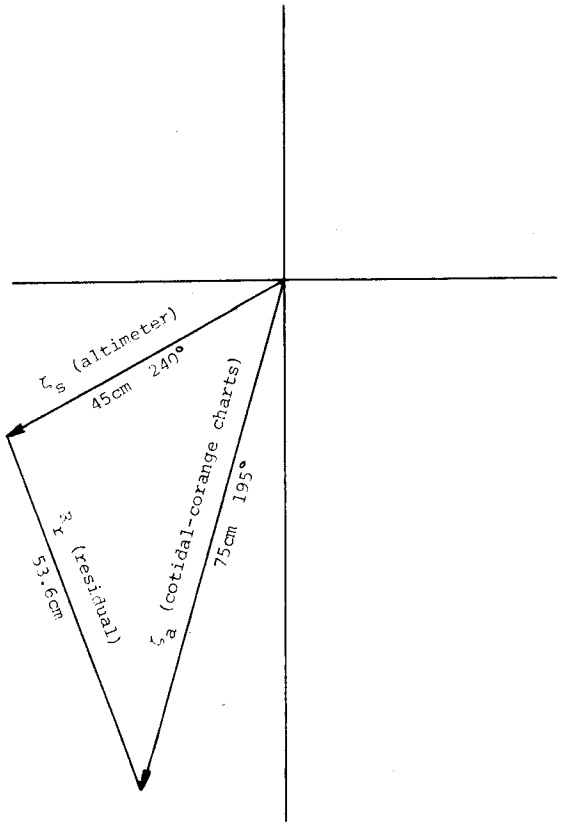

FIGURE 9.2

Sample graphical determination of the residual amplitude <R>. If the vector, ζ_a from corange-cotidal charts has an amplitude of 75 cm and phase 195°, and the vector from the analysis gives an amplitude of 45 cm and phase 240°, then the modulus of the residual vector, R_r is 53.6 cm. <R> is defined as R_r/ζ_a.

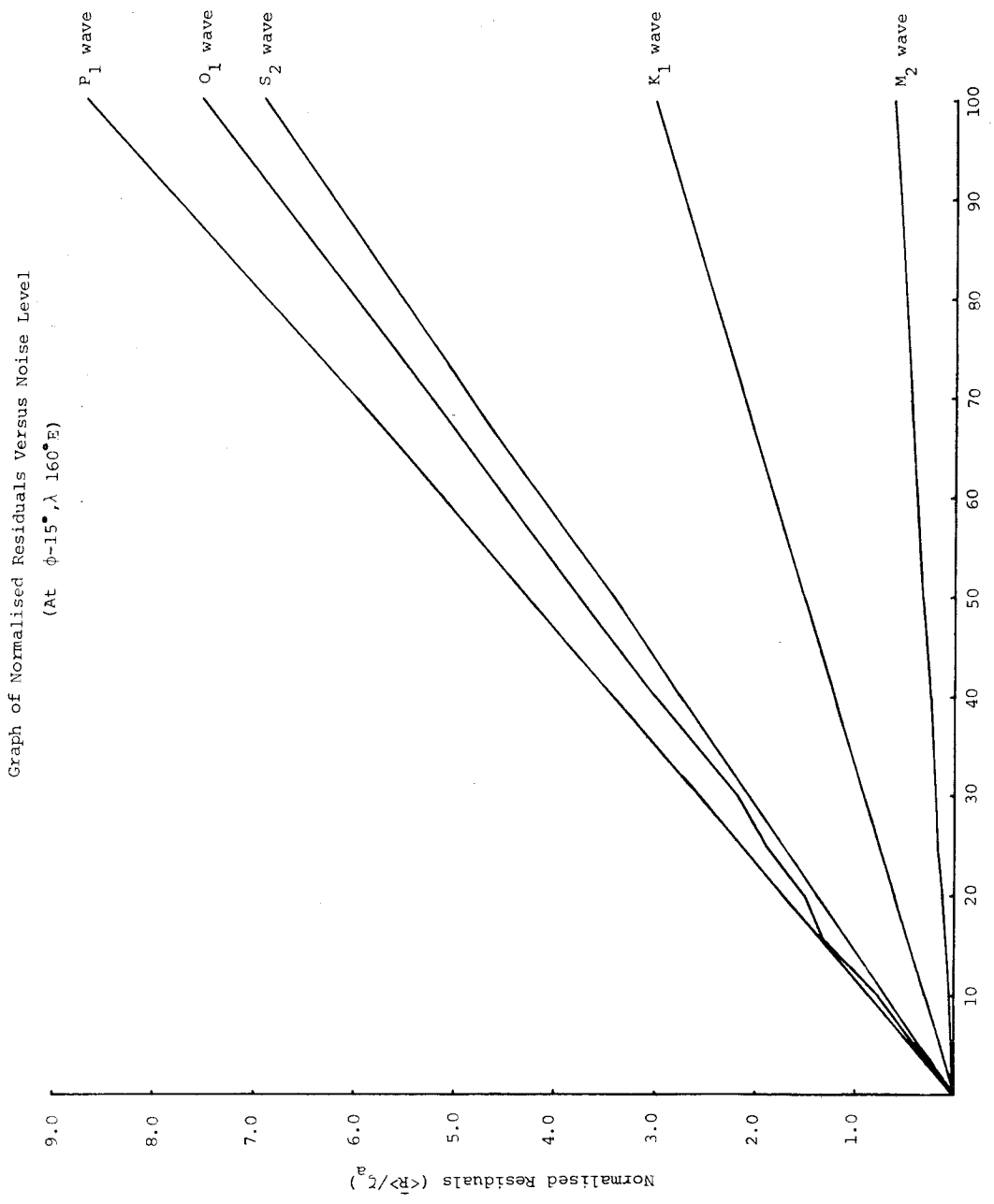
Graph of Normalised Residuals Versus Noise Level
(At ϕ-15°, λ 160°E)
P1 wave
O1 wave
S2 wave
K1 wave
M2 wave
Normalised Residuals (<R̃>/σa)
9.0
8.0
7.0
6.0
5.0
4.0
3.0
2.0
1.0
10
20
30
40
50
60
70
80
90
100
Percentage Noise

FIGURE 9.3

Graph of Normalised Residuals Verus Noise Over Wave Amplitude

(At ϕ -15°, λ 160°E)

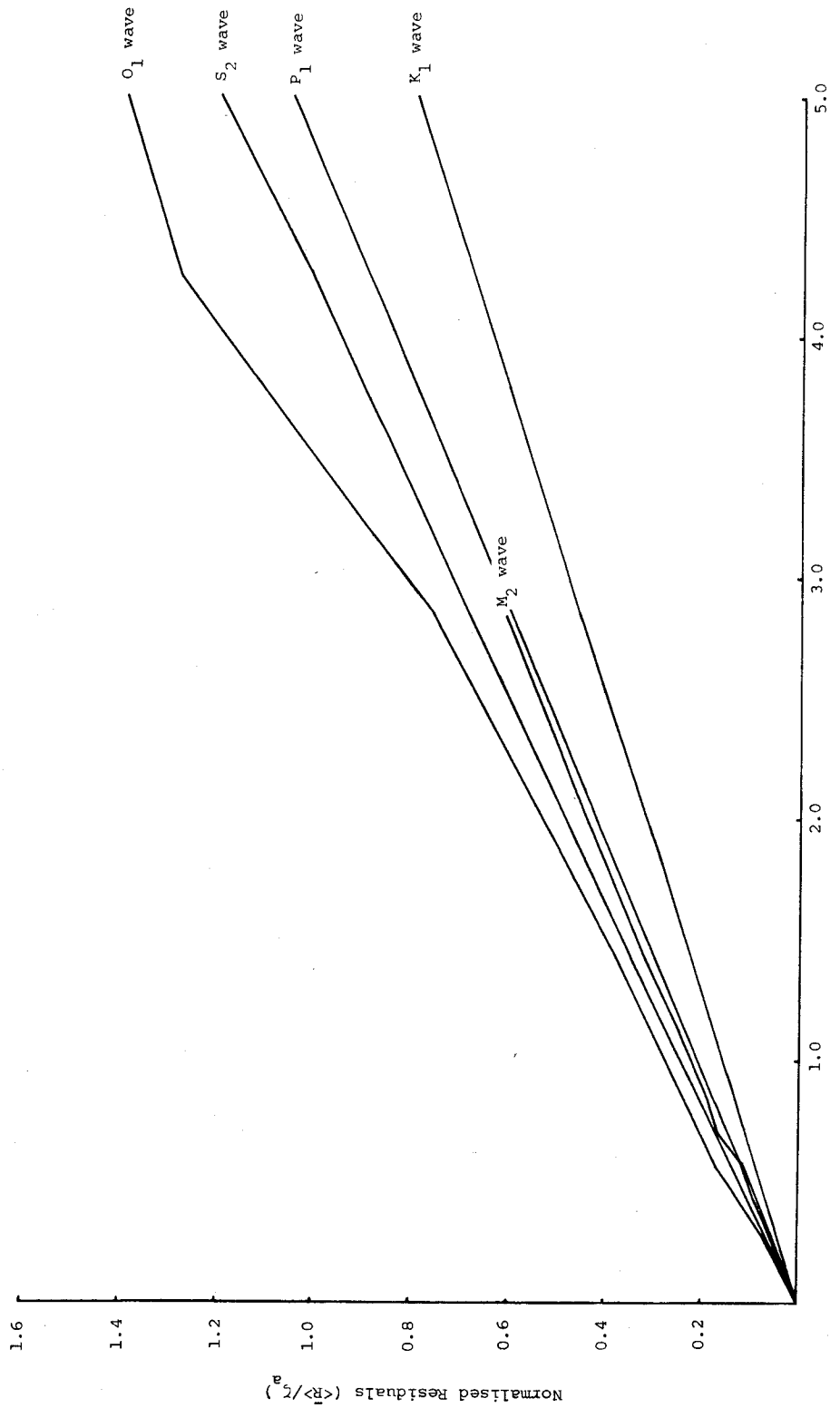

FIGURE 9.4

With the other waves, the percentage of tolerable noise decreased noticably, due to their small amplitudes as compared to the total tidal range. The waves were recoverable with errors around 20% of the signal in the presence of noise on the 5% level in the total tidal range. This level of noise corresponds to approximately the amplitude of the constituent waves.

Noise Level % of tidal range	Noise Level cm	M_2 wave $\langle\bar{R}\rangle/\zeta_a$	M_2 wave $\sigma_{S.O.}$	S_2 wave $\langle\bar{R}\rangle/\zeta_a$	S_2 wave $\sigma_{S.O.}$	K_1 wave $\langle\bar{R}\rangle/\zeta_a$	K_1 wave $\sigma_{S.O.}$	O_1 wave $\langle\bar{R}\rangle/\zeta_a$	O_1 wave $\sigma_{S.O.}$	P_1 wave $\langle\bar{R}\rangle/\zeta_a$	P_1 wave $\sigma_{S.O.}$
0.0		0.0		0.0		0.0		0.0		0.0	
< 0.5	< 1.4	0.004	.001	0.035	.025	0.015	.005	0.039	.026	0.042	.018
< 1.0	< 2.8	0.006	.003	0.069	.051	0.030	.015	0.075	.053	0.084	.033
< 2.0	< 5.7	0.013	.006	0.14	.10	0.06	.03	0.17	.14	0.17	.07
< 5.0	< 14.2	0.03	.01	0.35	.25	0.15	.08	0.38	.26	0.43	.16
< 10.0	< 28.4	0.06	.03	0.69	.51	0.30	.16	0.76	.53	0.86	.31
< 15.0	< 42.6	0.09	.04	1.04	.77	0.46	.24	1.29	.93	1.29	.46
< 20.0	< 56.8	0.13	.06	1.39	1.02	0.61	.32	1.51	1.05	1.72	.62
< 25.0	< 71.0	0.17	.10	1.73	1.28	0.76	.39	1.89	1.31	2.15	.77
< 30.0	< 85.2	0.19	.09	2.08	1.53	0.92	.47	2.17	1.65	2.57	.93
< 40.0	<113.6	0.25	.12	2.78	2.04	1.22	.63	3.03	2.10	3.44	1.24
< 50.0	<142.0	0.32	.15	3.43	2.60	1.52	.79	3.78	2.62	4.30	1.53
< 70.0	<198.0	0.44	.21	4.87	3.59	2.13	1.10	5.28	3.70	6.02	2.16
<100.0	<284.0	0.63	.30	6.94	5.11	3.04	1.58	7.57	5.24	8.74	3.19

TABLE 9.3

Normalised Residuals and Standard Deviations

Notes: $\langle\bar{R}\rangle/A$ is the mean of 10 values of the normalised residuals

$\sigma_{S.O.}$ is the standard deviation of a single observation

Based on data at ϕ - 15°N, λ 160°E

The relationship between the normalised wave residuals and the noise level with respect to each constituent wave amplitude is shown in Figure 9.4. This graph shows that the dependence of capacity for recovery to the noise is based on the constituent wave amplitude.

Thus, if the noise level of the altimetry is one metre in the Coral Sea area, the M_2 tide is recoverable. Further discussions on this subject are found in Section 9.4 and in Chapter 10.

The recoverability of any tidal signal is enhanced if the noise level is reduced. This reduction can be obtained by the elimination of any perturbations in the altimetry measurements. One of these perturbations, Earth tides is discussed in the following Section, 9.3.

9.3 Earth Tide Effects on Satellite Altimetry

9.3.1 Introduction

The satellite orbital parameter directly influencing the satellite altimeter measurement is the radial distance. Other parameters influence the altimeter measurements (see Section 9.2.3) but can usually be

eliminated. The following discussion will involve the type and magnitude of the Earth tide perturbation present in altimeter measurements.

9.3.2 Determination of Radial Perturbations

The theorical development follows from Section 7.2.2.

The perturbation in the radial distance δr, to the satellite can be expressed as

$$\delta r = \frac{r_s}{a_s} \delta a - a_s \cos E_s \delta e + \frac{a_s^2 e_s \sin E_s}{r_s} \delta M \qquad (9.4)$$

where E_s is the eccentric anomaly of the satellite, a_s is the semi-major axis of the satellite orbit, e_s is the eccentricity of the satellite orbit, while δa, δe and δM are the perturbations in the semi-major axis, eccentricity and mean anomaly of the satellite.

The expression for δr includes both long period and short period terms for the contributing orbital elements. The perturbations in δa and δe (see Section 7.2.2) have short period terms only, while δM has both long period and short period terms.

The eccentric anomaly is related to the mean anomaly by

$$M_s = E_s - e_s \sin E_s \qquad (9.5)$$

Due to the presence of the $\sin E_s$ term and the short period perturbations in a_s and e_s in equation 9.4 all radial distance perturbations are of short period. In addition, to solve for all radial distance perturbations long period terms in the mean anomaly have to be included in the analysis. Thus the total radial displacement at any instant is dependent on the long period mean anomaly terms.

A perturbation in the eccentricity or semi-major axis causes a change in the geometry of the satellite orbit. While a perturbation in the mean anomaly, can be compared to a timing error, where the satellite is presumed to be at a position S_1 in the orbit model used, but due to a tidal perturbation in the mean anomaly, the satellite is actually at a position S_2 (see Figure 9.5). This introduces an error in the radial distance to the satellite. The perturbation is relative to the model being adopted, and while different forcing functions will produce different perturbations in the radial distance, due to perturbations in the mean anomaly, the radial distance from the satellite ellipse centre will not alter between the different models.

Graphs for the perturbations in the radial distance are shown in Figure 9.6. Figure 9.6a shows the perturbations at an epoch on the 29.6.75, while Figure 9.6b has an epoch of 30.9.75. In both cases the graphs have a time span of 150 minutes. The full lines represent the radial perturbations due to short period terms in a_s, e_s and M_s, while the broken line represents the radial perturbations due to short period terms in a_s, e_s and M_s together with the long period terms in M_s. In the interval of 150 minutes the short period terms a_s, e_s and M_s contribute a range of about 5 cms, while the long period terms in M_s contribute a range of 20 cms in Figure 9.6a and 70 cms in Figure 9.6b.

The dominant terms in each contributing element are shown in Table 9.4. The perturbations in the radial distance can reach a maximum range of 20 cm for the short period contributing terms, depending on the configuration of the elements. The total radial distance perturbation reaches a maximum of one metre, due predominately to the long period perturbations in the mean anomaly.

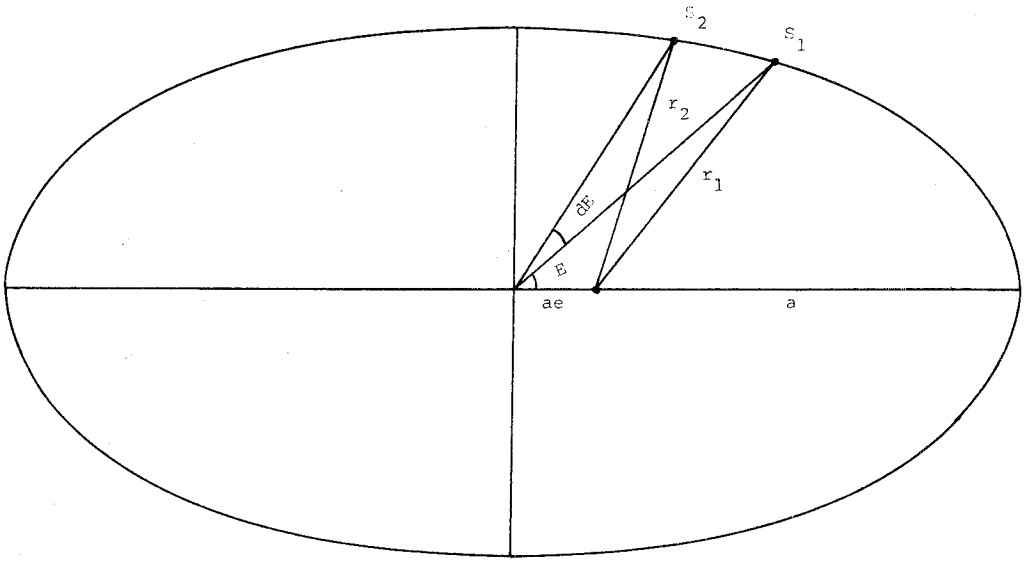

FIGURE 9.5

Satellite Perturbations in Radial Distance

TABLE 9.4

Tidal Perturbations in Radial Distance GEOS 3

Perturbation in Element	Resultant Perturbation in r_s		Period
	Dominant solar tidal amplitude	Dominant lunar tidal amplitude	
a_s	3 cm	6 cm	50 mins.
e_s	2 cm (0.25×10^{-8} in e_s)	4 cm (0.54×10^{-8} in e_s)	less than 100 mins.
M_s	2 cm (0.21" in M_s)	4 cm (0.45" in M)	less than 100 mins.
M_s	67 cm (7.6" in M_s)	6 cm (0.7" in M_s)	Long Period. For solar terms has periods of 468 and 1657 days.

9.3.3 Orbit Determinations

In the previous Section, it was necessary to distinguish between short period and long period terms. In the following Sections, it is necessary to determine if such perturbations need to be included

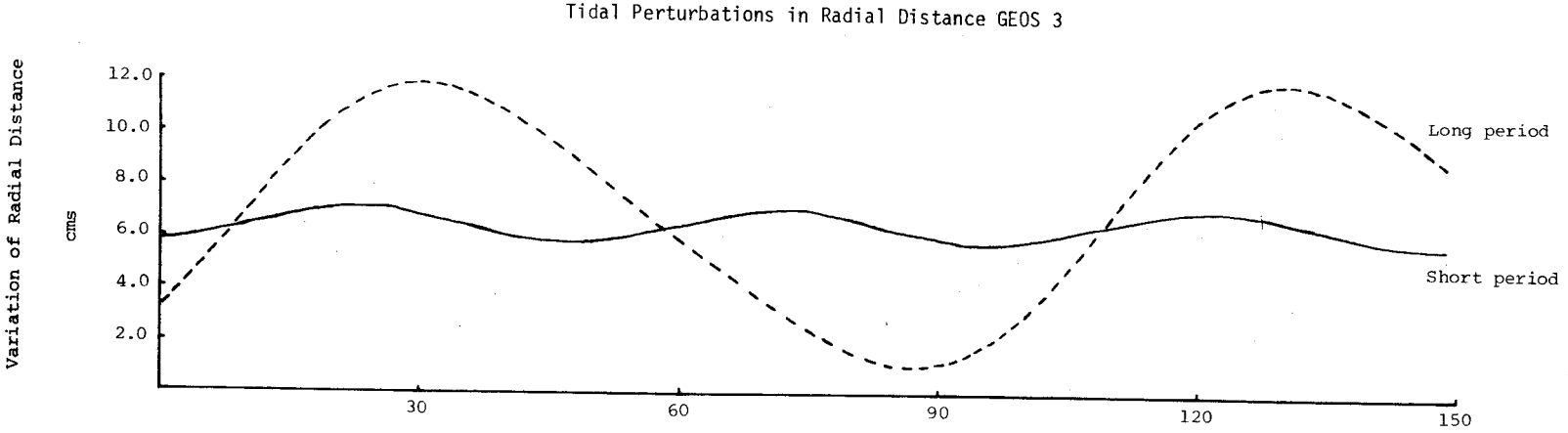

FIGURE 9.6a

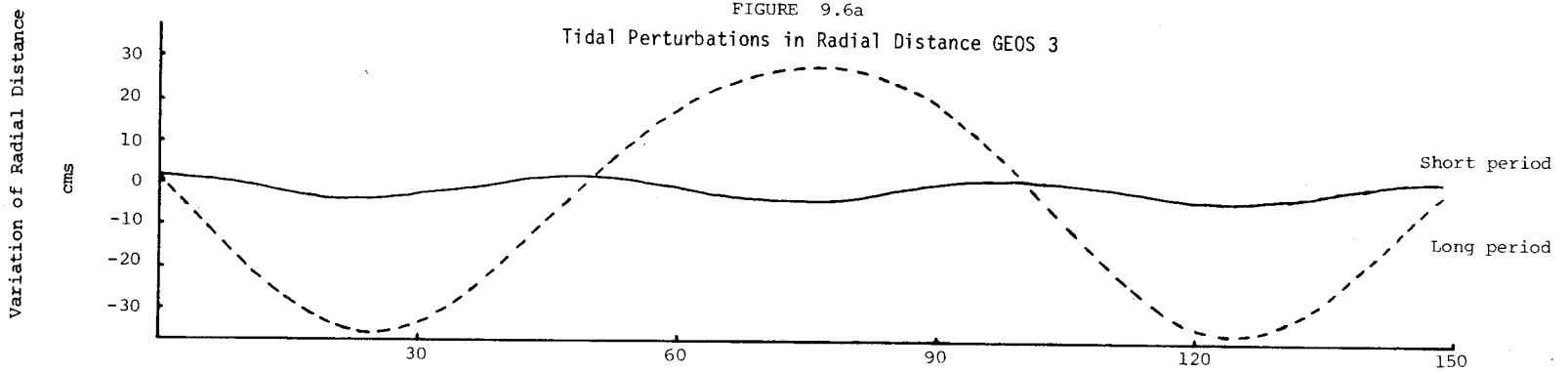

FIGURE 9.6b

in altimetry reductions and to determine if any perturbations have been indirectly included in the orbit determination models. Such a decision reduces to a choice between short period terms in a_s, e_s and M_s or both short period and long period terms in a_s, e_s and M_s in the radial distance perturbation calculations.

The inclusion of the long period terms is dependent on the method of the determination of the satellite orbital parameters from observational data, which will be outlined below.

In computations for the satellite orbit, observational data is collected for several passes and the orbital parameters determined by computation. These 'short arcs' are forced to absorb any unmodelled perturbations such as Earth tides into the orbital parameters.

In any analysis of Earth tide perturbations on satellite orbits, a longer time span is adopted. An arc of observational data is selected so that it is long enough for the tidal perturbations to reach significant amplitudes and if possible, time for a full cycle of the most dominant term. This is termed a 'long arc'. This is divided into shorter arcs and orbits are determined from the observational data for both the long and short arcs. Comparing the short arcs with the long arc parameters is basically equivalent to comparing observation with theory. The short arcs represent the true orbit at each of the observation points. The 'theoretical' orbit is produced by fitting one orbit to all the data covered by the short arcs. If the long arc covers sufficient time, the analysis will average through perturbations that are not accounted for in the integration of the orbit and it then becomes equivalent to the theoretical orbit. The short arcs are unable to average through any unmodelled perturbations that have periods longer than the time span of the arc. Subtracting the orbital parameters of the long arc from the parameters of the short arcs, therefore reveals perturbations that are not computed in the long arc as well as errors in the force models.

9.4 Conclusions

Conditions for the successful recovery of tidal singals from satellite altimetry measurements are dependent on the signal-to-noise ratio and this is a function of the particular tidal signal considered. If a result is required with 80% reliability, the noise levels in the Coral Sea are limited to approximately 100 cm with the M_2 wave, but only about 10 cm with any of the other waves. At present, it would be difficult to limit the total noise level to 10 cm for altimetry ranges, due basically to the orbital errors, but the M_2 wave could possibly be obtained.

It must be stated again that these results are relevant to a $5^o \times 5^o$ square, and deal with only 20 observations (i.e. 3 months of data acquisition). If the number of observations is increased, the noise level can be increased, while still retaining the same capacity for recovery. Also, if the size of the square is decreased, this will decrease the number of satellite passes over the area and thus lessen the number of altimeter observations.

If further improvements in the reduction of the white noise level in satellite altimetry ranges are made, tidal amplitudes and phases can be obtained for numerous adjacent ocean sites, and thus cotidal-corange charts can be obtained for the principal ocean tide constituents by satellite altimetry. For the present it would be necessary to reduce the noise in GEOS 3 orbits to the 1 metre level before conditions are favourable for the recovery of the M_2 tidal signal with 80% confidence using this technique.

In a successful analysis for the ocean tidal signal, it is necessary to determine the extent Earth tides effect the radial distance measured by the altimeter. This is governed by the method of orbit determination. If the satellite orbit is determined from short arcs, all long period perturbations could be expected to be absorbed into the orbital elements. The dominant mean anomaly terms (see Table 8.5a) have very long periods, and could not be separated in a short arc calculation.

The satellite altimetry measurements for the oceanic areas would be obtained from several passes, and the orbital parameters from short arc observations. Thus the expected radial displacements in a satellite pass would be obtained from the short period terms in the semi-major axis, eccentricity, and mean anomaly. These perturbations have a maximum amplitude of 20 centimetres.

CHAPTER 10

CONCLUSIONS

Tidal Gravity and Ocean Loading

The series of measurements discussed in Chapter 4 covers observations at the nine sites throughout Australia and Papua New Guinea. The tidal amplitudes and phase lags determined at each of the sites have been obtained with sufficient accuracy to meet the goals outlined in Chapter 1. The inland sites of Alice Springs and Broken Hill give results that approach the theoretical estimates of $\delta = 1.163$ and zero phase lag. The other sites, positioned at coastal regions show the effects of ocean tidal loading both in amplitude factor and phase lag. A detailed analysis and conclusion can be found in Section 4.5. The unexpected pattern of variations in the tidal parameters at the nine sites make it most desirable that additional sites be occupied.

A prerequisite for successful computations of ocean loading effects on tidal gravity using load deformation coefficients h'_n, k'_n is a reliable high degree harmonic model of the global ocean tide. It is questionable whether such a model is available at this point of time or whether the quality of data through the high degree terms in the model warrants the adoption of the load deformation coefficient approach as it is a relatively uneconomic procedure on the computer. The largest contribution to ocean loading effects on gravity with significant magnitude are usually as a consequence of local ocean tidal effects. These effects are best obtained from precise and detailed cotidal-corange charts of the local oceans. This data cannot be economically represented with sufficient accuracy by global harmonic models. The high resolution obtained from accurate local ocean tide data is not incorporated to its best advantage in solutions using load deformation coefficients. Ideally, it is recognised that the ocean tide itself should be used to evaluate the tidal loading effect on gravity, rather than harmonic representations of the height (e.g. see FARRELL 1972a).

The gravitational attraction due to the ocean tide in the inner zone can be calculated by using the first term in equation 5.15, without using harmonic representations of the ocean height, but any calculation of the total loading needs a harmonic representation of the ocean height. The total ocean tidal loading from the outer zone can be calculated using the attraction term (for the outer zone) as described in equations 6.3 to 6.5 as modified in terms of equation 5.15. Such a procedure would be more attractive than the method based on load deformation coefficients as it reduces the time used for calculation. It's adoption would also allow the use of more accurate data for evaluating the more variable local effects.

The magnitude of these effects on the basis of analyses of the data already collected in Australia is less than 5 μgal for the M_2 wave.

A comparison of the results presented in Chapter 6 from various ocean tide models for the ocean tidal loading on the Australian sites shows considerable variations in amplitude and phase. This is primarily due to the poorly modelled Pacific and Indian Oceans. European sites, generally have smaller discrepancies between various models because the Atlantic Ocean is better modelled. The large expanse of the Pacific and Indian together with the lack of suitable ocean tidal observations contributes directly into any solution of the Laplace Tidal Equations (see Section 5.1). Visual inspection of the cotidal-corange charts shows several instances where the amphidromes are displaced, especially in the Pacific Ocean. The differences in phases between models are due in part to the rotational variations of the amphidromes. The major discrepancies between the models occur in the Pacific, possibly due to the large expanse of oceans and perturbations due to island scattering and diffraction.

The calculations presented in Section 6.4 show that conservation of mass in ocean tide models is important in any tidal loading calculations throughout the world. The truncation function method attains its conservation of mass by neglecting zero degree terms in the summations. Comparisons of the truncation function method and the Longman-Farrell method shows many similarities, particularly in some models or in some stations with various models. The discrepancies, although smaller than on comparison with the absence of mass conservation calculations does lead to some conclusions on the truncation function method, with respect to other methods.

The truncation function method is based on a harmonic development of the global ocean tide, in the calculations presented to degree 20. When using models it would be reasonable to conclude that the model may not be accurately represented by a degree twenty representation. In particular some sites would present a better pole for a spherical harmonic analysis using the (ψ, α) system of coordinates, than other sites. The extent of harmonic development on various ocean tide models can be obtained through increased research. Additionally, the method of the initial digitisation of a ocean tide chart for ocean loading has to be further researched, as this could influence the calculations, especially with regard to systematic errors.

In a development to degree 20, which means a 9^{o} wavelength representation on the Earth's surface, the inner zone calculations (based on accurate local ocean models) should preferably continue to say 10^{o} out from the computation point. In Australia, such cannot be achieved due to the very limited local ocean models.

It becomes apparent that an accurate evaluation of the ocean tidal effects on gravity in Australia will not be forthcoming until there is an improvement in the quality of the Pacific Ocean models. The results presented in Chapter 6 show that any tidal gravity observations which have already been corrected for ocean loading effects should be examined closely because of the large variations between the various ocean tide models.

In view of the discrepancies between the various ocean tide models, there is a need to establish the credentials of a reliable global tide model. Earth tide observations could play a role in such development if:

a) tidal gravity were simultaneous recorded at several sites evenly distributed throughout the world;
b) these Earth tide observations were of sufficient accuracy with instrumental errors such as those due to calibration and drift, eliminated; and
c) all other perturbations of the gravity tide due to factors such as atmospheric tides and tectonic effects, were assumed to be negligible or reliably corrected for.

Such a global ocean tide model would have to be supplemented by regional models to produce a detailed representation of the global oceans.

The truncation function procedure can produce errors when solving for the harmonic coefficients of the ocean tide models due to

i) the size of the blocks sampled; and
ii) the number of harmonic coefficients being sought in the representation.

Furthermore, a disadvantage on the use of a restricted harmonic series for the representation of ocean tide models often produces small values for the ocean tide amplitudes on land.

Due to the differences between various ocean tide models, given a suitable global selection of Earth

tide stations there is a possibility of solving the inverse problem. This consists of obtaining ocean tide models from Earth tide results. Preliminary attempts have been performed on the North Atlantic Ocean (JACHENS & KUO 1973).

The tidal gravity corrections obtained at the Australian stations can be utilised in future gravity base line measurements. The determination of the tidal gravity corrections insure the elimination of systematic errors which are brought about by incorrect theoretical corrections of solid Earth tides and ocean loading.

One of the initial objectives of this project was the determination of the Earth's radial deformation in Australia. This requires both gravimeter and tiltmeter observations to solve for the Love number, h which is the basis for defining the radial deformation. Reliable tiltmeter observations are not available in Australia for reasons described in Section 4.5. Thus the radial deformation cannot be unambiguously obtained. The adoption of theoretical models for the radial deformation accounts for the majority of the signal, while the variations between the theoretical model and observation are predominately due to ocean loading.

The results presented in Chapter 6 show it is possible to model the discrepancies of the Australian tidal gravity results from theoretical predicted values, by a finite set of parameters to the 1-2% level. This method is in contrast to the conventional load-deformation coefficient method which requires numerous coefficients. The discrepancies between the theoretical and observed tidal gravity results are modelled by the use of truncation functions, surface integration procedures and a finite set of position dependent parameters.

In Section 6.7 it is shown that a ten parameter representation of the crustal response is adequate for representing the deformation of the Earth tide by ocean loading at any site in Australia with a resolution of ±2 μgal provided extrapolation is not performed over distances greater than 10^3 km. This is assessed as being of sufficient accuracy for all purposes in high precision geodesy. It was not possible to establish the stability of the model over long periods of time in excess of a few years in the absence of a continuous recording of tidal gravity over sufficiently long periods of time. The separation of the actual radial deformation due to ocean loading from the effect on tidal gravity could not be achieved in the absence of reliable tiltmeter data in the region which were only available at Cooney Observatory, Armidale.

On the basis of these results, it is not unreasonable to conclude that the radial deformation can be defined to the 1-2 centimetre level if tiltmeter observations can be combined with the present tidal gravity results in Australia. The procedures for determining the radial deformation using both gravimeters and tiltmeters are outlined in Chapter 5.

Satellite Studies

An estimate of the ocean tide - Earth tide perturbations on satellites can be obtained from the tables and graphs in Chapter 8. A major source of uncertainty in calculating ocean tide perturbations is the unreliable ocean tide models available at present. The dominant M_2 ocean tide (on the Earth), despite being the best modelled, still has its degree of uncertainty. The other tidal models can only be the basis of approximate evaluation of the total effect on the satellite perturbations.

All Love number determinations from satellite tracking prior to 1973 were not corrected for ocean tides. LAMBECK ET AL (1974) have obtained corrections for these, but the results are still not conclusive. The differences between the curves in Figure 8.4 suggests that the present ocean tide models are unreliable and that there could be some unmodelled influences of ocean tides. The reverse problem can be examined for improvement in the tidal models from the analysis of tracking residuals using a Love number estimate of 0.30. FELSETREGER ET AL (1976) and RUBINCAM (1976)

have attempted to determine the ocean tide parameters from satellite perturbations. This is achieved by modelling all known forces, including the solid Earth tide and atmospheric effects. The solutions suffer through inadequate modelling of the forces, e.g. solid Earth tides, solar radiation and atmospheric effects. The inadequacy of the solid Earth tide models comes through the Love number k_2, which is not constant for diurnal tides but is frequency dependent due to liquid core effects. The solution assumes the residuals are solely due to ocean tides of low order. The resultant harmonic coefficients are contaminated due to the neglect of the higher-order coefficients. A similar study by GOAD & DOUGLAS (1977) on the M_2 ocean tide were able to obtain good agreement with present ocean tide models.

Although these analyses are only in the preliminary stages, the results indicate there is a good capability of recovering ocean tide coefficients from satellite tidal perturbations especially after improvements in the force fields.

If the ocean tide perturbations will continue to be calculated from models, a closer examination of the tracking data and ocean tide models may be necessary. Precise ocean tide corrections on satellite orbits will be forthcoming only if substantial advances are made in both these fields.

The preceding discussion primarily centred on studies which have been researched with data, and results obtained. With the introduction of satellite altimetry, many researchers have described this as an important means of improving geodetic systems and global models, and the corresponding theory is developing.

In the Earth tide field, altimeter measurements are affected by the Earth tide perturbations. The type of perturbation that will be present in radial distance measurements from satellites is dependent on the orbit determination method. If the orbit is determined from a short arc, all the long period perturbations would be expected to be absorbed into the orbital elements. Also for perturbations in the radial distance, the most important element is the mean anomaly, since the other elements are of short period. The results in Section 9.3 show that the dominant mean anomaly perturbations would be absorbed in a short arc calculation, and therefore the expected radial displacements for a satellite pass should consist of short period terms in the semi-major axis, eccentricity and mean anomaly. A detailed conclusion can be found in Section 9.4.

The analyses of satellite altimetry measurements could improve calculations of tidal loading effects on Earth tide observations, through improvements in the ocean tide models. The results presented in Section 9.2 show that with further improvements in the orbit determinations and altimeter precision there is a possibility of recovering ocean tide signals from altimeter measurements. The conditions for the successful recovery of the tidal signals are dependent on the signal-to-noise ratio and this is a function of the particular tidal signal considered. With a reduction in the satellite altimeter measurement noise level, the tidal signal can be analysed from numerous adjacent ocean sites and thus tidal models can be obtained for the principal ocean tide constituents. This would require the present noise level in the GEOS 3 orbit to be less than 1 metre. Detailed results and conclusions are given in Section 9.4.

Further, if the goal is the determination of accurate tidal models,the satellite altimetry measurements together with Earth tide observations can be used in a complex solution for the ocean tide signal.

The results from both land based Earth tide results and from satellite studies suggest that present ocean tide models are unreliable, especially in open oceans. However, present research suggests that land based observations and satellites perturbations can be used in a complex solution for the ocean tide signal. The results presented in Chapters 6 and 8 appear to support these conclusions, where the present ocean tide models can be easily differentiated between, and the best fitting model adopted. The solution for the tidal signal can be enhanced by including satellite altimetry determined ocean

tide signals. The recovery of the tidal signal from satellite altimetry is dependent on the signal-to-noise ratio. The successful determination for the ocean tide model from satellite methods requires present noise levels in both orbit determinations and altimetry to be reduced, together with improvements in the tracking systems and methods.

REFERENCES

ALTERMAN, Z., JAROSCH, H. & PEKERIS, C.L. 1959. Oscillations of the Earth. *Proc. Roy. Soc. London A* 252, 80-95.

BAKER, T.F. & LENNON, G.W. 1973. Calibration: Confidence in the Performance of Tiltmeters and Gravimeters. *Proc. 7th Intern. Symp. Earth Tides*, G. Szádeczky-Kardos (ed.), Sopron, 223-230.

BARLOW, B.C., COUTTS, D.A. & SYDENHAM, P.H. 1973. Tidal Deviations of the Vertical in Armidale, Australia. *Proc.Symp.Earth's Grav.Field*, Univ. NSW, Sydney, 691-698.

BOGDANOV, K.T. & MAGARIK, V.A. 1967. Numerical Solution of the Distribution Problem for the Semi-diurnal Tidal Waves (M_2 and S_2) in the World Ocean. *Doklady, Acad.Sciences USSR, Earth Sciences Section* 172, 7-9.

BOGDANOV, K.T. & MAGARIK, V.A. 1969. A Numerical Solution of the Problem of Tidal Wave Propagation in the World Ocean. *Atmospheric and Oceanic Physics, Izvestiya* 5, 757-761.

BRIEN, R. 1969. Report on some Investigations Concerning Gravimeter Recordings in Frankfurt a.M. *Proc. 6th Symp.Earth Tides*. Observatoire Royal de Belgique, *Commun. Série* A 9, *Série Géophysique* 96, 30-36.

BRETREGER, K. 1975. Tidal Effects on Satellite Orbits. *Unisurv G* 22, 25-45.

BRETREGER, K. 1976a. Tidal Effects on GEOS 3 Satellite. *Unisurv G* 24, 101-102.

BRETREGER, K. 1976b. On Recovering the Ocean Tide Signal from Satellite Altimetry. *Unisurv G* 25, 85-94.

BRETREGER, K. & MATHER, R.S. 1976. On the Modelling of the Deformation of Tidal Gravity by Ocean Loading. *Unisurv G* 24, 71-80.

BRETREGER, K. & MATHER, R.S. 1977. Modelling Ocean Loading Effects on Tidal Gravity in Australia. *Proc.8th Intern.Symp.Earth Tides*, Bonn.

CAPUTO, M. 1961. Deformation of a Layed Earth by an Axially Symmetric Surface Mass Distribution. *J.Geophys.Res.* 66, 1479-1483.

COOK, A.H. 1950. The Calculation of Deflexions of the Vertical from Gravity Anomalies. *Proc.R.Soc. London A* 204, 374-395.

CSAPO, C. 1974. Vibration Experiments with Sharpe Gravimeters. *Studia geoph.et geod.* 18, 386-389.

DIVIS, K. & TOBYAS, V. 1974. The Effect of Vibrations on the Accuracy of Measurements with a CG-2 Gravimeter. *Studia geoph. et geod.* 18, 199-204.

DJUROVIC, D. & MELCHIOR, P. 1972. Recherche des terms de Marée dans les Variations de la Vitesse de Rotation de la Terre. *Bulletin de l'Académie royale de Belgique*, Classe de Sciences 63, 1248-1257.

DOODSON, A.T. 1921. The Harmonic Development of the Tide Generating Potential. *Proc.R.Soc.London A* 100, 305-329.

DOODSON, A.T. & WARBURG, H.D. 1941. *Admiralty Manual of Tides*, London, HMSO.

DUCARME, B. 1970. La Gravimétrie à l'Observatoire Royal de Belgique. *Ciel de Terre* 86(2), 1-20.

DUCARME, B. 1975a. A Fundamental Station for Trans World Tidal Gravity Profiles. *Phys.Earth & Planetary Interiors* 11, 119-127.

DUCARME, B. 1975b. The Computation Procedures at the International Centre for Earth Tides (ICET). *Marees Terrestres Bull. d'Inform.*, Observatoire Royal de Belgique, Bruxelles, 72, 4156-4181.

DUCARME, B. & MELCHIOR, P. 1977a. Tidal Gravity Profiles in Western Europe, Asia, Australia, New Zealand and Pacific Islands. *Marees Terrestres Bull. d'Observations*, Observatoire Royal de Belgique, Bruxelles, 4(4).

DUCARME, B. & MELCHIOR, P. 1977b. A Trans World Tidal Gravity Profile. *Phys.Earth & Planetary Interiors.* (in press).

DUCARME, B., MELCHIOR, P., MATHER, R.S., BARLOW, B.C. 1976. Tidal Gravity Profiles in Australia and Papua New Guinea (1974 - 1976). *Unisurv G* 25, 17-53.

EASTON, A.K. 1970. The Tides of the Continent of Australia. Horace Lamb Centre for Oceanographical Research, Flinders University of South Australia, *Research Paper No.* 37, 326 pp.

FAIRBRIDGE, R.W. 1966. *The Encyclopedia of Oceanography*. Vol. 1, Reinhold Pub. Co., New York.

FARRELL, W.E. 1970. *Gravity Tides*. Ph.D. Thesis, Univ. of Calif., San Diego.

FARRELL, W.E. 1972a. Deformation of the Earth by Surface Loads. *Rev.geophy. & Space phys.* 10, 761-797.

FARRELL, W.E. 1972b. Global Calculations of Tidal Loading. *Nature Phys.Sci.London* 238, 43-44.

FARRELL, W.E. 1973. Earth Tides, Ocean Tides and Tidal Loading. *Phil.Trans.R.Soc.London A* 274, 253-259.

FELSENTREGER, T.L., MARSH, J.G., & AGREEN, R.W. 1976. Analyses of the Solid Earth and Ocean Tidal Perturbations on the Orbits of the GEOS 1 and GEOS 2 Satellites. *J.Geophys.Res.* 81, 2557-2463.

FISHER, D. & FELSENTREGER, T.L. 1966. Effects of Solar and Lunar Tides on the Motion of an Artificial Earth Satellites. *Doc. X* - 547-66-560, NASA/GSFC, Greenbelt, Md.

GERSTENECKER, C. & GROTEN, E. 1976. Comparison of Tidal Gravity Observations with Sea Tidal Models. *Rivista Italiana di Geofisica* 3, 213-218.

GOAD, C.C. & DOUGLAS, B.C. 1977. Determination of M_2 Ocean Tide Parameters from Satellite Orbit Perturbations. *J.Geophys.Res.* 82, 898-900.

GROTEN, E. 1969. Calibration of a Gravimeter by Using a Heavy Mass. *Proc. 6th Symp.Earth Tides*. Observatoire Royal de Belgique, *Commun.Série* A9 , *Série Geophysique* 96, 197-202.

GROTEN, E. 1970. On the Spherical Harmonic Series of the Sea Tide Correction of Earth Tide Observations. *Proc. Symp.Coastal Geodesy* Techn.Univ.Munich, 537-549.

HARRISON, J.C. 1976. Cavity and Topographic Effects in Tilt and Strain Measurements. *J.Geophys.Res.* 81, 319-328.

HEISKANEN, W.A. & MORITZ, H. 1967. *Physical Geodesy.* Freeman, San Fransisco.

HENDERSHOTT, M.C. 1972. The Effects of Solid Earth Deformation on Global Ocean Tides. *Geophys.J.Roy.Astron.Soc.* 209, 389-402.

HENDERSHOTT, M.C. 1973. Ocean Tides. *EOS Trans.Amer.geophys. Un.* 54, 76-86.

HENDERSHOTT, M.C. & MUNK, M. 1970. Tides. *Ann.Rev.Fluid Mech.* 2, 205-224.

JACHENS, R.C. & KUO, J.T. 1973. The O_1 Tide in the North Atlantic Ocean as derived from Land-Based Tidal Gravity Measurements. *Proc. 7th Intern. Symp. Earth Tides.* G. Szádeczky-Kardos (ed.), Sopron. 165-175.

KAULA, W.M. 1963. Elastic Models of the Mantle Corresponding to Variations in the External Gravity Field. *J.Geophys.Res.* 68, 4967-4978.

KAULA, W.M. 1964. Tidal Dissipation and Orbital Perturbations. *Rev.geophys.* 2, 661-685.

KAULA, W.M. 1966. *Introduction to Satellite Geodesy.* Blaisdell,Waltham, Mass.

KAULA, W.M. 1969. Tidal Friction with Latitude-Dependent Amplitude and Phase Angle. *Astron.J.* 74, 1108-1114.

KOZAI, Y. 1959. The Motion of a Close Earth Satellite. *Astron.J.* 64, 367-377.

KOZAI, Y. 1960. Effect of Precession and Nutation on the Orbital Elements of a Close Earth Satellite. *Astron.J.* 65, 621-623.

KOZAI, Y. 1965. Effect of the Tidal Deformation of the Earth on the Motion of a Close Earth Satellite. *Publ. Astron.Soc.Japan* 17, 395-402.

KOZAI, Y. 1966. The Earth Gravitational Potential Derived from Satellite Motion. *Space Sci.Rev.* 5, 818-879.

KOZAI, Y. 1968. Love's Numbers of the Earth Derived from Satellite Observations. *Publ. Astron.Soc.Japan,* 20, 24-26.

KOZAI, Y. 1973. A New Method to Compute Lunisolar Perturbations in Satellite Motion. *Spec. Rep.* 349, Smithsonian Astrophy.Obs., Cambridge, Mass.

KUO, J.T. 1969. Static Response of a Multilayed Medium under Inclined Surface Loads. *J.Geophy.Res.* 74, 3195-3207.

KUO, J.T. & EWING, M. 1966. Spatial Variations of Tidal Gravity. Geophysical Monograph No. 10, *The Earth Beneath the Continents.* J.S. Steinhart & T. Jefferson Smith (ed.)., Amer.Geophys. Un., Washington, 595-610.

KUZNETSOV, M.V. 1972. Calculation of the Secular Retardation of the Earth's Rotation from up-to-date Cotidal Charts. *Izv.Acad.Sci.USSR, Phy.Solid Earth* 8, 779-784.

LACOSTE & ROMBERG 1973. *Instruction Manual for LaCoste and Romberg, Inc. Model G Geodetic Gravity Meter.* LaCoste & Romberg, Austin.

LAMBECK, K. 1973. Determination of Earth and Ocean Tides from the Analysis of Satellite Orbits. *Proc. Sym.Earth's Grav. Field,* Univ. NSW, Sydney, 522-528.

LAMBECK, K. & CAZENAVE, A. 1973. Fluid Tidal Effects on Satellite Orbit and Other Temporal Variations in the Geopotential. *Bulletin 7, Groupe de Recherches de Geodesie Spatiale,* Mendon, France.

LAMBECK, K., CAZENAVE, A. & BALMINO, G. 1974. Solid Earth and Ocean Tides Estimated from Satellite Orbit Analyses. *Rev.Geophys.Space Phys.* 12, 421-434.

LAMBERT, A. 1974. Earth Tide Analysis and Prediction by the Response Method. *J.Geophys.Res.* 79, 4952-4960.

LECOLAZET, R. 1956. L'Enregistrement de la Marée Gravimétrique avec un Gravimétre North-American. *Marees Terrestres Bull. d'Inform.* Observatoire Royal de Belgique, Bruxelles 1, 4-9.

LECOLAZET, R. & MELCHIOR, P. 1975. Experimental Determination of the Dynamical Effects of the Liquid Core of the Earth. *Proc. Interdisciplinary Symp. Tidal Interactions,* XVI General Assembly IUGG, Grenoble.

LENNON, G.W. & BAKER, T.F. 1973. The Earth Tide Signal and it's Coherency. *Q.Jl.R.astr.Soc.* 14, 161-182.

LEPPERT, K., HARMON, B.V. & MATHER, R.S. 1975. A Status Report on Investigations of Sea Surface along the Eastern Coast of Australia. *Unisurv G* 23, 60-67.

LONGMAN, I.M. 1962. A Green's Function for Determining the Deformation of the Earth under Surface Mass Loads, 1, Theory. *J.Geophys.Res.* 67, 845-850.

LONGMAN, I.M. 1963. A Green's Function for Determining the Deformation of the Earth under Surface Mass Loads, 2, Computations and Numerical Results. *J.Geophys.Res.* 68, 485-496.

LONGMAN, I.M. 1966. Computation of Love Numbers and Load Deformation Coefficients for a Model Earth. *Geophys. J.R. astr.Soc.* 11, 133-137.

LOVE, A.E. 1909. The Yielding of the Earth to Disturbing Forces. *Proc.R.Soc.London A* 82, 73-88.

MATHER, R.S. 1974. Geodetic Coordinates in Four Dimensions. *Canadian Surveyor* 28(5), 574-581.

MATHER, R.S. 1976. On the Realisation of a System of Reference in Four Dimensions for Ocean Dynamics. *Proc. Colloquium Radio Oceanography*, Hamburg.

MATHER, R.S. & BRETREGER, K. 1975. An Experiment to Determine Radial Deformation of Earth Tides in Australia by Ocean Tides. *Unisurv G* 23, 42-59.

McGOOGAN, J.T., LEITAO, C.D., MILLER, L.S. & WELLS, W.T. 1974. Skylab S-193 Altimeter Experiment Performances, Results and Applications. *Proc. Intern.Symp.Applications of Marine Geodesy*, Columbus, Ohio.

McGOOGAN, J.T., LEITAO, C.D. & WELLS, W.T. 1975. Summary of Skylab S-193 Altimeter Altitude Results. *NASA TMX* - 69355, Wallops Island, USA.

MELCHIOR, P. 1966. *The Earth Tides*. Pergamon, Oxford.

MELCHIOR, P. 1971a. Dynamic Effects of the Liquid Core of the Earth in Earth Tide and Nutation Phenomena. *Proc.Symp.Lunar Effects in Geophysics*, Moscow.

MELCHIOR, P. 1971b. *Physique et Dynamique Planétaires*. Vander, Bruxelles.

MELCHIOR, P. 1973a. *Trans World Tidal Gravity Profiles*. Obs. Royal de Belgique, Bruxelles.

MELCHIOR, P. 1973b. On Earth Tide Models for the Reduction of High Precision Quasi-Radial Range Measurements. *Proc.Symp.Earth's Grav. Field*. Univ. NSW, Sydney, 509-521.

MELCHIOR, P. 1974. Earth Tides. *Geophysical Surveys* 1, 275-303.

MELCHIOR, P. 1977. *The Tides of the Planet Earth*. Pergamon, Oxford.

MELCHIOR, P., KUO, J.T. & DUCARME, B. 1976. Earth Tide Gravity Maps for Western Europe. *Phys.Earth & Planetary Interiors* 13, 184-196.

MELCHIOR, P. & PAQUET, P. 1966. Station Uccle-Bruxelles. *Marees Terrestres Bull. D'Observations*, Observatoire Royal de Belgique,Bruxelles, 3(1).

MEONS, M. 1976a. *Oceanic Perturbations of the Earth Tides*. Institut d'Astronomie et de Géophysique, Louvain-la-Neuve.

MEONS, M. 1976b. Solid Earth Tide and Arctic Oceanic Loading Tide at Longyearbyen (Spitsbergen). *Phys. Earth & Planetary Interiors* 13, 197-211.

MOLODENSKII, M.S., EREMEEV, V.F. & YURKINA, M.I. 1962. *Methods for Study of the External Gravitational Field and Figure of the Earth*. Israel Program for Scientific Translation, Jerusalem.

MUNK, W.H. & MACDONALD, G.J.F. 1960. *The Rotation of the Earth*. Cambridge Univ. Press.

MUNK, W.H., SNODGRASS, F. & WIMBUSH, M. 1970. Tides off-shore:Transition from California Coastal to Deep-sea waters. *Geophys. Fluid Dyn.* 1, 161-235.

MUNK, W.H. & ZETLER, B.D. 1967. Deep-Sea Tides: A Program. *Science* 158, 884-886.

MUSEN, P. & ESTES, R. 1972. On the Tidal Effects in the Motion of Artifical Satellites. *Celestial Mechanics* 6, 4-21.

MUSEN, P. & FELSENTREGER, T. 1973. On the Determination of Long Period Tidal Perturbations in the Elements of Artifical Earth Satellites. *Celestial Mechanics* 7, 256-279.

NEWTON, R.R. 1965. An Observation of the Satellite Perturbations Produced by the Solar Tide. *J.Geophys.Res.* 70, 5983-5989.

NEWTON, R.R. 1968. A Satellite Determination of Tidal Parameters and Earth Deceleration. *Geophys. J.R.astr.Soc.* 14, 505-539.

OBSERVATOIRE ROYAL DE BELGIQUE. 1975. *TG-1, Tidal Recording Gravimeter*. Bruxelles.

PARIISKII, N.N., BARSENKOV, S.H., VOLKOV, K.A. GRIDNEV, D.G. & KRAMER, M.V. 1967. Results of 19 Months of Earth Tides in Talgar. *Izv.Acad.Sci.USSR, Phys.Solid Earth* 3, 107-114.

PEKERIS, C.L. & ACCAD, Y. 1969. Solution of Laplace's Equation for the M_2 Tide in the World's Oceans. *Phil.Trans.R.Soc.London A* 265, 413-436.

PEKERIS, C.L. & JAROSCH, H. 1958. The Free Oscillations of the Earth. *In Contributions in Geophysics: In honor of Beno Gutenberg*. Pergamon Press, Los Angeles, 171-192.

PERTSEV, B.P. 1958. The Calculation of Zero Point Drift during Observations of Elastic Tides. *Akademiya nauk SSSR, Bulletin (Izv.) Geophysics Series*, 376-377.

PERTSEV, B.P. 1960. Some Experience in Determining the Scale Coefficient of the Recordings in Observations of Tidal Variations of Gravity. *Bollettino di Geofisica theorica ed applicata* 2, 203-207.

REFORD, M.S. 1951. Tidal Variations of Gravity. *Trans.American Geophys.Un.* 32, 151-156.

ROBINSON, E.S. 1974. A Reconnaissance of Tidal Gravity in Southeastern United States. *J.Geophys.Res.* 79, 4418-4424.

RUBINCAM, D.P. 1976. Tidal Parameters Derived from the Perturbations in the Orbital Inclinations of the GEOS 1 and GEOS 2 Satellites. *Doc. X* - 921 - 76 - 72, NASA/GSFC, Greenbelt Md.

SMITH, D.E., KOLENKIEWICZ, R. & DUNN, P.J. 1972. Geodetic Studies of Laser Studies to Satellites. In *The Use of Artifical Satellites for Geodesy*. Geophysical Monograph Series Vol. 15, S.W. Henriksen et al (ed.), American Geophys.Un., Washington, 187-196.

SMITH, D.E., KOLENKIEWICZ, R. & DUNN, P.J. 1973. A Determination of the Earth Tidal Amplitude and Phase from the Orbital Perturbations of the Beacon Explorer C Spacecraft, *Nature* 244, 498-499.

SMITH, D.E., LERCH, F.J., MARSH, J.G., WAGNER, C.A., KOLENKIEWICZ, R., & KHAN, M.A. 1976. Contributions to the National Geodetic Satellite Program by Goddard Space Flight Center. *J.Geophys.Res.* 81, 1006-1026.

SNODGRASS, F.E. 1968. Deep Sea Instrument Capsule. *Science* 162, 78-87.

TAKEUCHI, H., SAITO, M. & KOBAYASHI, N. 1962. Statical Deformations and Free Oscillations of a Model Earth. *J.Geophys.Res.* 67, 1141-1154.

TANAKA, T. & SYDENHAM, P.H. 1977. The M_2 Earth Tides at Cooney Geophysical Observatory in Armidale, Eastern Australia. *Proc. 8th Intern.Symp.Earth Tides*, Bonn.

TIRON, K.D., SERGEEV, Y.N. & MICHURIN, A.N. 1967. Tidal Charts of the Pacific, Atlantic and Indian Oceans. *Leningrad Universitet Vestnik Geologiga* 24, 123-135.

VALLIANT, H.D. 1973. A Technique for the Precise Calibration of Continuously Recording Gravimeters. *Phil.Trans.R.Soc. London A* 274, 227-230.

VENEDIKOV, A.P. 1966a. Une méthode pour l'Analysis des Marées Terrestres a partir d'Enregistrements de Longueur Arbitraire. Observatoire Royal de Belgique, *Commun.* 250, *Série Géophysique* 71, 437-469.

VENEDIKOV, A.P. 1966b. Sur la Constitution de Filtres Numériques pour le Traitment des Enregistrements des Marées Terrestres. *Acad.R.Belg., Bull.I.Sc.* 5, LII, 6, 827-845.

ZAHEL, W. 1973. The Diurnal K_1 Tide in the World Ocean - A Numerical Investigation. *Pageoph* 109, 1819-1825.

ZETLER, B.D. & MAUL, G.A. 1971. Precision Requirements for a Spacecraft Tide Program. *J.Geophys.Res.* 76, 6601-6605.

ZÜRN, W., BEAUMONT, C. & SLICHTER, L.B. 1976. Gravity Tides and Ocean Loading in Southern Alaska. *J.Geophys.Res.* 81, 4923-4932.

APPENDIX A
THE HARMONIC DEVELOPMENT OF THE TIDE GENERATING POTENTIAL

DOODSON (1921) produced a purely harmonic treatment of the potential, based on Brown's theory of the Moon, and it is the basis of all modern methods of harmonic analysis.

The principal waves are developed from the second degree harmonic of the potential, which accounts for 99% of the total potential,

$$W_2 = G_D\left(\frac{a_b}{R_b}\right)^3 \left[\tfrac{1}{2}\left(\frac{2}{3} - 2\cos^2\delta\right)\left(1 - 3\sin^2\phi\right) - \sin 2\phi \sin 2\delta \cos H + \cos^2\phi \cos^2\delta \cos 2H \right] \quad \text{(A-1)}$$

This expression is unsuitable for tidal analysis due to the trigonometric functions being complex variations in time due to the orbital motions of the Earth, Sun and Moon with respect to each other. The relationship between the lunar and solar orbits can be seen in Figure A-1.

The Development of the Lunar Tide

The lunar orbit, being more complex than the solar orbit, will be dealt with first. The declination of the Moon, δ expressed in equation A-1 can be replaced with an expression in terms of the right ascension, RA and the longitude of the ascending node, N (DOODSON & WARBURG 1941)

$$\sin\delta = 0.406 \cos\left(RA - \tfrac{\pi}{2}\right) + 0.008 \cos\left(3RA - \tfrac{\pi}{2}\right) + 0.090 \cos\left(RA-N- \tfrac{\pi}{2}\right) + 0.006 \cos\left(3RA-N- \tfrac{\pi}{2}\right) \quad \text{(A-2)}$$

Thus the major terms for the semi-diurnal function become,

$$\cos^2\delta = 0.914 + 0.079 \cos(2RA) + 0.036 \cos(N - \pi) + 0.036 \cos(2RA - N) \quad \text{(A-3)}$$

for the diurnal function, the term becomes,

$$\sin 2\delta = 0.757 \cos\left(RA - \tfrac{\pi}{2}\right) + 0.158 \cos\left(RA-N- \tfrac{\pi}{2}\right) + 0.031 \cos\left(3RA - \tfrac{\pi}{2}\right) + 0.022 \cos\left(3RA-N- \tfrac{\pi}{2}\right) + 0.011 \cos\left(RA + N + \tfrac{\pi}{2}\right) \quad \text{(A-4)}$$

while the long period term becomes,

$$\frac{2}{3} - 2\sin^2\delta = 0.495 + 0.158 \cos(2RA) + 0.072 \cos(N - \pi) + 0.072 \cos(2RA - N) \quad \text{(A-5)}$$

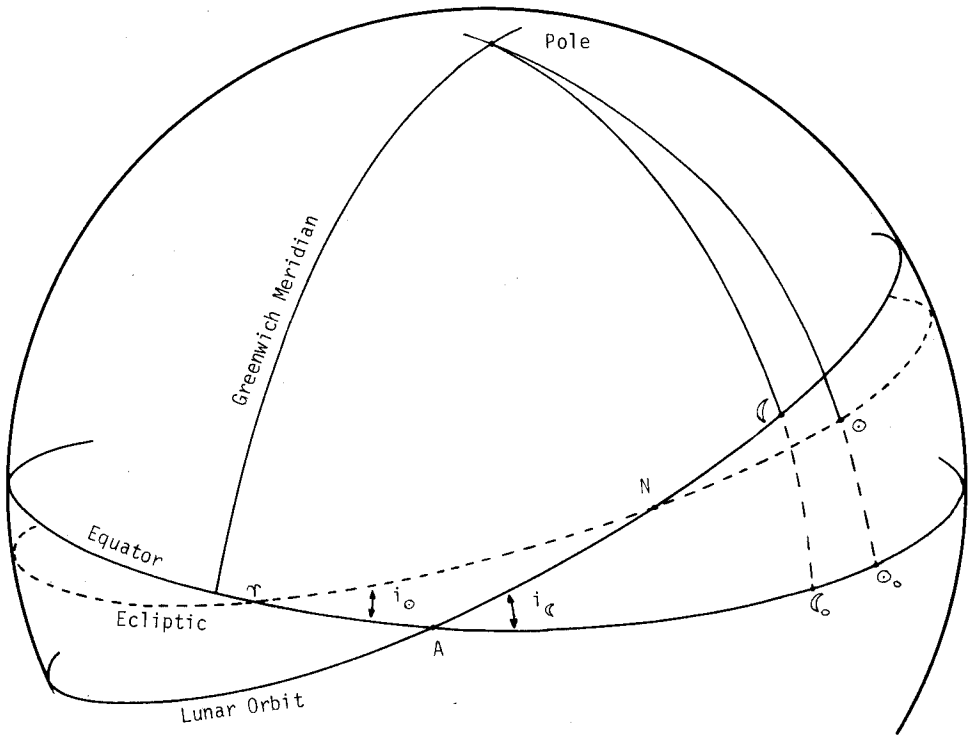

FIGURE A-1
Relationship Between the Equator, Ecliptic and Lunar Orbit

where

- γ is the vernal equinox
- $\odot$ defines the position of the Sun,
- $\leftmoon$ defines the position of the Moon,
- $\gamma\,\leftmoon_o$ is the Moon's right ascension,
- $\gamma\,\odot_o$ is the Sun's right ascension,
- $\odot_o\odot$ is the declination of the Sun,
- $\leftmoon_o\leftmoon$ is the declination of the Moon,
- $i_\odot$ is the obliquity of the ecliptic,
- $\gamma\,\odot$ is the (instantaneous) longitude of the Sun along the ecliptic,
- $\gamma\,N$ is the longitude (along the ecliptic) of ascending node,
- $A\,\leftmoon$ is the (instantaneous) longitude of the Moon, along its orbit,
- $i_\leftmoon$ is the inclination of the Moon's orbit to the Equator.

The hour angle, H can be expressed as

$$H = \theta - RA + \pi \tag{A-6}$$

where θ is the sidereal angle.

Thus the factor $\sin 2\delta \cos H$ in the diurnal species, expressed in terms of the right ascension and the sidereal angle become

$$\begin{aligned} -\sin 2\delta \cos H = {} & 0.379 \cos (\theta - \tfrac{\pi}{2}) + 0.379 \cos (\theta - 2RA + \tfrac{\pi}{2}) \\ & + 0.079 \cos (\theta - N - \tfrac{\pi}{2}) + 0.079 \cos (\theta + N - 2RA + \tfrac{\pi}{2}) \\ & + 0.015 \cos (\theta + 2RA - \tfrac{\pi}{2}) + 0.015 \cos (\theta - 4RA + \tfrac{\pi}{2}) \\ & + 0.011 \cos (\theta - N + 2RA - \tfrac{\pi}{2}) + 0.011 \cos (\theta + N - 4RA + \tfrac{\pi}{2}) \\ & + 0.006 \cos (\theta + N + \tfrac{\pi}{2}) + 0.006 \cos (\theta - N - 2RA - \tfrac{\pi}{2}) \end{aligned} \tag{A-7}$$

by using equations A-4 and A-6 together with the trigonometrical expression

$$\cos A \cos B = \tfrac{1}{2}\cos (A + B) + \tfrac{1}{2}\cos (A - B).$$

Similarly for the semi-diurnal species,

$$\begin{aligned} \cos^2\delta \cos 2H = {} & 0.914 \cos (2\theta - 2RA) \\ & + 0.040 \cos 2\theta + 0.040 \cos(2\theta - 4RA) \\ & + 0.018 \cos (2\theta + N - 2RA - \pi) \\ & + 0.018 \cos (2\theta - N - 2RA + \pi) + 0.018 \cos(2\theta - N) \\ & + 0.018 \cos (2\theta + N - 4RA) \end{aligned} \tag{A-8}$$

The right ascension of the Moon is a non-linear function of time, but can be approximated with the mean longitude of the Moon, s. The principal terms in equations A-7 and A-8 are

$$\theta - 2RA + \tfrac{\pi}{2}, \quad \theta + N - 2RA - \tfrac{\pi}{2}, \quad 2\theta - 2RA.$$

These being in the form $(A - 2RA)$ and can be expressed as

$$\begin{aligned} \cos (A - 2RA) &= \cos [(A - 2s) - (2RA - 2s)] \\ &= \cos (A - 2s) \cos (2RA - 2s) \\ &\quad + \cos (A - 2s - \tfrac{\pi}{2}) \sin (2RA - 2s) \end{aligned} \tag{A-9}$$

Using the approximation,

$$\sin (2RA - 2s) = 2RA - 2s$$

and introducing the mean longitude of the Sun, h and the longitude of the lunar perigee, p

$$\sin(2RA - 2s) = 0.220 \cos(s - p - \tfrac{\pi}{2}) + 0.086 \cos(2s + \tfrac{\pi}{2})$$
$$+ 0.044 \cos(s - 2h + p - \tfrac{\pi}{2})$$
$$+ 0.022 \cos(2s - 2h - \tfrac{\pi}{2}) + 0.008 \cos(2s - 2p - \tfrac{\pi}{2})$$
$$+ 0.038 \cos(N - \tfrac{\pi}{2}) + 0.038 \cos(2s - N + \tfrac{\pi}{2}) \qquad \text{(A-10)}$$

Also,

$$\cos(2RA - 2s) \doteqdot 0.988 + 0.012 \cos(2s - 2p) + 0.010 \cos(s + p)$$
$$+ 0.010 \cos(3s - p - \pi) \qquad \text{(A-11)}$$

Substituting the last two equations in A-9, and neglecting the smaller terms,

$$\cos(A - 2RA) = 0.988 \cos(A - 2s)$$
$$+ 0.110 \cos(A - 3s + p) + 0.110 \cos(A - s - p - \pi)$$
$$+ 0.043 \cos(A - 4s - \pi) + 0.043 \cos A$$
$$+ 0.022 \cos(A - 3s + 2h - p) + 0.022 \cos(A - s - 2h + p - \pi)$$
$$+ 0.019 \cos(A - 2s - N) + 0.019 \cos(A - 2s + N - \pi)$$
$$+ 0.019 \cos(A - 4s + N - \pi) + 0.019 \cos(A - N)$$
$$+ 0.011 \cos(A - 4s + 2h) + 0.011 \cos(A - 2h - \pi)$$
$$+ 0.010 \cos(A - 4s - 2p) \qquad \text{(A-12)}$$

Applying this equation in equations A-7 and A-8, the diurnal and semi-diurnal tides become

$$-\sin 2\delta \cos H = 0.376 \cos(\theta - 3s + \tfrac{\pi}{2}) + 0.361 \cos(\theta - \tfrac{\pi}{2})$$
$$+ 0.072 \cos(\theta - N - \tfrac{\pi}{2}) + 0.071 \cos(\theta + N - 2s + \tfrac{\pi}{2})$$
$$+ 0.042 \cos(\theta - 3s + p + \tfrac{\pi}{2}) + 0.042 \cos(\theta - s - p - \tfrac{\pi}{2})$$
$$+ 0.015 \cos(\theta + 2s - \tfrac{\pi}{2}) + 0.011 \cos(\theta - N + 2s - \tfrac{\pi}{2})$$
$$+ 0.009 \cos(\theta + N - 3s + p + \tfrac{\pi}{2}) + 0.009 \cos(\theta + N - s - p - \tfrac{\pi}{2})$$
$$+ 0.009 \cos(\theta + N + \tfrac{\pi}{2}) + 0.008 \cos(\theta - 3s + 2h - p + \tfrac{\pi}{2})$$
$$+ 0.008 \cos(\theta - s - 2h + p - \tfrac{\pi}{2}) \qquad \text{(A-13)}$$

and

$$\cos^2\delta \cos 2H = 0.903 \cos (2\theta - 2s) + 0.101 \cos (2\theta - 3s + p)$$
$$+ 0.101 \cos (2\theta - s - p - \pi) + 0.079 \cos 2\theta$$
$$+ 0.035 \cos (2\theta + N - 2s - \pi) + 0.035 \cos (2\theta - N)$$
$$+ 0.020 \cos (2\theta - 3s + 2h - p) + 0.020 \cos (2\theta - s - 2h + p - \pi)$$
$$+ 0.010 \cos (2\theta - 4s + 2h) + 0.010 \cos (2\theta - 2h - \pi)$$
$$+ 0.009 \cos (2\theta - 4s + 2p) \qquad \text{(A-14)}$$

Further development is based on the relationship for the parallax factor,

$$\left(\frac{a_b}{R_b}\right)^3 = 1 + 0.165 \cos (s - p) + 0.031 \cos (s - 2h + p)$$
$$+ 0.027 \cos (2s - 2h) + 0.013 \cos (2s - 2p) \qquad \text{(A-15)}$$

where a_b is the semi-major axis of the disturbing body's orbit and R_b is the distance from the geocentre to the disturbing body. The above equation applied to the principal terms in equations A-13 and A-14 give

$$-\left(\frac{a_b}{R_b}\right)^3 \sin 2\delta \cos H = 0.376 \cos \left(\theta - 2s + \frac{\pi}{2}\right)$$
$$+ 0.361 \cos \left(\theta - \frac{\pi}{2}\right) + 0.073 \cos \left(\theta - 3s + p + \frac{\pi}{2}\right)$$
$$+ 0.072 \cos \left(\theta - N - \frac{\pi}{2}\right) + 0.071 \cos \left(\theta - 2s + N + \frac{\pi}{2}\right)$$
$$+ 0.030 \cos \left(\theta - s + p - \frac{\pi}{2}\right) + 0.030 \cos \left(\theta + s - p - \frac{\pi}{2}\right)$$
$$+ 0.015 \cos \left(\theta + 2s - \frac{\pi}{2}\right) + 0.015 \cos \left(\theta - 3s + p + N + \frac{\pi}{2}\right)$$
$$+ 0.014 \cos \left(\theta - 3s + 2h - p + \frac{\pi}{2}\right)$$
$$+ 0.011 \cos \left(\theta - s - p - \frac{\pi}{2}\right)$$
$$+ 0.011 \cos \left(\theta + 2s - N - \frac{\pi}{2}\right)$$
$$+ 0.009 \cos \left(\theta + N + \frac{\pi}{2}\right) \qquad \text{(A-16)}$$

and

$$\left(\frac{a_b}{R_b}\right)^3 \cos^2\delta \cos 2H = 0.903 \cos (2\theta - 2s)$$
$$+ 0.176 \cos (2\theta - 3s + p) + 0.079 \cos 2\theta$$
$$+ 0.035 \cos (2\theta - 2s + N + \pi) + 0.035 \cos (2\theta - N)$$
$$+ 0.034 \cos (2\theta - 3s + 2h - p) + 0.026 \cos (2\theta - s - p + \pi)$$
$$+ 0.023 \cos (2\theta - 4s + 2p) + 0.021 \cos (2\theta - 4s + 2h)$$
$$+ 0.007 \cos (2\theta - s + p) \qquad \text{(A-17)}$$

The lunar long period tidal terms are obtained from equation A-5 and follow the same procedure as outlined for the semi-diurnal and diurnal waves,

$$\left(\frac{a_b}{R_b}\right)^3 \left(\frac{2}{3} - 2\sin^2 \delta\right) = 0.502 + 0.156 \cos 2s + 0.082 \cos (s - p) + 0.069 \cos (N + \pi) + 0.069 \cos (2s - N) + 0.030 \cos (3s - p) \quad \text{(A-18)}$$

Harmonic Development of Solar Tide

The motion of the Sun is simplier than that of the Moon, thus simplifying the formula considerably, with

$$\sin \delta \doteqdot 0.406 \cos \left(RA - \frac{\pi}{2}\right) + 0.008 \cos \left(3RA - \frac{\pi}{2}\right)$$

thus

$$\sin^2\delta \doteqdot 0.082 + 0.079 \cos (2RA - \pi) \quad \text{(A-19)}$$

$$\cos^2\delta \doteqdot 0.918 + 0.079 \cos 2RA \quad \text{(A-20)}$$

$$\sin 2\delta \doteqdot 0.764 \cos \left(RA - \frac{\pi}{2}\right) + 0.032 \cos \left(3RA - \frac{\pi}{2}\right) \quad \text{(A-21)}$$

The factors $\sin 2\delta \cos H$ and $\cos^2\delta \cos 2H$ become, in terms of sidereal time and right ascension,

$$-\sin 2\delta \cos H = 0.382 \cos \left(\theta - \frac{\pi}{2}\right) + 0.382 \cos \left(\theta - 2RA + \frac{\pi}{2}\right) + 0.016 \cos \left(\theta + 2RA - \frac{\pi}{2}\right) + 0.016 \cos \left(\theta - 4RA + \frac{\pi}{2}\right) \quad \text{(A-22)}$$

and

$$\cos^2\delta \cos 2H = 0.918 \cos (2\theta - 2RA) + 0.040 \cos 2\theta + 0.040 \cos (2\theta - 4RA) \quad \text{(A-23)}$$

Introducing the mean longitude of the Sun, h and the longitude of the solar perigee, p_s for the right ascension,

$$\sin (2RA - 2h) \doteqdot 2RA - 2h \doteqdot 0.068 \cos \left(h - p_s - \frac{\pi}{2}\right) + 0.086 \cos \left(2h + \frac{\pi}{2}\right) \quad \text{(A-24)}$$

Thus a solar equivalent to equation A-9 becomes

$$\cos (A - 2RA) = \cos (A - 2h) + \cos \left(A - 2h - \frac{\pi}{2}\right) \sin (2RA - 2h) \quad \text{(A-25)}$$

after making the approximation

$$\cos (2RA - 2h) \doteqdot 1.0 .$$

The principal terms occur for $A = \theta + \frac{\pi}{2}$ and 2θ, thus the expansion for $\cos (A - 2RA)$ becomes

$$\begin{aligned}\cos (A - 2RA) = {} & \cos (A - 2h) + 0.043 \cos A \\ & + 0.043 \cos (A - 4h + \pi) \\ & + 0.034 \cos (A - h - p_s + \pi) \\ & + 0.034 \cos (A - 3h + p_s)\end{aligned} \tag{A-26}$$

Equations A-22 and A-23 in terms of the sidereal angle and orbital elements become,

$$\begin{aligned}- \sin 2\delta \cos H = {} & 0.382 \cos (\theta - 2h + \tfrac{\pi}{2}) \\ & + 0.366 \cos (\theta - \tfrac{\pi}{2}) \\ & + 0.016 \cos (\theta + 2h - \tfrac{\pi}{2}) \\ & + 0.013 \cos (\theta - h - p_s - \tfrac{\pi}{2}) \\ & + 0.013 \cos (\theta - 3h + p_s + \tfrac{\pi}{2})\end{aligned} \tag{A-27}$$

and

$$\begin{aligned}\cos^2\delta \cos 2H = {} & 0.918 \cos (2\theta - 2h) + 0.079 \cos 2\theta \\ & + 0.031 \cos (2\theta - h - p_s + \pi) \\ & + 0.031 \cos (2\theta - 3h + p_s)\end{aligned} \tag{A-28}$$

The solar parallax factor is,

$$(\frac{a_b}{R_b})^3 = 1.0 + 0.051 \cos (h - p_s)$$

and combines with equations A-27 and A-28 to give

$$\begin{aligned}- (\frac{a_b}{R_b}) \sin 2\delta \cos H = {} & 0.382 \cos (\theta - 2h + \tfrac{\pi}{2}) \\ & + 0.366 \cos (\theta - \tfrac{\pi}{2}) \\ & + 0.023 \cos (\theta - 3h + p_s + \tfrac{\pi}{2}) \\ & + 0.016 \cos (\theta + 2h - \tfrac{\pi}{2})\end{aligned} \tag{A-29}$$

and

$$\begin{aligned}(\frac{a_b}{R_b})^3 \cos^2\delta \cos 2H = {} & 0.918 \cos (2\theta - 2h) \\ & + 0.079 \cos 2\theta \\ & + 0.054 \cos (2\theta - 3h + p_s)\end{aligned} \tag{A-30}$$

While the long period tide is obtained from the expression

$$\left(\frac{a_b}{R_b}\right)^3 \left(\frac{2}{3} - 2\sin^2\delta\right) = [\,1 + 0.051\cos(h - p_s)\,][\,0.503 + 0.158\cos 2RA]$$

to obtain

$$\left(\frac{a_b}{R_b}\right)^3 \left(\frac{2}{3} - 2\sin^2\delta\right) = 0.503 + 0.158\cos 2h + 0.026\cos(h - p_s) \qquad \text{(A-31)}$$

In all cases the arguments in the tidal periods can be expressed in terms of Greenwich mean solar time, t

$$t = \tau + s - h, \text{ and}$$

$$= t + h - \pi$$

where τ is lunar time.

The Sun's mass is approximately 27×10^6 times the Moon's mass, and the Sun's distance from the Earth is about 390 times the Moon's distance from the Earth. Consequently, the ratio of the Sun's tide generating forces to those of the Moon is 1 to 2.17. This factor of 0.4605 applied to the Sun's amplitude factors equates them to the Moon's factors.

APPENDIX B

LOCATION SKETCHES OF SITES

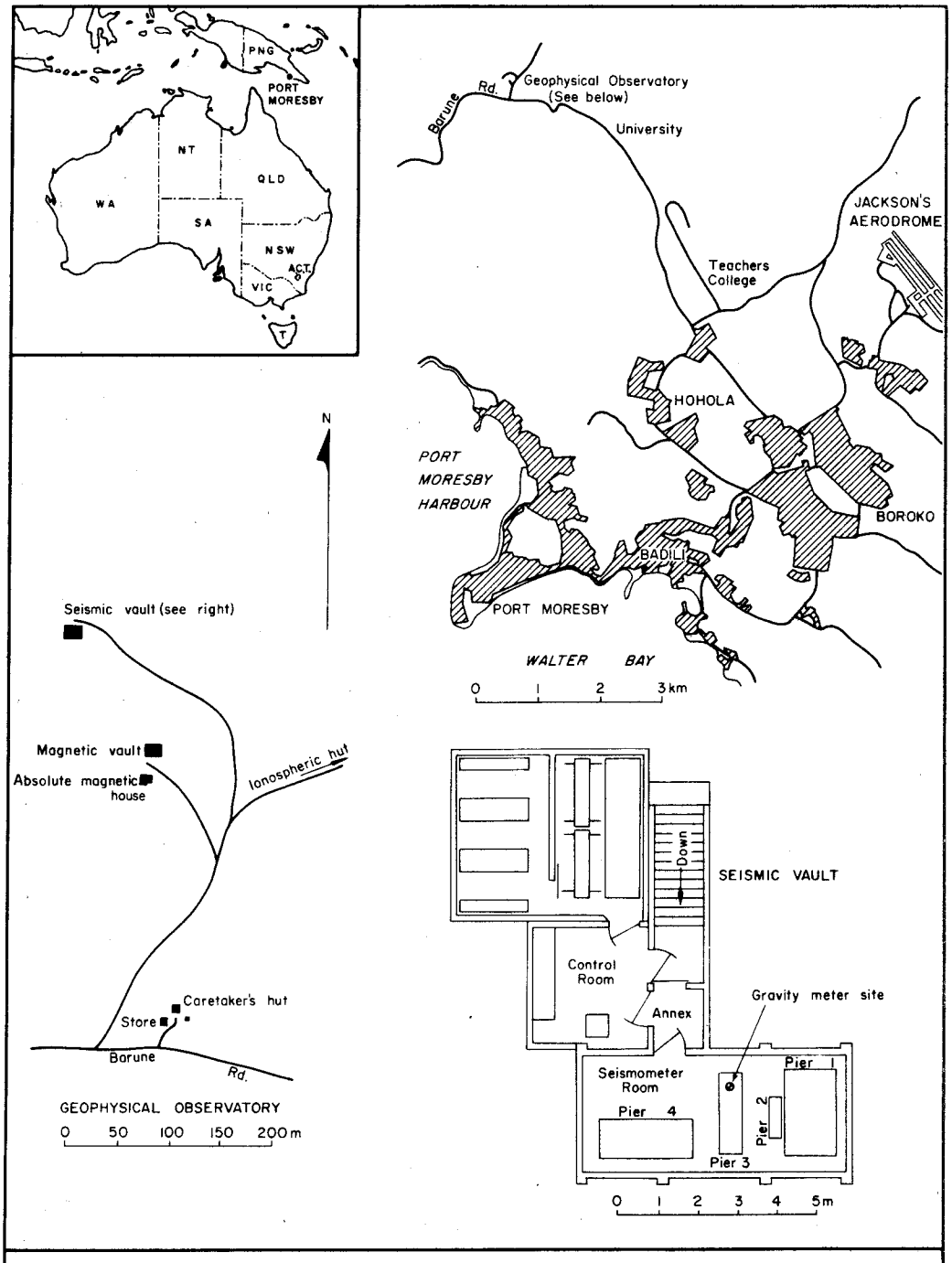

FIGURE B-1 **EARTH TIDE GRAVITY METER SITE PORT MORESBY (GEOPHYSICAL OBSERVATORY)**

C55/B2-27A

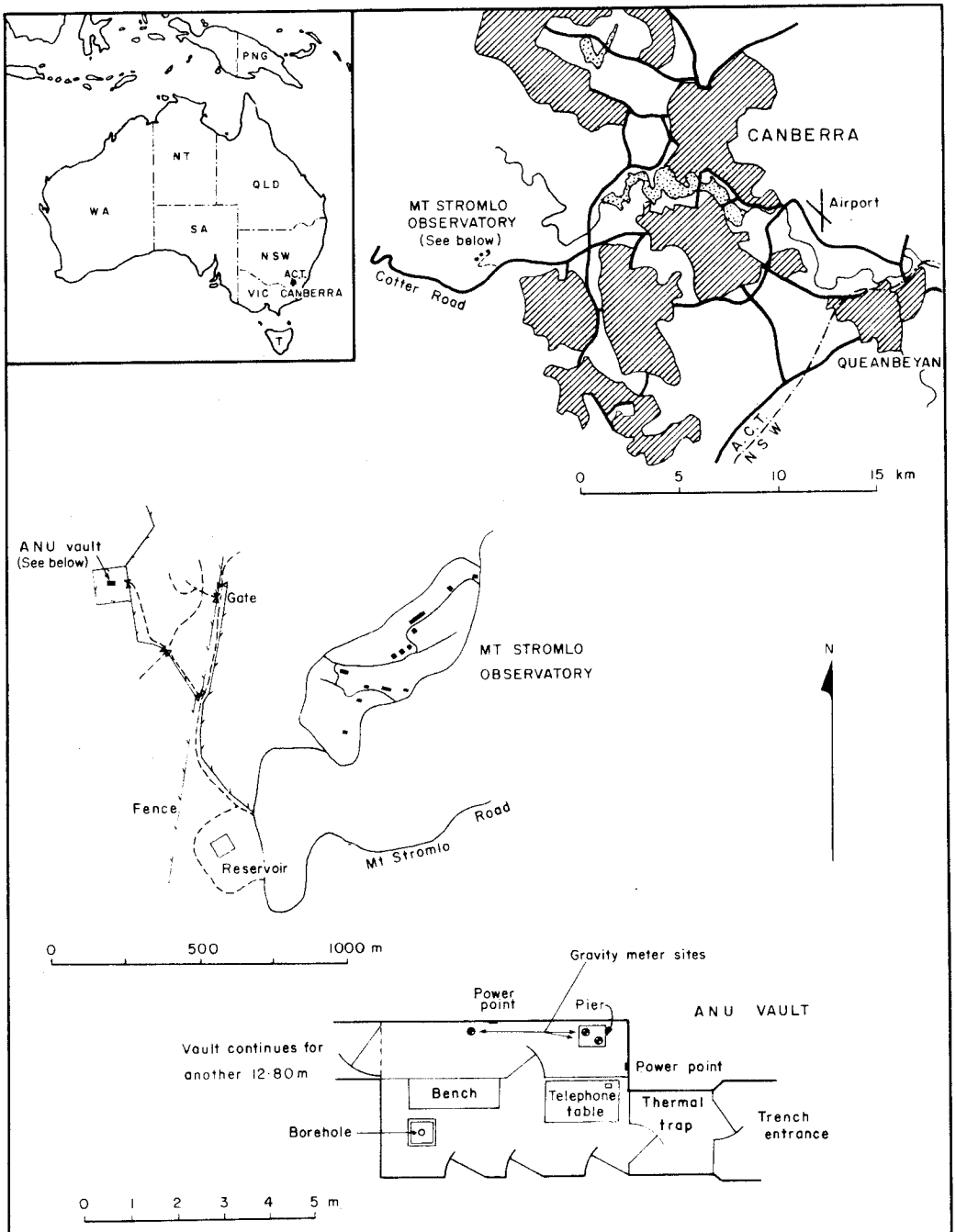

FIGURE B-2 **EARTH TIDE GRAVITY METER SITE CANBERRA (MT STROMLO OBSERVATORY)**

I 55/B2-67A

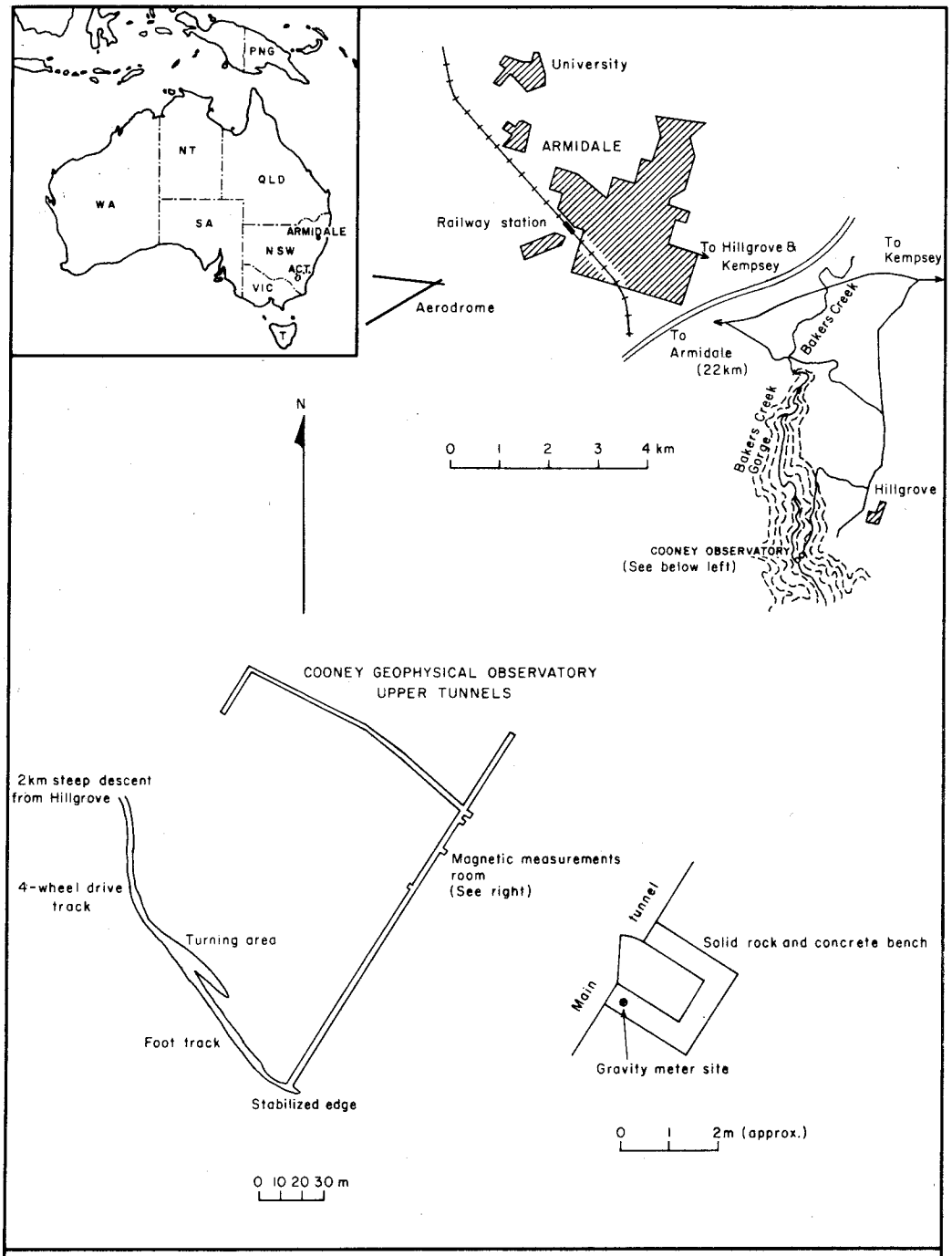

FIGURE B-3 **EARTH TIDE GRAVITY METER SITE ARMIDALE (COONEY GEOPHYSICAL OBSERVATORY)**

H 56/B2-31 A

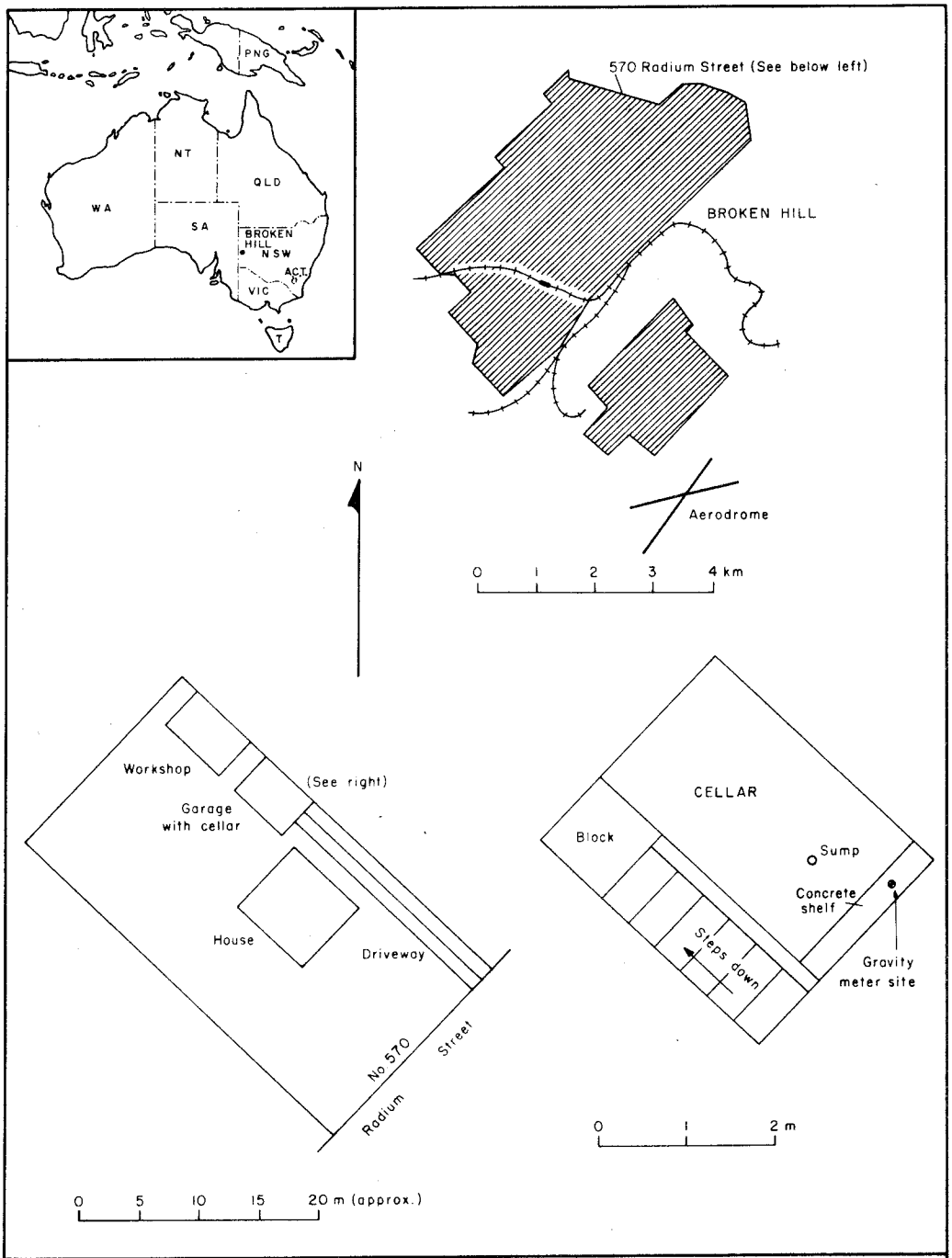

FIGURE B-4 **EARTH TIDE GRAVITY METER SITE BROKEN HILL (PRIVATE CELLAR)**

H54/B2-27 A

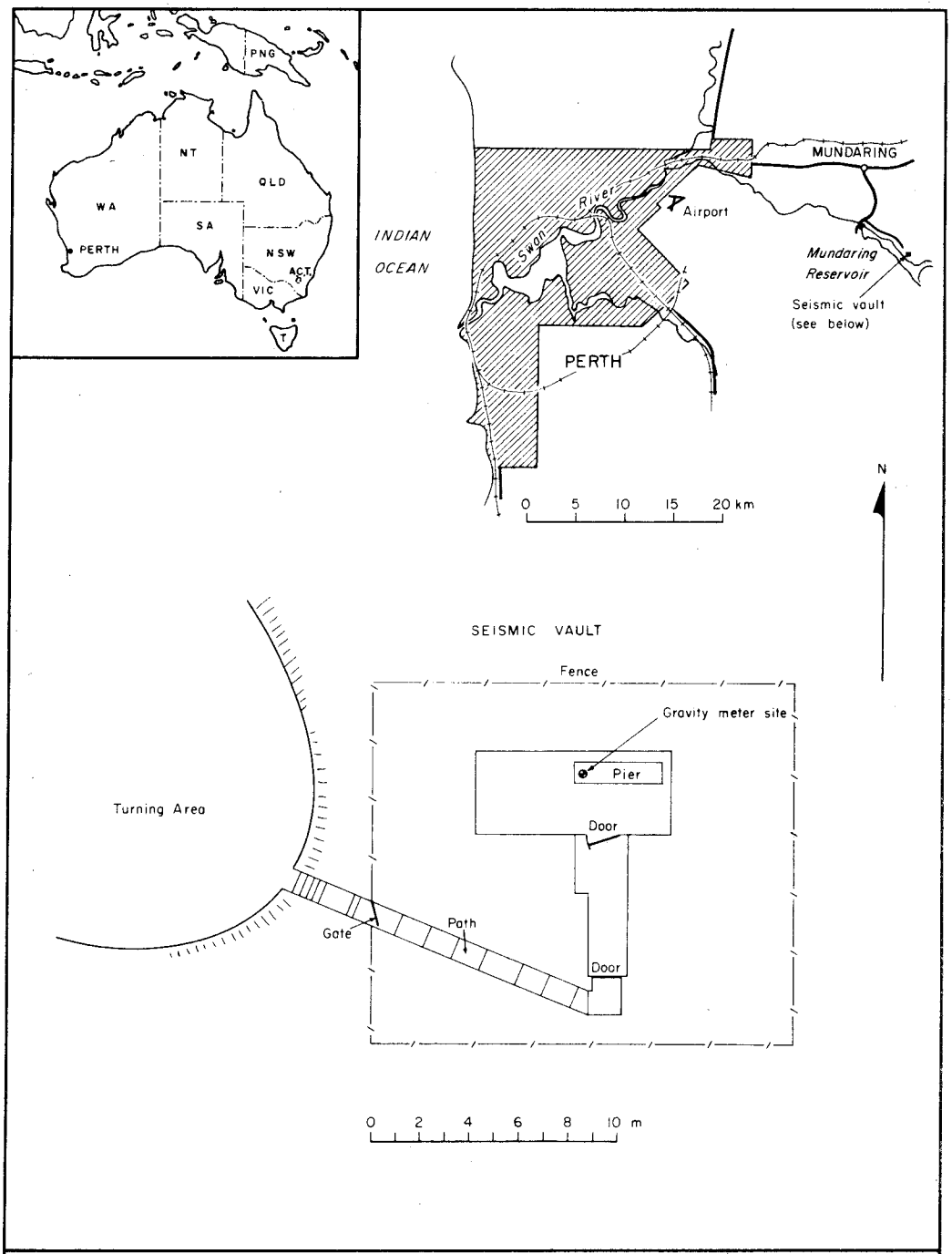

FIGURE B-5 **EARTH TIDE GRAVITY METER SITE PERTH (MUNDARING GEOPHYSICAL OBSERVATORY)**

H 50/82-32 A

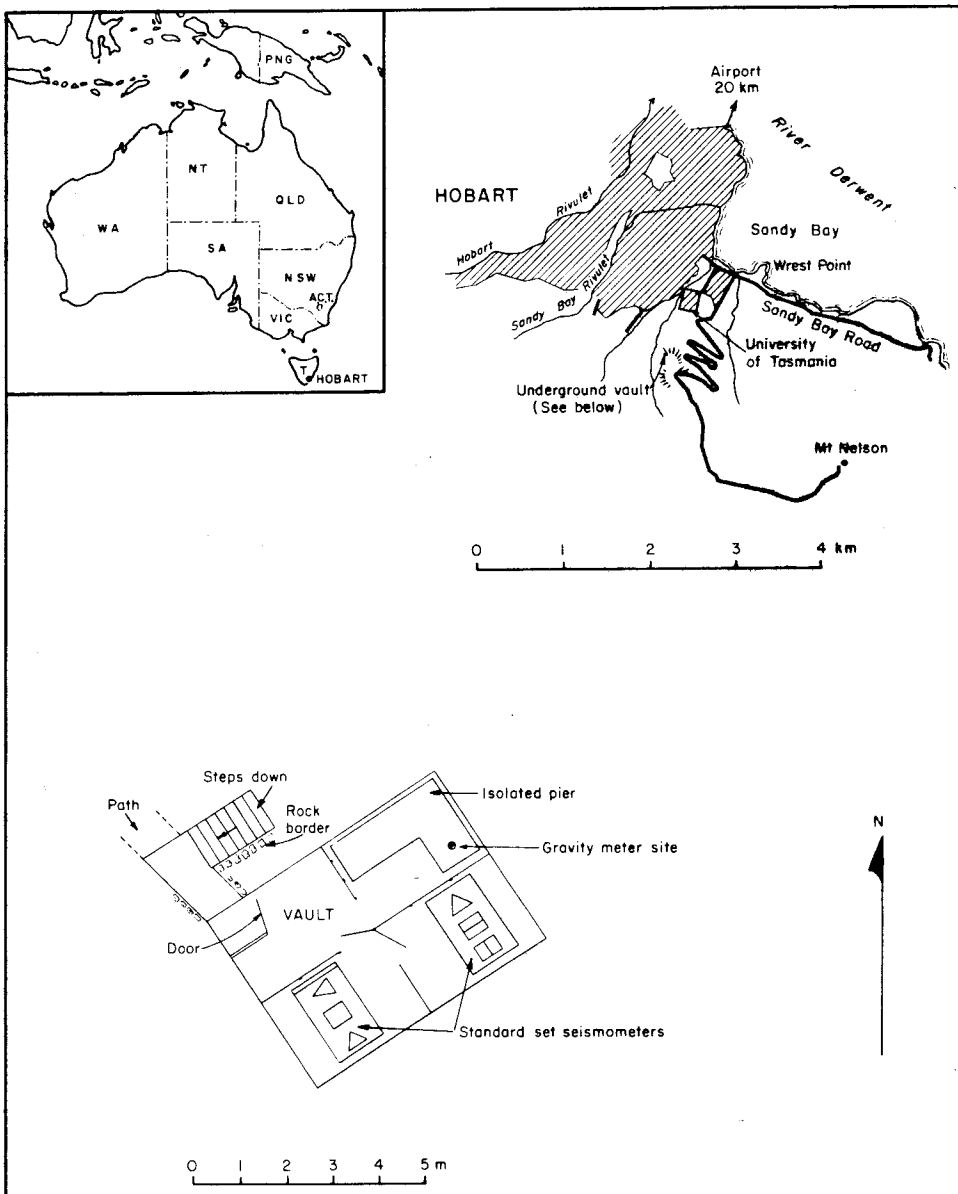

FIGURE B-6 EARTH TIDE GRAVITY METER SITE
HOBART (UNIVERSITY OF TASMANIA SEISMIC VAULT)

K55/B2-36A

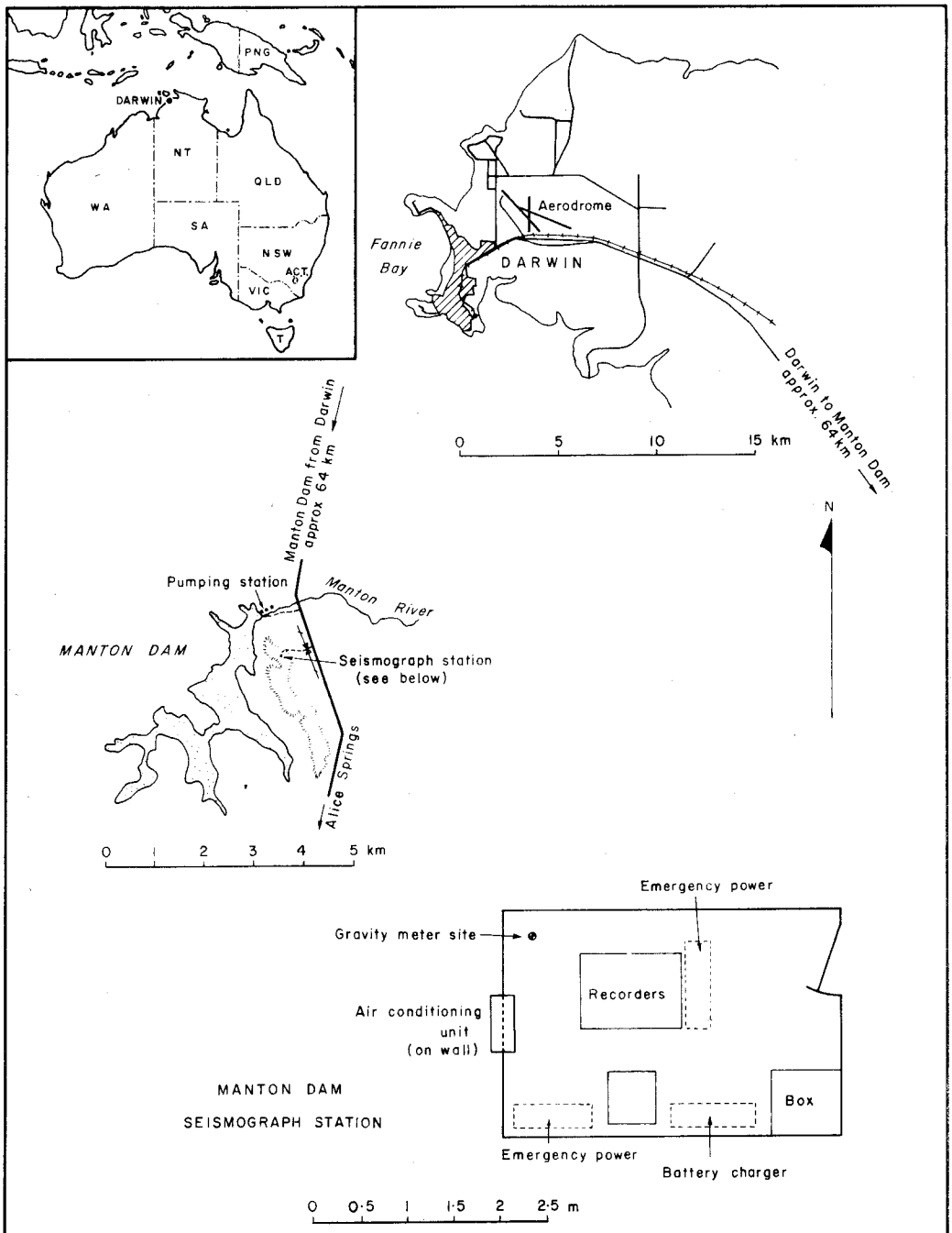

FIGURE B-7 **EARTH TIDE GRAVITY METER SITE DARWIN (MANTON SEISMOGRAPH STATION)**

D52/B2-38A

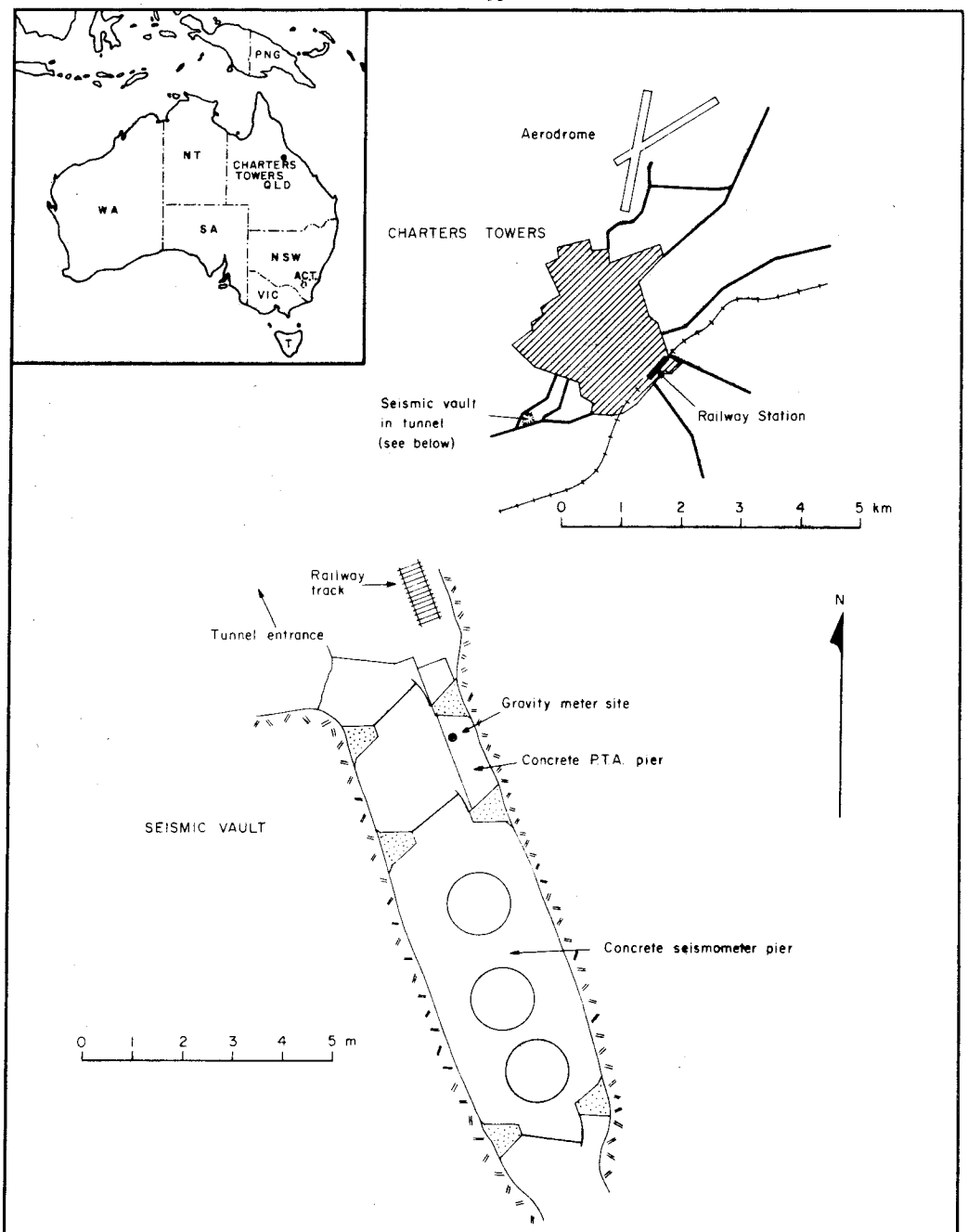

FIGURE B-8 **EARTH TIDE GRAVITY METER SITE CHARTERS TOWERS (SEISMOGRAPH STATION)**

F 55/82-83A

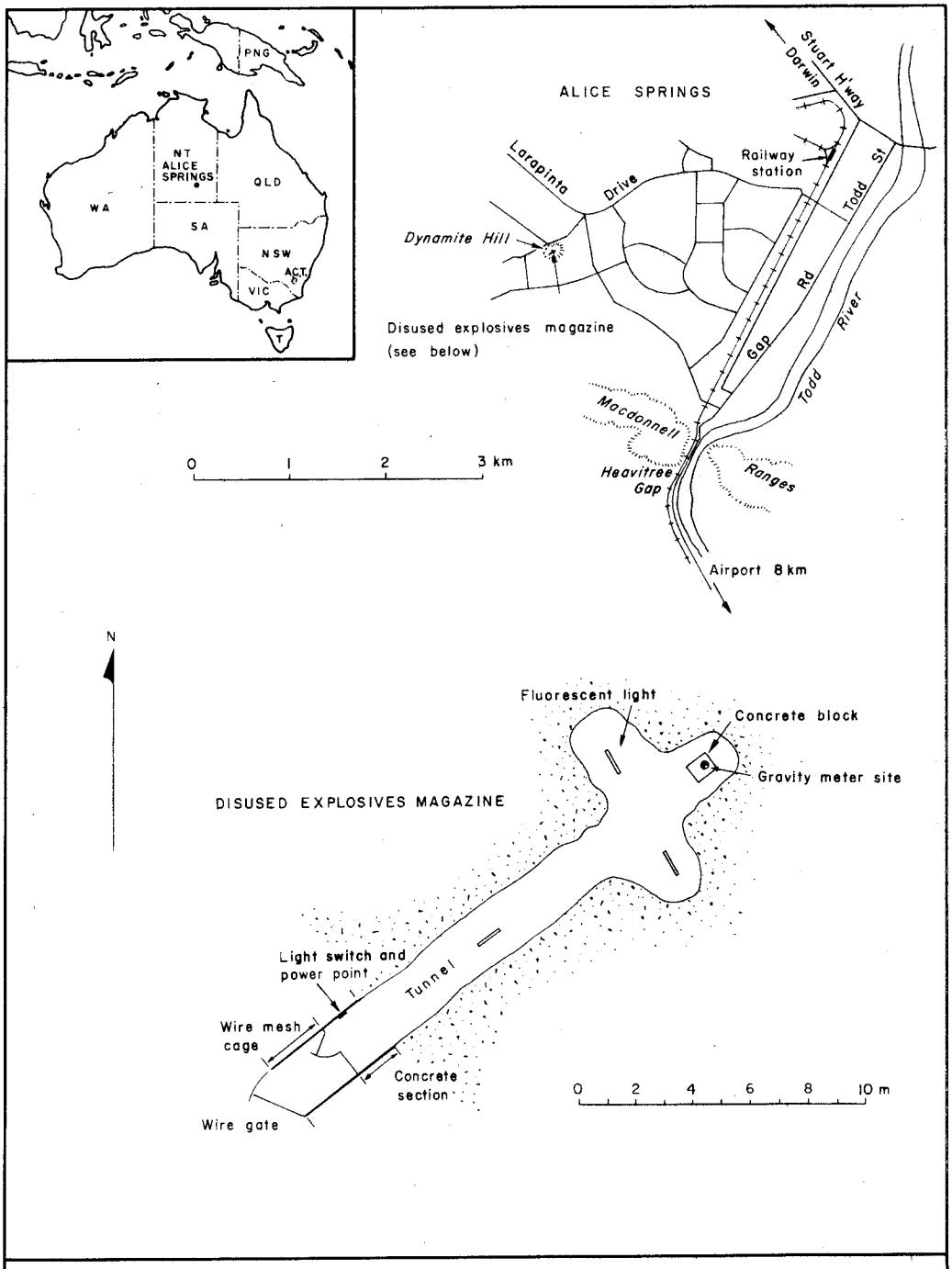

FIGURE B-9 **EARTH TIDE GRAVITY METER SITE ALICE SPRINGS (DISUSED EXPLOSIVES MAGAZINE)**

F53/B2-76A

Publications from

THE SCHOOL OF SURVEYING, THE UNIVERSITY OF NEW SOUTH WALES

P.O. Box I, Kensington, N.S.W. 2033

AUSTRALIA

Reports

1.*	The discrimination of radio time signals in Australia *G.G. Bennett*		*Unisurv Rep.* D-1	(G 1)
2.*	A comparator for the accurate measurement of differential barometric pressure *J.S. Allman*	9pp	*Unisurv Rep.* D-3	(G 2)
3.	The establishment of geodetic gravity networks in South Australia *R.S. Mather*	26pp	*Unisurv Rep.* R-17	(G 3)
4.	The extension of the gravity field in South Australia *R.S. Mather*	26pp	*Unisurv Rep.* R-19	(G 4)
5.*	An analysis of the reliability of barometric elevations *J.S. Allman*	335pp	*Unisurv Rep.* 5	(S 1)
6.*	The free air geoid for South Australia and its relation to the equipotential surfaces of the earth's gravitational field *R.S. Mather*	491pp	*Unisurv Rep.* 6	(S 2)
7.*	Control for mapping (Proceedings of Conference, May 1967) *P.V. Angus-Leppan (Editor)*	329pp	*Unisurv Rep.* 7	(G 5)
8.*	The teaching of field astronomy *G.G. Bennett & J.G. Freislich*	30pp	*Unisurv Rep.* 8	(G 6)
9.*	Photogrammetric pointing accuracy as a function of properties of the visual image *J.C. Trinder*	64pp	*Unisurv Rep.* 9	(G 7)
10.*	An experimental determination of refraction over an icefield *P.V. Angus-Leppan*	23pp	*Unisurv Rep.* 10	(G 8)
11.*	The non-regularised geoid and its relation to the telluroid and regularised geoids *R.S. Mather*	49pp	*Unisurv Rep.* 11	(G 9)
12.*	The least squares adjustment of gyro-theodolite observations *G.G. Bennett*	53pp	*Unisurv Rep.* 12	(G 10)
13.*	The free air geoid for Australia from gravity data available in 1968 *R.S. Mather*	38pp	*Unisurv Rep.* 13	(G 11)
14.*	Verification of geoidal solutions by the adjustment of control networks using geocentric Cartesian co-ordinate systems *R.S. Mather*	42pp	*Unisurv Rep.* 14	(G 12)
15.*	New methods of observation with the Wild GAKI gyro-theodolite *G.G. Bennett*	68pp	*Unisurv Rep.* 15	(G 13)
16.*	Theoretical and practical study of a gyroscopic attachment for a theodolite *G.G. Bennett*	343pp	*Unisurv Rep.* 16	(S 3)
17.	Accuracy of monocular pointing to blurred photogrammetric singals *J.C. Trinder*	231pp	*Unisurv Rep.* 17	(S 4)
18.	The computation of three dimensional Cartesian co-ordinates of terrestrial networks by the use of local astronomic vector systems *A. Stolz*	47pp	*Unisurv Rep.* 18	(G 14)
19.	The Australian geodetic datum in earth space *R.S. Mather*	130pp	*Unisurv Rep.* 19	(G 15)
20.*	The effect of the geoid on the Australian geodetic network *J.G. Fryer*	221pp	*Unisurv Rep.* 20	(S 5)
21.*	The registration and cadastral survey of native-held rural land in the Territory of Papua and New Guinea *G.F. Toft*	441pp	*Unisurv Rep.* 21	(S 6)
22.	Communications from Australia to Section V, International Association of Geodesy, XV General Assembly, International Union of Geodesy & Geophysics, Moscow 1971 *R.S. Mather et al*	72pp	*Unisurv Rep.* 22	(G 16)
23.	The dynamics of temperature in surveying steel and invar measuring bands *A.H. Campbell*	195pp	*Unisurv Rep.* S 7	

* Out of print

Publications from the School of Surveying
(contd.)

Reports (contd)

24. Three-D Cartesian co-ordinates of part of the Australian geodetic network by the use of local astronomic vector systems
A. Stolz 182pp *Unisurv Rep.* S 8

25. Papers on Four-dimensional Geodesy, Network Adjustments and Sea Surface Topography
R.S. Mather, H.L. Mitchell, A. Stolz 73pp *Unisurv* G 17

26. Papers on photogrammetry, co-ordinate systems for survey integration, geopotential networks and linear measurement
L. Berlin, G.J.F. Holden, P.V. Angus-Leppan, H.L. Mitchell and A. Campbell 80pp *Unisurv* G 18

27. Aspects of Four-dimensional Geodesy
R.S. Mather, P.V. Angus-Leppan, A. Stolz and I. Lloyd 100pp *Unisurv* G 19

28. Relations between MSL & Geodetic Levelling in Australia
H.L. Mitchell 264pp *Unisurv Rep.* S 9

29. Study of Zero Error & Ground Swing of the Model MRA101 Tellurometer
A.J. Robinson 200pp *Unisurv Rep.* S 10

30. Papers on Network Adjustments, Photogrammetry and 4-Dimensional Geodesy
J.S. Allman, R.D. Lister, J.C. Trinder and R.S. Mather 133pp *Unisurv* G 20

31. An Evaluation of Orthophotography in an integrated Mapping System
G.J.F. Holden 232pp *Unisurv Rep.* S 12

32. The Analysis Precision and Optimization of Control Surveys
G.J. Hoar 200pp *Unisurv Rep.* S 13

33. Papers on Mathematical Geodesy, Coastal Geodesy and Refraction
E. Grafarend, R.S. Mather and P.V. Angus-Leppan 100pp *Unisurv* G 21

34. Papers on Gravity, Levelling, Refraction, ERTS Imagery, Tidal Effects on Satellite Orbits & Photogrammetry
R.S. Mather, J.R. Gilliland, F.K. Brunner, J.C. Trinder, K. Bretreger and G. Halsey 96pp *Unisurv* G 22

35. Papers on Earth Tides, Sea Surface Topography, Atmospheric effects in physical geodesy, Mean sea level, Systematic errors in levelling
R.S. Mather, E.G. Anderson, C. Rizos, K. Bretreger, K. Leppert, B.V. Hamon, P.V. Angus-Leppan 96pp *Unisurv* G 23

36. Papers on Adjustment theory, Sea surface topography determinations, applications of Landsat imagery, Ocean loading of Earth tides, physical geodesy, photogrammetry and oceanographic applications of satellites
R. Patterson, R.S. Mather, R.C. Coleman, O.L. Colombo, J.C. Trinder, S.U. Nasca, T.L. Duyet, K. Bretreger *Unisurv* G 24

37. The Effect of Topography on Solutions of Stokes' Problem
E.G. Anderson 252pp *Unisurv Rep.* S 14

38. The Computation of Deflections of the Vertical from Gravity Anomalies
A.H.W. Kearsley 161 pp *Unisurv Rep.* S 15

39. Papers on Hydrostatic Equilibrium Figures of the Earth, Earth Tides, Gravity Anomaly Data Banks for Australia, Recovery of Tidal Signals from Satellite Altimetry, Meteorological Parameters for Modelling Terrestrial Refraction, Crustal Motion Studies in Australia
S.M. Nakiboglu, B. Ducarme, P. Melchior, R.S. Mather, B.C. Barlow, C. Rizos, B. Hirsch, K. Bretreger, F.K. Brunner, P.V. Angus-Leppan *Unisurv* G 25

40. Papers on Four Dimensional Geodesy, GEOS-3 Altimetry Data Analysis, Analysis of Meteorological Measurements for Microwave EDM, Meteorological Data Logging System for Geodetic Refraction Research
R.S. Mather, E.G. Masters, R. Coleman, C. Rizos, B. Hirsch, C.S. Fraser, F.K. Brunner, P.V. Angus-Leppan, A.J. McCarthy, C. Wardrop 113 pp *Unisurv* G 26

Reports (contd)

41. Papers on Micrometeorology in Geodetic Refraction, Landsat Imagery in Topographic Mapping, Adjustment of Large Systems, GEOS-3 Data Analyses, Kernel Functions, EDM Reductions over Sea
F.K.Brunner, C.S.Fraser, S.U.Nasca, J.C. Trinder, L. Berlin, R.S.Mather, O.L. Colombo P.V.Angus-Leppan 101 pp *Unisurv G 27*

42. Earth Tide Effects on Geodetic Observations
K. Bretreger 173 pp *Unisurv S 16*

Proceedings

Proceedings of conference on refraction effects in geodesy & electronic distance measurement
P.V.Angus-Leppan (Editor) 264 pp Price: $10.00**

Australian Academy of Science/International Association of Geodesy Symposium on Earth's Gravitational Field & Secular Variations in Position
R.S. Mather & P.V. Angus-Leppan (eds) 764 pp Price: $20.00**

Monographs

1. The theory and geodetic use of some common projections (2nd edition)
R.S. Mather 125 pp Price: $5.00**

2. The Analysis of the earth's gravity field
R.S. Mather 172 pp Price: $5.00**

3. Tables for Prediction of Daylight Stars
G.G. Bennett 24 pp Price: $2.25**

4. Star Prediction Tables for the fixing of position
G.G. Bennett, J.G.Freislich & M.Maughan 200 pp Price: $8.00**

5. Survey Computations
M. Maughan 98 pp Price: $3.50**

6. Adjustment of Observations by Least Squares
M. Maughan 57 pp Price: $3.50**

7. Introduction to Electronic Distance Measurement
J.M. Rueger 122 pp Price: $5.00** Individuals
$8.00** Libraries

** Including postage

Prices

G. General Series

Subscription for 1978 Postfree
To Libraries $16.
To Individuals $ 11.

S. Special Series (Limited Printing)

Postfree
To Libraries $17. each copy
To Individuals $12. each copy.